Characterization of a Pressure Sensitive Adhesive (PSA) for Mechanical Design

by

John Hennage

Thesis submitted to the Faculty of Virginia Polytechnic Institute and State University in partial fulfillment of the requirements of the degree of

MASTER OF SCIENCE

in

MECHANICAL ENGINEERING

APPROVED:

L. D. Mitchell, Chairman

R. L. West **D. C. Ohanehi**

October 12, 2004

Blacksburg, Virginia

Keywords: PSA, Adhesive, Strength, Design

Characterization of a Pressure Sensitive Adhesive (PSA) for Mechanical Design

by

John Hennage

Committee Chairman: L. D. Mitchell
Mechanical Engineering

Abstract

This thesis outlines a methodology for formatting and applying stress models, collecting visco-elastic material properties, and presenting the material data for use in adhesive joint designs. There are a number of models/theories that can be applied to the design of Pressure Sensitive Adhesive (PSA) joints. Unfortunately, few design engineers are familiar with these models and the models are not formatted in a manner that can easily be applied to joint designs. By developing a format that is based on the existing knowledge of the designer and presenting them in a familiar manner the theories/models can easily be used in joint designs. This technique was demonstrated with Beam-on-Elastic Foundation, Shear Lag, and Shape Factors. Design examples successfully demonstrated the application of all of these models in the analysis and design of simple adhesive joints.

The material properties of PSAs are a function of loading/displacement rate, temperature, relative humidity, and stress state. The Arcan$_m$ fixture was used to test VHB™ 4950 over a range loading and stress states including fixed load and displacement rates. Several bond widths were tested to determine the extent of the shape factor effect. A second fixture was used to determine the impact of gradient-tensile stresses on the failure strength.

All of the collected data was used to generate design plots. The strength data was presented as allowable strength envelopes with respect to rate. The moduli were calculated from the load-displacement data and plotted with respect to the displacement rate. The failure strength from the fixed load and displacement data were used to transform from one loading case to the other and a plot was generated. These three plots were used in the design and analysis of several adhesive joints.

The methods demonstrated in this thesis show a great deal of promises as a design tool, but there is still a large amount of work to be done. The design space for this material is much larger than what was covered by this work. Additional strength testing needs to be conducted to fully characterize the material for all key applications. The principle of time-temperature superposition, beam-on-elastic foundation, shear lag, and shape factors all need to be validated for this material.

Dedication

This is for you granddad.

Over the past few years I have come to realize that much of who I am and how I view live is because of my grandfather. It has taken me a long time to appreciate and understand many of the pieces of wisdom that he imparted to me. I can only hope that I will eventually come to understand every thing that he told and showed me. I only wish that I had been able to learn more from him

Thank you for everything and I love you.

F. A. Hennage Sr., 1910-1990.

Acknowledgements

I would be remiss if I didn't thank everyone that had a hand in the completion of this research. There were a number of faculty, staff, students, and departments that made this research possible.

Both Appy Hayes and Josh Grohs helped conduct the numerous tests. Ali Feizollahi spent countless hours making the hundreds of specimens that were required. Bob West, Dave Dillard, John Dillard, and Don Ohanehi provided continuous input and advice on conducting the experiments and interpreting the data. Dave Simmons and Darrell Link made the many fixtures and jigs become a reality. The Department of Mechanical Engineering and the Department of Engineering Science and Mechanics provided me with the office and lab space necessary to conduct this research.

Most of all, I would like to thank Larry Mitchell for taking a chance on me and acting as my advisor. I know that I am not the typical student and may not be the easiest to work with, especially when it comes to timelines. I am grateful for all of your understanding, guidance, and friendship. I will try to make the next step a little easier.

Lastly, I would like to recognize the support and guidance provided by 3M Corporation, without which this project would not have been possible.

Table of Contents

Table of Contents (Continued)

List of Figures

List of Figures (Continued)

List of Figures (Continued)

List of Figures (Continued)

List of Tables

Nomenclature

Symbol	Quantity	Units[1]
A	Area	m^2
E	Modulus of Elasticity (Young's Modulus)	Pa
E_{app}	Apparent Modulus of Elasticity	Pa
F	Distributed Load	N/mm
G	Modulus of Rigidity (Shear Modulus)	Pa
I	Area Moment of Inertia	mm^4
J	Rotational Moment of Inertia	mm^4
K	Stiffness	N/mm
K_{app}	Apparent Stiffness	N/mm
K_{sys}	System Stiffness	N/mm
K_{g1}	Geometric Stress Concentration Factor (Tensile)	Dimensionless
K_{efl}	Elastic Foundation Stress Concentration Factor	Dimensionless
K_{g2}	Geometric Stress Concentration Factor (Shear)	Dimensionless
K_t	Theoretical Stress Concentration Factor	Dimensionless
L	Moment Arm Length	mm
M	Moment	N-m
N	Safety Factor	Dimensionless
N_l	Load Safety Factor	Dimensionless
N_s	Stress Safety Factor	Dimensionless
P	Applied Load	N
P_d	Design Load	N
P_u	Ultimate Load	N
R_d	Displacement Rate	mm/min
R_{eff}	Effective Displacement Rate	mm/min
RH	Relative Humidity	%
R_l	Load Rate	N/s
S_s	Strength in Shear	Pa
S_{sy}	Yield Strength in Shear	Pa
S	Strength in Tension	Pa
S_y	Yield Strength in Tension	Pa
T	Torque	N-m
$Temp$	Temperature	°C
T_g	Glass Transition Temperature	°C
a	Regression Variable	MPa/Deg^2
a_H	Relative Humidity Shift Factor	Dimensionless
a_T	Temperature Shift Factor	Dimensionless
b	Regression Variable	MPa/Deg
c	Distance From Centroid	mm
d	Regression Variable	MPa
h	Total Thickness	mm
l	Bond Length	mm

[1] Unless otherwise stated

Nomenclature (Continued)

Symbol	Quantity	Units
k	Beam-on-Elastic Foundation Parameter	Pa
p	Probability of Failure	%
r	Distance From Center	mm
t	Thickness	mm
u_d	Distortion Energy	$Nm/m^3(Pa)$
w	Width	mm
x	Position	mm
ΔT	Change in Temperature	˚C
α	Coefficient of Thermal Expansion	Dimensionless
β	Beam-on-Elastic Foundation Parameter	mm^{-1}
δ	Displacement	mm
ε	Normal Strain	mm/mm
ε_t	Thermal Strain	mm/mm
ε_{xy}	Shear Strain (Single Face)	rad
λ	Beam-on-Elastic Foundation Parameter	mm^{-1}
θ	Rotation Angle	rad
θ_{Arcan}	Arcan Loading Angle	rad
θ_{eff}	Effective Rotation Angle	rad
γ	Engineering Shear Strain	rad
ν	Poisson's Ratio	Dimensionless
ρ	Radius of Curvature	mm
σ	Normal Stress	Pa
σ_d	Design Normal Stress	Pa
σ_{eng}	Engineering Normal Stress	Pa
$\sigma_{1,2,3}$	Principal Normal Stress	Pa
$\sigma_{f,}$	Failure Normal Stress	Pa
$\sigma_{,MDET}$	Von Mises Stress	Pa
σ_{MMST}	Maximum-Shear-Stress-Theory Stress	Pa
τ	Shear Stress	Pa
τ_{eng}	Engineering Shear Stress	Pa
$\tau_{1,2}$	Principal Shear Stress	Pa
ω	Stiffness Ratio	mm^{-1}

Subscript

a	Adhesive
ave	Average Value
max	Maximum Value
s	Substrate (Adherend)
x	In the x direction
y	In the y direction

1.0 Introduction

The purpose of this thesis is to outline a methodology for collecting, presenting, and applying visco-elastic data for a pressure sensitive adhesive (PSA) intended for use in structural-joint design. The use of PSAs is common in some industries and has been so for many years, yet the design methodology is not well known by most mechanical designers. There are many applications that would benefit from the ability of PSAs to bond dissimilar materials and provide a continuously sealed bond line. The lack of knowledge tends to decrease the use of PSAs or completely eliminates them from consideration in joint designs. This thesis focuses on three areas critical to the success and widespread acceptance of adhesives in the design community.

Designers need to be become familiar with the modeling tools available to predict the stress distributions in adhesive joints and rate/temperature/humidity dependence of adhesive properties. This must be done in a manner that builds on the existing knowledge and experience that is possessed by the design engineer. Without this link to current engineering understanding, the methods will be rejected by the productivity driven engineer. This can be accomplished by formatting these theories in a manner that is similar to techniques already used in the design community, such as stress concentration factors. This approach will be demonstrated for Beam-on-Elastic-Foundation Theory, Shear-Lag Theory, and Shape-Factor Theory. In addition, an overview of Time-Temperature-Superposition will be given with respect to the impact that load rate and temperature have on the adhesive material properties.

There are many material properties that need to be determined in order to fully characterize a PSA for use in mechanical design. Unlike many engineering materials, the material properties of PSAs vary widely with respect to temperature, stress/strain rate, and relative humidity. It is common for the modulus to vary by several orders of magnitude with respect to temperature. This requires all material properties be known over a range of operating conditions. In this thesis a modified Arcan test fixture was used to collect strength and modulus data over a range of test conditions. The majority of the data was collected using displacement rates of 0.05, 0.5, 5.0, and 50 mm/min. These rates were applied to loading angle of 0, 30, 60, and 90° with 0° being pure tension and 90° being pure shear. Additional Arcan testing was conducted to determine the relationship between fixed-load rate and fixed-displacement rate as well as to study shape-factor theory validity. A second fixture was used to gain insight on the impact of gradient tensile stresses on adhesive strength. To better demonstrate the impact of time-temperature superposition shift-factor data was presented. Time-temperature superposition analysis and the associated data is outside the scope of this thesis, but was necessary to bring everything together and better demonstrate the complexity of adhesive joint design and analysis.

All the material data in the world doesn't do any good at all unless it can be interpreted by the designer. With this in mind this thesis outlines a method for generating strength-based failure envelopes and moduli curves from the acquired test data. The stress-based failure envelopes are a graphical representation of the failure/allowable stresses under

given loading conditions. The concept of defining an allowable stress is well understood by design engineers and is used in strength-based designs. The design envelopes will allow the engineer to use traditional design methods including safety factors and probabilistic design techniques.

For PSAs to become more widely accepted their material properties and design techniques need to be available to design engineers. By generating a design methodology that is based upon material properties that are familiar to engineers, the understanding of and confidence in PSA-joint design will be enhanced.

2.0 Literature Review

Understanding the concepts and the analyses presented in this thesis requires the understanding of some basic concepts in material testing and stress analysis. To facilitate this understanding an overview of these concepts is presented. Particular attention has been given to the analysis of PSAs.

2.1 Material Testing

To complete any joint design it is necessary to have the material properties to begin the analysis. In order to get the mechanical properties it is necessary to test the material. There are many standard test methods for determining the material properties of PSAs used in bonded joints. Those issued by the American Society of Testing and Materials (ASTM) are the most commonly used. The ASTM has issued standards for a wide variety of test specimen geometries and loading conditions including tensile, shear, cleavage, and peel. These test geometries are shown in Figure 2.1-1.

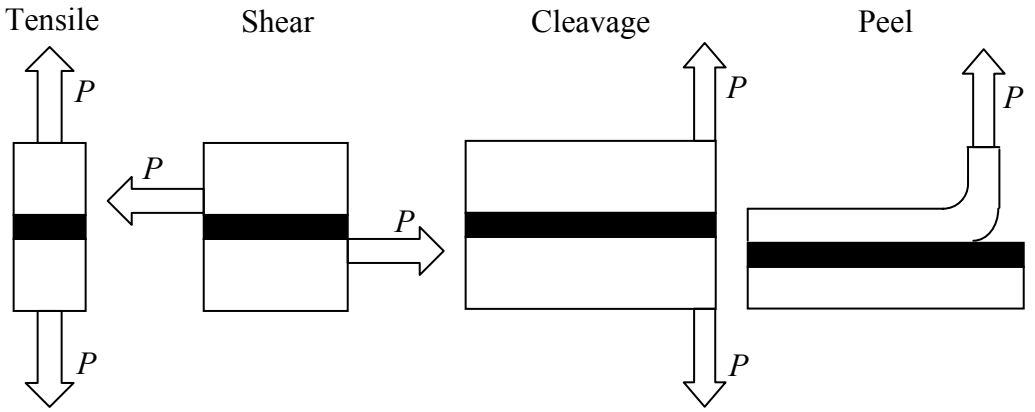

Figure 2.1-1 Joint geometries for various ASTM Tests.

A brief overview of the ASTM standards relevant to PSAs can be found in Table 2.1-1 [1]*. It should be noted that the analysis techniques for many of these tests result in average stress or load values. For example, the stress calculated under ASTM D897-95a (Tensile Properties of Adhesive Bonds) results in an average tensile stress. No mention is given to the possibility of a stress distribution or a method of calculating the peak stress.

In real-world applications most joints are not loaded in simple tensile or shear. The stress state results from a combination of many components. Shear, normal, bending, and torsional stresses may all be present. At this time, ASTM does not have standards for testing a range of biaxial stress states. Even the ASTM standards for testing in cleavage specify that only the failure load/unit width be recorded. The individual bending and

* Numbers in brackets refer to references listed at the end of each chapter.

normal stress components are not calculated. The material properties need to be known for all possible stress states or each joint must be redesigned to only have pure shear or pure normal loading. The reality is that this redesign is not practical or possible in many situations. To be useful in design the material properties need to be known for the entire application range of stress states.

Table 2.1-1 Standards for testing PSAs.

Designation	Title
ASTM D 896–96	Standard Test Method for Resistance of Adhesive Bonds to Chemical Reagents
ASTM D 897-95a	Standard Test Method for Tensile Properties of Adhesive Bonds
ASTM D 950	Standard Test Method for Impact Strength of Adhesive Bonds
ASTM D 1151	Standard Test Method for Effect of Moisture and Temperature on Adhesive Bonds
ASTM D 3433-93	Standard Test Method for Fracture Strength in Cleavage of Adhesive in Bonded Metal Joints
ASTM D 543-95	Standard Practice for Evaluating the Resistance of Plastics to Chemical Reagents
ASTM D 1002-99	Standard Test Method for Apparent Shear Strength of Single-Lap-Joint Adhesively Bonded Metal Specimens by Tension Loading (Metal-to-Metal)
ASTM D 3330/ D 3330M-99	Standard Test Methods for Peel Adhesion of Pressure-Sensitive Tape
ASTM D 3654 / D 3654M-96e1	Standard Test Method for Holding Power of Pressure-Sensitive Tapes
ASTM D 3762-98	Standard Test Method for Adhesive-Bonded Surface Durability of Aluminum (Wedge Test)
ASTM D 3933	Practice for Preparation of Aluminum Surfaces for Structural Adhesives (Phosphoric Acid Anodizing)
ASTM D 3983-98	Standard Test Method for Measuring Strength and Shear Modulus of No rigid Adhesives by the Thick-Adherend Tensile-Lap Specimen
ASTM D 3654–96	Standard Test Method Holding Power of Pressure-Sensitive Tapes
ASTM D 3759–96	Standard Test Method for Tensile Strength and Elongation of Pressure-Sensitive Tapes
ASTM D 3715–98	Standard Practice for Quality Assurance for Pressure-Sensitive Tapes
ASTM E 229-2003 (Withdrawn)	Standard Test Method for Shear Strength and Shear Modulus of Structural Adhesives (Napkin Ring)

2.1.1 Arcan

The "Arcan" fixture consists of a "butterfly" specimen installed in a circular aluminum plate with two asymmetric cutouts, see Figure 2.1.1-1. The "butterfly" is typically cast or machined as one continuous piece. The shape of the specimen concentrates the stress at the center where it has the smallest cross section.
The "Arcan" test fixture was developed to collect strength data on fiber-reinforced materials (FRM) under various biaxial stress states [2,3,4]. The FRM was tested at loading angles from -25º to 25º (0º was referenced as a pure tensile stress state) in 5º increments. The failure loads were recorded and average shear (τ_{ave}) and normal (σ_{ave}) stresses calculated using simple sine and cosine relationships. The average stresses at failure were then cross plotted. This data was then fit using several different failure theories and complete failure envelopes generated.

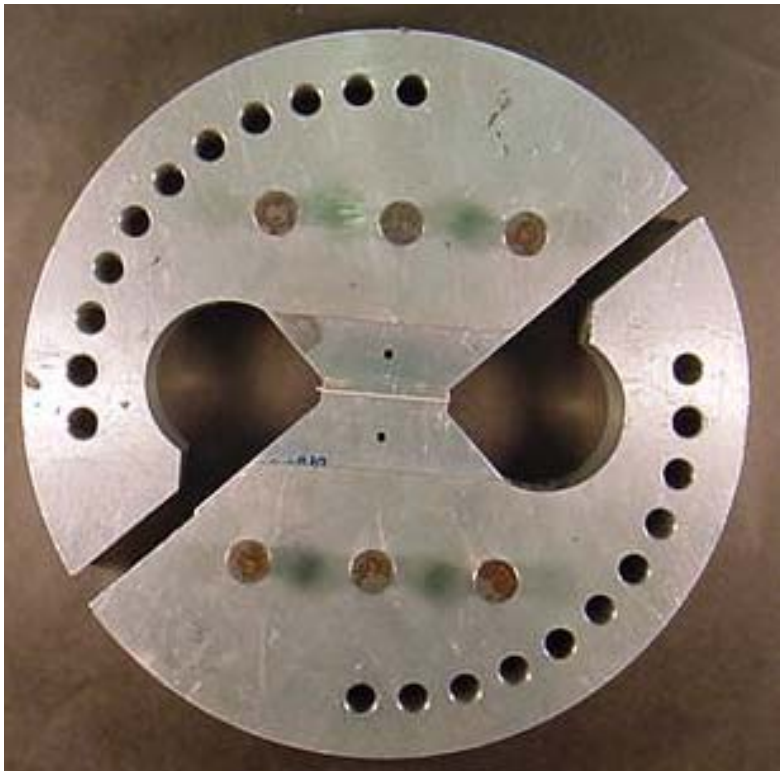

Figure 2.1.1-1 "Arcan" test fixture.

2.1.2 Dynamic Mechanical Analysis (DMA)

Dynamic Mechanic Analysis (DMA) is used to determine constitutive properties of a material over a range of excitation frequencies and temperatures [5]. Both shear and tensile tests can be conducted. However, shear testing can only be conducted above the glass transition temperature (T_g) of the material. Testing below the T_g requires the use of a correctly configured rheology machine. From the data collected the modulus of

elasticity (E) and modulus of rigidity (G) can be determined as functions of frequency and temperature.

In real-world applications it is difficult to define the proper modulus for use in an analysis. For example, with thin adhesive specimens, the determination of the modulus of elasticity becomes problematic since the adhered portions of the PSA are not free to contract under Poisson's Ratio effects. The adhesive interfaces are in a state of nearly plane strain, while the material near the center of the PSA is able to contract under the Poisson's Ratio effect in both in-plane directions, thus approaching plane stress. This results in a mixed plane-stress and plane-strain test specimen (see section 2.4). Attempts have been made to correct for such conditions through the use of shape factors [6,7,8]. However, such corrections are limited because the factors are dependent upon specimen shape, Poisson's Ratio, and proportions. Good estimates of shape factors for specific specimens may not be available. Therefore, the most reliable data from the DMA is the shear modulus which is thought by many to have no shape factor effects. Using the shear modulus it is possible to estimate the tensile modulus using the relationships discussed in section 2.4. This unfortunately does not solve the problem of determining the in-situ tensile modulus. Again, the in-situ properties will depend on the joint geometry and may only be determined by experimentation if the joint shape factor has not already been determined.

Using the principle of linear superposition this data can be analyzed to generate master curves and shift-factor plots. This allows the constitutive properties to be predicted outside of the test region of temperature, loading frequency, or relative humidity [5, 6].

2.2 Stress Calculations

The start of any joint design requires a stress analysis of the load-bearing members. In order to determine the stress state it is necessary to have an understanding of the materials used in the design and how they interact with each other. In many cases the engineer has to make some assumptions in order to complete the analysis. Typically, the material is assumed to be homogeneous and isotropic. These assumptions greatly simplify the calculations required to determine the normal, shear, bending, and torsional stresses.

2.2.1 Normal Stress

The application of a centric tensile load results in a normal stress (σ). Typically, σ is calculated using Equation (2.2.1-1) which uses the original cross sectional area (A) and is known as the engineering or average stress. This is an average stress and should only be used away from the loading point. The stresses at a concentrated load will be higher than the rest of the cross section and require a different analysis technique. Use of Equation (2.2.1-1) in the analysis of an adhesively bonded joint requires adherends that are rigid relative to the PSA.

$$\sigma_{ave} = \frac{P}{A} = E\varepsilon \text{ (Plane Stress)} = \frac{E\varepsilon}{1-\nu^2} \text{ (Plane Strain)} \qquad (2.2.1\text{-}1)$$

For Poisson's Ratio (ν), see section 2.3, equal to 0.5 the plane strain version of Equation (2.2.1-1) becomes the more familiar form shown in Equation (2.2.1-2)

$$\sigma_{ave} = \frac{4}{3}E\varepsilon \text{ (Only for } \nu\text{=0.5, incompressible)} \qquad (2.2.1\text{-}2)$$

If the tensile load is eccentric from the center of the support provided by the PSA patch a moment (M) is generated. The moment produces an additional normal stress. The moment-based normal stress is calculated using Equation (2.2.1-3), where c is the distance from the centroid of the cross-section to the outer fiber and I is the area moment of inertia.

$$\sigma(c) = \frac{Mc}{I} \qquad (2.2.1\text{-}3)$$

The magnitude and sign of the moment-based stress depend on the direction of the moment and the signed distance from the centroid. Assuming linear superposition, the axial-load-based normal stress and the moment-based normal stress can be added together vectorially to calculate the total normal stress. This assumption will have limitations should the stress-strain diagram for the adhesive be substantially nonlinear in the calculated stress range.

In a bonded joint Equation (2.2.1-1) may not be a good approximation of the peak stress. The constraints imposed by the bond line result in a non-uniform stress distribution across the width of the bond. The bond line will be in a combined shear and normal stress state. The shear stress results from the bond-line resistance to transverse motion in the adhesive resulting from Poisson's Ratio effects. The analysis for a long, incompressible strip has been developed by Gent and Meinecke[6]. The geometry and resulting mathematical model for this analysis are shown in Figure2.2.1-1 and Equation (2.2.1-4). In Figure 2.2.1-1 F is the force per unit length of the beam.

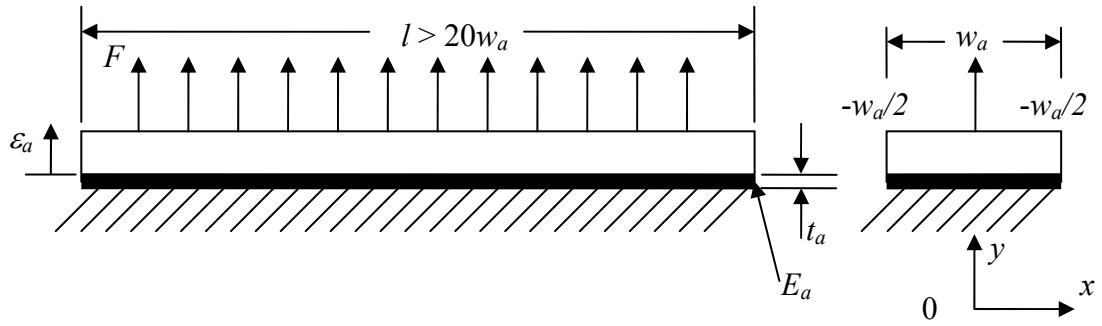

Figure 2.2.1-1 Shape factor geometry – Rigid-infinite beam.

$$\sigma_a(x) = E_a \varepsilon_a \left(\frac{4}{3} + \frac{w_a^{\,2}}{2t_a^{\,2}} - \frac{2x^2}{t_a^{\,2}} \right) \qquad (2.2.1\text{-}4)$$

This analysis will be within 5% as long as the bond length (l) is 20 times the bond width (w_a). In this equation x has a range of $\pm w_a / 2$ and the bulk adhesive Poisson's Ratio (v_a) is assumed to be 0.5 (see section 2.3). In this system σ_a is not uniform across the width as one would expect based on the engineering stress, Equation (2.2.1-1). It should be noted that under a constant adhesive strain (ε_a), adhesive modulus of elasticity (E_a), and adhesive thickness (t_a) the stress level in the center of the cross section is a function of the bond width (w_a). This is driven by the second term in Equation (2.2.1-4). Stress gradients have been shown to exist in circular and semicircular geometries [7, 8] as well as the rectangular geometries discussed here.

Engineers are familiar with geometric effects that result in higher stress states than those predicted by the average engineering stress. These effects have been dealt with by applying a theoretical stress concentration factors (K_t). For example, engineers use stress concentration factors to account for shaft chamfer radii as well as holes and notches in plates when performing strength-based designs. This is critical when performing fatigue failure analysis.

For this geometry the solution of Equation (2.2.1-4) for $x = \pm w_a / 2$ is equivalent to σ_{ave} as defined in Equation (2.2.1-2). It is convenient to reformulate Equation (2.2.1-4) into a geometric stress concentration factor (K_{g1}) referenced to σ_{ave} (plane stress) as indicated in Equation (2.2.1-5).

$$K_{g1}(x) = \frac{\sigma_a(x)}{\sigma_{eng}} = \frac{E_a \varepsilon_a \left(\frac{4}{3} + \frac{w_a^{\,2}}{2t_a^{\,2}} - \frac{2x^2}{t_a^{\,2}} \right)}{E_a \varepsilon_a} = \frac{4}{3} + \frac{1}{2}\left(\frac{w_a}{t_a} \right)^2 - 2\left(\frac{x}{t_a} \right)^2 \qquad (2.2.1\text{-}5)$$

In this equation the K_{g1} is a function of x. This is not the form that engineers are accustomed to seeing. One will notice that σ_{eng} is used in this equation. This is done to indicate that engineering judgment was used in determining the method used to perform a calculation. This convention will be used throughout the text to call attention to these decisions.

The peak σ_a is at $x = 0$ and this is the stress of interest, therefore, this is the K_{g1} of interest. Solving Equation (2.2.1-5) for $x = 0$ results in Equation (2.2.1-6).

$$K_{g1} = \frac{\sigma_a(0)}{\sigma_{eng}} = \frac{E_a \varepsilon_a \left(\frac{4}{3} + \frac{w_a^{\,2}}{2t_a^{\,2}} \right)}{E_a \varepsilon_a} = \frac{4}{3} + \frac{1}{2}\left(\frac{w_a}{t_a} \right)^2 \qquad (2.2.1\text{-}6)$$

This equation can be represented graphically with K_{g1} as a function of the adhesive width to thickness ratio (w_a / t_a) as shown in Figure 2.2.1-2.

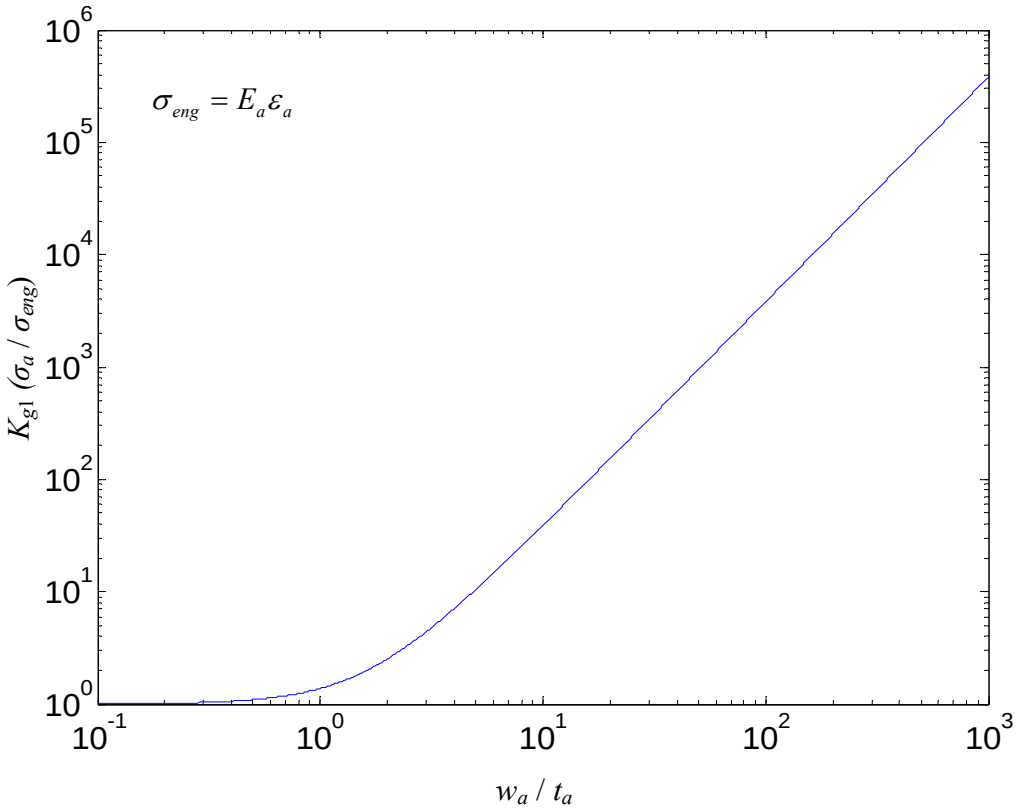

Figure 2.2.1-2 Stress Concentration Factor vs. w_a / t_a for l / w_a > 20.

This indicates that the peak adhesive stress can be considerably higher than what would be predicted by the engineering stress. Calculating the normal stress within a PSA joint requires an understanding of the stress gradient for the specific joint geometry. Great care must be taken when calculating σ_a using these equations due to the assumption that v_a is 0.5. It has been shown by Dillard and Lai [9] that a 1% change in v_a can result in an 80% drop in the peak σ_a.

If the joint consists of a flexible adherend bonded to a rigid or flexible adherend with a PSA it is necessary to use a beam-on-elastic-foundation analysis. The solution to a flexible adherend bonded to a rigid adherend with a transverse end loading was developed by Winkler [10]. The joint can be end loaded with a force (P), a moment (M), or both as indicated in Figure 2.2.1-3. Winkler's beam-on-elastic-foundation model is shown in Equations (2.2.1-5) and (2.2.1-6) [10] and plotted in Figure 2.2.1-4.

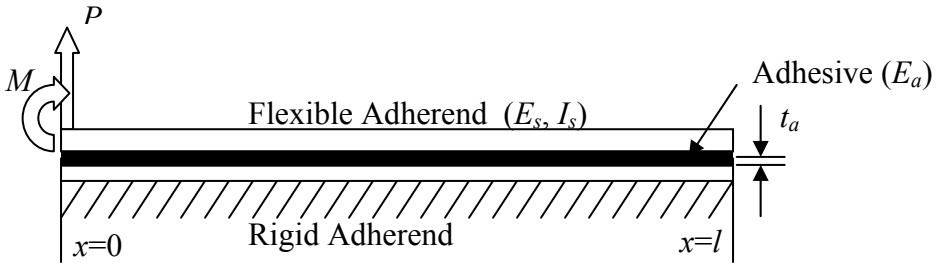

Figure 2.2.1-3 Beam-on-elastic-foundation geometry.

$$\sigma_a(x) = \frac{E_a}{2t_a E_s I_s \beta^3} e^{-\beta x}\left[P\cos(\beta x) + M\beta(\cos(\beta x) - \sin(\beta x))\right] \qquad (2.2.1\text{-}4)$$

$$\beta = \sqrt[4]{\frac{E_a w_a}{4E_s I_s t_a}} \qquad (2.2.1\text{-}5)$$

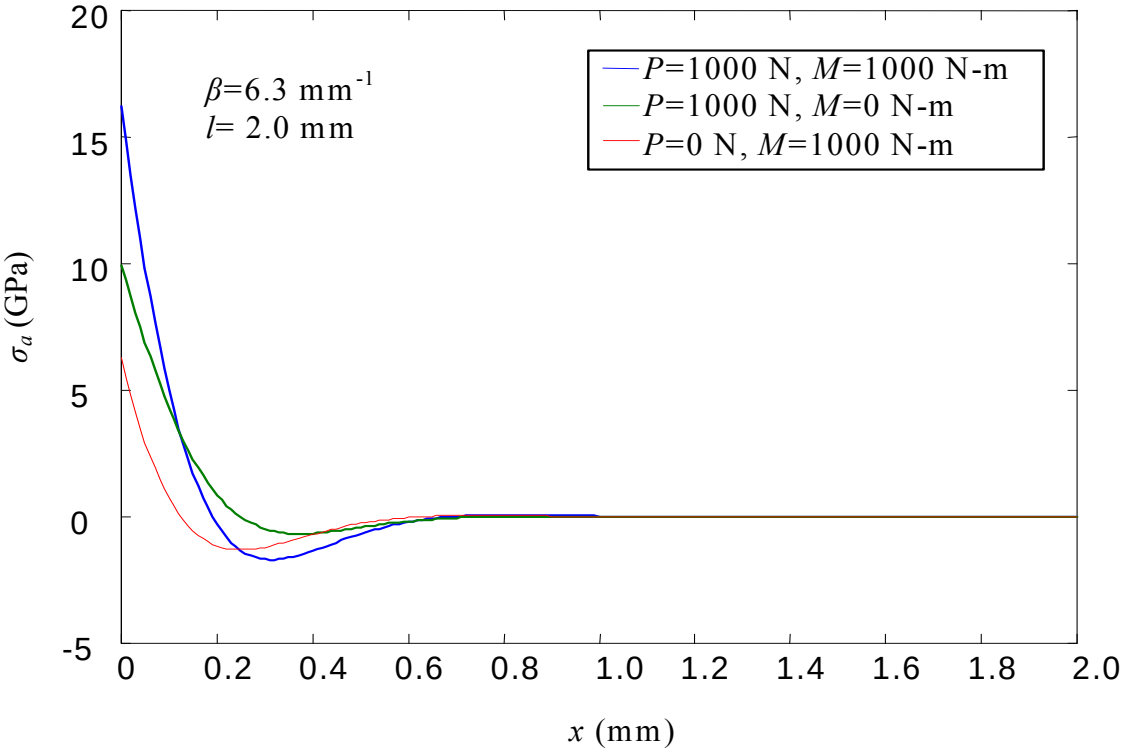

Figure 2.2.1-4 Beam-on-elastic foundation with end load and moment.

This model only considers a transverse stress state and is only valid if the total bond length (l) is greater than 5 / β, because of an assumption of infinite bond length. As shown in Figure 2.2.1-4, the stress at the end of the beam is much greater than the stress in the remaining section. For the load cases shown there is approximately zero load carried by the section past 1.0 mm. If the stress were calculated using Equation (2.2.1-1), the engineering stress, the stress level would be grossly underestimated.

This analysis is a good starting point to get a better understanding of the stress distributions associated with flexible adherends. The analysis of other loading conditions, finite lengths, and a variety of boundary conditions can be found in Hetenyi [11] as well as Young [12]. For example, the solutions for the peak displacement in a finite strip supported by an elastic foundation with an end load is shown in Equations (2.2.1-6), (2.2.1-7), and (2.2.1-8). This geometry is the same as the one shown in Figure 2.2.1-3 with the load (P) applied at the midpoint and the moment (M) equal to zero.

$$\delta_{max} = \frac{2P\lambda}{k} * \frac{\sinh(\lambda l)\cosh(\lambda l) - \sin(\lambda l)\cos(\lambda l)}{\sinh^2(\lambda l) - \sin^2(\lambda l)} \tag{2.2.1-6}$$

where

$$\lambda = \sqrt[4]{\frac{k}{4E_s I_s}} \tag{2.2.1-7}$$

$$k = \frac{w_a E_a}{t_a} \tag{2.2.1-8}$$

The method that an engineer would use to calculate the tensile stress in a rectangular section subjected to an end load would be as follows. First the load would be moved to the center of the section. Second, a moment couple would be added to compensate for moving the load. Third, the resulting stress would be calculated using the principle of superposition. For an end load it is known that the largest stress will be at the end of the section where the two stresses are the in the same direction. This method is represented in Equations (2.2.1-9) through (2.2.1-11).

$$\sigma_{eng} = \frac{P}{A} + \frac{Mc}{I} \tag{2.2.1-9}$$

$$\sigma_{eng} = \frac{P}{w_a l} + \frac{P\frac{l}{2} * \frac{l}{2}}{\frac{w_a l^3}{12}} \tag{2.2.1-10}$$

$$\sigma_{eng} = \frac{4P}{w_a l} \tag{2.2.1-11}$$

Combing Equations (2.2.1-8) and (2.2.1-11) one can formulate a stress concentration factor for a finite strip with an end load. The first stress concentration factor for elastic foundations (K_{ef1}) is shown in Equation (2.2.1-12) and Figure 2.2.1-5.

$$K_{ef1} = \frac{\sigma_a}{\sigma_{eng}} = \frac{\lambda l}{2} * \frac{\sinh(\lambda l)\cosh(\lambda l) - \sin(\lambda l)\cos(\lambda l)}{\sinh^2(\lambda l) - \sin^2(\lambda l)} \qquad (2.2.1\text{-}12)$$

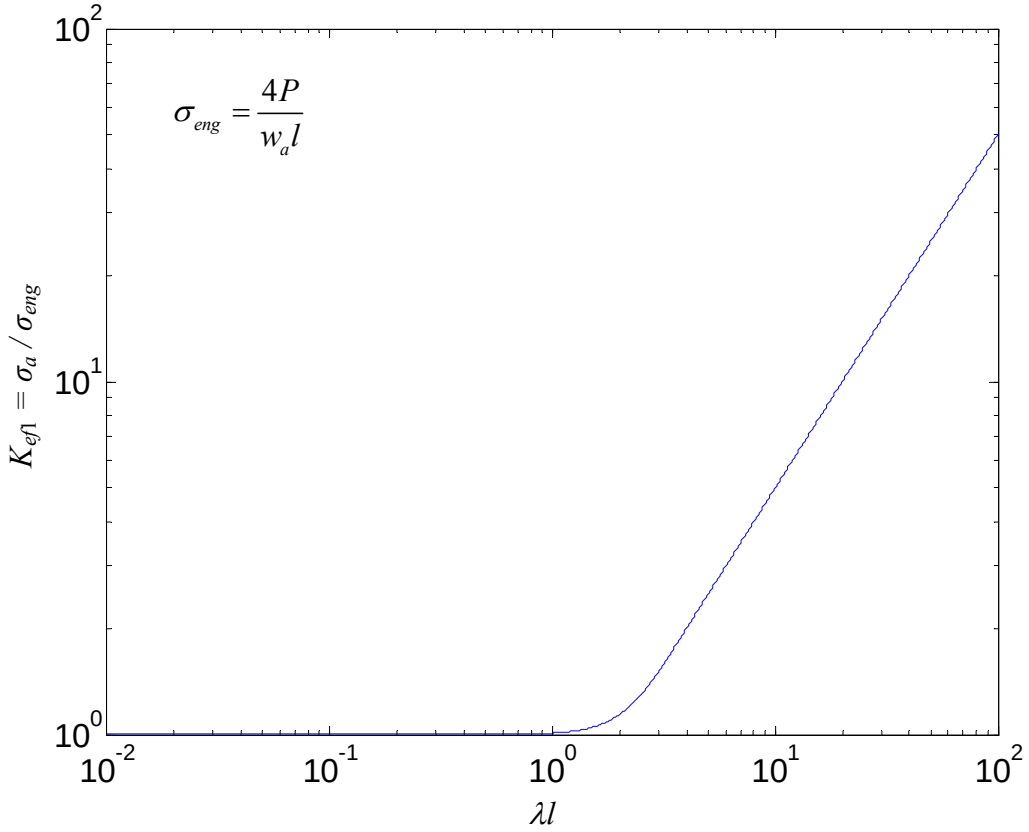

Figure 2.2.1-5 End-load elastic foundation stress concentration factor, K_{ef1}.

As one can see a good estimate of the stress concentration factor is 1.0 for all values of $\lambda l \leq 1.0$. In this region the adherend will act as a rigid body and the engineering stress can be used.

These techniques can be applied to flexible adherends bonded together. If the adherends are the same, symmetry can be used by using half of the actual bond thickness (t_a) and applying the equations as usual. It is important to note that in these analyses the adhesive modulus (E_a) is required. As discussed in the previous section the in-situ modulus and the bulk modulus may not be the same and therefore, these equations should be used with caution.

2.2.2 Shear Stress

The application of a longitudinal load to a lap shear joint such as that shown in Figure 2.2.2-1 will result in a shear stress (τ).

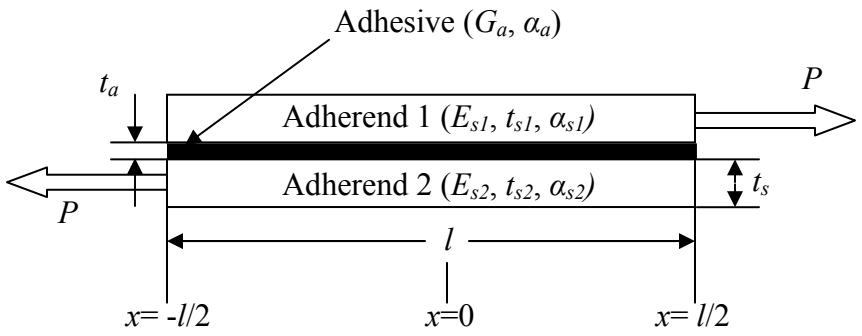

Figure 2.2.2-1 Shear-lag geometry.

Assuming rigid (see Equations (2.2.2-6) and (2.2.2-9)) substrates, the average shear stress can be calculated using Equation (2.2.2-1).

$$\tau_{ave} = \frac{P}{A} \tag{2.2.2-1}$$

The application of a torque (T) to rigid substrates also results in shear stress. Assuming linear superposition, the torque-based shear stress can be added vectorially to the load-based shear stress to calculate the total shear stress. The torque-based shear stress is a function of the distance from the centroid (c) and the polar-area-moment of inertia (J) as indicated in Equation (2.2.2-2). The direction is orthogonal to c and is directed in the direction of the torque.

$$\tau(c) = \frac{Tc}{J} \tag{2.2.2-2}$$

Thus, the shear stress has a linear gradient from the centroid of the bond area to any portion of the adhesive cross-section. The maximum shear stress is at the furthest radial position from the centroid. This will not be the case if there are large rotations or if the cross-section becomes twisted as is the case of a rectangular cross-section. Methods have not been developed and verified in adhesive design applications to deal with torsion in rectangular sections as has been done in weld-design technology. As such Equation (2.2.2-2) is only valid for pure torsion applied to a circular cross-section.

The shear stress in a bonded joint containing a PSA will not be uniform when the adherends are flexible. When calculating the shear stresses in bonded joints with flexible adherends Equation (2.2.2-1) should not be used (flexible is defined in the following paragraph). If the adherends are flexible and one assumes there are no longitudinal or transverse normal stresses in the adhesive, the stress distribution can be calculated using Volkerson's shear-lag model [10,13,14]. Volkerson's model is presented in Equations (2.2.2-3) and (2.2.2-4). The joint geometry and model parameters are shown in Figure 2.2.2-1

$$\tau_a(x) = \frac{P\omega}{2w_a \sinh\left(\frac{\omega l}{2}\right)}\cosh(\omega x) + \left(\frac{P\omega}{2w_a \cosh\left(\frac{\omega l}{2}\right)}\frac{E_{s2}t_{s2} - E_{s1}t_{s1}}{E_{s1}t_{s1} + E_{s2}t_{s2}}\right)\sinh(\omega x) \tag{2.2.2-3}$$

where

$$\omega = \sqrt{\frac{G_a}{t_a}\left(\frac{E_{s1}t_{s1} + E_{s2}t_{s2}}{E_{s1}t_{s1}E_{s2}t_{s2}}\right)} \tag{2.2.2-4}$$

The stress distribution is dependent on the joint geometry as well as the material properties of the adhesive and the adherends. This model can be simplified to Equations (2.2.2-5) and (2.2.2-6) if both adherends are identical.

$$\tau_a(x) = \frac{P\omega}{2w_a \sinh\left(\frac{\omega l}{2}\right)}\cosh(\omega x) \tag{2.2.2-5}$$

where

$$\omega = \sqrt{\frac{2G_a}{t_a E_s t_s}} \tag{2.2.2-6}$$

Dividing Equation (2.2.2-5) by the τ_{ave} (Equation 2.2.2-1) one obtains the second geometry-dependent stress concentration factor (K_{g2}) shown in Equation (2.2.2-7) below.

$$K_{g2}(x) = \frac{\tau_a(x)}{\tau_{eng}} = \frac{\frac{P\omega}{2w_a \sinh\left(\frac{\omega l}{2}\right)}\cosh(\omega x)}{\frac{P}{w_a l}} = \frac{\omega l}{2\sinh\left(\frac{\omega l}{2}\right)}\cosh(\omega x) \tag{2.2.2-7}$$

In most instances the peak stress is what is of interest. In Equation (2.2.2-7) the peak stress will occur at $x = l/2$. This relationship is shown in Equation (2.2.2-8) and is plotted in Figure 2.2.2-2.

$$K_{g2} = \frac{\omega l}{2\sinh\left(\frac{\omega l}{2}\right)}\cosh\left(\frac{\omega l}{2}\right) \tag{2.2.2-8}$$

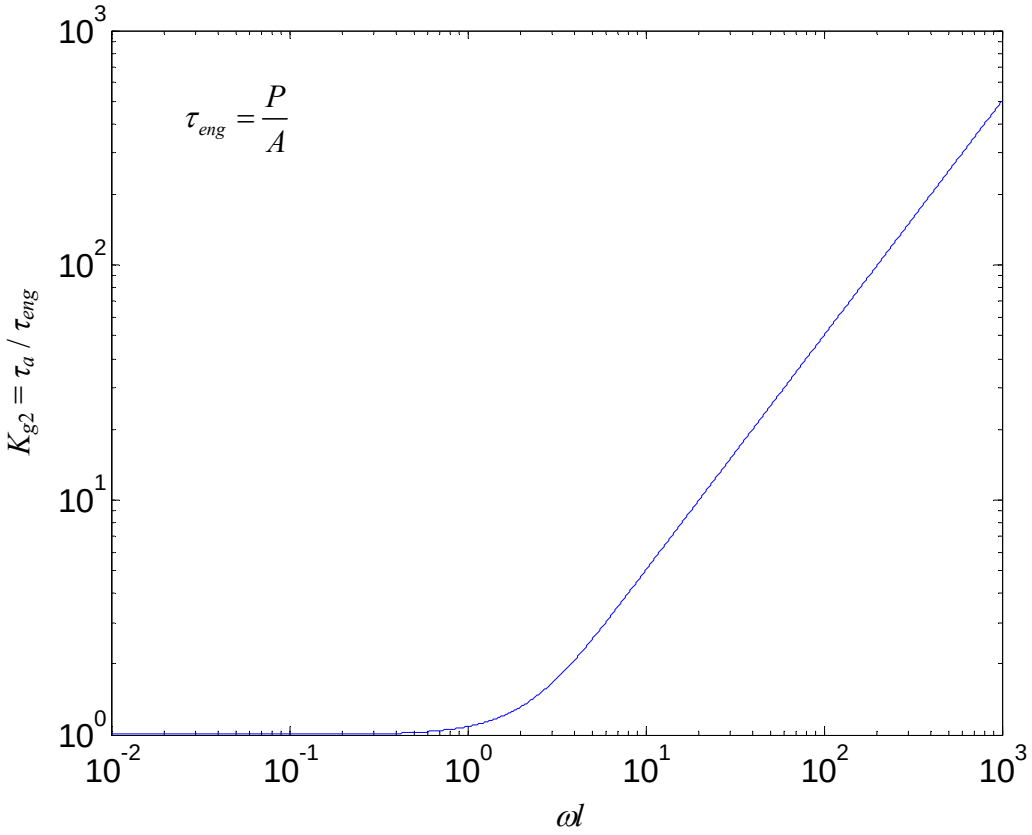

Figure 2.2.2-2 Shear stress concentration factor, K_{g2}.

As one can see K_{g2} is approximately 1.0 for values of ωl less than 1.0. This leads us to a definition of flexible for this geometry. For $\omega l \leq 0.75$ the peak τ_a will be no more than 5% larger than τ_{ave}. If $\omega l > 0.75$ there will more than a 5% difference and the beam should be treated as flexible using Volkerson's relations, Equations (2.2.2-3) or (2.2.2-5). These relationships can be represented as shown in Equation (2.2.2-9).

$$\tau_a = \begin{Bmatrix} \tau_{eng} = \frac{P}{A} \middle| \omega l \leq 0.75 \\ K_{g2} * \tau_{eng} \middle| \omega l > 0.75 \end{Bmatrix} \qquad (2.2.2\text{-}9)$$

To provide additional insight into the effect of t_a and $E_s t_s$ on the stress distribution the stress distributions for two cases are presented in Figures 2.2.2-3 and 2.2.2-4. In each case increasing the respective parameter (t_a in Figure 2.2.2-3 and $E_s t_s$ in Figure 2.2.2-4) results in a decrease in the stress gradient. For rigid adherends and thick adhesive layers the stress level will approach the value calculated using Equation (2.2.2-1).

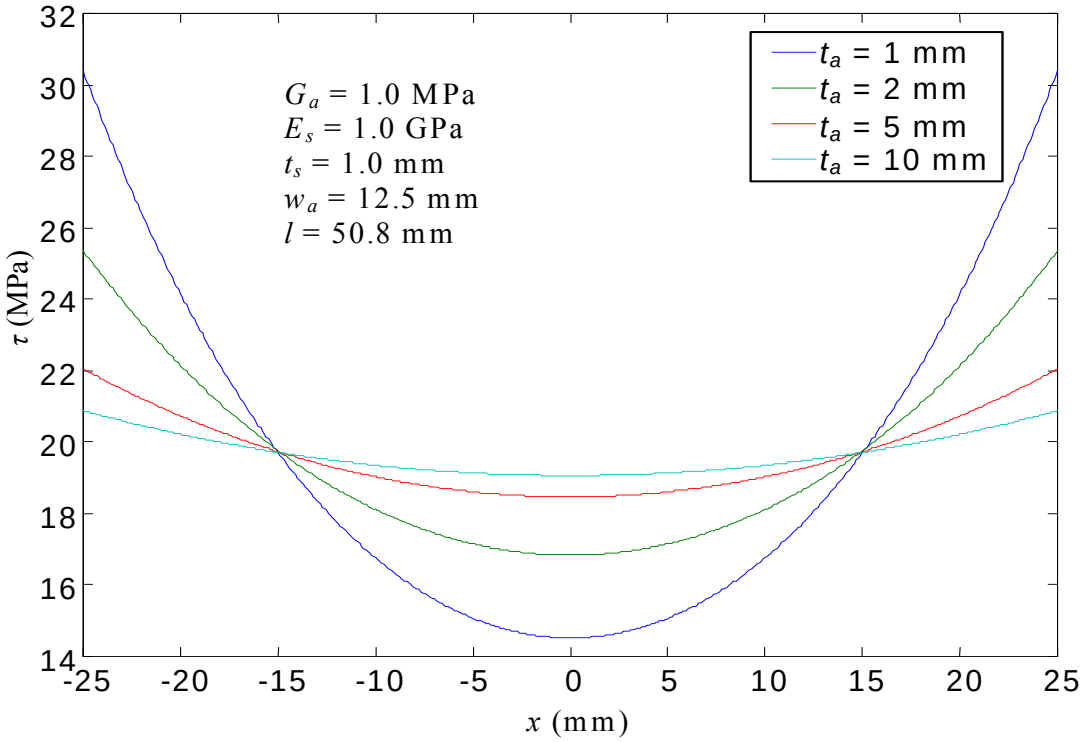

Figure 2.2.2-3 Effect of t_a on the shear stress distribution.

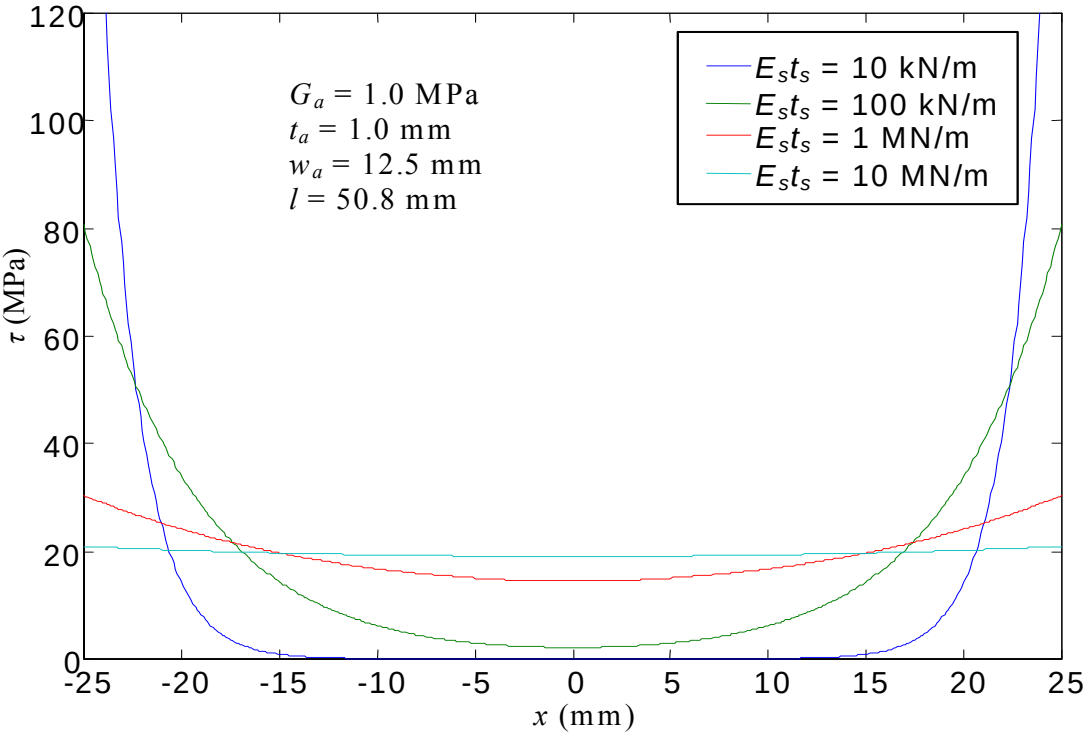

Figure 2.2.2-4 Effect of E_st_s on the shear stress distribution.

Volkerson's analysis is intended for pure shear loading which is very difficult to achieve. The thickness of the adherends and adhesive will result in a moment given the loading in Figure 2.2.2-1. To account for bending or torsional loading a different model must be used. Goland and Reissner [15], and Adams and Peppiat [16] have presented models for these loading conditions. These models are more complex and will not be presented here.

2.3 Strain Calculation

In some designs, the stress level may not be the controlling factor in determining failure. The design may have a design parameter that limits the maximum strain. The application of a tensile load will result in an increase in length (thickness). The ratio between the change in length (δ) to the original length (thickness) is the normal strain (ε). This relationship is shown in Equation (2.3-1).

$$\varepsilon_x = \frac{\delta_x}{t_a} \tag{2.3-1}$$

In an elastic material a strain in the loading axis will result in a negative strain in the transverse axes as shown in Figure 2.3-1a.

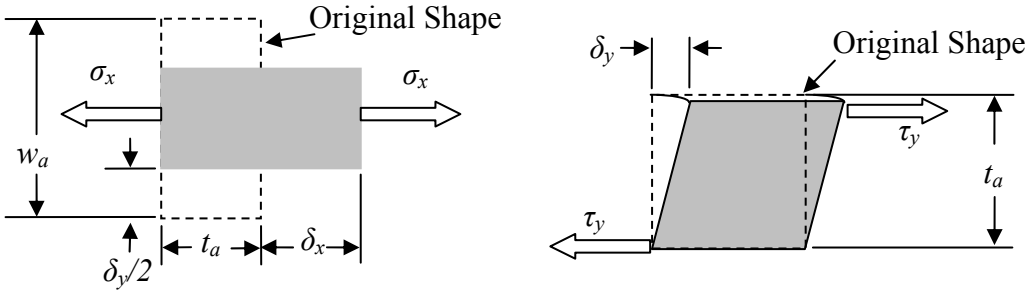

Normal and Transverse Strain
(a)

Shear Strain
(b)

Figure 2.3-1 Shear geometries.

This leads to the definition of another material property known as Poisson's Ratio (v), which is calculated using Equation (2.3-2).

$$v = -\frac{\varepsilon_y}{\varepsilon_x} = -\frac{\varepsilon_z}{\varepsilon_x} \tag{2.3-2}$$

Poisson's Ratio must be between 0.0 and 0.5. For steel v is typically 0.26 - 0.30 and for elastomers v is very close to 0.5. A v of 0.0 indicates that a strain in one axis will not result in a strain in the other two axes. This is approximately the case in foam materials.

In shear the equivalent concept to ε is the shear strain (γ). The γ represents the angular rotation in radians as indicated in Figure 2.3-1b. Equation (2.3-4) is used to calculate γ.

$$\gamma = \tan^{-1}\left(\frac{\delta_y}{t_a}\right) \tag{2.3-3}$$

It should be apparent from Equation (2.3-3) that the shear strain will approach $\pi/2$ as $\delta_y \Rightarrow \infty$. Also note that the sides of the element do not change length and the longitudinal sides move toward one another. In real-world applications these conditions are difficult to obtain. These conditions limit $\delta_y \leq t_a$ since at $\delta_y = t_a$ the two longitudinal sides approach one another. With $\delta_y = t_a$ Equation (2.3-3) yields $\gamma = \pi/4$, but one can see that the geometry demands that $\gamma = \pi/2$ for this case. This is strong evidence that the conventional engineering shear strain definition is inadequate for dealing with PSA's with large shear deflections. Physical testing has yielded δ_y up to 8 times t_a. These deflections require large extension in the element sides and violate the basic assumptions made in the formulation of Equation (2.3-3). Not withstanding these problems the definition given in Equation (2.3-3) will be used to keep with engineering convention.

2.4 Moduli

The ratio between σ_x and ε_x is known as the modulus of elasticity or Young's Modulus (E). This property can be used to determine the deformation associated with a normal stress. This is only valid in the linear portion of the σ-ε diagram before plastic deformation sets in. Young's Modulus is calculated for the plane-stress and plane-strain conditions using Equations (2.4-1) and (2.4-2), respectively.

$$E = \frac{\sigma_x}{\varepsilon_x} \text{ (Plane Stress)} \tag{2.4-1}$$

$$E = \frac{\sigma_x(1-v^2)}{\varepsilon_x} \text{ (Plane Strain)} \tag{2.4-2}$$

In shear, the equivalent property is known as the shear modulus or modulus of rigidity (G). The modulus of rigidity is the ratio of τ_x to γ_x as shown in Equation (2.4-3).

$$G = \frac{\tau_x}{\gamma_x} \tag{2.4-3}$$

In the linear region of an isotropic material stress-strain relationship Equation (2.4-4) can be used to calculate E, G, or v as long as two of the quantities are known.

$$E = 2G(1+v) \tag{2.4-4}$$

Both of the moduli are obtained based on stress and strain, which are calculated nominal values. The calculated values of stress and strain are limited by the measurement technique used. In a bonded system it may be very difficult to calculate E and G from measured stress and strain. This is due to the difficulties associated with obtaining accurate values for the cross-sectional area, specimen displacement, and stress distribution. In addition to the errors associated with measurement resolution, the constraints at the interface must also be taken into account. In general, the adhesive joint is a mixed plane-stress and plane-strain problem. As indicated in section 2.2.1, bonded joints loaded in tension develop σ and τ due to the constraint at the bond line. This constraint also results in an increase in the stiffness of the bonded system compared to the constitutive properties. This is because the bonded surface cannot contract under Poisson's Ratio effect, as they should in a plane-stress situation. This results in shear stresses at the surface of the adhesive to hold the adhesive in place. Applying Equation (2.4.1) to a bonded joint will result in the apparent E (E_{app}). For adhesive joints containing PSAs, the E_a is much lower than E_s. Therefore, the E will represent the in-situ adhesive E_{app}. To determine E_a one must correct E_{app} based on the specific joint geometry. Shape factors can be used to calculate E_a from E_{app}. The relationship between E_{app} and E_a is show in Equation (2.4-5).

$$E_{app} = E_a\left(\frac{4}{3} + \frac{{w_a}^2}{3{t_a}^2}\right) \tag{2.4-5}$$

Equation (2.4-5) is only valid for an infinite strip and $v = 0.5$, the same type of relationship can be found for other geometries as mentioned in section 2.2.1. By graphing Equation (2.4-5) (see Figure 2.4-1) one can see that the joint geometry can have a significant effect on the in-situ modulus.

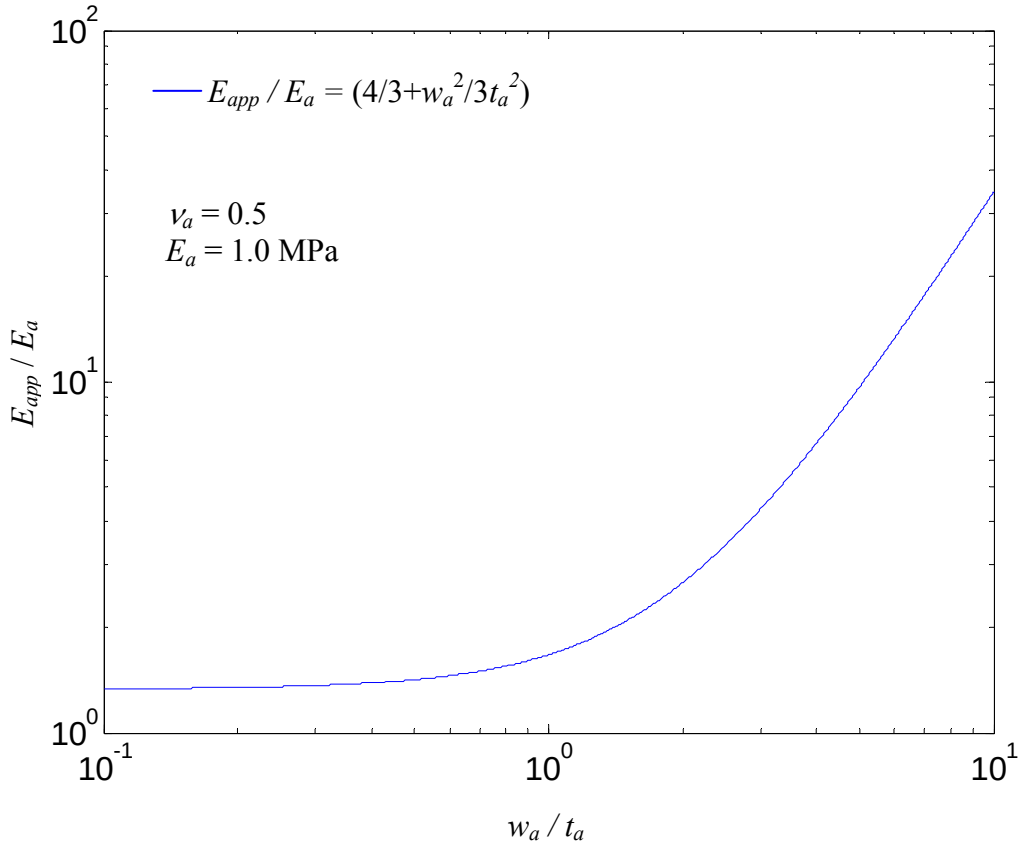

Figure 2.4-1 The effect of the bond geometry on the apparent E.

For example, when w_a is 10 times larger than t_a the E_{app} is predicted to be over 30 times the constitutive E_a. The E_{app} of the bonded system would need to be calculated for the particular joint geometry using the E_a and ν_a. Experience with some PSA's, however, indicates that these theoretical shape factors do not accurately predict the relationship between E_{app} and E_a. Therefore, it is suggested that experimental data be taken for the development of empirical shape factors for the PSA material being used.

2.5 Coefficient of Thermal Expansion

As a material is elevated in temperature, it tends to increase in volume. The ratio between the thermal strain (ε_t) and the change in temperature (ΔT) is known as the coefficient of thermal expansion (α). This relationship is shown in Equation (2.5-1).

$$\alpha = \frac{\varepsilon_t}{\Delta T} \qquad (2.5\text{-}1)$$

The importance of α becomes apparent when adhesively bonded joints are exposed to operating environments containing large ΔT. In an adhesively bonded joint, the adhesive is not free to expand and stresses develop due to the constraint at the bond line. For

joints in which the adhesive and adherends have dissimilar α, normal stresses develop in the adhesive layer. Using the nomenclature and joint geometry are shown in Figure 2.5-1, the relationship for the normal stresses are shown for uniaxial and biaxial stresses in Equations (2.5-2) and (2.5-3), respectively [10]. In Equations (2.5-2) and (2.5-3) α_{s1} and α_{s2} are the same resulting in uniform strain across the thickness of the bond.

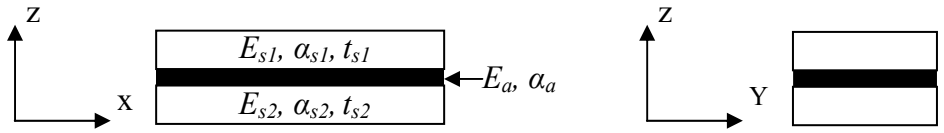

Figure 2.5-1 Thermal expansion geometry.

$$\sigma_x = -E_a \Delta T \left(\alpha_a - \alpha_s \right) \tag{2.5-2}$$

$$\sigma_x = \sigma_y = -\frac{E_a \Delta T}{1 - \nu_a} \left(\alpha_a - \alpha_s \right) \tag{2.5-3}$$

Equation (2.5-2) is only valid for uniaxial stress states, as would be seen in a long narrow bond line. Equation (2.5-3) is more realistic for most bonded systems in that it takes into account the additional stress caused by the Poisson's Ratio effect.

If the adherends have different α_s the normal strain will not be uniform across the bond thickness. Normal and shear stresses occur in the adhesive layer due to this strain state. Both the normal and shear stresses will be non-uniform along the length of the bond as indicated in Equations (2.5-4) and (2.5-5) [10].

$$\sigma_a(x) = -E_a \Delta T \left[\frac{\left(\alpha_{s1} - \alpha_{s2} \right) x + t_a \left(\alpha_a - \alpha_{s1} \right)}{t_a} \right] \tag{2.5-4}$$

$$\tau(x) = \frac{\left(\alpha_{s1} - \alpha_{s2} \right) \Delta T \omega}{\left(\frac{1}{E_{s1} t_{s1}} + \frac{1}{E_{s2} t_{s2}} \right) \cosh\left(\frac{\omega l}{2} \right)} \sinh(\omega x) \tag{2.5-5}$$

Again, these equations are intended for long narrow bonds. For both equations $x = 0$ is the center of the bond length. In Equation (2.5-5) ω is calculated using Equation (2.2.2-4).

These equations indicate that even the process of assembling the joint itself can result in stresses. Many PSAs are applied as a liquid and then cure to a solid. This process of changing state most often results in an exothermic reaction and, most often, in a volume change. After the reaction is complete, the change in the volume of the adhesive will produce residual stresses. As the adhesive and adherends return to ambient temperature, additional residual stresses can develop.

2.6 Temperature/Humidity/Rate Effects

The material properties of PSA are governed by the operating conditions; including temperature, relative humidity, and loading rate. The breaking strength of a PSA joint will become greater as the strain rate increases or as the temperature decreases [5, 17, 18]. Both of these conditions result in an increase in the modulus of the adhesive. As the temperature approaches the glass transition temperature (T_g) the adhesive will become brittle. This same effect can be seen above the T_g if the strain rate is high enough. Conversely, an increase in the relative humidity (RH) will result in a decrease in the breaking strength [19, 20]. Water acts as a plasticizer, which decreases the modulus of the adhesive. In addition to the effect on the modulus, water can cause swelling which will induce "environmental" stresses at the bond line similar to those caused by α mismatch [18, 21].

The humidity effect is a time-dependent process. The diffusion and wicking of the water molecules into the adhesive and along the bond line is not instantaneous. This process is controlled by the adhesive properties, temperature, and the stress state [6, 21]. Work has been done to predict the effect of exposure time on the joint properties (adhesive and interfacial strength) [22, 23].

For any design to be successful, the worst-case operating conditions must be known. This allows for the correct material properties to be used in the design process. The use of master curves and shift-factor plots [5] will allow the material properties to be known for a wide range of environmental conditions and loading rates. If this data is not available, the material cannot be used safely in any design that is not operating under the exact same condition as the available test data.

2.7 Stress Analysis

After the stresses on the joint have been determined, it is necessary to relate them to the known material properties. Typically, the stress state of the joint will be compared to the known shear strength (S_s) or tensile strength (S_t), which is obtained from test data. In most cases only one of these values will be available and, therefore, it is necessary to transform the design stress state to one that can be directly related to the known strength. One approach to solving this problem is to use the linear mechanics Mohr's Circle analysis. Mohr's Circle is a graphical/analytical method of transforming/rotating a combined stress state to an equivalent stress state, typically one of only shear or one of only normal stresses. This is known as the principal stress state. Both biaxial and triaxial stress elements can be transformed using Mohr's circle. In using one of the variants of the Mohr's circle approach, tensile stresses and clockwise shear stresses are positive, while, compressive stresses and counterclockwise shear stresses are negative. The Mohr's circle method is illustrated in Figure 2.7-1, for a biaxial stress element ($\sigma_z = \tau_{xy} = \tau_{xy} = 0$). The following analysis has been done using the nomenclature normally associated with a triaxial analysis. This has been done to eliminate any confusion associated with failure criteria.

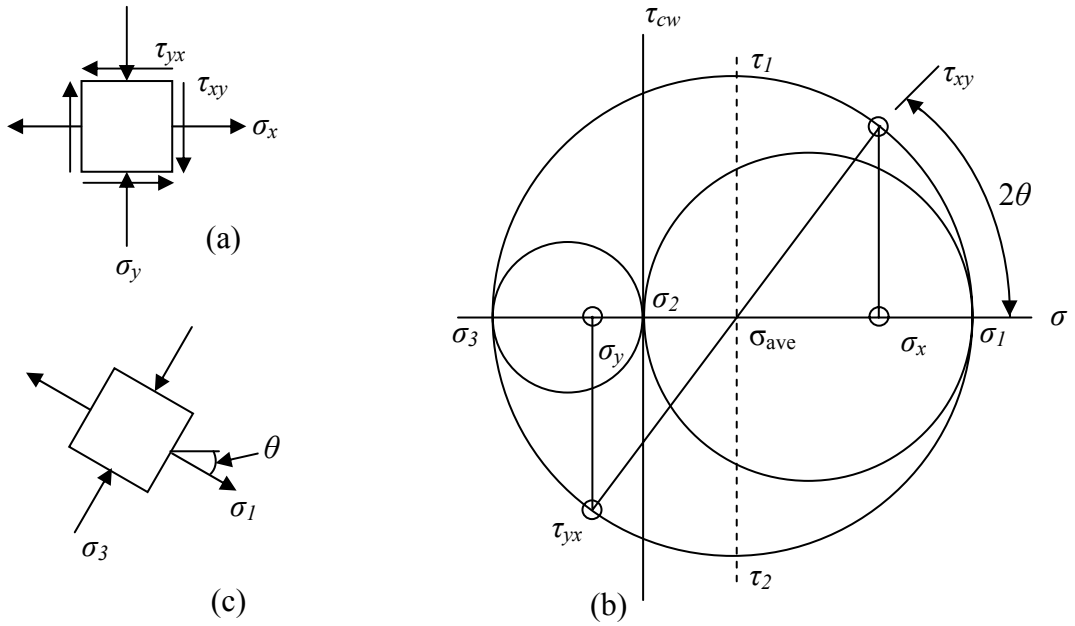

Figure 2.7-1 Mohr's circle analysis for a biaxial-stress element (σ_y = -0.2σ_x, σ_z = 0).

As indicated, the stresses are plotted on σ-τ axes, then the circle diameter and the rotation angle (θ) are calculated using simple trigonometry. Knowing the diameter, the stress circle can be drawn with the average of the normal stresses (σ_{ave}) as the origin. Finally, the principal stresses (σ_1 - σ_3) can be determined with $\sigma_1 > \sigma_2 > \sigma_3$. Using these values the new stress element drawn, as shown in Figure 2.7-1(c). Principal stresses are used to predict failure in brittle materials under tensile stress. However, ductile materials are found to fail or yield under shear stress action or through shear (distortion) strain energy accumulation. Thus, the maximum shear stress (τ_{max}) is important. As indicated in Figure 2.7-1(b) the $\tau_{max} = \tau_1 = -\tau_2$. Mohr's circle helps determine the τ_{max} for the stress element so that the selected failure theory can be applied.

The values obtained using Mohr's circle can be obtained numerically using Equations (2.7-1)-(2.7-4) [24].

$$\tan(2\theta) = \frac{2\tau_{xy}}{\sigma_x - \sigma_y} \tag{2.7-1}$$

$$\sigma_{ave} = \frac{\sigma_x + \sigma_y}{2} \tag{2.7-2}$$

$$\sigma_1, \sigma_3 = \sigma_{ave} \pm \sqrt{\left(\frac{\sigma_x - \sigma_y}{2}\right)^2 + \tau_{xy}^2} \tag{2.7-3}$$

$$\tau_{max} = \tau_1, \tau_2 = \pm\sqrt{\left(\frac{\sigma_x - \sigma_y}{2}\right)^2 + \tau_{xy}^2} \tag{2.7-4}$$

This same approach can be used to determine the principal strains as indicated in Equations (2.7-5) through (2.7-8) [25].

$$\tan(2\theta) = \frac{\gamma_{xy}}{\varepsilon_x - \varepsilon_y} \tag{2.7-5}$$

$$\varepsilon_{ave} = \frac{\varepsilon_x + \varepsilon_y}{2} \tag{2.7-6}$$

$$\varepsilon_1, \varepsilon_3 = \varepsilon_{ave} \pm \sqrt{\left(\frac{\varepsilon_x - \varepsilon_y}{2}\right)^2 + \frac{\gamma_{xy}^2}{4}} \tag{2.7-7}$$

$$\gamma_{max} = \gamma_1, \gamma_2 = \pm\sqrt{\left(\frac{\varepsilon_x - \varepsilon_y}{2}\right)^2 + \frac{\gamma_{xy}^2}{4}} \tag{2.7-8}$$

Typically these equations are written using the facial shear strain (ε_{xy}). They were reformulated and presented here using the engineering shear strain (γ_{xy}) for consistency.

2.8 Yield Criteria (Ductile Materials)

There are many different failure theories that can be used in design. In this thesis the focus is on static strength-based design techniques and, therefore, fracture and fatigue theories will not be covered. In ductile systems exceeding the yield strength will result in a permanent deformation in the material. This deformation changes the system geometry and is used as the failure criteria. Of the many static theories the maximum-shear-stress theory and the maximum-distortion-energy theory (von Mises-Hencky theory) are the most widely used. Both of these theories can be related to the principal stresses and the known material yield strength to predict yield or failure. The predicted failure envelope for each of these theories is shown in Figure 2.8-1. It is important to note that the distortion-energy theory has a larger envelope and, therefore, a larger design space.

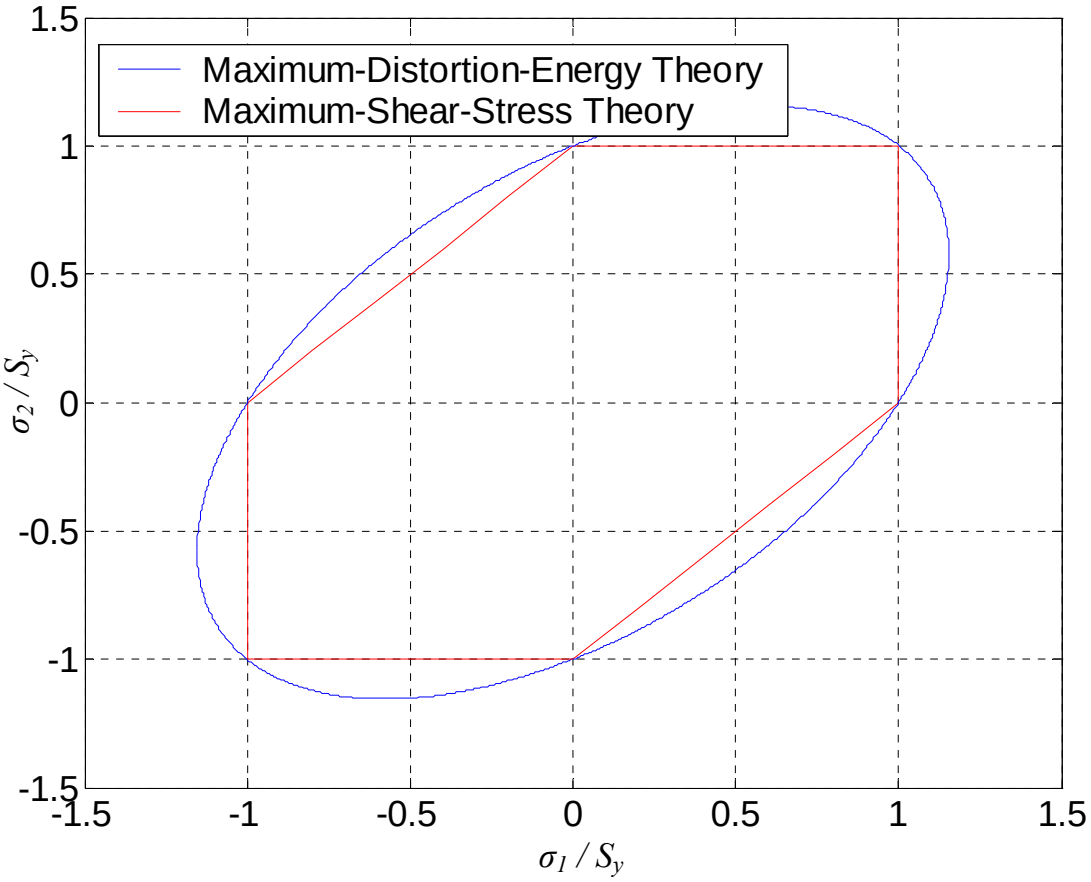

Figure 2.8-1 Failure theory design space.

2.8.1 Maximum-Shear-Stress Theory (MSST)

The maximum-shear-stress theory [24,25] is based on the observation that a tensile specimen loaded past their yield point will neck down. This reduction in cross-section is due to slippage of the material along oblique planes caused by shearing. Therefore, the tensile yield strength (S_y) is associated with a shear yield strength (S_{sy}). Using Mohr's circle the magnitude of S_{sy} can be shown to be ½ of S_y. Failure is not predicted as long as the maximum-shear-stress (τ_{max}) is less than S_{sy}. For a triaxial stress state Equations (2.8.1-1) and (2.8.1-2) can be used to calculate τ_{max} and predict failure.

$$\tau_{max} = \frac{\sigma_1 - \sigma_3}{2}; \ \sigma_1 > \sigma_2 > \sigma_3 \qquad (2.8.1\text{-}1)$$

where σ_1, σ_2, and σ_3 are the principal stresses.

$$\tau_{max} \leq \frac{S_y}{2} = S_{sy} \qquad (2.8.1\text{-}2)$$

Most strength data has been collected on tensile specimens and, therefore, S_y is generally reported. This makes it logical to predict failure based on an equivalent tensile stress (σ'_{MSST}). This represents the predicted stress for the design and is calculated using Equation (2.8.1-3). By combining Equations (2.8.1-3) and (2.8.1-2) one can develop an equation to predict yield failure based on σ'_{MSST} and S_y. This final relationship is shown in Equation (2.8.1-4). The maximum-shear-stress theory is very easy to apply and is conservative compared to test data. Again it is only valid for predicting failure in yield and, therefore, should only be applied to ductile materials.

$$\sigma'_{MSST} = 2\tau_{max} = \sigma_1 - \sigma_3 \tag{2.8.1-3}$$

$$\sigma'_{MSST} \leq S_y \tag{2.8.1-4}$$

2.8.2 Maximum-Distortion-Energy Theory (MDET)

It has been observed that elements stressed hydrostatically have yield strengths that are much higher than those stressed in uniaxial tension. This indicates that yielding is not directly related to hydrostatically induced strain energy, but rather to the angular distortion energy in the stress element. The maximum-distortion-energy theory is based on the energy required to produce the angular distortion [24, 25]. The distortion energy (u_d) can be calculated by subtracting the hydrostatic strain energy from the total strain energy induced by the externally applied forces. The hypothesis of the theory is that as long as u_d is less than u_d at yield, yield failure will not occur. To make use of this theory, it is necessary to relate the u_d to stresses. This derivation can be found in *Mechanical Engineering Design* [24]. The triaxial failure criterion for the distortion-energy theory is given in Equation (2.8.2-1).

$$(\sigma_1 - \sigma_2)^2 + (\sigma_2 - \sigma_3)^2 + (\sigma_3 - \sigma_1)^2 < 2S_y^2;\ \sigma_1 > \sigma_2 > \sigma_3 \tag{2.8.2-1}$$

For the biaxial stress state, one of the principal stresses will be zero. In practice it is more convenient to define the von Mises stress for the biaxial stress case in terms of the principal or the operating stresses as indicated in Equations (2.8.2-2) and (2.8.3-3).

$$\sigma'_{MDET} = \sqrt{\frac{(\sigma_1 - \sigma_2)^2 + (\sigma_2 - \sigma_3)^2 (\sigma_3 - \sigma_1)^2}{2}} \leq S_y \tag{2.8.2-2}$$

$$\sigma'_{MDET} = \sqrt{\sigma_x^2 + \sigma_y^2 - \sigma_x \sigma_y + 3\tau_{xy}^2} \leq S_y \tag{2.8.2-3}$$

2.9 Design Methodology

In any design there is uncertainty and variability in the design load(s) and the material properties. To achieve a safe and reliable design it is necessary to account for these

uncertainties. One approach is to use factors of safety (N). The safety factor can be calculated with respect to the allowable load (P_u) or the yield strength (S_y) as indicated in Equations (2.9-1) and (2.9-2).

$$N_l = \frac{P_u}{P_d} \tag{2.9-1}$$

$$N_s = \frac{S_y}{\sigma_d} \tag{2.9-2}$$

In Equation (2.9-1) P_d is the design load and in Equation (2.9-2) σ_d is the design stress. In many cases the design stresses do not directly reflect the external design load. Moreover, in some cases the design stress is not a linear function of the design load or can be a function of many loads, not all of which can be overloaded. This makes Equation (2.9-2) dangerous to use. Equations (2.9-1) and (2.9-2) are not necessarily equivalent. Equation (2.9-1) should be used unless the designer is absolutely sure of the applicability of the stress-based approach, Equation (2.9-2).

A second approach is a probabilistic method. This technique is based on the variability in each of the design parameters including the material properties, applied loads, environment, etc.. The reported value for S_y is an average taken from a population. Not all of samples of a material will have the same failure strength. Using S_y as the failure criteria will result in 50% yield failures, if exactly that stress is applied to samples of the material. If the probability density function is known, S_y can be calculated for any desired failure rate. This method predicts failure based on the known variability of S_y. This is fundamentally different from the safety factor concept that actually allows the nominal load or loads to be user overloaded. Safety factors indicate how much abuse a machine or structure can take. The probabilistic method expresses the probability of success or failure based on the interaction (overlap) between the know distribution of the loading function and the material strength. The distribution of the loads attempts to account for the variability in the loading (user misuse) and the distribution over the strength attempts to deal with the material variability. In many cases these distributions will not be known and assumptions have to be made or extensive testing is required to establish an understanding of the applicable distributions.

2.10 Overview of Adhesive Joint Analysis

This chapter contains many equations and theories that are used to predict the stresses and strains in materials. Four of these theories are very important when dealing with adhesive joints. The basic principles of time-temperature superposition, shape factors, beam-on-elastic foundation, and shear lag will be covered again here. This is being done in an attempt to provide the reader with an appreciation for these theories with respect to adhesive joints.

As stated in section 2.1.2 time-temperature superposition is used to predict the properties of visco-elastic materials over a wide range of frequencies and temperatures. Typically modulus data will be collected over a frequency range of 0.1 Hz to 100 Hz and a temperature range of -100 °C to 200 °C. This data is used to generate shift factors which allow material properties to be predicted (shifted) for several decades outside of the test domain. There are two important assumptions that are made in doing this. First: there is no change in state over the shifted domain and second, Poisson's Ratio is constant over the shifted domain [26]. Both of these assumptions may be violated when dealing with adhesive, especially if the applications will include large temperature gradients or if the loading conditions range from creep to impact. One must also ask if time-temperature superposition is valid if there is a change in the failure mode of the joint itself.

Shape factors are intended to predict the tensile-stress gradient and tensile modulus in an adhesive joint (see sections 2.2.1 and 2.4). Both the stress gradient and the apparent modulus are a result of the constraint of the adhesive at the bond line. In an adhesive joint the adhesive is not allowed to contract under Poisson's Ratio effects. This constraint causes the adhesive to appear stiffer than the bulk material; the greater the constraint of the adhesive the larger the difference between the true modulus and the apparent modulus. The constraint of the adhesive will increase from the free edge to the center of the bond. A uniform tensile strain will result in tensile stress gradient across the width of the bond due to the variation in apparent modulus. To complicate things even more the level of constraint is dependent of the joint geometry and Poisson's Ratio.

Beam-on-elastic foundation is probably one of the most useful theories for designing adhesive joints, especially those with polymeric adherends. As indicated in section 2.2.1 a flexible adherend will deform under a load or moment which will result in large stress/strain gradient along the length of the beam. This indicates that any stress calculation made using the full length of the joint (Equations (2.2.1-1) and (2.2.1-3)) will underestimated the tensile stress. This was very evident in Figure 2.2.1-5 which demonstrated the difference between the stress predicted by beam-on-elastic foundation and the engineering stress. As the beam becomes more flexible or as the length increases the discrepancy between the stress calculations will intensify. One must remember that the models presented do not include Poisson's Ratio effects. One possibility method of dealing with this limitation is to use the apparent-adhesive modulus in the beam equations.

In section 2.2.2 Volkerson's shear-lag model was presented. In this section the shear stress distribution was shown to be a function of both the adherends and the adhesive. Fundamentally the stress gradient will be controlled by the ratio of the adhesive-shear stiffness and the adherend-tensile stiffness. As the adherends become more compliant with respect to the adhesive the stress gradient will become more severe. As the shear stress is transferred to the adherends the adherends experience local tensile strain. The stiffness ratio determines the length of the shear transfer and tensile strain. This causes the stressed area to be far less than the total area and the stresses to be much greater than those predicted by Equation (2.2.2-1).

2.11 Visco-Elastic Joint Design

As the previous sections have indicated designing adhesive joints requires a complete understanding of the materials and the stress distribution. The strength of an adhesive joint will be affected by temperature, relative humidity, and the joint geometry. The strength of the bond will be influenced by the pretreatment applied to the adherends. It will be very difficult to bond to an oily piece of steel or maintain consistent bond strengths in a dirty work environment. Even with carefully prepared adherends and a controlled operating environment it may still be difficult to obtain a consistently strong joint. There are some general guidelines that have been established to improve the strength of adhesive joints [10, 13, 27]. Several of these are listed below:

1. Design the joint to minimize tensile-normal stresses. Most, but not all, adhesives have a lower tensile strength than shear strength. Redesigning the joint into a compression or shear mode will improve the joint strength. However, there are exceptions to the strength relationship in some PSAs.
2. Use ductile adhesives when possible. This will reduce the stresses at the edges and increase the resistance to crack propagation.
3. Make the bond area larger so that the joint can survive a partial debond or errors during manufacturing which result in unbonded regions.
4. Bond to multiple surfaces if possible to minimize the impact of loading in other directions.
5. Use aggressive substrate pretreating to improve the bond strength. This can increase the bond strength by 10 - 20 times [6].
6. Design fixtures to hold the adherends in the correct orientation while the adhesive is cured and use a consistent curing process.
7. Design the substrate to be "rigid", if possible, to prevent large stress gradients.
8. TEST THE JOINT SYSTEM.

These guidelines are general and may not be applicable to every joint system, but they are a good starting point. Other modifications to the joint geometry can be made to reduce the stresses associated with shear lag. The use of scarf, bevel, and step joints has been shown to reduce the peak-shear stress by more than 50% [28, 29, 30, 31]. These joint can be difficult and expensive to manufacture. Another option to reduce the peak stresses is to round the edge of the adherend and/or add an adhesive fillet. These techniques are less expensive and can increase the strength up to 50% [32]. These systems are difficult to analyze and the equations that have been presented to calculated stress contain many assumptions. Unless these equations are used with great care large errors will result. Regardless of the final design geometry, it is very important to test the joint system to validate the design.

3.0 Test Procedures

It has already been stated that the strength of PSAs is affected by rate, temperature and relative humidity. It has also been shown that the normal stress distribution and the measured elastic modulus can be effected by the width of the bond. The strength tests conducted for this work were designed to capture the rate dependence of the strength and to determine the effect of the bond width on the in-situ material properties. Additional tests were conducted to determine the effects of load rates, displacement rates, and moments on the bond strength. All of the tests were conducted under recorded ambient lab conditions. To minimize the affect of variations in the temperature and relative humidity the tests were conducted over as short a time as possible.

For each test load-displacement data was recorded using National Instruments Labview® program along with a 12-bit data acquisition board referenced to 10 volts. The load cell and cross-head displacement voltages were sampled at 100 points/mm (10 μm/point) and saved as a text files using the part number as the file name. This data was then scaled using Microsoft Excel® into the units of newtons and millimeters.

3.1 Test Specimen

The test specimen consists of two 6061-T6 adherends bonded together with double-sided tape as shown in Figure 3.1-1.

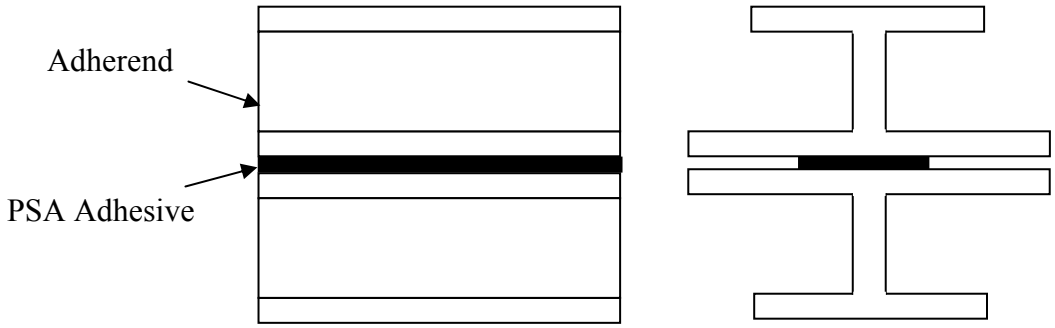

Figure 3.1-1 Specimen configuration.

The adherends are 2.000±0.002 in (50.80 ± 05 mm) long and were manufactured from Alpco roof bow #250 [33]. This product is used in the manufacture of trailers and is considered a good representation of a real-world-adhesive application. The dimensions and cross-section of the roof bow is shown in Figure 3.1-2.

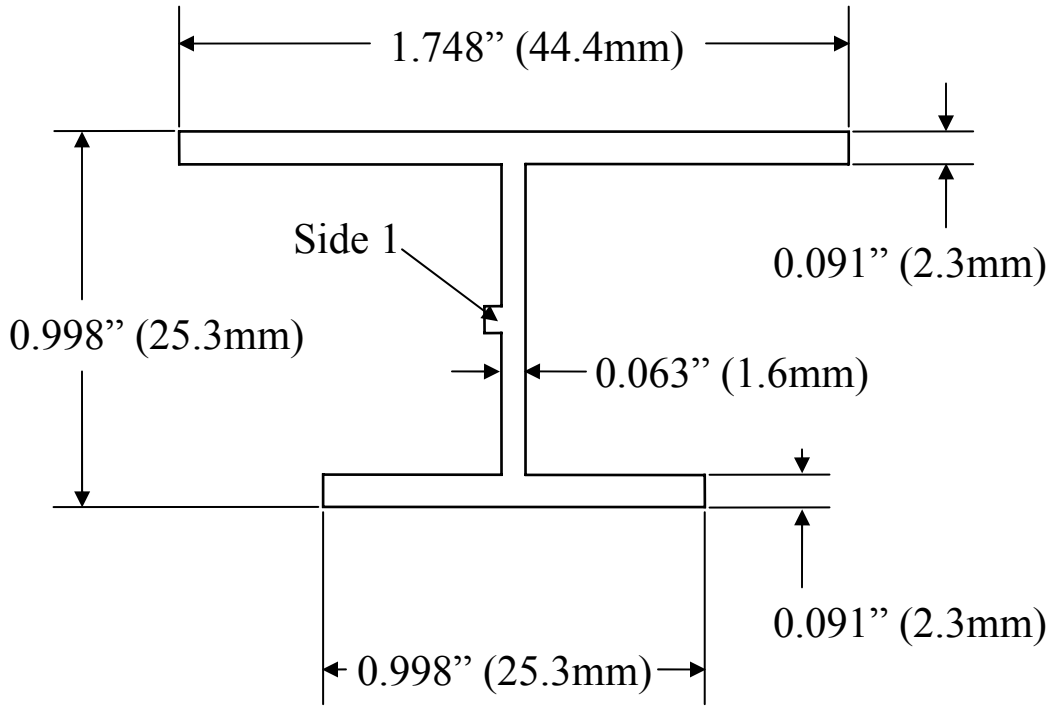

Figure 3.1-2 Adherend cross section.

As one can see the web of the I-beam is not symmetric. The side with the protrusion will be designated “Side 1” for future reference. The adhesive is 3M^{TM} VHB^{TM} 4950 acrylic tape. This is a multilayer acrylic foam tape with a nominal thickness of 0.045 in (1.1 mm). Unless otherwise indicated the specimens were assembled using 0.5 in (12.7 mm) wide adhesive tape.

3.1.1 Test Specimen Analysis

To better understand the stress distribution under both shear and tensile loading an analysis of the proposed specimen was conducted. Under tensile loading it is possible that the strain across the width of the bond will not be uniform. The flange (bond surface) of the specimen is thin and may deform under loading. This deformation would result in a non-uniform tensile stress and further complicate the stress analysis. To determine the axial strain across the bond a continuum based transfer matrix analysis was conducted. BEAM VI version 6.1 [34] and the material data collected from preliminary testing was used to predict the axial strain across the bond width. For a bond width of 12.7 mm the axial strain was found to vary by ≈ 2.0%. This variation increases to ≈ 13% for bond widths of 38.1 mm. Most of the testing will be conducted using 12.7 mm wide tape and, therefore, will result in a “uniform” axial stress state. The results from this analysis can be found in Appendix A.

To determine the shear gradient the stress concentration form of Volkerson’s Shear Lag Theory (Equation 2.2.2-8) was applied. As stated in section 2.2.2 the shear stress will

very less than 5% if $\omega l \leq 0.75$. Using preliminary test data for G_a and equivalent t_s the ωl for the proposed specimen was calculated to be 0.075. This value is well below the 0.75 suggested. This means that the adherends are rigid relative to the adhesive, thus implying a close to uniform shear strain/stress applied to the adhesive. These calculations can be found in Appendix A.

3.1.2 Surface Preparation

The surface preparation and cleaning procedure are based on the recommendations of 3M [35, 36]. The manufacturing and handling of the aluminum roof bows results in a non-uniform surface finish. In order to produce a visually consistent surface finish, the bond surface of each of the adherends were abraded using 3M™ Scotch-Brite™ #7447 pads mounted on a Black and Decker® palm orbital sander. After abrading, the bond surfaces were cleaned with Kimberly-Clarke® Kimwipes® EX-L using a 50:50 mixture of isopropyl alcohol and distilled water. The cleaning process was repeated until the Kimwipe® did not pick up any additional observable contaminants from the surface. The adherends were then allowed to dry before bonding. A representative abraded and cleaned surface pair is shown in Figure 3.1.2-1.

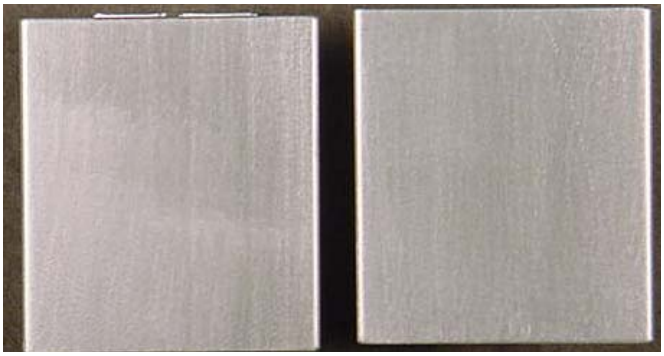

Figure 3.1.2-1 Surface finish of 6061-T6 aluminum.

At this point the adherends are ready to be bonded. This was started immediately after the surface preparation was completed to minimize the possibility of surface contamination.

3.1.3 Specimen Assembly

The following procedure was used to bond the adherends into specimens:

1. One of the adherends was placed bond side up and with side 1 facing the assembler.

2. Approximately 3 inches of tape was removed from the tape roll.

3. The tape was then applied along the length of the bond surface going from left to right. A tape guide was used to center the tape, as indicated in Figure 3.1.3-1 and 3.1.3-2. This part of the specimen will be referred to as Adherend A.

4. The tape guide and the adhesive liner were then removed.

5. The second adherend (Adherend B) was then brought into contact with the adhesive (both with Side 1 facing the assembler) using the alignment jig, (see Figure 3.1.3-3)

6. The excess tape was trimmed to the end of the specimen using a razor blade.

7. The bonded specimen was then loaded to 20-30 psi for 15 seconds. This was accomplished using the using the preloaded fixture shown in Figure 3.1.3-4. The fixture uses a pneumatic cylinder to provide the desired pressure and the application time is controlled by a timing relay. The applied preload exceeds the manufacture's requirement of 15 psi for 15 seconds.

8. The completed specimen was then labeled on both sides. The label consists of the letter "a" to indicate an Arcan specimen, date of assembly, number assigned, and the adherend designation (A or B). [Ex. a08-07-01-24A].

9. The adhesive was allowed to wet the adherends for at least 72 hours before testing.

Detail drawings of the tape guide, alignment jig, and preload fixture can be found in Appendix B.

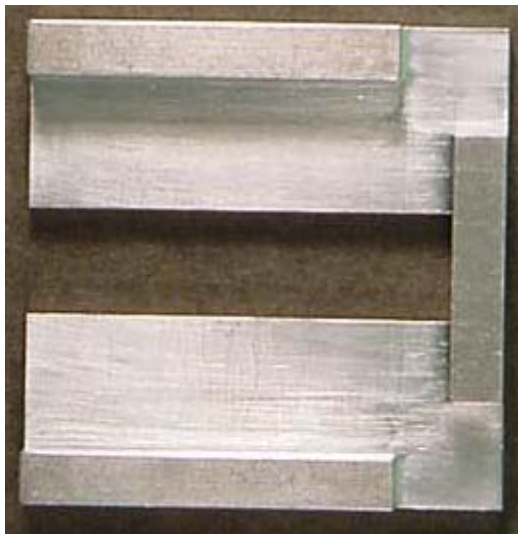

Figure 3.1.3-1 Tape alignment guide (Bottom view).

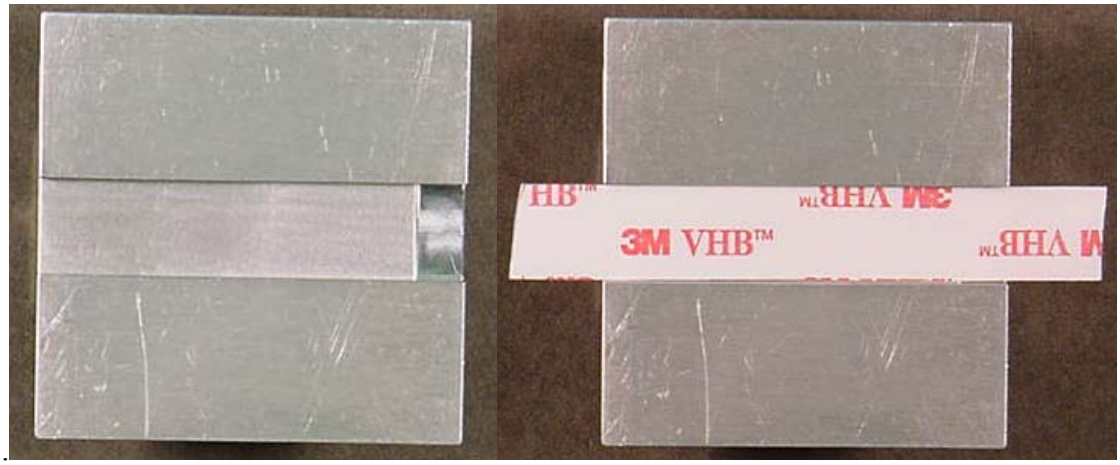

a) Tape guide positioned on adherend A.

b) Tape applied to adherend A using the alignment guide.

Figure 3.1.3-2 Aligning tape on Adherend A. (Top View of tape guide with adherend A inserted below.)

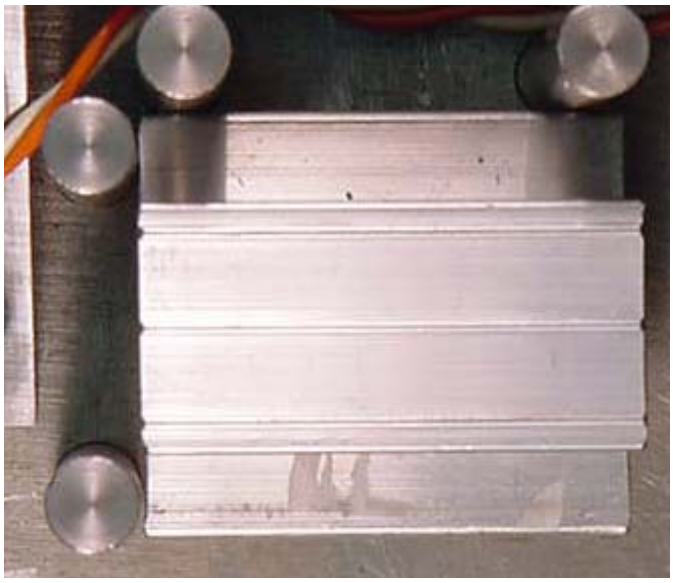

Figure 3.1.3-3 Bonding Adherend B using alignment jig. (Tape guide and adhesive backing removed. Adherend A positioned in alignment pins. Adherend B brought into contact with tape guided by alignment pins.)

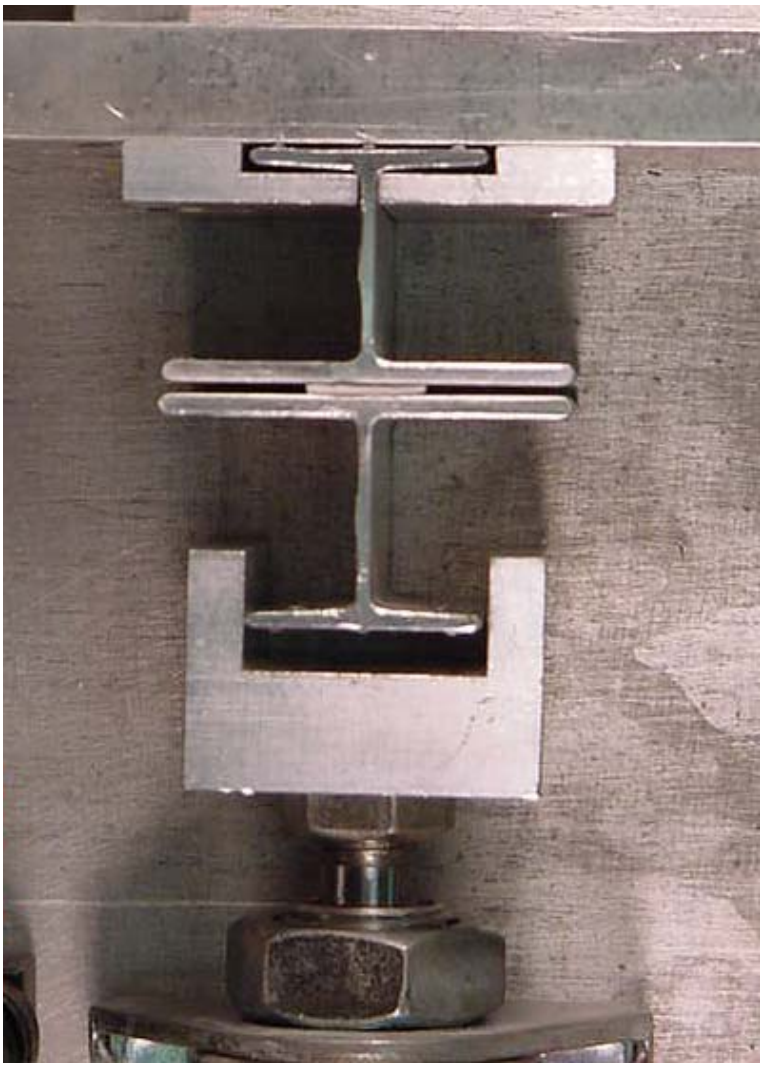

Figure 3.1.3-4 Specimen in preloading fixture. (Specimen removed from alignment jig and placed in preload fixture.)

3.2 Arcan Testing

All of the strength data was collected using a modified Arcan fixture ($Arcan_m$). The Arcan butterfly specimens were replaced with butterfly grips designed to accept the I-beam specimens. The ability to balance the Arcan fixture (each half independently) was also added to eliminate the moment generated by the asymmetry of the design. This moment may be very small compared to the loads applied when testing high strength materials, but will be significant when testing PSAs. To eliminate this moment, weights were added to the Arcan to generate a counter moment. Using this method it was possible to balance the Arcan to within the mounting-pin friction. An exploded view of the modified Arcan fixture ($Arcan_m$) is shown in Figure 3.2-1. The application of the counterweights can be seen in Figure3.2-2 and complete detail drawings are can be found in Appendix B.

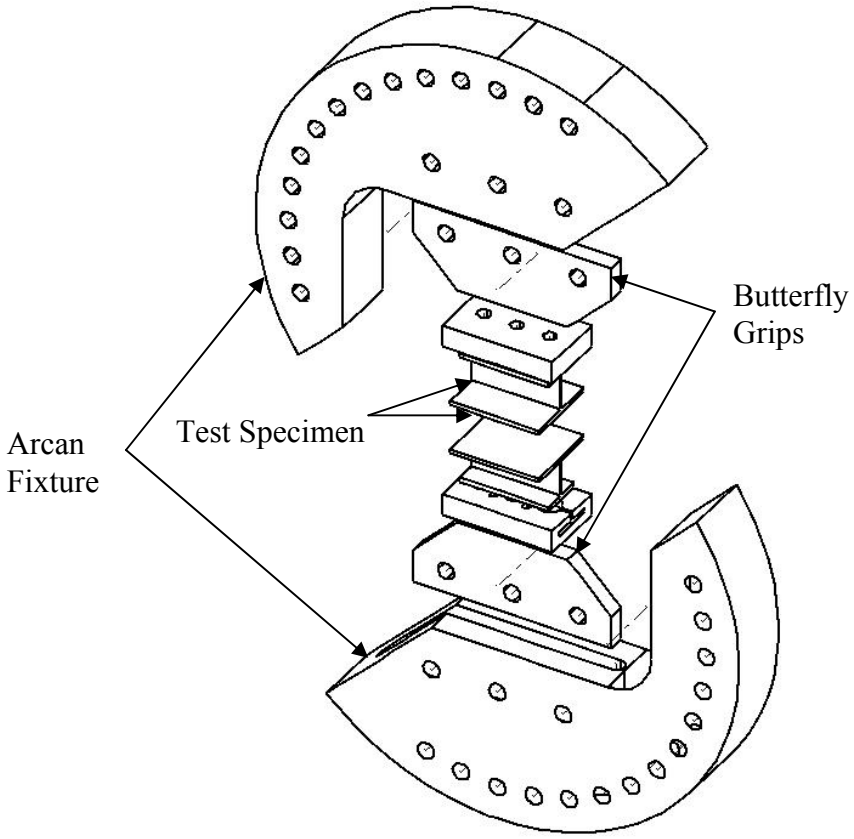

Figure 3.2-1 Modified Arcan ($Arcan_m$) test fixture. (See Figure 3.2-2 for illustration of counterweights.)

Strength tests were conducted over a range of combined normal and shear stress states at various displacement rates using the $Arcan_m$ in an Instron Model 4505 load frame equipped with a 1 kN load cell. The maximum displacement of the cross head was adjusted to reduce the cycle time and increase the signal-to-noise ratio. The stress state of the test specimen is controlled by the orientation of the $Arcan_m$ during loading. Pure normal is referenced as 0° rotation and pure shear as 90° rotation. In addition to these two rotation angles, 30° and 60° rotations were tested. These four rotation angles were selected based on preliminary testing and are sufficient to capture the shape of the failure curve. The 0° and 60° rotation angles are shown in Figure 3.2-2. Each rotation angle was loaded at displacement rates of 0.05, 0.5, 5.0 and 50.0 mm/min. Note the balancing weights in these photographs. Each test sequence was repeated four times resulting in a total of 64 tests at ambient lab conditions. The load-displacement data was analyzed to determine the best method to represent the strength and modulus data for use in design.

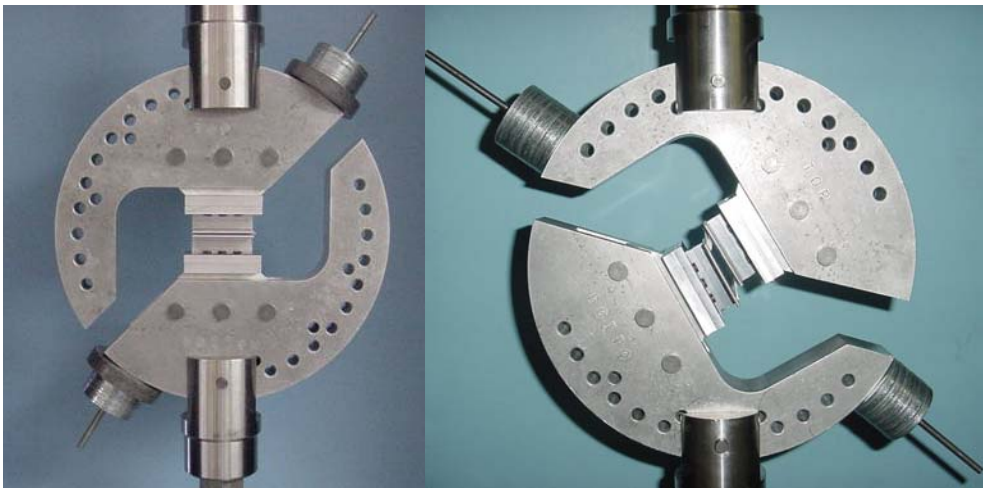

a) 0°-Pure Normal b) 60°-Pure Shear

Figure 3.2-2 Arcan$_m$ at 0° and 60° rotation.

3.2.1 Load-Train Stiffness

As stated in the previous section the cross-head displacements were recorded during the tests. The cross-head displacement included the displacement in all of the mechanical joints as well as the strain in the Arcan$_m$ Fixture the adherends, and the adhesive. To determine the load-train displacement a "rigid" specimen was constructed by bonding a specimen together using 3M Scotch-Weld™ DP100 Plus Epoxy. The bond line was made as thin as possible (≈ 0.03 mm) to minimize the contribution of the adhesive layer in the displacement measurements. This specimen was then tested at a rotation angle of 0° and a displacement rate of 5 mm/min. The load-displacement data was recorded and used to determine the amount of recorded displacement associated with the load-train.

3.3 Shape Factor Analysis Testing

As indicated in sections 2.2.1 and 2.4 the width of the bond may effect the stress distribution and modulus calculation. A series of test with different bond widths were conducted to determine if the calculations of σ_a and E_a need to be corrected. Bond widths of 0.5 in, 1.0 in, and 1.5 in were tested at 0° rotation (pure normal stress) and 0.5 mm/min displacement rate. Four specimens were tested at each test configuration and load – displacement data recorded. The peak stresses and elastic moduli of the three bond widths were compared to determine if this system has a geometric width effect.

3.4 Load-Control versus Displacement-Control Testing

The linear portion of the 0° rotation data was used to determine the range the equivalent loading rates. Tests were then conducted under load control using the Arcan$_m$ and an MTS 204. The same load train was used in both machines to reduce the impact of non

adhesive-based displacements. Tests were then conduced over the load range previously determined. Four tests were conducted at four load rates and load-displacement data collected. The peak stress and strain under load control and displacement control were then compared to determine if there is a relationship between the two loading conditions.

3.5 Complex-Load Testing

The strength data that was collected using the $Arcan_m$ does not give any insight into how moments will affect the strength of the joint. It has been shown that some materials do not have the same tensile strength when subjected to gradient rather than uniform normal stresses [37, 38]. To determine if VHB demonstrated this behavior a second test fixture was designed which allows for the load to be applied through an adjustable moment arm. This fixture consists of a fixed loading angle of 60° and a moment arm that can be adjusted from 0.0 mm to 75.0 mm. This fixture is shown in Figure 3.5-1 and complete detail drawings can be found in Appendix B.

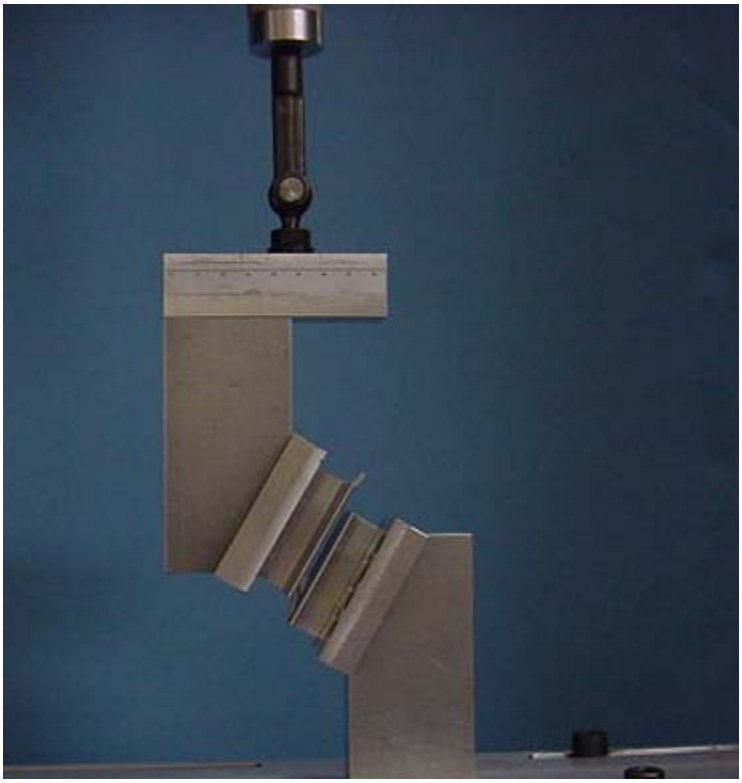

Figure 3.5-1 Complex-Load Fixture (12.0 mm moment arm).

This configuration results in a normal stress that is a function of both the load and the moment arm length and a shear stress that is only a function of the load. Assuming linear superposition the normal stress can be calculated using Equations (3.5-1). The shear stress is represented by Equation (3.5-2).

$$\sigma_{eng} = \frac{P*L*c}{I} + \frac{P}{A_a}\cos(60^\circ) \quad (3.5\text{-}1)$$

$$\tau_{eng} = \frac{P}{A_a}\sin(60^\circ) \quad (3.5\text{-}2)$$

In these equations P is the applied load and L is the moment arm length. It should be noted that the fixture is not symmetric and this asymmetry results in an additional moment that is not a function of the moment arm length. This geometric-moment was determined to be 156.6 N-mm, which corresponds to ≈ 10% of the tensile stress at $L = 0$ mm. The fixture moment acts in the opposite direction of the load-based moment and, therefore, will need to subtracted when calculating the normal stress.

Knowing the individual tensile and shear stresses the equivalent Arcan_m loading angle can be calculated using Equation (3.5-3). This allows the complex-load and bi-axial strength data to be compared directly.

$$\theta_{eff} = \tan^{-1}\left(\frac{\tau_{eng}}{\sigma_{eng}}\right) \quad (3.5\text{-}3)$$

Tests were conducted at a displacement rate of 5.0 mm/min at the loading point of the moment arm. Moment arm lengths of 0, 6, 12, 16, and 20 mm were used. The tests were repeated four times and the load-displacement data was recorded. These tests were conducted during the summer and the lab environment was not the same as previous testing. To reduce the effects of temperature and *RH* additional strength tests were conducted in parallel with the complex-load tests using the Arcan_m. This allowed for direct comparison of the complex-load data and the strength data. These tests were conducted at 5.0 mm/min and 0°, 15°, 30°, 45°, and 60° rotation. It was not necessary to retest at 90° since the complex-load data is limited to a maximum of a 60° loading angle. The additional rotation angles were added to further define the strength envelope over this region. This was helpful since the complex-load scenarios produce many different equivalent Arcan angles per Equation (3.5-3).

4.0 Results

This sections details the methods used to analyze the test data to determine the material properties of the adhesive. This includes the strength and modulus of the adhesive, as well as determining the effects of joint geometry, moments, and "load" rate (load control vs. displacement control). Specific attention was given to dealing with the differences in the in-situ properties verses the bulk adhesive constitutive properties. For the constitutive-adhesive properties to be useful in joint designs they must be independent of the geometry and the loading conditions. This means that a method of applying the bulk-material properties to any joint design is critical for any mechanical design to be successful.

4.1 Strength

As stated in section 3.0 the cross-head displacement was recorded, not the adhesive displacement. This can result in inflated displacement rates which are not representative of the adhesive load rate. The load-displacement data collected on the "rigid" specimen (see section 3.2.1) was used to determine the extent of the load-train displacement. This data is shown in Figure 4.1-1.

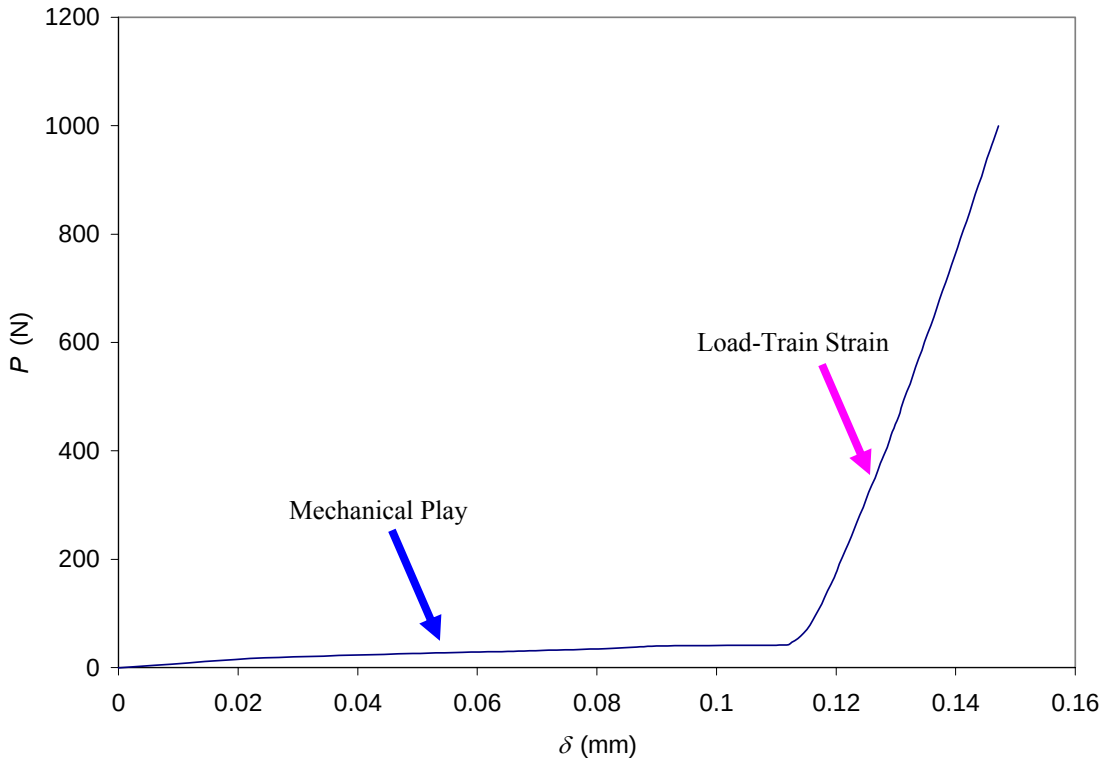

Figure 4.1-1 Load-Train Data (θ_{Arcan}=0°, R_d=5.0 mm/min, *Temp*≈20°C, and *RH*≈25%).

As one can see there is a large span of deflection where the load does not increase very much with increased displacement (marker with blue arrow). It is believed that this is

associated with mechanical play in the test fixture and is not associated with true load-induced strain in the load-train.

To get a better idea of the load-train strain the original data was shifted to eliminate the "mechanical slop". The shifted load-displacement data is shown in Figure 4.1-2.

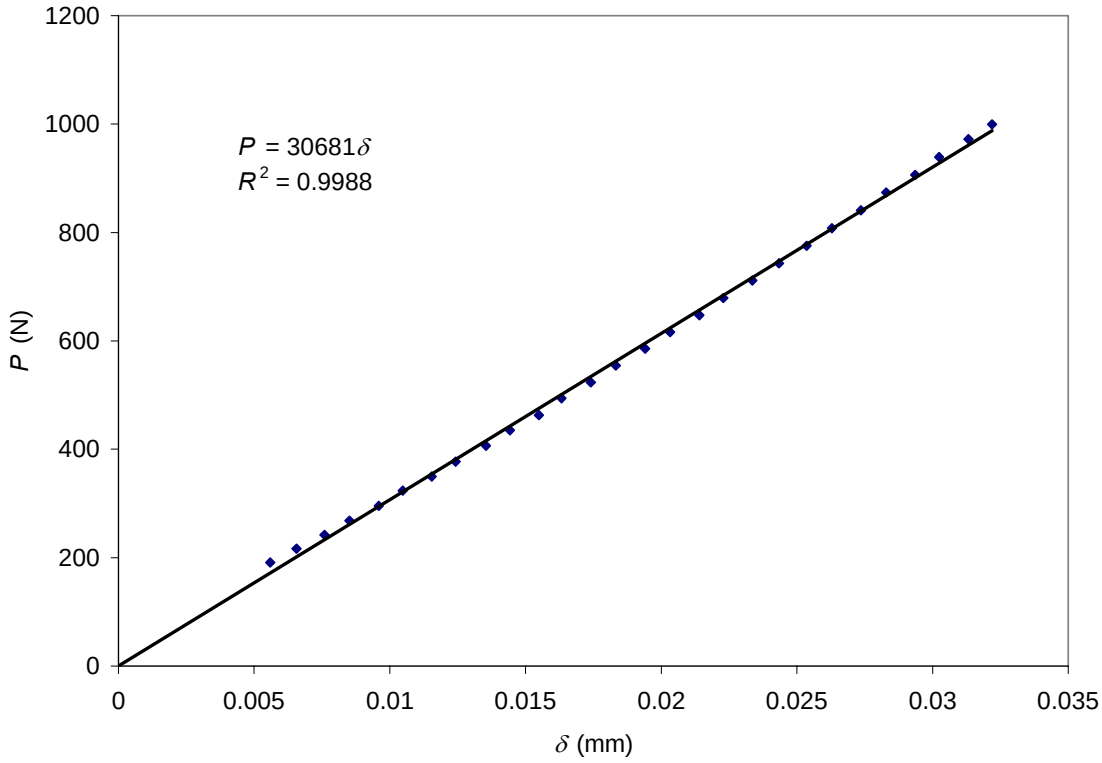

Figure 4.1-2 Adjusted Load-Train Stiffness.

This data indicates that the load-train will displace 0.033 mm with an applied load of 1.0 kN. This represents ≈ 10% of the total displacement recorded in tension at 50 mm/min. For this reason the data collected for $\theta_{Arcan} = 0.0°$ were corrected for the load-train displacements. The displacement in the load-train causes the loading rate of the adhesive to be decreased. A cross-head displacement rate of 50 mm/min will correspond to approximately a 45 mm/min adhesive displacement rate. This is approximate due to the nonlinear nature of the adhesive. In reality the adhesive displacement will vary throughout the test. For simplicity the cross-head displacement will still be reported. The displacements at the other test angles were greater than 1.0 mm making the load-train displacement less than 5%. This is small when compared to the errors associated with determining the peak displacement and the variation between specimens. For this reason no corrections were made for the lower test rates.

The load-displacement data for several specimens of different loading conditions are shown in Figure 4.1-3 and 4.1-4. Data for all of the tests can be found in Appendix C.

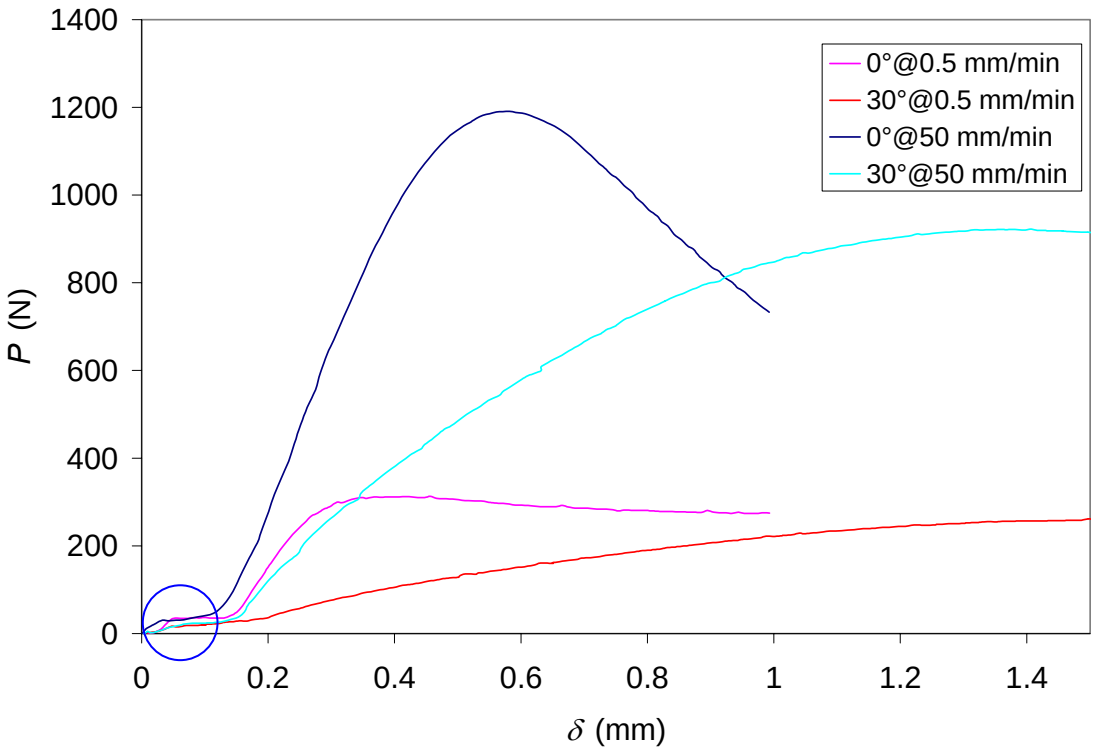

Figure 4.1-3 Load-Displacement Data – VHB 4950 at 20°C and 25%*RH*.

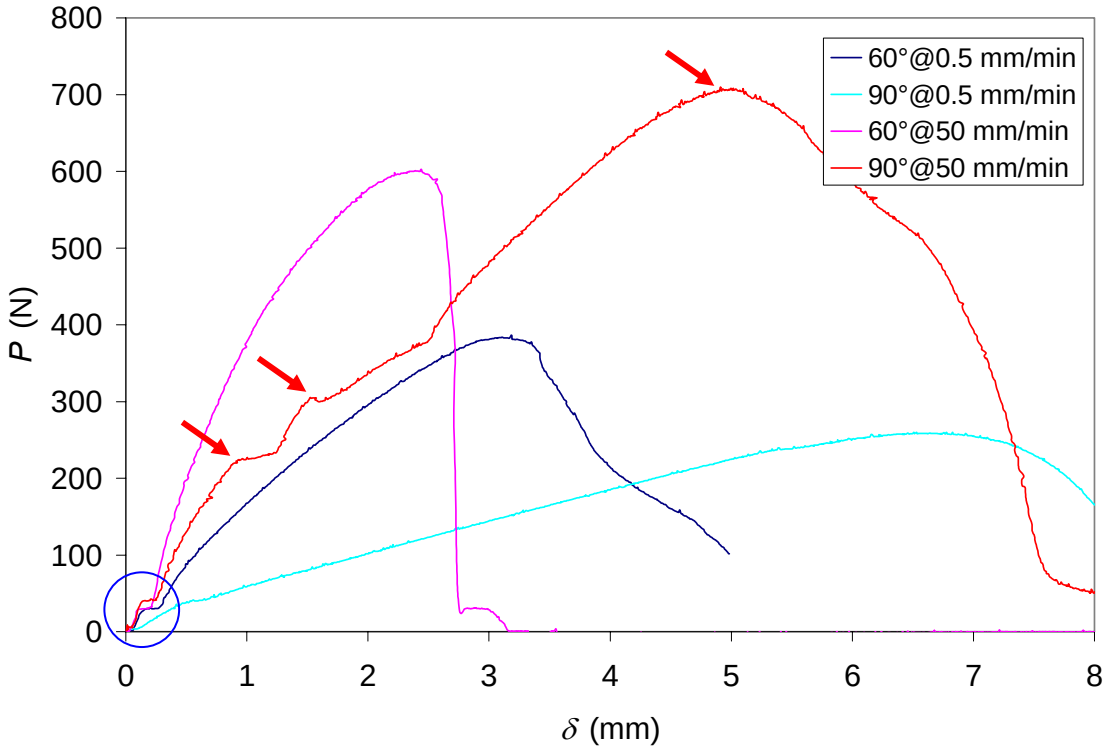

Figure 4.1-4 Load-Displacement Data – VHB 4950 at 20°C and 25%*RH*.

As one can see this data is nonlinear and in some cases shows multiple peaks before adhesive failure. These are indicated by the red arrows in Figure 4.1-4. The blue circle in Figure 4.1-3 and 4.1-4 indicates the load-train mechanical slop which was previously discussed. The data does show some addition load and displacement noise indicated by the red arrows. Much of this may be do to stick slip and cavitation of the adhesive.

A great deal of information can be extracted from the load-displacement data. Equations (4.1-1) through (4.1-4) were used to determine the stress and strain.

$$\sigma_a = \cos\theta_{Arcan}\frac{P_{max}}{A_a} \tag{4.1-1}$$

$$\tau_a = \sin\theta_{Arcan}\frac{P_{max}}{A_a} \tag{4.1-2}$$

$$\varepsilon_a = \cos\theta_{Arcan}\frac{\delta_{max}}{t_a} \tag{4.1-3}$$

$$\gamma_a = \tan^{-1}\left(\frac{\cos\theta_{Arcan}\delta_{max}}{t_a}\right) \tag{4.1-4}$$

These equations separate the Arcan_m load-displacement data into its normal and shear components as well as scale them to stress and strain. As indicated in section 3.1 the nominal adhesive area (A_a) is 645 mm^2 (1.0 in^2) and the nominal adhesive thickness (t_a) is 1.14 mm (0.045 in). In these equations δ_{max} is the corrected displacement. The displacements associated with the mechanical slop have been subtracted from the total displacement to obtain δ_{max}.

Plots of the stress-strain data were then generated and the failure stresses and strains were determined. This was not as simple a task as it may sound. The PSA tape has a non-linear stress-strain curve with some plastic deformations before failure. ASTM standard D 638-01 [1] was used as a guide determining the methods used for calculating the failure stresses and strains. Based on this standard the peak stress was reported as well as the corrected peak strain. As with ductile materials it is desirable to have a material property that establishes a strength just prior to permanent damage. Many of the curves have a pronounced change in slope before the last peak. This change in slope is correlated to failure of the adhesive and, in some cases, rotation of the Arcan_m fixture. For this reason the last peak or the slope transition was set as the failure point in establishing maximum design strengths. In reality some damage to the adhesive has occurred at this point, but for consistency and convenience these values were used.

This requires that each of the curves be examined to determine the point at which failure initiated. In most cases the curves demonstrate a clear change in slope that could be correlated to the failure. This process is demonstrated in Figure 4.1-5 and 4.1-6.

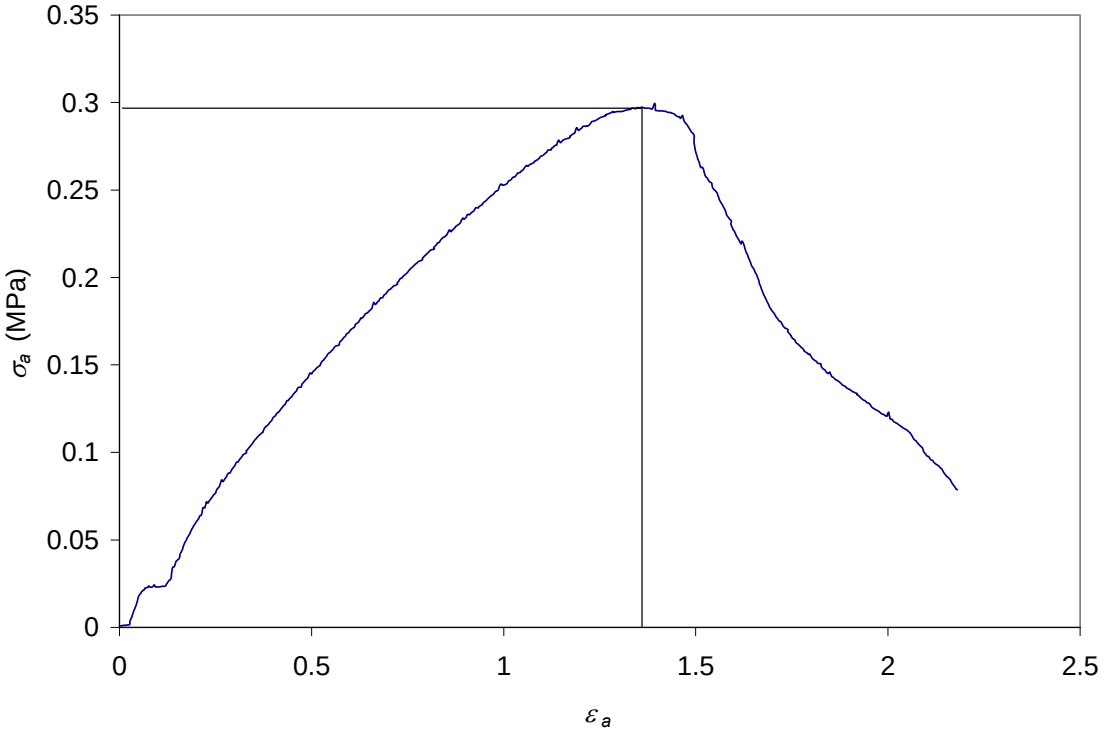

Figure 4.1-5 σ_a vs. ε_a (θ_{Arcan}=60°, R_d=5.0 mm/min, *Temp*≈20°C, and *RH*≈25%).

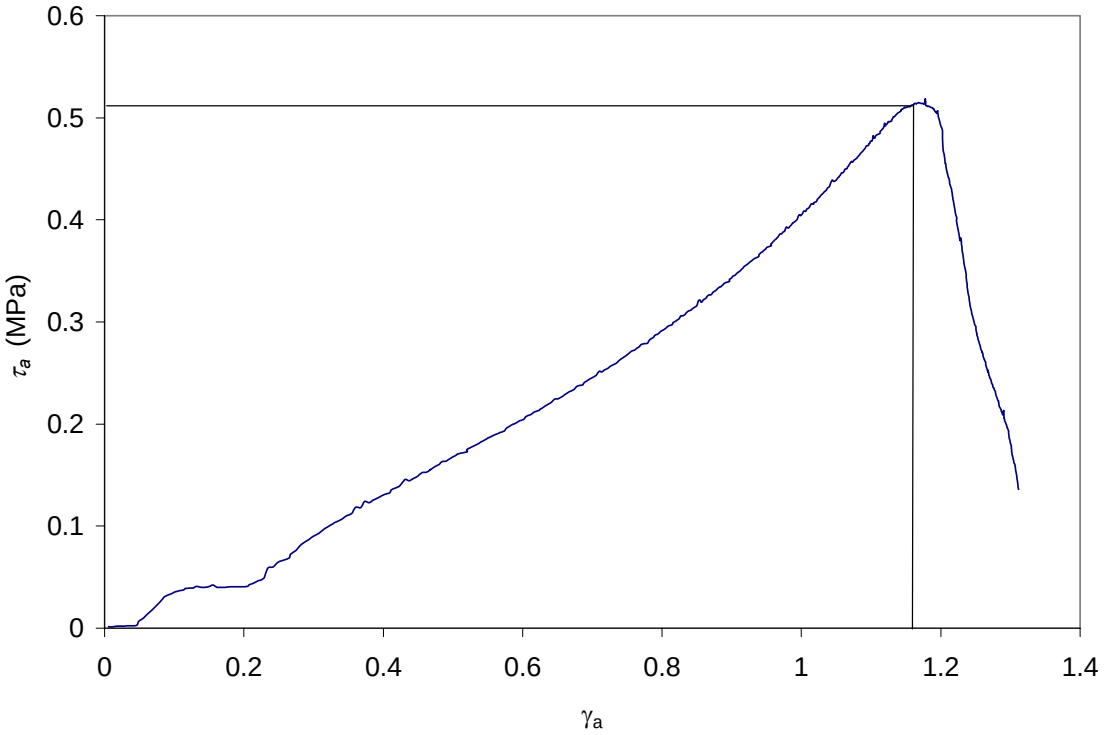

Figure 4.1-6 τ_a vs. γ_a (θ_{Arcan}=60°, R_d=5.0 mm/min, *Temp*≈20°C, and *RH*≈25%).

The difference between the shape of Figure 4.1-5 and 4.1-6 is due to the method used to calculate the shear strain as indicated in Equation (4.1-4). The inverse tangent function is nonlinear and can never exceed π/2 or 1.57 (see Section 2.3). This results in a skewed plot with respect to strain. For example, the actual shear displacement at peak load was 6.24 mm compared to t_a = 1.14 mm. This displacement is well beyond the small displacement region that makes Equation (4.1-4) valid. This issue is not pursued here, but is pointed out so that other researchers can study and define a more appropriate definition for shear strain in visco-elastic materials.

A sample of the peak stresses and strain for the strength data is presented in Table 4.1-1. A complete set of strength data can be found in Appendix D.

Table 4.1-1 Strength Data – VHB 4950 at 20°C and 25%*RH*.

Part #	θ_{Arcan} (Deg)	R_d (mm/min)	σ_{max} (MPa)	τ_{max} (MPa)	ε_{max}	γ_{max}
a-03-02-01-02	0	0.05	0.33	0.00	0.18	0.00
a-03-05-01-05	0	0.5	0.49	0.00	0.21	0.00
a-03-05-01-04	0	5	0.77	0.00	0.24	0.00
a-03-05-01-01	0	50	1.99	0.00	0.40	0.00
a-03-06-01-06	30	0.05	0.21	0.12	1.24	0.62
a-03-02-01-05	30	0.5	0.40	0.23	1.69	0.77
a-03-02-01-23	30	5	0.59	0.34	0.90	0.48
a-03-02-01-29	30	50	1.06	0.61	0.90	0.48
a-03-02-01-15	60	0.05	0.15	0.26	2.13	1.31
a-03-02-01-21	60	0.5	0.16	0.27	1.48	1.20
a-03-02-01-14	60	5	0.24	0.42	1.16	1.11
a-03-02-01-30	60	50	0.49	0.85	1.09	1.08
a-03-02-01-16	90	0.05	0.00	0.32	0.00	1.39
a-03-06-01-10	90	0.5	0.00	0.49	0.00	1.41
a-03-06-01-08	90	5	0.00	0.75	0.00	1.41
a-03-05-01-16	90	50	0.00	1.34	0.00	1.39

The collected strength data will only be valuable if it can be used to predict failures in future joint designs. One possible method is to present the data in a form that can be used with existing failure theories or at least in a form that is familiar to designers. With this in mind the strength data was plotted in as many possible combinations as feasible. The plots shown in Figures 4.1-7 through 4.1-13 were considered relevant to design and will be discussed. Additional plots of the data can be found in Appendix H. For clarification a single curve has been added to each plot to insure the correct interpretation of the data. These curves were generated using the trend-line function in Microsoft Excel® and are only intended as a guide. The color of the added curve is the same as the corresponding data set. In addition the Arcan_m angle has been added to the appropriate figures.

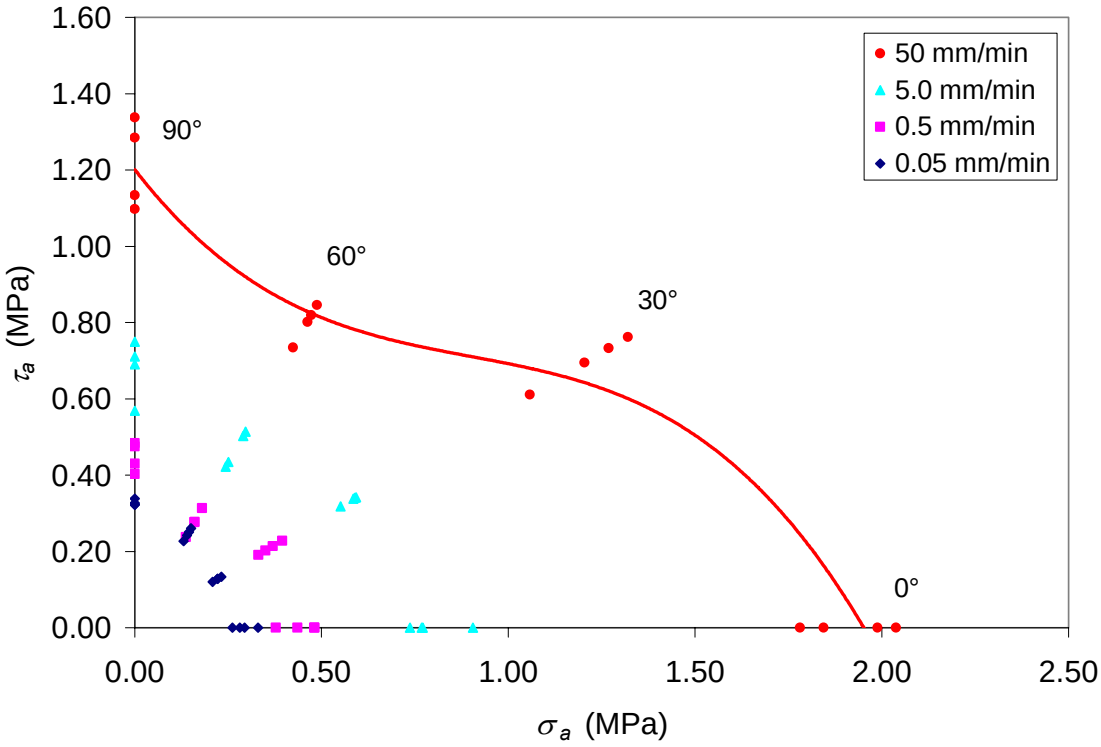

Figure 4.1-7 Stress Based Design Envelope – VHB 4950 at 20°C and 25%*RH*.

In Figure 4.1-7 the shear stress is plotted against the normal stress. This results in an allowable stress envelope for each of the tested rates. Each envelope spans stress states from pure normal to pure shear. The change in the level and shape of the envelopes demonstrates the rate dependence of the system. The dip in the 50 mm/min, 5.0 mm/min, and the 0.5 mm/min data at 60° is most likely due to a change in the failure mode of the adhesive layer. The variation in the curve shapes makes it very difficult to compress this data into a single curve and brings into to question the validity of applying time-temperature superposition. This requires that a family of design envelopes be generated covering the intended loading rates from creep to impact. This group of curves represents sections through a design surface which is continuous in rate. With enough test data the surface can be completely defined for all rates and stress states. With this surface an engineer could easily determine the validity of a design for a specified loading rate and stress state.

Figure 4.1-8 is the stain version of Figure 4.1-7. In this case the shear strain is plotted with respect to the normal strain. Again this results in a series on design envelopes covering the entire test domain. The rate effect is very apparent when looking at the strain at failure. This is especially true at the 30° and 60° loading angles. Again, this will make it very difficult to develop a single design envelope and, therefore, requires a series of curves. Unlike the stress plot, the strains in pure shear and pure tension have a small rate effect. This may make strain a better design criterion for these stress states. However, when a more general state of stress/strain is applied the allowable strains very by as much as 250% with respect to the displacement rate.

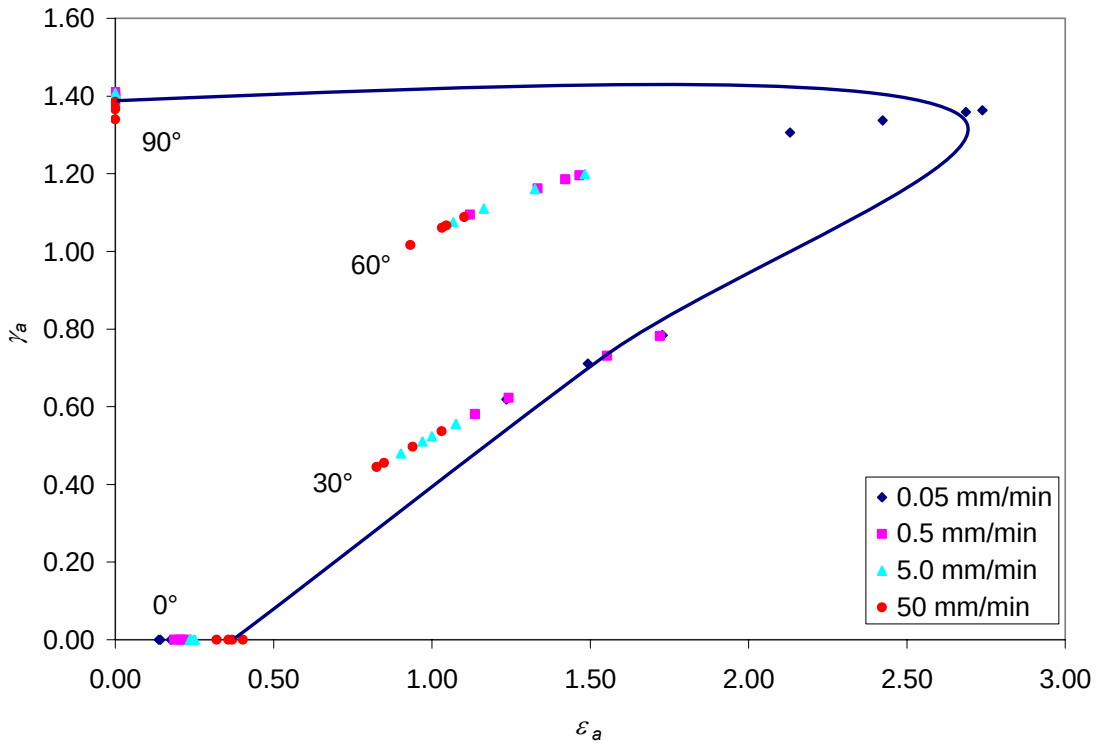

Figure 4.1-8 Strain-Based Design Envelope – VHB 4950 at 20°C and 25%*RH*.

Figures 4.1-9 and 4.1-10 were generated using Mohr's Circle analysis of the stress and strain data resulting in the principal stresses and strains. The use of Mohr's Circle and the relevant equations are described in section 2.7. It is a common practice to use the principal stresses and strains in the analysis of brittle mechanical systems. Here where the adhesive is visco-elastic little usefulness is expected. The principal stresses shown in Figure 4.1-9 have little to no correlation to the curves presented in Figure 2.8-1. Figure 2.8-1 demonstrated the design space associated with the Maximum-Shear-Stress Theory and the Maximum-Distortion-Energy Theory. The lack of correlation between the Arcan_m data and the common failure theories is another indicator of the uniqueness of this adhesive compared to linear-elastic materials. Unfortunately, this may prohibit the application of a rate dependent form of one of the failure theories used and understood by design engineers for this adhesive. The variation in the pattern of the principal stress and strain data as well as the strong rate dependence makes it very difficult to develop a new material specific failure model. At this point it does not appear that the principal stresses or strains will be of much value in this design process.

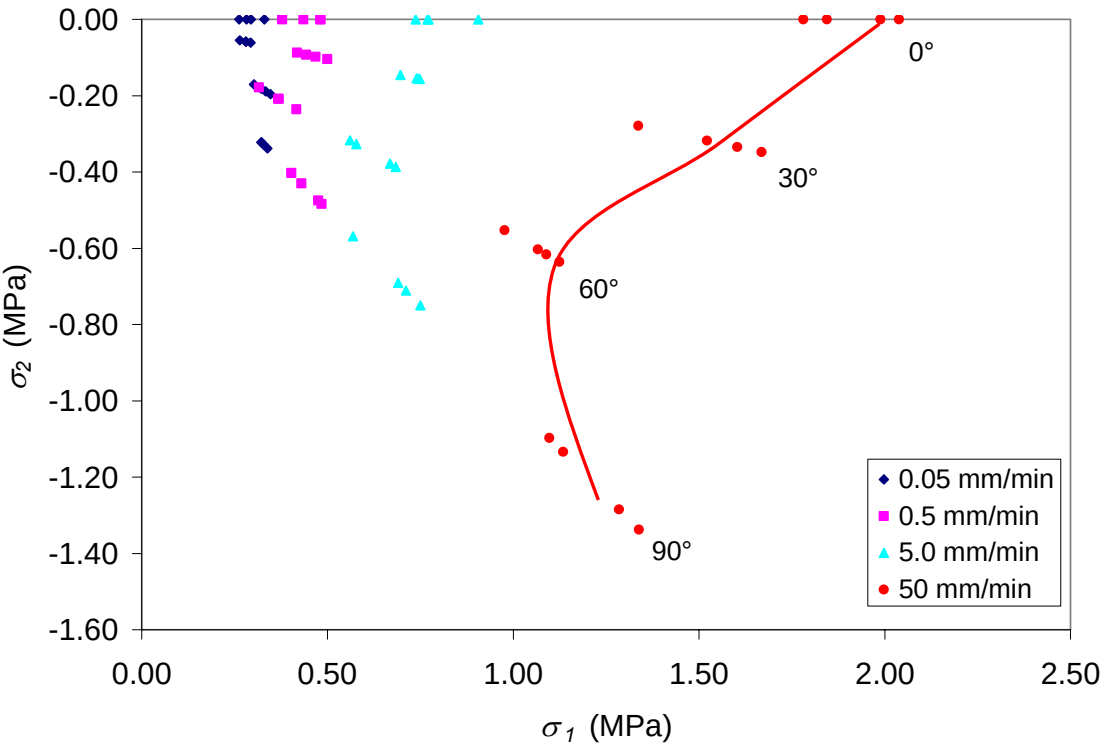

Figure 4.1-9 Principal Stresses – VHB 4950 at 23°C and 35%*RH*.

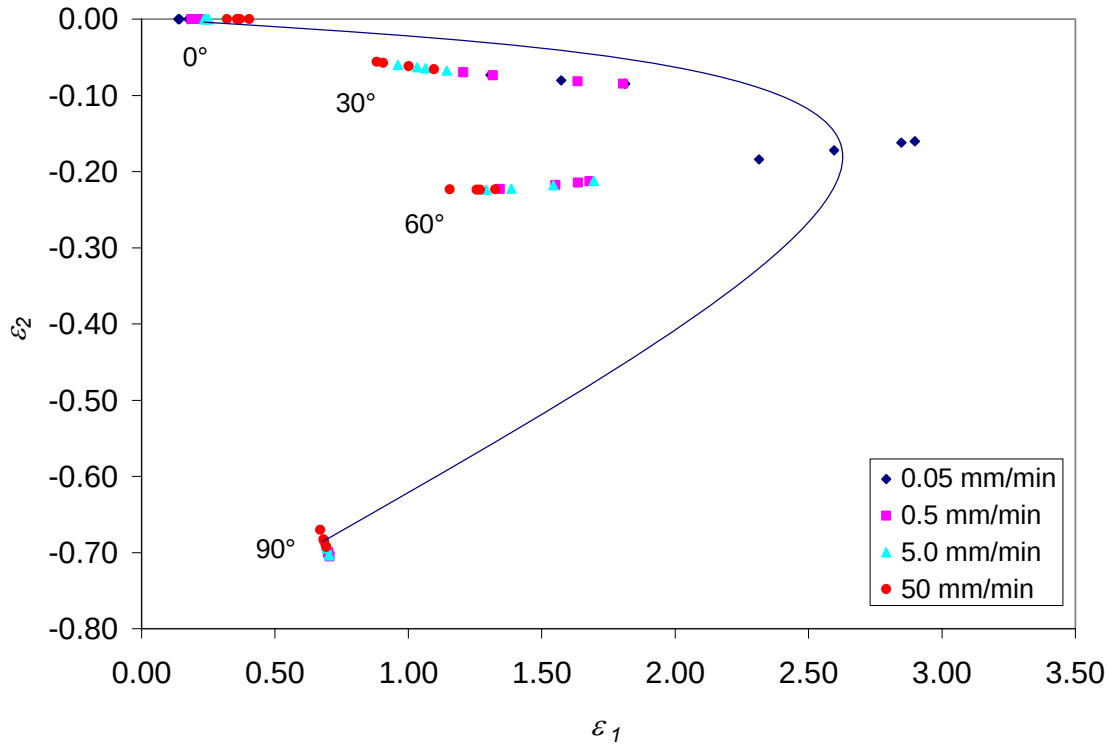

Figure 4.1-10 Principal Strains – VHB 4950 at 23°C and 35%*RH*.

Engineers are familiar with using a failure criteria based on a single strength value. Typically the yield strength is used and there are no rate effects. For linear-elastic materials this method has been proven to be reliable. The $Arcan_m$ data has shown that VHB is far from a linear-elastic material. This requires that any design methodology for VHB must include rate. But, this does not rule out using a rate dependent form of one of the failure theories.

Figures 4.1-11 through 4.1-13 are the application of the MSST, MDET, and the Maximum-Shear Strain Theory. The appropriate equations for the MSST and the MDET can be found in sections 2.8.1 and 2.8.2. The Maximum Shear Strain was obtained from a Mohr's Circle analysis of the strains at yield (see Section 2.7).

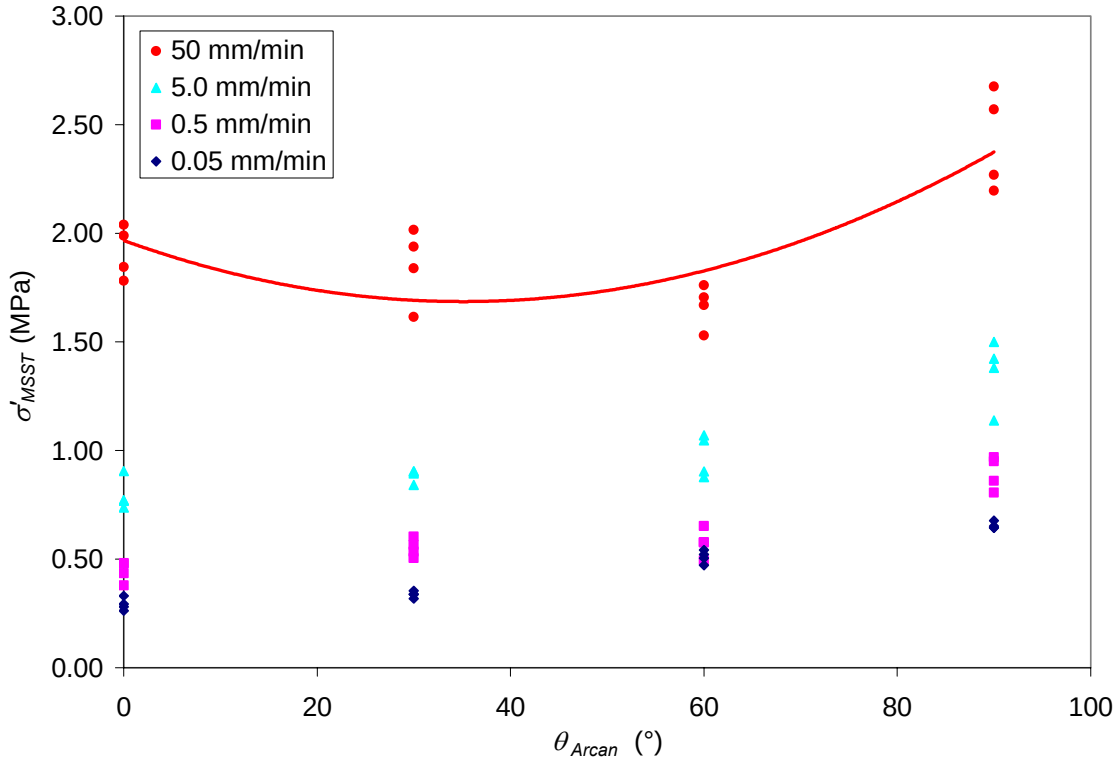

Figure 4.1-11 MSST vs. θ_{Arcan} – VHB 4950 at 20°C and 25%*RH*.

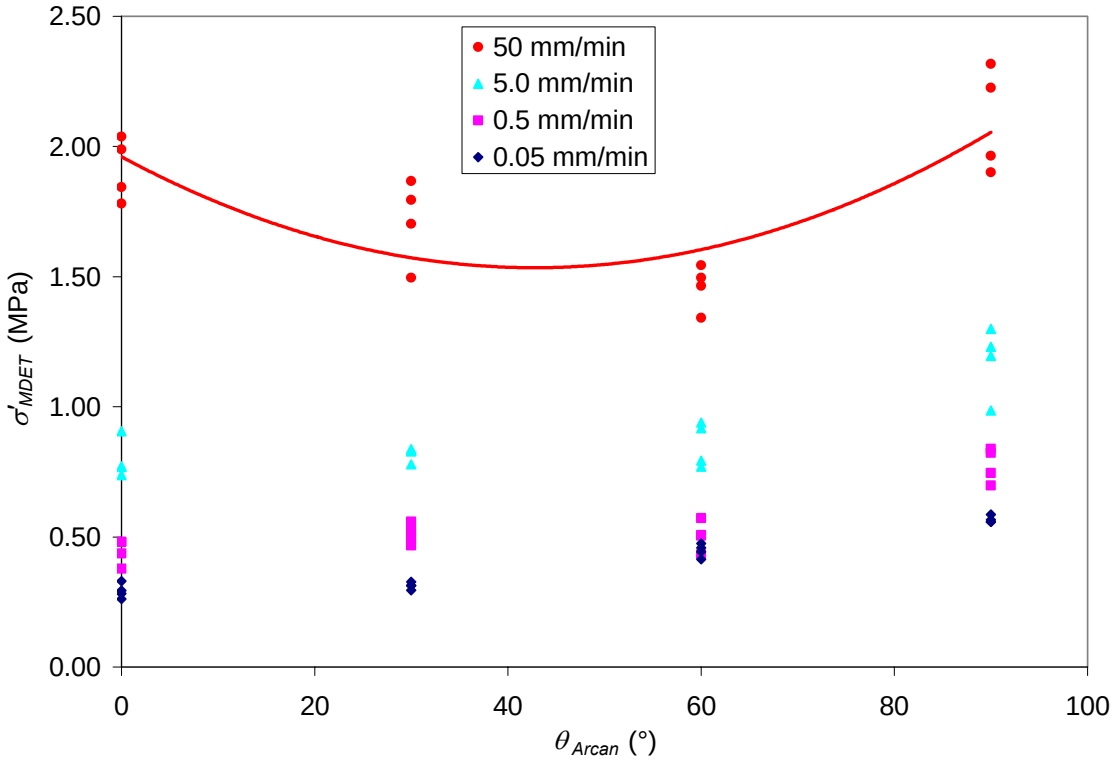

Figure 4.1-12 MDET vs. θ_{Arcan} – VHB 4950 at 20°C and 25%*RH*.

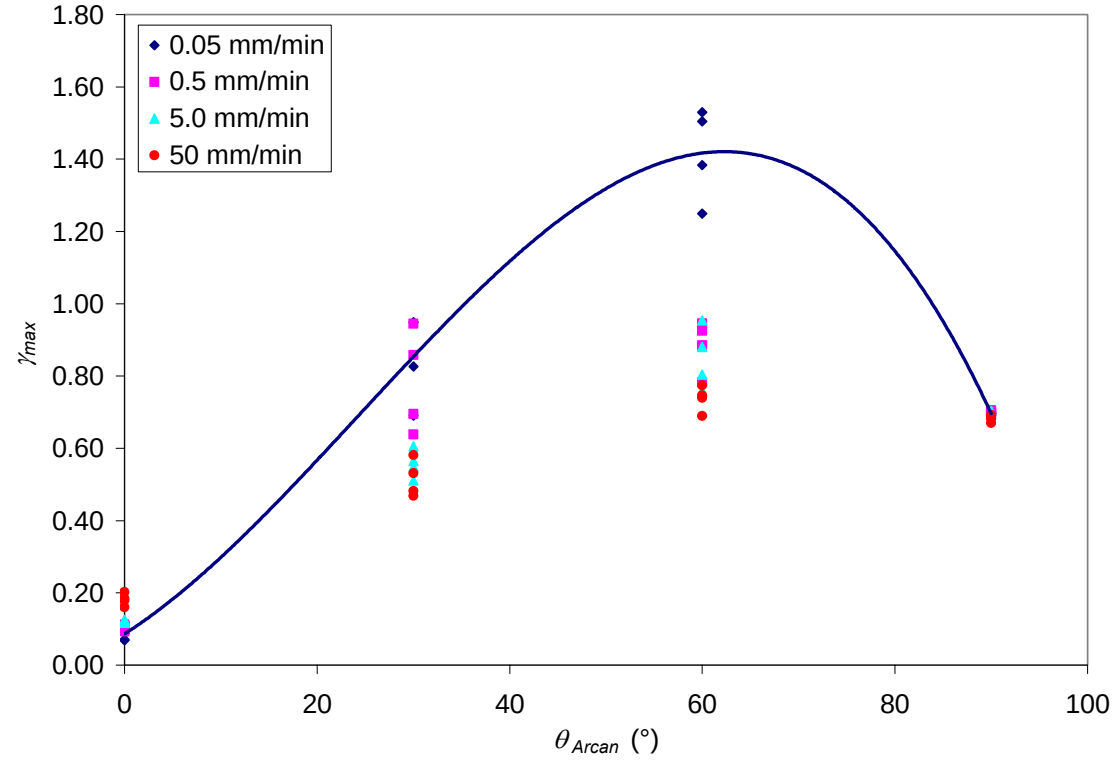

Figure 4.1-13 Maximum Shear Strain vs. θ_{Arcan} – VHB 4950 at 20°C and 25%*RH*.

All three of these figures display a strong rate effect. This is most apparent in the 50 mm/min displacement data. The 0.05 mm/min, 0.5 mm/min, and 5.0 mm/min data sets show a similar pattern. This allows each data set to be fit with a common formula as a function of Arcan angle. This process was completed for the MSST data since the order of the curve was the lowest. For simplicity a second-order fit was applied to each of the data sets using the trend function in Microsoft Excel©. The resulting envelopes are shown on Figure 4.1-14 and the values for *a*, *b*, and *d* for each of the curves can be found in Table 4.1-2.

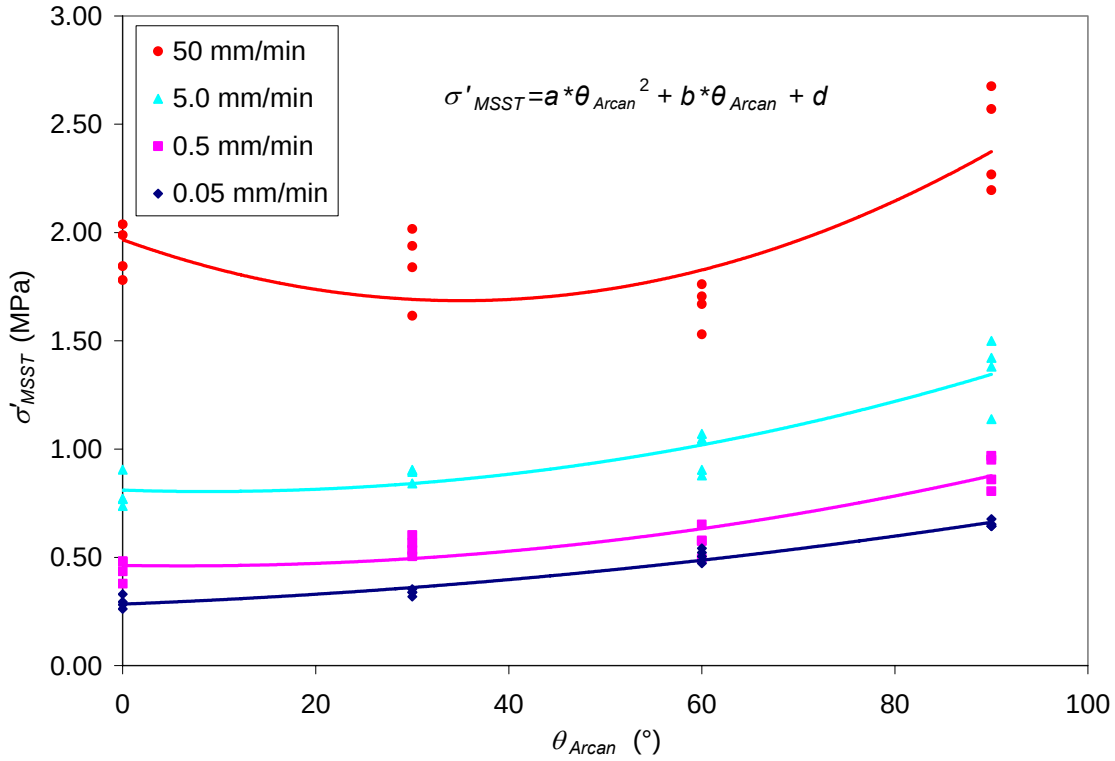

Figure 4.1-14 MSST Regression – VHB 4950 at 23°C and 35%*RH*.

Table 4.1-2 MSST Regression Equations – VHB 4950 at 23°C and 35%*RH*.

R_d (mm/min)	a (10^{-5})	b (10^{-3})	d	R^2
0.05	2.7	1.7	0.28	0.9666
0.5	5.9	–0.4	0.46	0.8550
5.0	8.2	–1.4	0.81	0.8387
50	22.8	–16.0	1.97	0.6529

As one can see the four curves have very different shapes and coefficients. At this point the complexity of the final equation must be decided. To generate the best fit the coefficients on θ_{Arcan} (a and b) and the intercept (d) need to be functions of R_d. A "fit" for each of these values was performed using Microsoft Excel©. The plot of the data and resulting fit for a, b, and d are shown in Figures 4.1-15 to 4.1-17

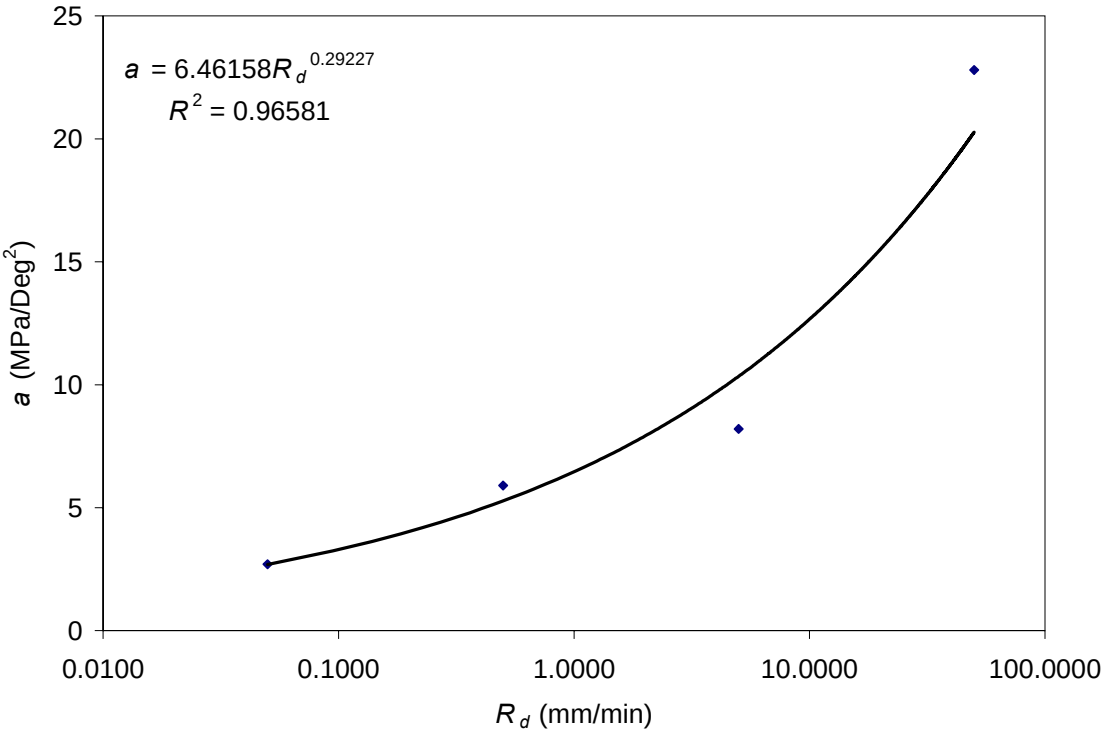

Figure 4.1-15 Coefficient "a" Regression – VHB 4950 at 23°C and 35%RH.

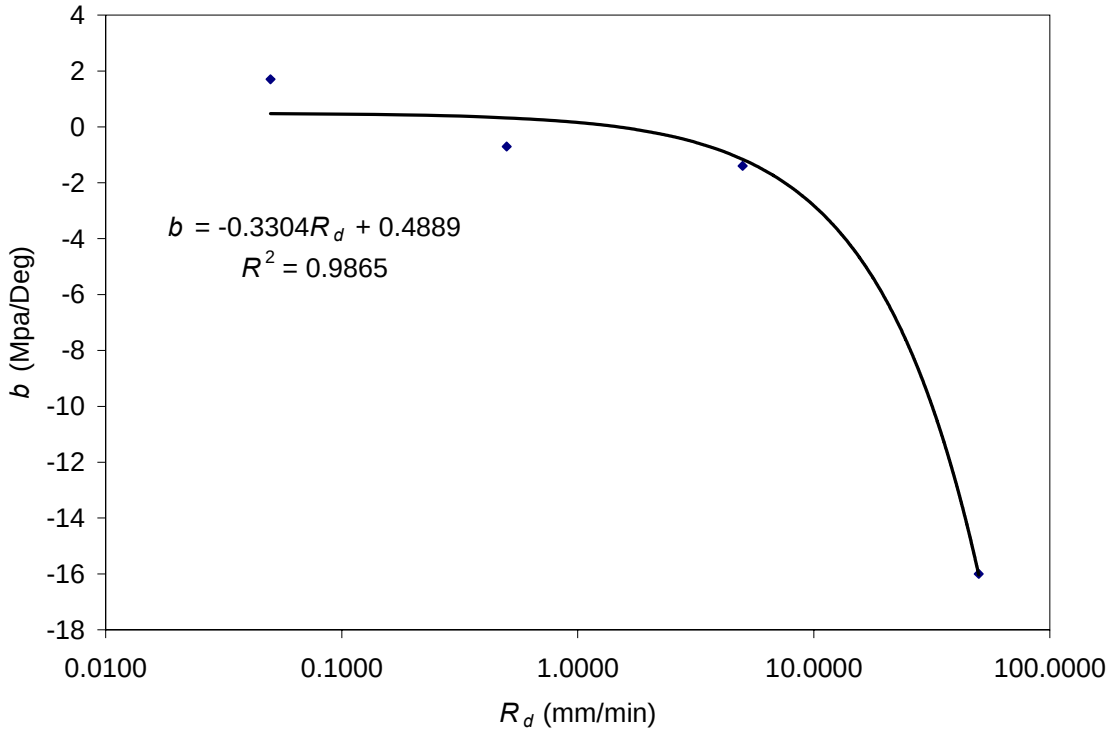

Figure 4.1-16 Coefficient "*b*" Regression – VHB 4950 at 23°C and 35%*RH*.

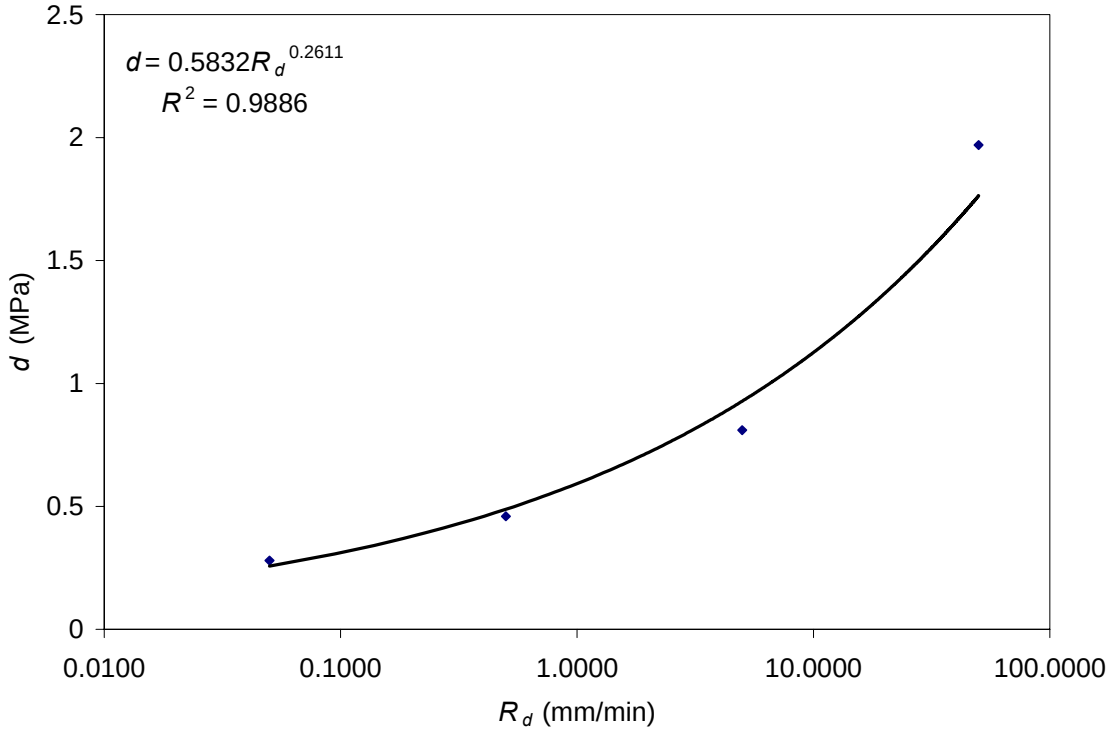

Figure 4.1-17 Intercept "*d*" Regression – VHB 4950 at 23°C and 35%*RH*.

All four data sets were then refit using $a(R_d)$, $b(R_d)$, and $c(R_d)$ the selected coefficients and resulting intercepts. This is shown in Figure 4.1-18.

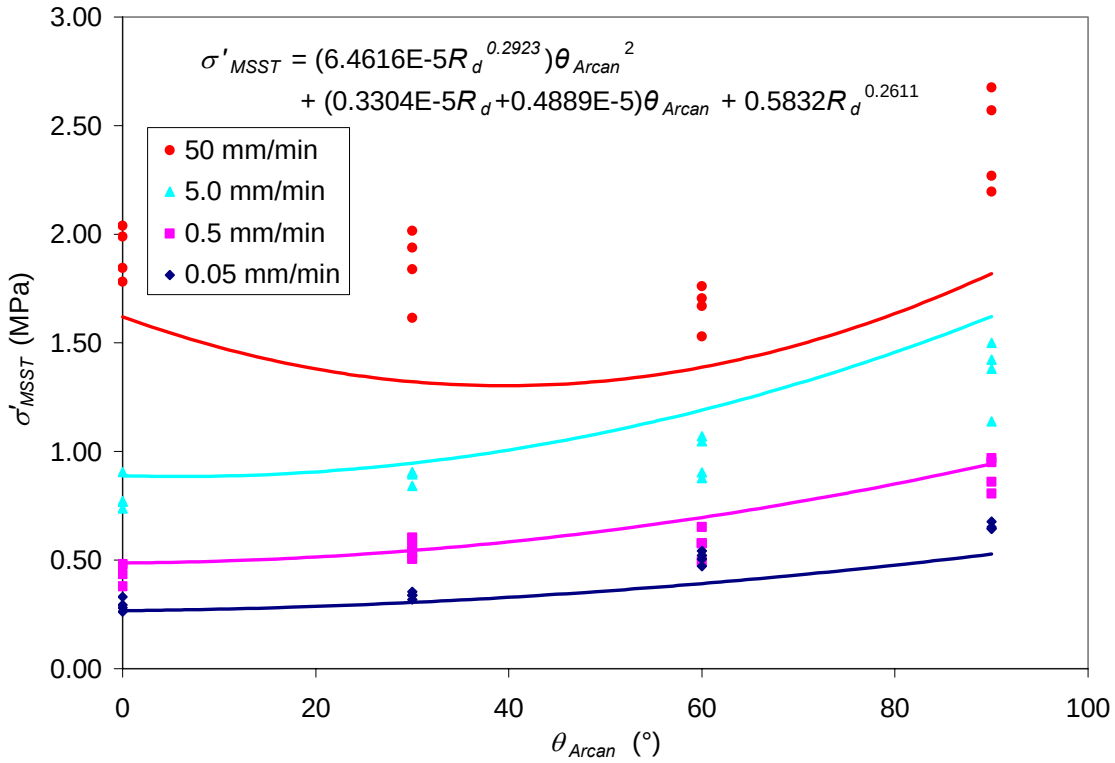

Figure 4.1-18 MSST Regression – VHB 4950 at 23°C and 35%*RH*.

As one can see this method results in a non-conservative prediction of the available design space. For example, the strength for an R_d of 50 mm/min and a θ_{Arcan} of 60° is overestimated by > 10%. For quick calculations this may be acceptable to get an idea about the system, but not for final calculation of the joint stresses and failure predictions. A better fit of the data is required for actual design work. This would require a regression to be performed over all of the data including the R_d. It may be necessary to use a higher order equation and allow each exponent and coefficient to be functions of R_d. This would allow for a statistical basis of the fit and facilitated the generation of prediction intervals which can be used in a probabilistic design.

Using a unified failure theory will require an additional step beyond the Tau-Sigma Design Envelopes, but is more inline with traditional design methodology.

4.2 Shape Factor Analysis

Before it is possible to determine the modulus of the adhesive it is necessary to determine the effects of the joint geometry on the apparent modulus of the system. The first step in the process was to use the load-displacement data to determine the stiffness of the

system. Two data points from the linear region of the load-displacement curve were selected and Equation (4.2-1) was used to calculate the system stiffness (K_{sys}).

$$K_{sys} = \frac{P_2 - P_1}{\delta_2 - \delta_1} \tag{4.2-1}$$

The system stiffness includes the stiffness of the load frame, the Arcan$_m$ fixture, and the two adherends. The load-train stiffness must be taken into account to correctly calculate the adhesive tensile modulus and determine the geometric effect. In section 4.1 the load train stiffness was calculated to be 30681 N/mm. Modeling the system stiffness as a series of springs and using the calculated load-train stiffness one can determine the in-situ adhesive stiffness (K_{app}). This relationship is shown in Equation (4.2-2).

$$K_{app} = \frac{30681 * K_{sys}}{30681 - K_{sys}} \tag{4.2-2}$$

The apparent-tensile modulus of the adhesive was then calculated using Equation (4.2-3).

$$E_{app} = K_{app}\frac{l}{A} = K_{app}\frac{1.14\text{mm}}{w_a * 50.8\text{mm}} = 2.27(10)^{-2}\frac{K_{app}}{w_a} \tag{4.2-3}$$

The resulting values for the system stiffness, adhesive stiffness, and apparent adhesive modulus are shown in Table 4.2-1. To better demonstrate the width effect Equation (2.4-5) was used to predict the E_{app} using a constitutive E_a of 0.81 MPa (see section 4.3). Both the calculated and predicted E_{app} are plotted with respect to bond width in Figure 4.2-1.

Table 4.2-1 Stiffness Data – VHB 4950 at 23°C and 35%*RH*.

Part #	w_a (mm)	K_{sys} (N/mm)	K_{app} (N/mm)	E_{app} (MPa)
a-05-29-01-01	12.7	1155.06	1200.24	2.13
a-05-29-01-05	12.7	1268.49	1323.19	2.34
a-05-29-01-04	12.7	1814.90	1929.01	3.42
a-05-29-01-19	12.7	1532.33	1612.89	2.86
a-05-29-01-08	25.4	2325.27	2515.95	2.23
a-05-29-01-09	25.4	2225.43	2399.47	2.13
a-05-29-01-10	25.4	2421.81	2629.36	2.33
a-05-29-01-11	25.4	2489.62	2709.48	2.40
a-05-29-01-15	38.1	2523.62	2467.89	1.46
a-05-29-01-13	38.1	2116.49	2273.31	1.34
a-05-29-01-12	38.1	2726.21	2338.78	1.38
a-05-29-01-14	38.1	2041.48	2187.00	1.29

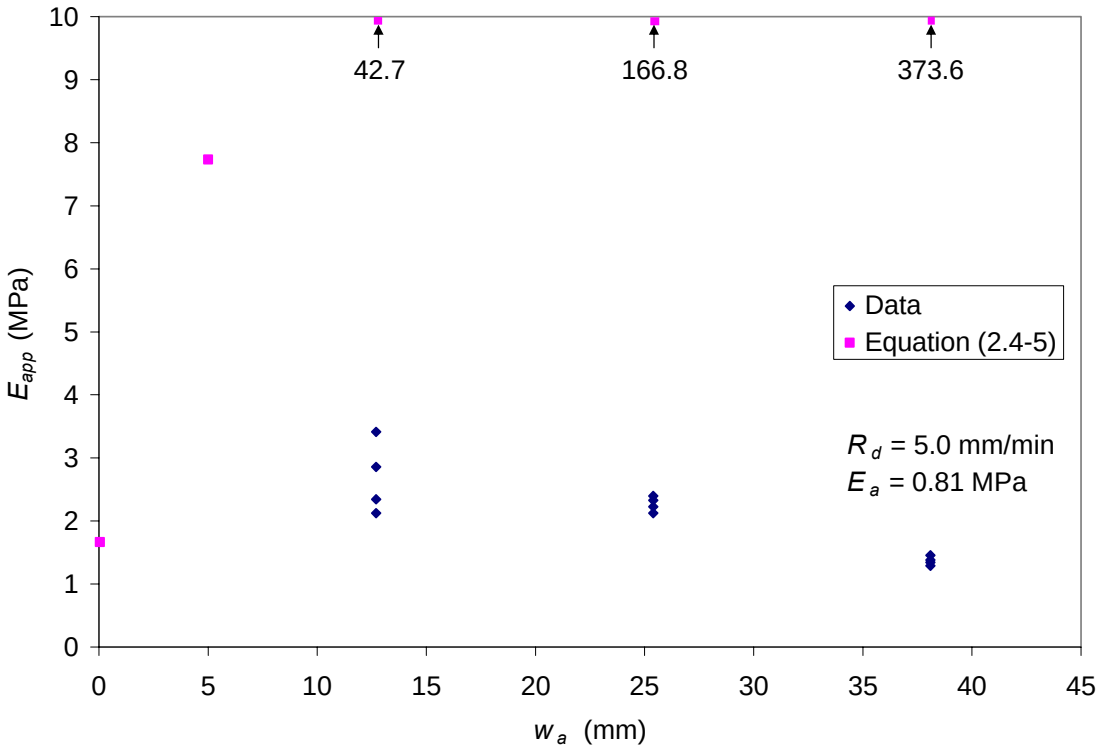

Figure 4.2-1 Measured and Predicted E_{app} vs. w_a – VHB 4950 at 23°C and 35%*RH*.

As one can see the E_{app} do not follow the trend that would be expected based on the discussion given in section 2.4 and Equation (2.4-5). The in-situ modulus was expected to significantly increase with greater bond width. As previously stated the width effects are strongly influenced by the Poisson's Ratio of the bonding material. Equation (2.4-5) is based on a Poisson's Ratio of 0.5. If the Poisson's Ratio of VHB is not 0.5 the geometric effects will be considerable less or possibly non-existent, as demonstrated by the data. Any trend in the data may be due to the inherent variability of the material and, therefore, additional work needs to be done to answer this question for VHB.

4.3 Modulus

Both the tensile and shear moduli are needed to perform mechanical designs. It was thought that both of these properties could be determined from the slope of the tensile and shear stress-strain data. Unfortunately, as indicated in the previous section the shape factor is not known for this adhesive. Without the correct shape factor it is not possible to calculate the adhesive constitutive modulus from the in-situ modulus. Because of this the tensile modulus was calculated from the shear modulus using Equation (4.3-1).

$$E_a = 2G_a\left(1+\mu_a\right) \approx 2G_a\left(1+0.5\right) \approx 3G_a \qquad (4.3\text{-}1)$$

In this equation the Poisson's Ratio is assumed to be 0.5. Small errors in this value will not cause large errors in the tensile modulus. Moreover, the determination of the shear

modulus is thought by most, but not all investigators, to be independent of the geometry [11]. That is, there is no shape factor associated with the in-situ versus constitutive shear modulus. Thus, the shear modulus is used to determine the Young's Modulus. The resulting shear and tensile moduli are shown in Figure 4.3-1.

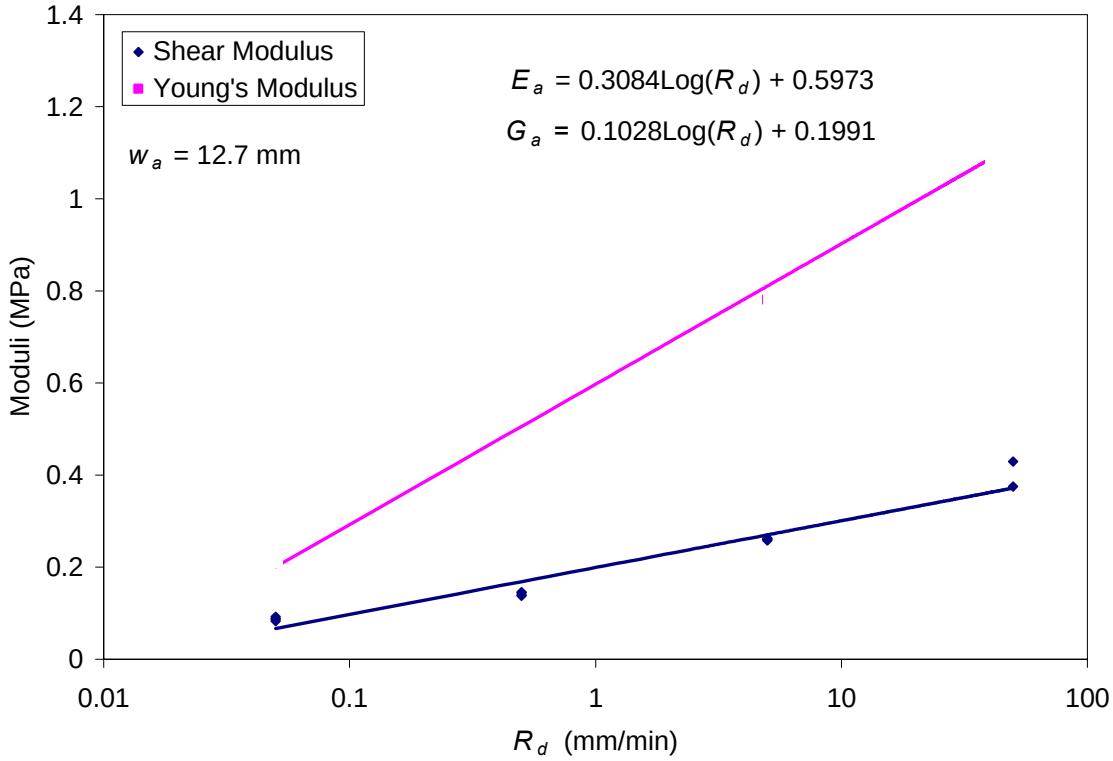

Figure 4.3-1 Adhesive Moduli vs. R_d – VHB 4950 at 20°C and 25%*RH*.

It is important to note that the shear modulus was calculated based on the slope of the stress-strain curves. In many cases large strain values (> 0.75) were used to determine the slope. Shear strains of this magnitude correspond to large displacements and may not be valid. Unfortunately, this is the accepted method for calculating the shear strain and is carried over to the calculations of the shear modulus.

Without knowing if the selected approach is valid or even accurate it is difficult to draw any conclusions from the calculated moduli. If we believe that the method is reasonably accurate for the strain region several observations can be made. First, if one compares the E_{app} from Figure 4.2-1 and the E from Figure 4.3-1 it is apparent that there is a difference between the in-situ and bulk adhesive modulus. Second, the in-situ modulus will be larger than the bulk modulus by as much as 3.5 times, for the geometries tested.

4.4 Load-Control versus Displacement-Control Testing

Mechanical systems are subjected to displacement- and load-controlled excitations. For this reason it is necessary to be able to transform from one loading state to the other. If

not complete data sets would need to be generated for both loading states. This transformation requires the relationship between load- and displacement-control be determined. The loading rate (N/sec.) was determined for each of the displacement-control data sets using Equation (4.4-1).

$$R_l = \left(\frac{P_2 - P_1}{\delta_2 - \delta_1} \right) \frac{R_d}{60\,\text{sec}} \tag{4.4-1}$$

In this equation the loads (P) and displacements (δ) were taken from the linear portion of the load-displacement curves. The same method was used to determine the displacement rate for the load-control data using Equation (4.4-2). The resulting data points for both the displacement-control and load-control cases are shown in Figure 4.4-1.

$$R_d = \left(\frac{\delta_2 - \delta_1}{P_2 - P_1} \right) R_l * 60\,\text{sec} \tag{4.4-2}$$

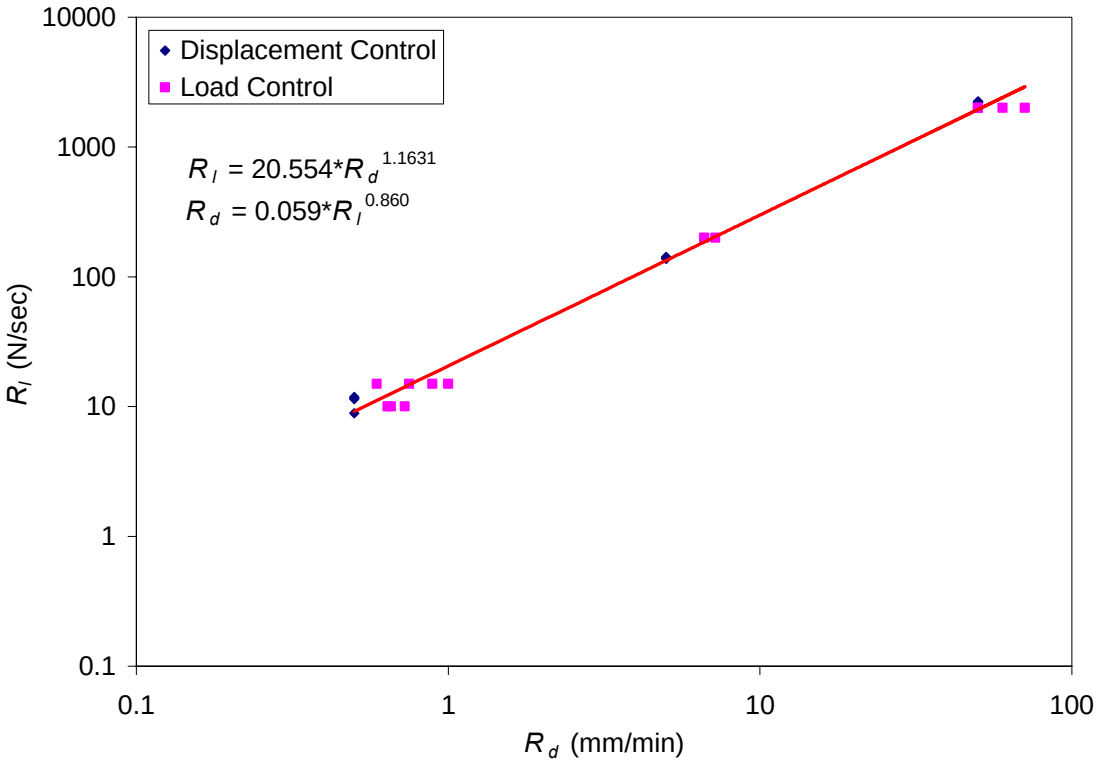

Figure 4.4-1 Load/Displacement Rate Conversion – VHB 4950 at 25°C and 35%*RH*.

4.5 Complex-Loading

Uniform stresses are only half the story as far as stresses go. Bending-moment-induced-gradient stresses do not affect materials in the same way as uniform stresses. In many cases the apparent failure stress of a material will be larger when subjected to a gradient

stress. This difference is typically neglected and results in a more conservative design when gradients stresses are present [37, 38]. If this phenomenon can be understood in VHB the increase in allowable failure stress can be used to reduce the amount of tape required in a design. This could make VHB more competitive.

The data collected with the complex loading fixture (see section 3.5) was used to generate Tau-Sigma data to be compared to Arcan$_m$ Tau-Sigma data. For the complex loading fixture the normal stress is a combination of the bending stress, the tensile component of the combined stress, and the residual fixture stress (see section 3.5). The geometric–moment resulting from the fixture was calculated to be 156.6 N-mm and corresponds to a σ_a of 0.029 MPa. The shear stress is simply the shear component of the combined stress. Both of these relationships are shown in Equations (4.5-1) and (4.5-2).

$$\sigma_{eng} = \left| \frac{P*L*c}{I} - 0.029\text{MPa} \right| + \frac{P}{A_a} * \cos(60°) \qquad (4.5\text{-}1)$$

$$\tau_{eng} = \frac{P}{A_a} * \sin(60°) \qquad (4.5\text{-}2)$$

In Equation (4.5-1) the stress that results from the gravity effects of the asymmetry of the complex loading fixture has been subtracted from the load-based gradient stress. The absolute value of the resultant is then added to the uniform tensile stress. The absolute value is used to account for the fact that under the gradient stress one end of the specimen is under tension, while the other is under compression of equal magnitude. From experience it is known that the specimens failed under tension and, therefore, the peak tensile stress is of interest. The peak tensile stress will occur when the moment-based stress and the uniform stress are in the same direction and are added together.

The new Arcan$_m$ data and the complex loading data are shown in Figure 4.5-1.

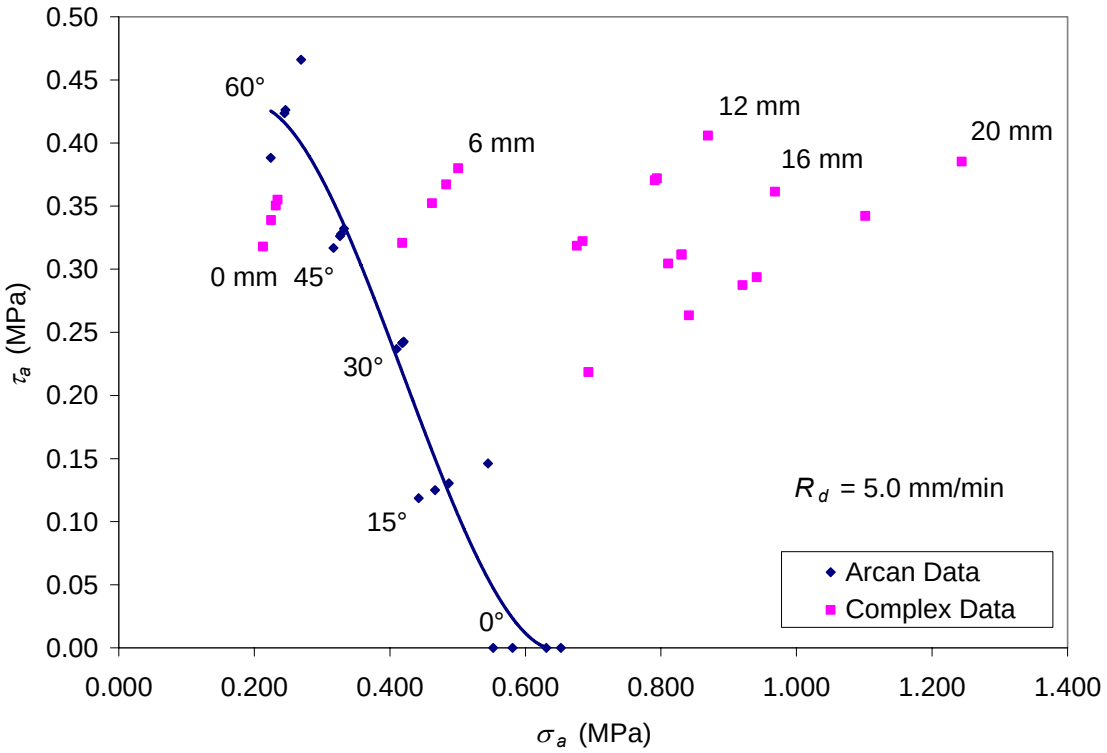

Figure 4.5-1 Gradient Normal Stress Effect – VHB 4950 at 20°C and 25%*RH*.

As one can see, the failure stresses under complex loading tend to be larger than what would be predicted by the uniform stress data. It is interesting to note that the failure stress with no moment (from the moment arm) is lower than those obtained with the Arcan_m. One would expect these values to be the same or slightly higher than those obtained from the Arcan_m. The complex-loading fixture and the Arcan_m, at a $\theta_{Arcan} = 60°$, should give the same results given that both fixtures have the same loading state ($\theta_{Arcan} = 60°$, and $R_d = 5.0$ mm/min). The moment that results from the asymmetry of the complex-loading fixture should increase the tensile failure stress, if gradient stresses act as predicted and is demonstrated by all of the rest of the test data. This disagreement between the data makes it very difficult to determine the effect of the gradient stress on this system. The most reasonable explanation is that the two test fixtures do not produce the same stress state at this test point. A misalignment in the fixture or incorrect placement of the moment arm would result in errors in the calculated adhesive stress.

To demonstrate the effect of the moment arm length (l) on the adhesive stress the stresses were recalculated with $\pm$ 1.0 mm error. These results are shown in Figure 4.5-2.

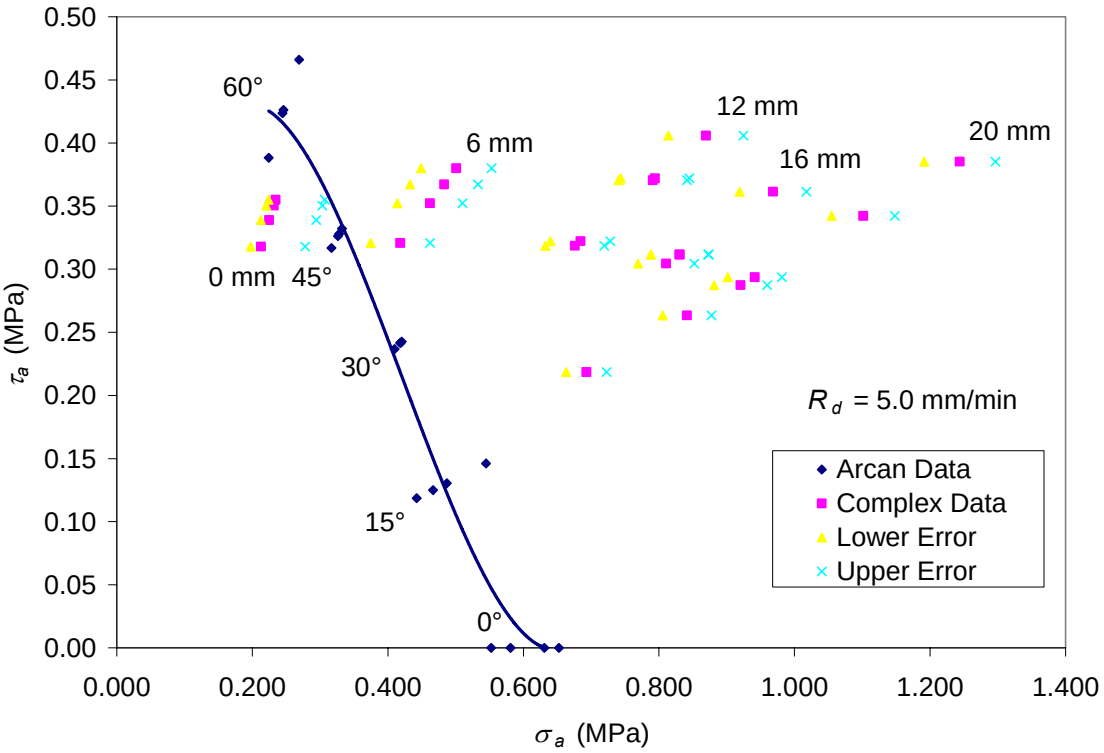

Figure 4.5-2 Gradient Normal Stress Effect – With $\pm$ 1.0mm error.

As one can see a 1.0 mm error has a significant impact on the adhesive stress. It is conceivable that there was an error in the moment arm length. This could have been caused when the locking nut was tightened. This would also explain the consistent error in the data.

At this point all that can be said is there is an effect and the effect is considerable when the moment arm is $\geq$ 12 mm. Any other conclusions at this time would be unjustified. Additional work needs to be done to resolve the gradient stress effect for moment arms < 12 mm.

4.6 Preliminary Data

A great deal of additional data has been collected on VHB tape. All of which is outside the scope of this thesis. Some of this additional research will be presented in this section to help the reader understand section 5.5 and the recommendations made in Chapter 7.

4.6.1 Shift Factors

In section 2.6 the importance of temperature and relative humidity were discussed. To develop the temperature shift factor DMA data was collected for multiple frequencies over a range of temperatures. The shift factor for relative humidity was generated from a series of tensile tests conducted at a fixed loading rate (5.0 mm/min) and at 0-100 %RH. The resulting shift factors are shown in Figures 4.6.1-1 and 4.6.1-2.

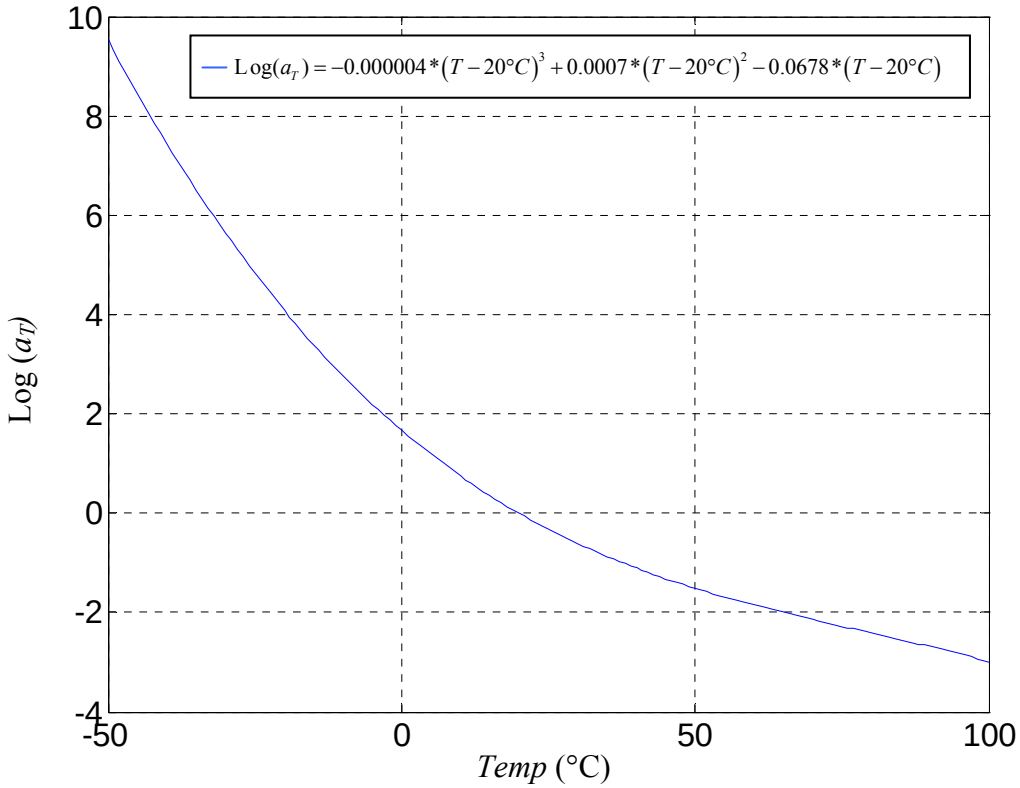

Figure 4.6.1-1 VHB Temperature Shift Factor – T_{ref} = 20°C.

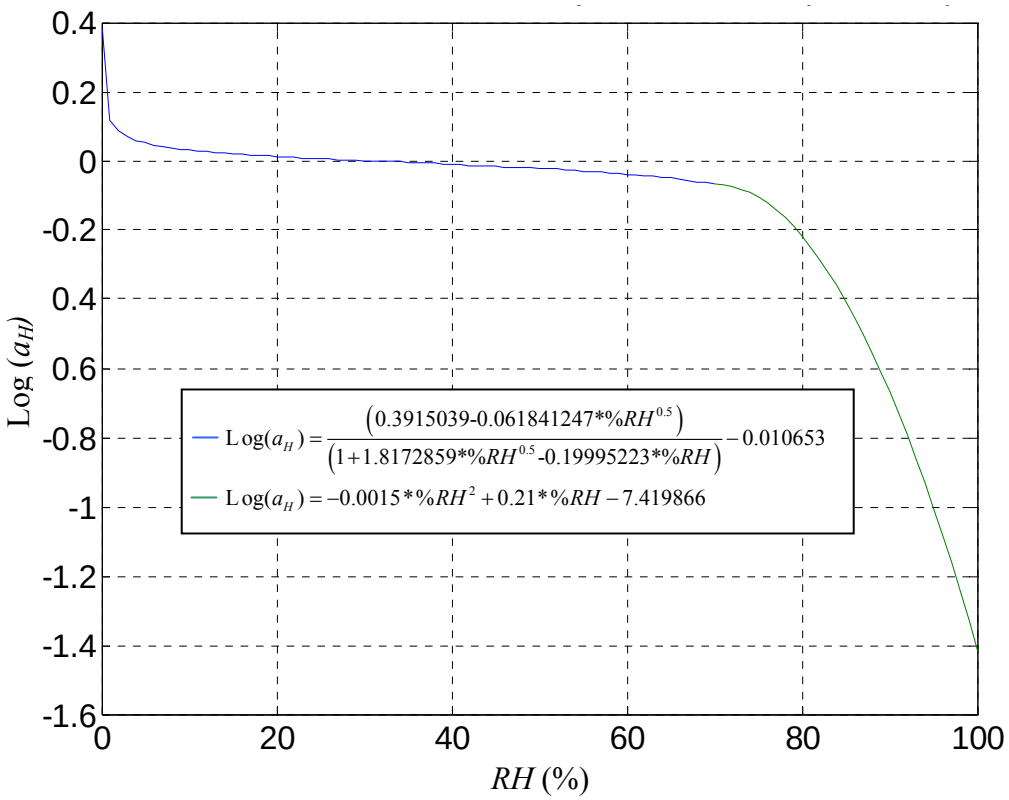

Figure 4.6.1-2 VHB Relative Humidity Shift Factor – RH_{ref} = 30%.

As one can see the temperature shift factor predicts a substantial impact on the effective loading rate with small changes in temperature. A 10 °C shift in temperature could represent a loading rate 100 times faster, when compared to the reference test conditions. The impact of relative humidity is not as great. The data indicates that the relative humidity has little impact below 60 %RH.

The usefulness of these shift factors has not been determined. During adhesive testing a change in the failure mode was found between low and high rate as well as low and high temperature. At low rates and high temperatures the failures tended to be adhesive, while the failures at high rates and low temperatures tended to be cohesive. There is no justification to believe that the shift factors will be valid over changing failure modes.

4.6.2 Loading/Displacement Rate

The effects of loading and displacement rate have already been shown, but the rate data that has been collected is incremental and very limited. What is needed is continuous rate data that spans all possible loading/displacement rates. By testing at multiple rates and temperatures it was possible to develop strength curves that span many decades of loading rates. This is accomplished by combining test data and the shift factors. The shift factors allow the data which was collected at multiple temperatures to be "shifted" in rate to a common temperature. Preliminary work in this area has been completed. The resulting σ_a and τ_a strength curves are shown in Figures 4.6.2-1 and 4.6.2-2 respectively.

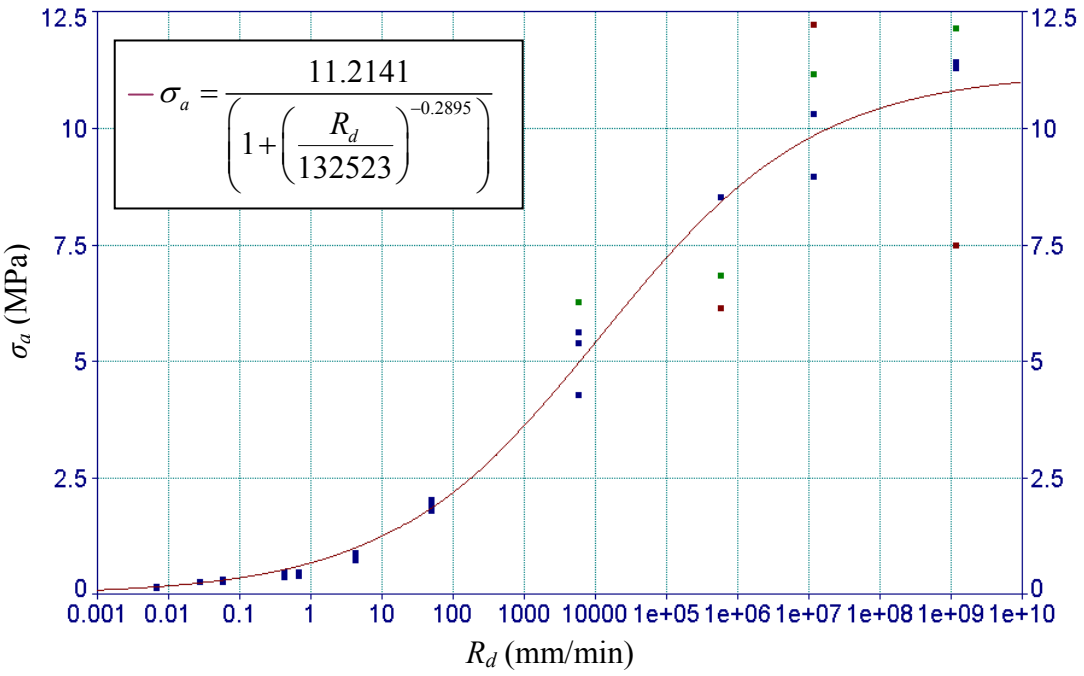

Figure 4.6.2-1 Preliminary Tensile Data – VHB

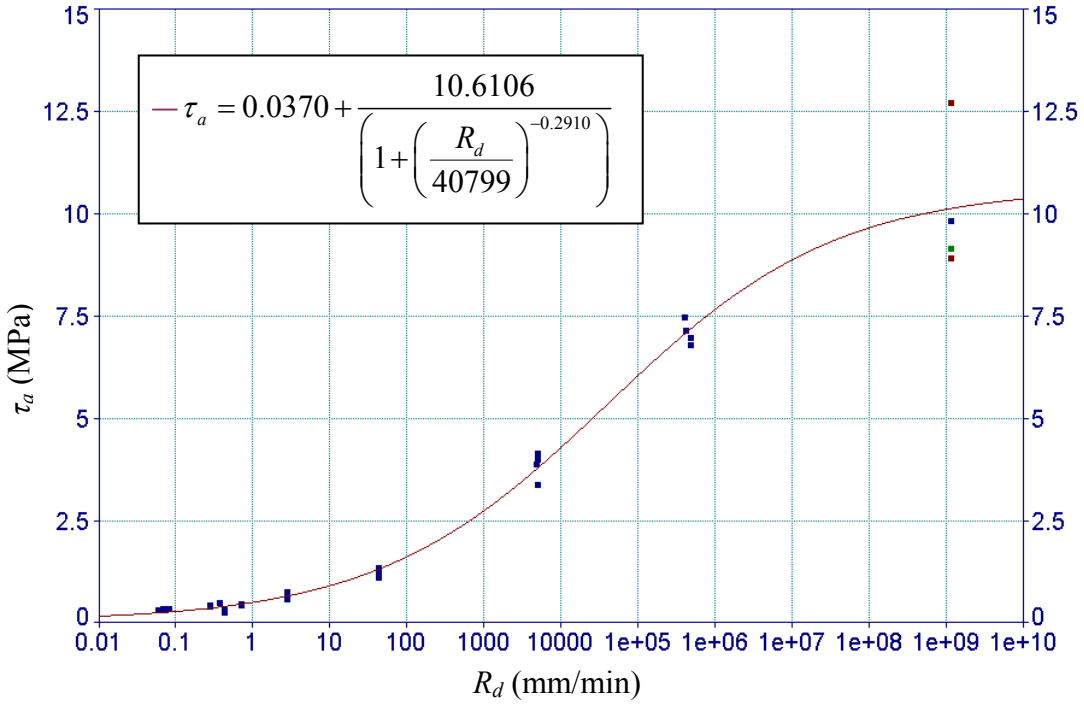

Figure 4.6.2-2 Preliminary Shear Data - VHB

These curves give us an idea of what is possible with limited testing and shift factors. This data is by no means usable in a design. It is presented here just as an example of the process. Many more tests need to be conducted to provide statistical significance to the data and to validate the shift factors. Even though this method is widely accepted [26] it has not been validated for this adhesive.

5.0 Design Examples

The intent of this research was to develop a design methodology for PSAs, specifically VHB™ tape. All of the data that was collected and the design charts that have been produced are without purpose unless they can be applied to real-world design problems. To this end the following design examples are presented to demonstrate that this work can be used to design and analyze adhesive joints. The first three design examples are intended to familiarize the reader with the design/analysis process and the use of the τ - σ plot. The fourth example was taken from a real application of VHB™ tape. In all of the examples it has been assumed that the environment is the same as the test environment (*Temp* = 20°C and *RH* = 25%).

5.1 Eccentric Tensile Load

The first geometry is an end-loaded rigid block as shown in Figure 5.1-1.

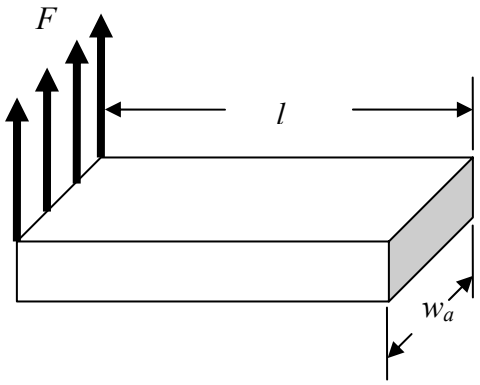

Figure 5.1-1 End-Loading of Rigid Block

Two separate analyses have been completed using this geometry. In the first case the stress and safety factor were calculated. For the second case the size of the joint was determined based on the desired safety factor.

Case # 1:

The calculations in this example are based on the data given in Table 5.1-1.

Table 5.1-1 Stress Calculation Data.

Variable	Value
F	7.0 N/mm
l	75 mm
w_a	50 mm
R_l	10 N/s

The stress in the adhesive was calculated as shown in Equations (5.1-1) and (5.1-2).

$$P = F * w_a = 7.0\text{N/mm}*50\text{mm}=350\text{N} \quad (5.1\text{-}1)$$

$$\sigma_{eng} = \frac{P}{A} + \frac{Mc}{I} = \frac{P}{w_a l} + \frac{P\left(\frac{l}{2}\right)\left(\frac{l}{2}\right)}{\frac{w_a l^3}{12}} = \frac{4P}{w_a l} = \frac{4*350\text{N}}{50\text{mm}*75\text{mm}} = 0.37\text{MPa} \quad (5.1\text{-}2)$$

To determine the safety factor the allowable stress is needed. Unfortunately, all of the strength data is with respect to the displacement rate. Using the relationship between R_d and R_l found in Figure 4.4-1 the loading rate can be converted to a displacement rate as shown in Equation (5.1-3).

$$R_d = 0.059*10\text{N/s}^{0.860} = 0.427\text{mm/min} \quad (5.1\text{-}3)$$

At this point a decision has to be made concerning the allowable stress. All of the data was collected at fixed displacement rates and nothing is known outside of these test points. In addition this loading results in a gradient stress. In Figure 4.5-1 it was shown that there is strong relationship between the stress gradient and the allowable stress. Unfortunately, there is no data at this displacement rate or for a pure tensile gradient. Therefore, there is no choice but to use the data found in Figure 4.1-7. Since the displacement rate is between test rates both the upper and lower displacement rates must be considered or an attempt at interpolation must be made. In this case interpolating would be a guess at best do to the non-linear nature of the data and it is considered safer to use the existing data points. From Figure 4.1-7 the allowable stress were determined to be 0.44 MPa (R_d = 0.50 mm/min) and 0.29 MPa (R_d = 0.05 mm/min). Using these values the safety factor for each case was calculated as shown in Equations (5.1-4) and (5.1-5).

$$n_{s(0.05\text{mm/min})} = \frac{S_{y(0.05\text{mm/min})}}{\sigma_a} = \frac{0.29\text{MPa}}{0.37\text{MPa}} = 0.78 \quad (5.1\text{-}4)$$

$$n_{s(0.50\text{mm/min})} = \frac{0.44\text{MPa}}{0.37\text{MPa}} = 1.19 \quad (5.1\text{-}5)$$

As one can see the rate dependence of the adhesive can be critical. The safety factor for the higher displacement rate is marginal at best and one would predict failure of the joint at the lower displacement rate. The allowable stress must be known for the applied displacement rate to correctly perform the analysis of this joint.

Case # 2:

In this case the design is worked in reverse using the data provided in Table 5.1-2. The design is to determine the length (l) required to meet the specified safety factor, n_d = 3.0.

Table 5.1-2 Design Calculation Data.

Variable	Value
F	7.0 N/mm
R_l	10 N/s
w_a	50 mm
n_d	3.0

From the first case it is already known that the loading rate corresponds to an R_d of 0.427 mm/min. Again both the upper and lower allowable stresses must be considered in this design. The design stresses for each case was determined using the corresponding yield strength and desired safety factor as shown in Equations (5.1-6) and (5.1-7).

$$\sigma_{d(0.05\text{mm/min})} = \frac{0.29\text{MPa}}{3.0} = 0.097\text{MPa} \tag{5.1-6}$$

$$\sigma_{d(0.50\text{mm/min})} = \frac{0.44\text{MPa}}{3.0} = 0.147\text{MPa} \tag{5.1-7}$$

To determine the required joint lengths Equation (5.1-1) is rearranged to solve for l. The calculated joint lengths are shown in Equations (5.1-8) and (5.1-9).

$$l_{(0.05\text{mm/min})} = \frac{4P}{w_a \sigma_{d(0.05\text{mm/min})}} = \frac{4*350\text{N}}{50\text{mm}*0.097\text{MPa}} = 289\text{mm} \tag{5.1-8}$$

$$l_{(0.50\text{mm/min})} = \frac{4*350\text{N}}{50\text{mm}*0.147\text{MPa}} = 190\text{mm} \tag{5.1-9}$$

Again the displacement rate plays an important role in the design. There is more than a 50% difference in the length of the joint and the amount of tape required for the design. This represents a significant difference in the size and cost of the design.

5.2 Shear Load

The second design example is a joint consisting of two polycarbonate bars bonded together and subjected to a shearing load as shown in Figure 5.2-1.

Figure 5.2-1 Symmetric Shear Joint.

The necessary data to determine the shear stress in the adhesive and the safety factor is shown in Table 5.2-1

Table 5.2-1 Stress Calculation Data.

Variable	Value
P	100 N
R_l	10 N/s
w_a	50 mm
t_a	1.143 mm
E_s	2.4 GPa
t_s	5.0 mm
l	250 mm

It is very simple calculate the engineering shear stress in the adhesive as shown in Equation (5.2-1). This assumes a rigid substrate.

$$\tau_{eng} = \frac{P}{A} = \frac{P}{w_a l} = \frac{100\text{N}}{50\text{mm}*250\text{mm}} = 8.0\text{kPa} \qquad (5.2\text{-}1)$$

Unfortunately this is not the end of this analysis. As stated in section 2.2.2 the geometry of an adhesive joint may effect the stress distribution under shear loading. To complete the analysis the joint needs to be check for "shear lag"

Using the relationship found in Figure 4.3-1 the adhesive modulus of rigidity was determined, as shown in Equation (5.2-2), to be 0.16 MPa.

$$G_a = 0.1028 * Log(0.427) + 0.1991 = 0.161\text{MPa} \qquad (5.2\text{-}2)$$

The stress concentration was then calculated using Equations (5.2-3) and (5.2-4) (see section 2.2.2 for additional information).

$$\omega = \sqrt{\frac{2G_a}{t_a E_s t_s}} = \sqrt{\frac{2*0.161\text{MPa}}{1.143\text{mm}*2.4\text{GPa}*5.0\text{mm}}} = 0.0048\text{mm}^{-1} \qquad (5.2\text{-}3)$$

$$K_{g2} = \frac{\omega l}{2\sinh\left(\frac{\omega l}{2}\right)}\cosh\left(\frac{\omega l}{2}\right) = \frac{1.2}{2\sinh(0.6)}\cosh(0.6) = 1.12 \qquad (5.2\text{-}4)$$

This indicates that the shear stress will be 1.12 times higher than calculated in Equation (5.2-1). In some designs a 12% error in the stress calculations would result in failure of the joint since the centricity of the applied load and load rate are in question.

From the previous example it is known that a loading rate of 10 N/s corresponds to a displacement rate of 0.427 mm/min. From Figure 4.1-7 the allowable shear stress was

determined to be 0.31 MPa (R_d = 0.05 mm/min) and 0.45 MPa (R_d = 0.50 mm/min). The corresponding safety factors were calculated as shown in Equations (5.2-5) and (5.2-6).

$$n_{s(0.05\text{mm/min})} = \frac{S_{sy}}{\tau_a} = \frac{310\text{kPa}}{8.0\text{kPa}} = 38.75 \qquad (5.2\text{-}5)$$

$$n_{s(0.50\text{mm/min})} = \frac{450\text{kPa}}{8.0\text{kPa}} = 56.25 \qquad (5.2\text{-}6)$$

In this example the rate was not critical due to the size of the safety factor. It is worth noting that there was a 32% difference between the two safety factors. This is a substantial difference and must not be taken lightly.

5.3 Combined Loading

The focus of this example will be the process of working with both a shear and tensile load and how to apply use the τ - σ plot in this case. For this reason "shear lag" and beam on elastic foundation will not be considered to simplify the analysis. In this example the adhesive stress will be determined for a rigid bracket/hook attached to a rigid surface as shown in Figure 5.3-1.

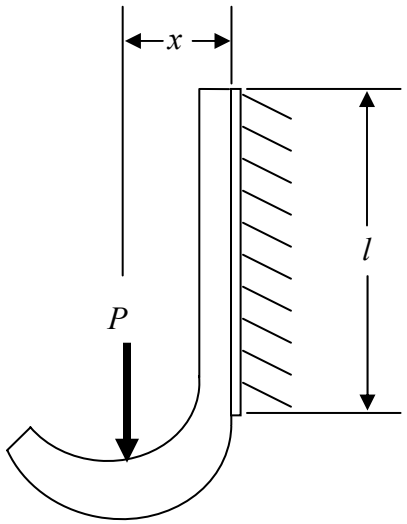

Figure 5.3-1 Combined Loading Example

All calculations were performed using the data in Table 5.3-1.

Table 5.3-1 Stress Calculation Data.

Variable	Value
P	350 N
R_d	5.0 mm/min
w_a	25 mm
t_a	1.143 mm
l	50mm
x	20 mm

The tensile and shear stresses were calculated in a similar manner to that used in the previous examples. The stresses in the adhesive were calculated to be 0.67 MPa (tensile) and 0.28 MPa (shear) as shown in Equations (5.3-1) and (5.3-2).

$$\sigma_{eng} = \frac{Mc}{I} \frac{xP\frac{l}{2}}{\frac{w_a l^3}{12}} = \frac{20\text{mm}*350\text{N}*25\text{mm}}{\frac{25\text{mm}*(50)^3\ \text{mm}}{12}} = \frac{50\text{kN-mm}^2}{2.60\text{E}5\text{mm}^4} = 0.67\text{MPa} \quad (5.3\text{-}1)$$

$$\tau_{eng} = \frac{P}{A} = \frac{P}{w_a l} = \frac{350\text{N}}{25\text{mm}*50\text{mm}} = 0.28\text{MPa} \quad (5.3\text{-}2)$$

To determine the allowable shear and tensile stresses the equivalent Arcan angle must first be calculated. This was accomplished using simple geometry as demonstrated in Equation (5.3-3)

$$\theta_{Arcan} = \tan^{-1}\left(\frac{\tau_{eng}}{\sigma_{eng}}\right) = \tan^{-1}\left(\frac{0.28\text{MPa}}{0.67\text{MPa}}\right) = 22.7^{o} \quad (5.3\text{-}3)$$

In a perfect world this would mean that the same stress state can be achieved by applying the load at an angle of 22.7° on the σ - τ profile. This is the point that gradient stresses become a problem again. In this case we do have a pretty good idea of what expect for this displacement rate and stress state. To demonstrate this effect the load line for this stress state has been plotted on both Figures 4.1-7 and 4.5-1. They are both presented here as Figures 5.3-2 and 5.3-3.

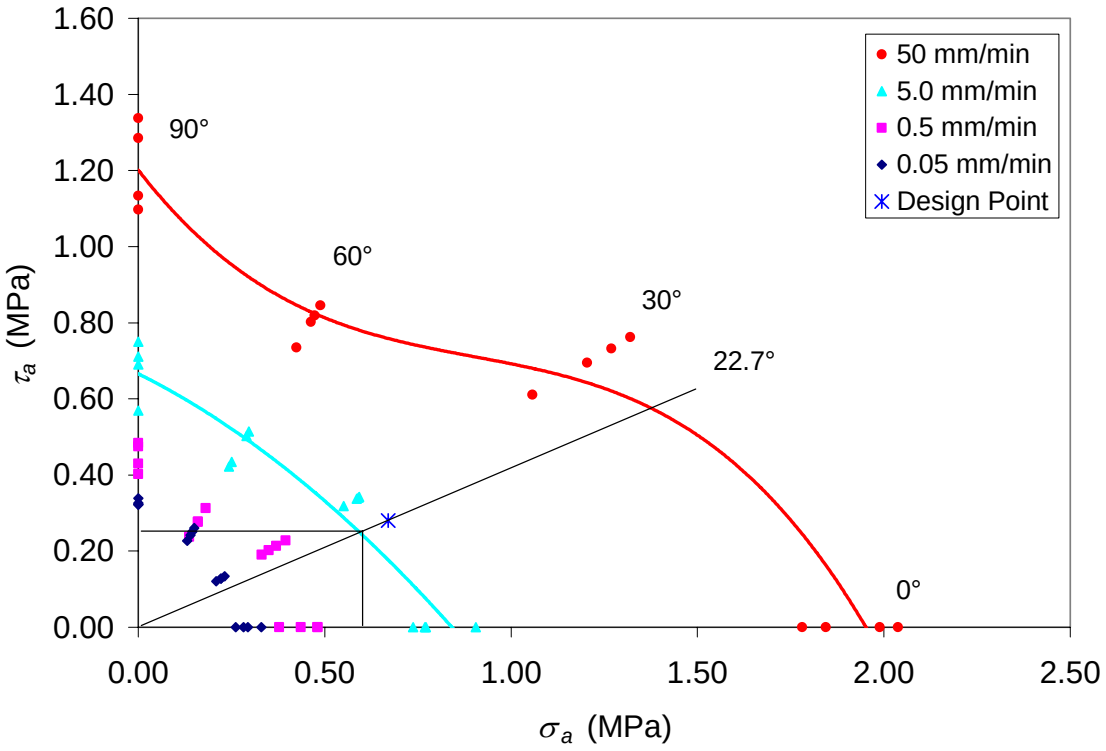

Figure 5.3-2 τ-σ plot with 22.7° load line.

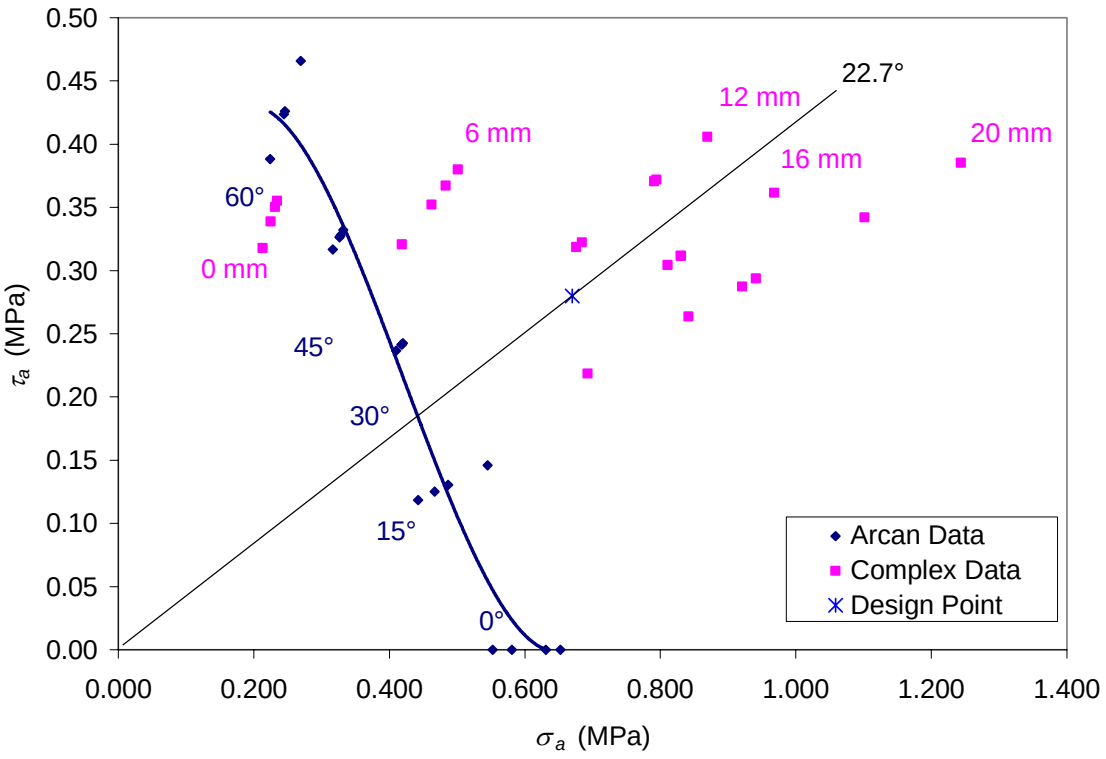

Figure 5.3-3 5.0 mm/min gradient stress τ-σ data with 22.7° load line.

As one can see this design is very close to failure using the data from Figure 4.1-7 (Figure 5.3-2). If the gradient stress effect is as shown in Figure 4.5-1 (Figure 5.3-3) the design is well below the allowable stress level for this stress state. Understanding the gradient stress effect has the potential to greatly increase the design space and reduce design costs.

5.4 Beam-on-Elastic Foundation

VHB™ tape has been used successfully to bond handles onto appliances for some time. One such application is the handle of a freezer as shown in Figure 5.4-1.

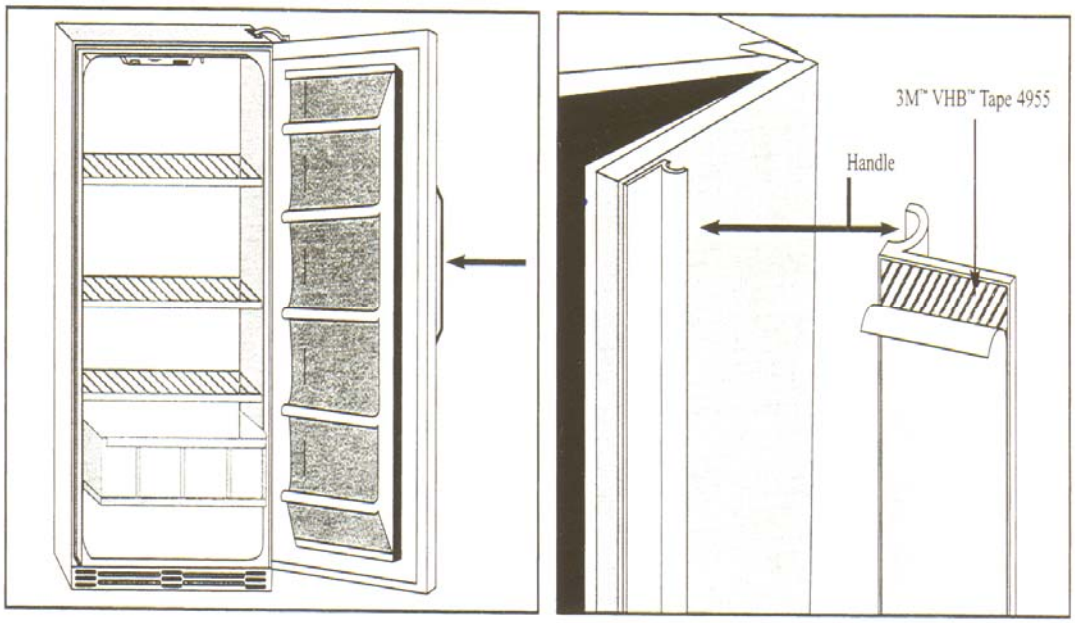

Figure 5.4-1 VHB™ Appliance Application.

The handle is typically manufactured from an aluminum extrusion and can either run the full length of the door or just long enough to grab. The geometry shown in Figure 5.4-1 will be used for this example with an end load as shown in Figure 5.4-2.

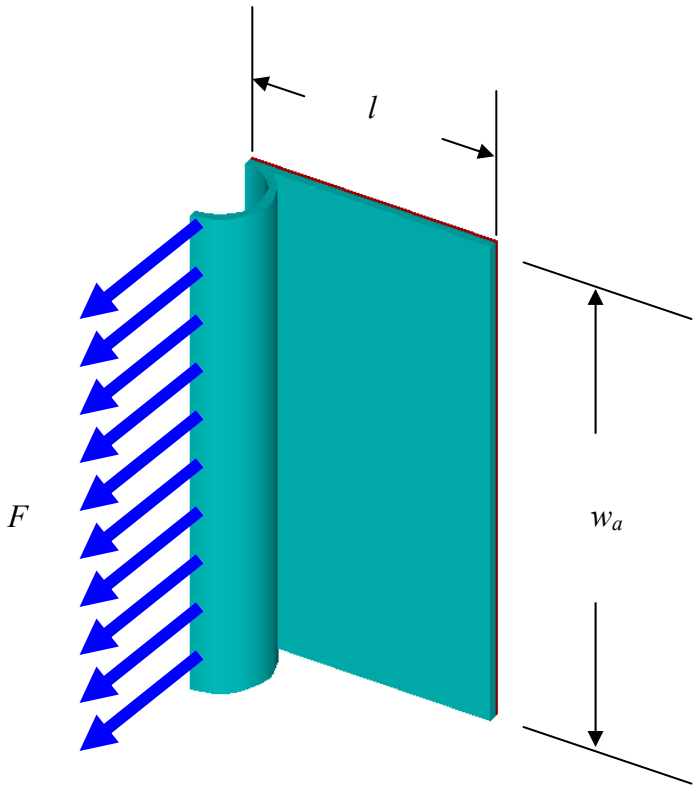

Figure 5.4-2 Handle with edge load.

Without knowing the exact geometry of the handle and the force required to open the doors several assumptions needed to be made to calculate the stress in the adhesive. All of the assumptions can be found in Table 5.4-1.

Table 5.4-1 Design Data.

Variable	Value
F	0.33 N/mm
R_l	1000 N/s
w_a	150 mm
t_a	1.143 mm
E_s	70 GPa
t_s	2.5 mm
l	75 mm
I_s	50mm^4

The adhesive stress was calculated to be 0.018 MPa as shown in Equations (5.4-1) and (5.4-2)

$$P = F * w_a = 0.33\text{N/mm}*150\text{mm}=50\text{N} \quad (5.4\text{-}1)$$

$$\sigma_{eng} = \frac{P}{A} + \frac{Mc}{I} = \frac{4P}{w_a l} = \frac{4*50\text{N}}{11250\text{mm}^2} = 0.018\text{MPa} \quad (5.4\text{-}2)$$

Due to the geometry of the handle it is necessary to check for a beam on elastic foundation effect. This analysis requires the adhesive's Young's modulus, which is a function of the displacement rate.

The displacement rate was calculated using the relationship found in Figure 4.4-1. For a load rate of 1000 N/s the equivalent displacement rate was calculated to be 22.4 mm/min as shown in Equation (5.3-3).

$$R_d = 0.059*1000\text{N/s}^{0.860} = 22.4\text{mm/min} \quad (5.4\text{-}3)$$

The Young's modulus was then calculated using Equation (5.4.4) from Figure 4.3-1 and was found to be 1.01 MPa.

$$E_a = 0.3084*Log(22.4) + 0.5973 = 1.01\text{MPa} \quad (5.4\text{-}4)$$

This provides all of the necessary information to determine any beam effects. In section 2.2.1 this specific loading case was discussed and formulated in to stress concentration factor (K_{ef1}). K_{ef1} is a function of λl which is calculated to be 2.96. These calculations are shown in Equations (5.4-5), (5.5-6), and (5.4-7).

$$k = \frac{w_a E_a}{t_a} = \frac{150\text{mm}*1.01\text{MPa}}{1.143\text{mm}} = 133\text{MPa} \quad (5.4\text{-}5)$$

$$\lambda = \sqrt[4]{\frac{k}{4E_s I_s}} = \sqrt[4]{\frac{133\text{MPa}}{4*70\text{GPa}*195.3\text{mm}^4}} = 0.039\text{mm}^{-1} \quad (5.4\text{-}6)$$

$$\lambda l = 0.039\text{mm}^{-1}*75\text{mm} = 2.96 \quad (5.4\text{-}7)$$

The stress concentration factor (K_{ef1}) was calculated to be 1.49 using Equation (2.2.1-12), as shown in Equation (5.4-8)

$$\begin{aligned} K_{ef1} &= \frac{\lambda l}{2} * \frac{\sinh(\lambda l)\cosh(\lambda l) - \sin(\lambda l)\cos(\lambda l)}{\sinh^2(\lambda l) - \sin^2(\lambda l)} \\ &= \frac{2.96}{2} * \frac{9.62*9.67 - 0.18*(-0.98)}{92.6 + 0.03} = 1.49 \end{aligned} \quad (5.4\text{-}8)$$

This leaves two options for determining the safety factor. The allowable stress for 5.0 mm/min or 50 mm/min can be used. Since the allowable stress increases with rate it will be more conservative to use the one corresponding to 5.0 mm/min. From Figure 4.1-7

the allowable stress was determined to be 0.84 MPa (R_d = 5.0mm/min). This results in a safety factor of 31.3 as shown in Equation (5.4.7).

$$n_{s(5.0\text{mm/min})} = \frac{0.84\text{MPa}}{1.49*0.018\text{MPa}} = 31.3 \qquad (5.4.7)$$

This indicates that there will be at least a factor of safety of 31.3 based on the assumptions made here. Unfortunately, this is only half of the story for this geometry. For simplicity it was assumed that the load was evenly distributed along the length. The handle is longer than most hands are wide, therefore, the loading would be non-uniform. To complete the analysis a similar set of calculations would also need to be performed on the handle in the *y*-axis (along the length). The actual estimated stress in the adhesive would be a combination of the two analyses.

5.5 Limitations of the Method

The previous examples demonstrate that the collected data can be used to solve specific design problems. Unfortunately, the solutions for these problems demonstrate the shortcomings of the method and data set. First, the relative humidity and temperature were picked to be the same as the test conditions. It goes without saying that this will not be the case in the real operating environment. Figures 4.6.1-1 and 4.6.1-2 demonstrate how large an impact the operating environment can have on the material characteristics. For any design to be successful the material properties for the actual design environment must be used. Second, in all but one of the examples the allowable stress(es) could not be determined accurately. The displacement rate was between one of the test rates resulting in an upper and lower bound on the allowable stress(es). This results in huge uncertainty in the design and inefficient designs. The allowable stress data must be continuous for the entire application range. Figures 4.6.2-1 and 4.6.2-2 give some insight into what is needed, but even this is not enough. These figures only deal with tensile and shear loading, nothing has been done to try and generate a continuous surface which encompasses all combined stress states and rates (for the desired design space). This will not be possible without a great deal of testing and validation of the shift factors. Third, both shear lag and beam-on-elastic-foundation were applied in these examples. Neither of these models has been shown to be valid for this system. VHB demonstrates large plastic regions before failure which may cause the stress distribution to be very different that those predicted by these models. Fourth, shape factors and gradient stresses have effectively been ignored in these examples. Considerable work needs to be done to understand the impact that the geometry and gradient stresses have on the failure stress of the joint.

6.0 Conclusions

This thesis details the unique requirements associated with designing PSA joints. A methodology for analyzing adhesive stresses, collecting material data, and presenting the strength data as failure envelopes has been presented. During the course of collecting and analyzing the data many observations were made and additional questions arose. The following list is an overview of these conclusions, observations, and questions;

1. Existing analytical models can be formatted in a manner easily understood by designers as was shown by the generation of stress-concentration factors and the application of these factors in simple design examples. At this point it is unclear how to apply the stress-concentration factors together. This is especially of concern when dealing with beam-on-elastic foundation problems with multiple loading points. The plots that have been generated are based on the peak stress which occurs at one point in the adhesive. With multiple loading points the peak stress will be determined by summing the stress distributions along the length of the beam and can not be accomplished with stress-concentration plots, since the stress concentration factors may be associated with a different location in the adhesive.

2. The modified Arcan fixture has been shown to be a very useful in collecting a range of material data. With a limited number of tests the strength has been determined over a range of stress states and displacement rates. The data are taken at discrete load or displacement rates and does not span the entire design space, but it does show the utility of the fixture as a testing tool.

3. By testing in both load control and displacement control it was determined that it is possible to translate between the two loading conditions. This will allow the designer to use one set of data (displacement controlled) for both displacement and load controlled problems. However, the relationship found here for VHB is most probably limited in use to VHB. Testing should be done on any other adhesive that is being considered.

4. Shape factors, based on a Poisson's Ratio of 05, have been shown to seriously overestimate the peak stress in this material. It is known that small changes in Poisson's Ratio have a large effect on the stress distribution predicted by shape factor. For shape factors to be useful in design they need to a function of Poisson's Ratio.

5. The moduli were determined as a function of rate, but there is a great deal of uncertainty in the data. First, it was not possible to measure the Young's Modulus directly due to the lack of understanding of the shape factor's (Poisson's Ratio) effect on the apparent modulus. Thus, the true Young's Modulus can not be reliability from the measured apparent

modulus. This required that Young's Modulus be calculated from the shear modulus. This calculation is dependent on Poisson's Ratio, but not as heavily. The major issue is in how the shear modulus is calculated. It was assumed that there is not shape factor in shear. This implies that the in-situ shear modulus is the same as the bulk shear modulus. This is a huge assumption and, unfortunately, the only one available currently.

6. Using the complex-loading fixture it was shown that there is a substantial tensile-gradient effect. Under a linear stress gradient the materials appear substantially stronger than under uniform stress or strain. Since the fixture was designed with a fixed angle of 60° the effects are not know outside of this test condition. Without testing to determine the effects of tensile-gradient stresses over the entire design space it will not be possible to safely use the increased failure strength. This will result in a less efficient design, but it will be conservative.

7. Using the Arcan data failure envelopes were generated. These envelopes were successfully used in the design and analysis of simple adhesive joints. This demonstrates that design envelopes are an effective method of presenting adhesive strength data. These envelopes that were generated are incremental in rate and only span tension to shear. This limits their usefulness, but is a result of the limited testing that was conducted. With additional data or a method of applying shift factors the range and precision can be greatly improved.

The groundwork for this design process has been laid in the pages of this thesis. The application of stress-concentration factors and strength envelopes to simple deign problems has shown the validity of the process. With additional testing this design process can become a useful deign tool.

7.0 Recommendations

The work conducted in this thesis demonstrates the potential for collecting, presenting, and applying adhesive data in a manner familiar to designers. Unfortunately, there are many questions to be answered and steps to be completed before a design methodology can be developed. The following list represents, what are believed to be, the most critical problems left to be solved enroute to a complete adhesives design methodology:

1. Beam-on-Elastic Foundation.

   At this point beam-on-elastic foundation is only a theory that has not been validated for this visco-elastic adhesive system. To make it useful as a design tool stress concentration factors for the most common\useful loading conditions need to be developed. Each one of the factors must then be validated with test data and the application range defined. Superposition must also be show to be applicable. This will most likely require the development of a computer program due to the complexity involved in determining the location and value of the peak stress.

2. Shape Factors.

   Shape factors are readily available for many joint geometries, but most of them are based on a Poisson's Ratio of 0.5 and, therefore, not applicable to this adhesive system. Shape factors for the most common joint geometries need to be derived as a function of Poisson's Ratio. These shape factors will then need to be validated with test data and the limits of their application range defined... In addition the question of whether or not shape factors exist in shear needs to be addressed. If they do the entire process will have to be repeated in shear.

3. Shear Lag.

   Volkersen's Shear-Lag Model assumes no bending in the substrates. In many systems this will not be the case. It is more realistic to use Goland and Reissner's model which does include bending. This will require that their model be reformulated and developed into a stress concentration factor form as was Volkerson's model. Both models will then need to be validated with test data and the limits of its application range defined.

4. Shift Factors.

   Shift factors have the potential of being one of the most valuable tools available to adhesive designers. At this point there are just too many

questions regarding the development of shift factors and there application. Basically one can not force the adhesive, in this case a PSA, to obey linear-time-temperature superposition. It either does or does not. If it does obey the theory the useful range must be determined by conducting low and high rate experiments that span the design space (creep to impact in this case). This data should match the values predicted from the "shifted" adhesive data. It is doubted that there will be a magic-universal shift factor for all of the adhesives material properties. This may require that this process will need to be repeated for every material property that will be shifted. A similar approach will need to be taken to develop and validate a shift factor for relative humidity.

5. Characterization of Design Space.

   The design space has been referred to several times, but what is it? All of the testing and validation is to be done in a manner that will encompass the entire design space. With all of the material properties dependent on rate, temperature, and relative humidity the design space needs to be defined upfront to provide guidance in the experimental design and will greatly effect the difficulty in characterizing the adhesive.

6. Gradient Stress Effects.

   Very little is known about gradient stress other than gradient-tensile stresses have an impact on the failure stress. This does not allow for the added design space to be used safely. Unfortunately, a great deal of testing is required to fully characterize this phenomenon. The testing up to this point was conducted with a fixed Arcan angle of 60° and variable moment arm. .The same tests need to be run with Arcan angles of 0, 30, and 90°. All four angles will need to be tested at multiple rates and temperatures as well to determine validity of time-temperature superposition. After all this has been complete the same tests need to be conducted with gradient-shear stresses.

7. Load State Effects.

   Constant load and displacement rates were used to collect all of the data in this thesis, but this is not the only loading state in real-world applications. Many designs will undergo a static load (gravity) and a dynamic (ramp) load. At this point it is not know how to analyze this loading state to determine the allowable stresses. Tests need to be run with a range of static loads/stresses and dynamic loads/stresses to determine the failure stresses. Temperature, rate, and relative humidity will also need to be considered in this analysis.

8. Global Superposition

All of the stress concentration factors and theories are being developed and validated independent of the rest. In a design many of them could be applied to the same design, but at this point it is unknown how this will be done. When should the apparent modulus be used instead of the true modulus? Can all of the stress-concentration factors be multiplied together? If so, over what operating range will this be valid? These questions must be answered before this methodology is released to the design community.

9. Develop Design Methodology.

After all of these issues have been resolved a detailed design methodology must be developed. All of the techniques must be explained in a clear concise manner, especially all of the assumptions made and the valid operating range of each technique. The application of each stress-concentration factor and shift factor must be explained in detail and demonstrated in sample joint designs.

References

1. American Society of Testing and Measuring, *Annual Book of ASTM Standards*, ASTM International, New York, 2003.

2. Voloshin, A. and Arcan, M., "Failure of Unidirectional Fiber-Reinforced Materials-New Methodology and Results," *Experimental Mechanics*, Vol. 20,No. 8, Aug. 1980, pp. 280-284.

3. Banks-Sills, L. and Arcan M., "Toward a Pure Shear Specimen For K_{IIc} Deformation," *International Journal of Fracture*, Vol. 22, 1983, pp. R9-R14.

4. Banks-Sills, L. and Arcan, M., "A Mixed Mode Fracture Specimen For Mode II Dominant Deformation," *Engineering Fracture Mechanics*, Vol. 20, No. 1, Jan. 1984, pp. 145-157.

5. Ferry, J. D., *Viscoelastic Properties of Polymers*, 3rd ed., John Wiley & Sons, New York, 1980, pp. 130-365.

6. Reinhart. T. J., *Engineered Materials Handbook*, vol 3, ASM International, USA, 1990, pp. 622-627.

7. Gent, A. and Meinecke, E., "Compression, Bending, and Shear of Bonded Rubber Blocks," *Polymer Engineering and Science*, Vol. 10, No. 1, Jan. 1970, pp. 48-53.

8. Adams, R. D., Coppendale, J., and Peppiatt, N. A., "Stress Analysis of Axisymetric Butt Joints Loaded in Torsion and Tension," *Journal of Strain Analysis*, Vol. 13, No. 1, Jan. 1978, pp. 1-10.

9. Lai, Y., Dillard, D. A., and Thornton, J. S., "The Effect of Compressibility on the Stress Distributions in Thin Elastomeric Blocks and Annular Bushings," *Transactions of the ASME*, Vol. 59, Dec. 1992, pp. 902-908.

10. Shigley, J. E. and Mischke, C. R., *Mechanical Engineering Design*, 6th ed., McGraw-Hill, New York, 2001, pp. 562-579.

11. Hetenyi, M., *Beam on Elastic Foundation; Theory With Application in the Fields of Civil and Mechanical Engineering*, University of Michagan Press, Ann Arbor, MI, 1946.

12. Young, W. C. and Budynas, R. G., *Roark's Formulas for Stress and Strain*, 7th ed., McGraw-Hill, New York, 2002.

13. Adams, R. D. and Wake, W. C., *Structural Adhesive Joints in Engineering*, Elsevier Applied Science Publications, London, 1984, pp. 14-114.

14. Volkersen, V. O., “Dei Nietkraftverteilung in Zugbeanspruchten Neitverbindungen mit Konstanten Laschenquerschnitten,” *Luftfahrtforschung*, Vol. 15, 1938, pp. 41-47.

15. Goland, M. and Reissner, E., “The Stress in Cemented Joints,” *Journal of Applied Mechanics*, March 1944, pp. A-17-A27.

16. Kinloch, A. J., *Adhesion and Adhesives Science and Technology*, Chapman and Hall, London, 1994, pp. 188-246.

17. Brown, T. A., “The Strain-Rate Sensitivity of Adhesive Tape and Its Significance For Design,” *Proceedings of the Second Australasian Congress on Applied Mechanics*, ACAM 1999, Canberra, Australia, Feb. 1999.

18. Weitsman, Y., “Stresses in Adhesive Joints Due To Moisture and Temperature,” *Journal of Composite Materials*, Oct. 1977, Vol. 11, pp. 378-394.

19. Parker, B. M., “The Strength of Bonded Carbon Fiber Composite Joints Exposed to High Humidity,” *International Journal of Adhesion and Adhesives*, 1990, Vol. 10, pp. 187-191.

20. Gledhill, A., and Kinloch, A. J., “Environmental Failure of Structural Adhesive Joints,” *Journal of Adhesion*, 1974, Vol. 6, pp.315-330.

21. Sargent, J. P. and Ashbee, K. H., “Hign Resolution Optical Interference Investigation of Swelling Due to Water Uptake by Model Adhesive Joints,” *Journal of Adhesion*, 1980, Vol. 11, pp.175-189.

22. Gledhill, A., Kinloch, A. J., and Shaw, S. J., “A Model for Predicting Joint Durability,” *Journal of Adhesion*, 1980, Vol. 11, pp.3-15.

23. Kinloch, A. J., Ed., *Durability of Structural Adhesives*, Applied Science Puplishers LTD, London, 1983, pp. 85-131.

24. Shigley, J. E. and Mitchell, L. D., *Mechanical Engineering Design*, 4th Edition, McGraw-Hill, New York, 1993, pp. 195-245.

25. Beer, F. P. and Johnston, E. R., *Mechanics of Materials*, 2nd Ed., McGraw-Hill, New York, 1992, pp. 364-371.

26. Tschoegl, N. W., “Time Dependence in Material Properties: An Overview,” *Mechanics of Time-Dependent Materials*, 1997, Vol. 1, pp. 3-31.

27. van Straalen, I. J., Wardenier, L., Vogelesang, F., and Soetens, F., "Structural Adhesive Bonded Joints in Engineering-Drafting Design Rules," *International Journal of Adhesion and Adhesives*, 1998, Vol. 18, pp. 41-49.

28. Hart-Smith, L. J., "*Adhesive-Bonded Double-Lap Joints*," National Aeronautics and Space Administration, Jan. 1973, NASA CR 112235.

29. Hart-Smith, L. J., "*Adhesive-Bonded Single-Lap Joints*," National Aeronautics and Space Administration, Jan. 1973, NASA CR 112236.

30. Hart-Smith, L. J., "*Adhesive-Bonded Scarf and Stepped-Lap Joints*," National Aeronautics and Space Administration, Jan. 1973, NASA CR 112237.

31. Hart-Smith, L. J., "*Non-Classical Adhesive-Bonded Joints in Practical Aerospace Construction*," National Aeronautics and Space Administration, Jan. 1973, NASA CR 112238.

32. Adams, R. D. and Harris, J. A., "The Influence of Local Geometry on the Strength of Adhesive Joints," *International Journal of Adhesion and Adhesives*, Vol. 7, No. 2, April 1987, pp. 69-80.

33. Anonymous, "*ALPCO Product Catalog*," Aluminum Line Products Company, July, 1999, pp. F-60.

34. Mitchell, L. D., Young, J. K., and Mitchell, S. D., *BEAMIV*, ver 6.0, Department of Mechanical Engineering, Virginia Polytechnic Institute and State University, Blacksburg, VA, 1992

35. Anonymous, "*VHB™ Double Coated Acrylic Foam Tapes and Adhesive Transfer Tapes*," 3M Bonding System Division, March 1998, pp. 9-12.

36. Anonymous, "*Surface Preparation for 3M™ VHB™ Tape Applications*," 3M Bonding System Division, Jan. 1995, pp. 1-2.

37. Peretz, D., and Ishai, O., "Mechanical Characterization of an Adhesive Layer *in situ* under Combined Load," *Journal of Adhesion*, 1980, Vol. 10, pp.317-320.

38. Sors, L., *Fatigue Design of Machine Components*, Pergamon Press, New York, 1971, pp. 42.

Appendix A

Test Specimen Stress Analysis

Table A-1A BEAMVI Model Data.

For section # 1 :		
Length of this section	6.2400D-01	in
Cross Sectional Area	1.8200D-01	in^2
Area Moment of Inertia	1.2560D-04	in^4
Modulus of Elasticity	1.0100D+07	psi
Weight Density	9.8000D-02	lb/in^3
Distance to Outer Fiber	4.5500D-02	in
Shape of this Beam Section	Rectangular Solid	
Shear Stress Correction Factor	1.5000D+00	
For section # 2 :		
Length of this section	2.1850D-01	in
Cross Sectional Area	1.8200D-01	in^2
Area Moment of Inertia	1.2560D-04	in^4
Modulus of Elasticity	1.0100D+07	psi
Weight Density	9.8000D-02	lb/in^3
Continuum Beam Foundation Stiffness	7.7757D+03	lb/in/in
Distance to Outer Fiber	4.5500D-02	in
Shape of this Beam Section	Rectangular Solid	
Shear Stress Correction Factor	1.5000D+00	
For section # 3 :		
Length of this section	6.3000D-02	in
Cross Sectional Area	1.8200D-01	in^2
Area Moment of Inertia	1.2560D-04	in^4
Modulus of Elasticity	1.0100D+07	psi
Weight Density	9.8000D-02	lb/in^3
Continuum Beam Foundation Stiffness	7.7757D+03	lb/in/in
Magnitude of Uniformly Distributed Load	-4.6280D+03	lb/in
Distance to Outer Fiber	4.5500D-02	in
Shape of this Beam Section	Rectangular Solid	
Shear Stress Correction Factor	1.5000D+00	
For section # 4 :		
Length of this section	2.1850D-01	in
Cross Sectional Area	1.8200D-01	in^2
Area Moment of Inertia	1.2560D-04	in^4
Modulus of Elasticity	1.0100D+07	psi
Weight Density	9.8000D-02	lb/in^3
Continuum Beam Foundation Stiffness	7.7757D+03	lb/in/in
Distance to Outer Fiber	4.5500D-02	in
Shape of this Beam Section	Rectangular Solid	
Shear Stress Correction Factor	1.5000D+00	

Table A-1B BEAMVI Model Data.

For section # 5 :		
Length of this section	6.2400D-01	in
Cross Sectional Area	1.8200D-01	in^2
Area Moment of Inertia	1.2560D-04	in^4
Modulus of Elasticity	1.0100D+07	psi
Weight Density	9.8000D-02	lb/in^3
Distance to Outer Fiber	4.5500D-02	in
Shape of this Beam Section	Rectangular Solid	
Shear Stress Correction Factor	1.5000D+00	
Boundary Condition	FREE-FREE	

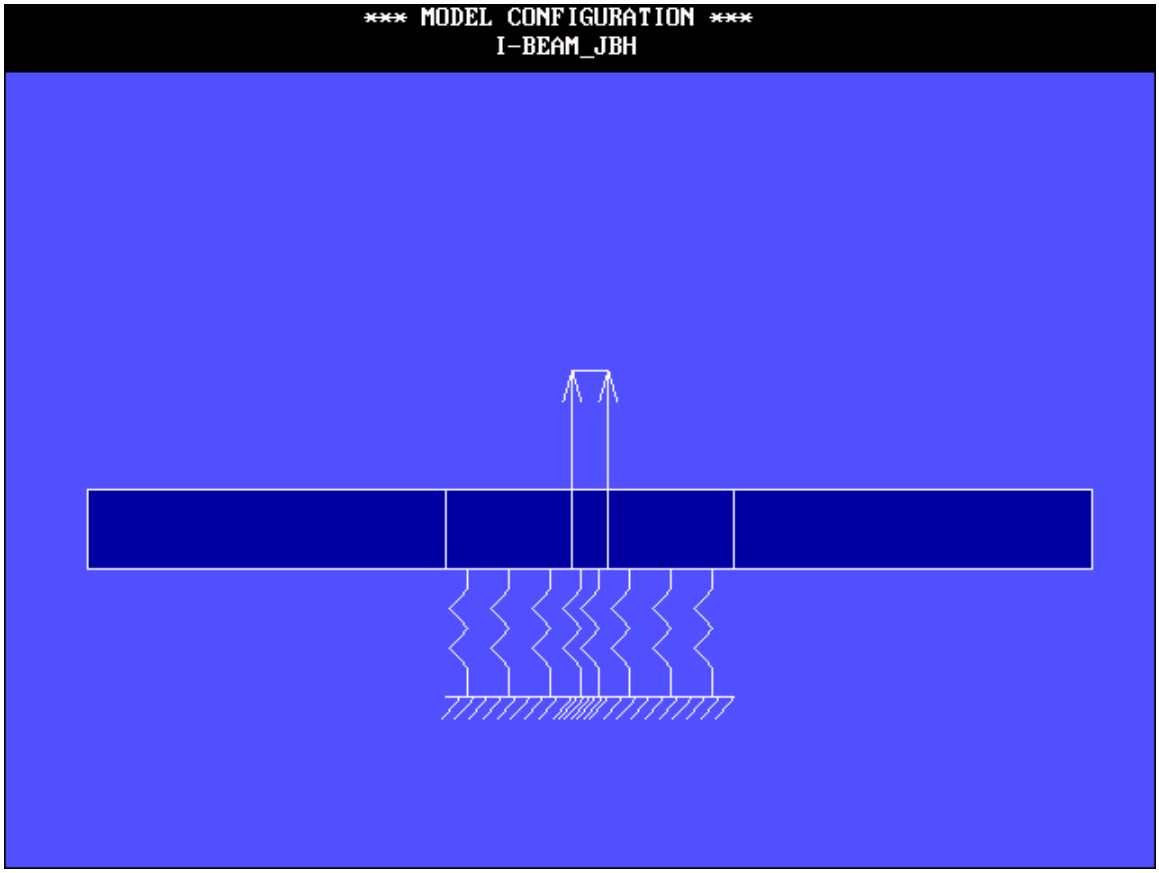

Figure A-1 I-BEAMIV model geometry.

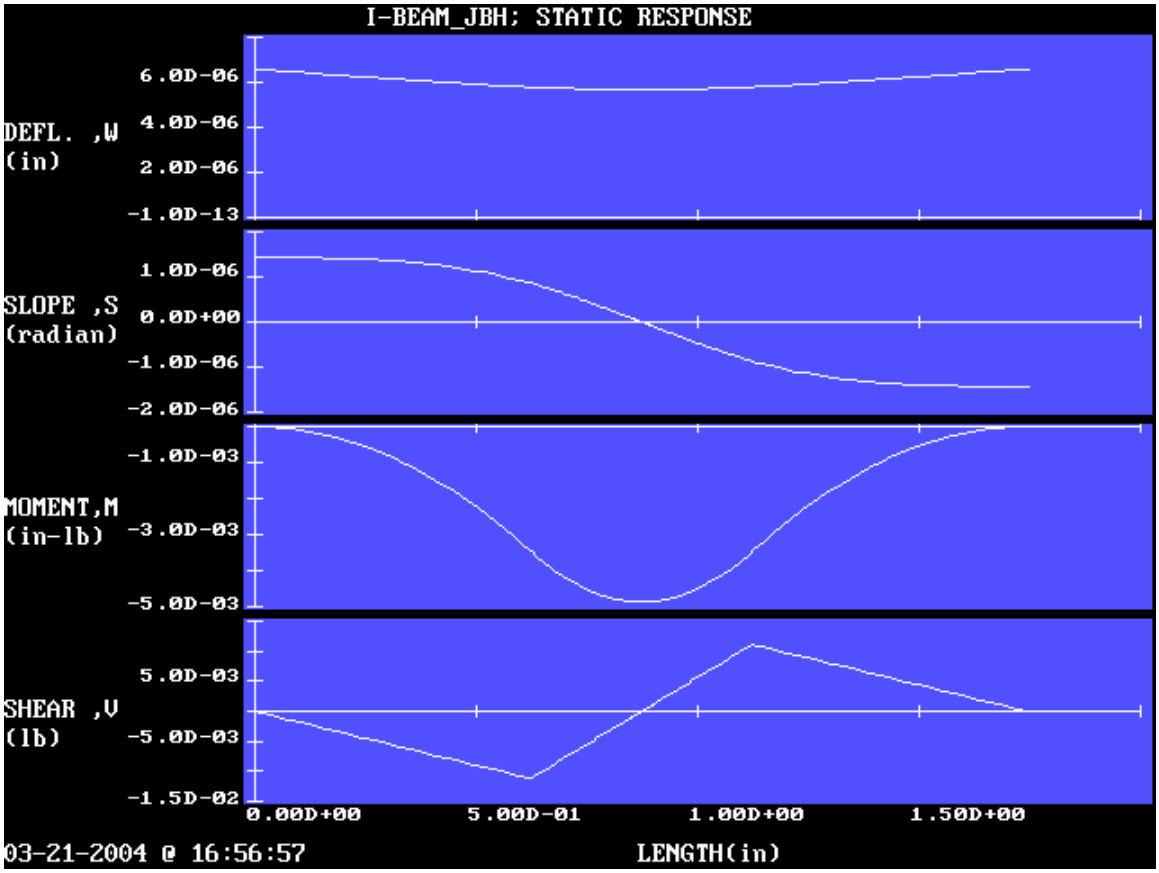

Figure A-2 BEAMVI output for I-Beam Model.

Table A-2A BEAMVI Static Results.

LENGTH (in)	DEFLECTION (in)	SLOPE (radians)	MOMENT (in-lb)	SHEAR (lb)
0.000D+00	6.608D-06	1.436D-06	0.000D+00	0.000D+00
1.248D-02	6.590D-06	1.436D-06	-1.389D-06	-2.226D-04
2.496D-02	6.572D-06	1.436D-06	-5.556D-06	-4.452D-04
3.744D-02	6.554D-06	1.436D-06	-1.250D-05	-6.678D-04
4.992D-02	6.536D-06	1.436D-06	-2.222D-05	-8.904D-04
6.240D-02	6.518D-06	1.435D-06	-3.472D-05	-1.113D-03
7.488D-02	6.500D-06	1.435D-06	-5.000D-05	-1.336D-03
8.736D-02	6.482D-06	1.434D-06	-6.806D-05	-1.558D-03
9.984D-02	6.465D-06	1.434D-06	-8.889D-05	-1.781D-03
1.123D-01	6.447D-06	1.433D-06	-1.125D-04	-2.003D-03
1.248D-01	6.429D-06	1.431D-06	-1.389D-04	-2.226D-03
1.373D-01	6.411D-06	1.430D-06	-1.681D-04	-2.449D-03
1.498D-01	6.393D-06	1.428D-06	-2.000D-04	-2.671D-03
1.622D-01	6.375D-06	1.426D-06	-2.347D-04	-2.894D-03
1.747D-01	6.358D-06	1.424D-06	-2.722D-04	-3.116D-03
1.872D-01	6.340D-06	1.421D-06	-3.125D-04	-3.339D-03
1.997D-01	6.322D-06	1.417D-06	-3.556D-04	-3.561D-03
2.122D-01	6.304D-06	1.414D-06	-4.014D-04	-3.784D-03
2.246D-01	6.287D-06	1.409D-06	-4.500D-04	-4.007D-03
2.371D-01	6.269D-06	1.405D-06	-5.014D-04	-4.229D-03
2.496D-01	6.252D-06	1.400D-06	-5.556D-04	-4.452D-03
2.621D-01	6.234D-06	1.394D-06	-6.125D-04	-4.674D-03
2.746D-01	6.217D-06	1.388D-06	-6.723D-04	-4.897D-03
2.870D-01	6.200D-06	1.381D-06	-7.348D-04	-5.120D-03
2.995D-01	6.182D-06	1.373D-06	-8.001D-04	-5.342D-03
3.120D-01	6.165D-06	1.365D-06	-8.681D-04	-5.565D-03
3.245D-01	6.148D-06	1.356D-06	-9.390D-04	-5.787D-03
3.370D-01	6.132D-06	1.346D-06	-1.013D-03	-6.010D-03
3.494D-01	6.115D-06	1.336D-06	-1.089D-03	-6.233D-03
3.619D-01	6.098D-06	1.325D-06	-1.168D-03	-6.455D-03
3.744D-01	6.082D-06	1.313D-06	-1.250D-03	-6.678D-03
3.869D-01	6.065D-06	1.300D-06	-1.335D-03	-6.900D-03
3.994D-01	6.049D-06	1.287D-06	-1.422D-03	-7.123D-03
4.118D-01	6.033D-06	1.272D-06	-1.513D-03	-7.346D-03
4.243D-01	6.018D-06	1.257D-06	-1.606D-03	-7.568D-03
4.368D-01	6.002D-06	1.241D-06	-1.702D-03	-7.791D-03
4.493D-01	5.987D-06	1.224D-06	-1.800D-03	-8.013D-03
4.618D-01	5.971D-06	1.205D-06	-1.902D-03	-8.236D-03
4.742D-01	5.956D-06	1.186D-06	-2.006D-03	-8.459D-03
4.867D-01	5.942D-06	1.166D-06	-2.113D-03	-8.681D-03
4.992D-01	5.927D-06	1.145D-06	-2.222D-03	-8.904D-03
5.117D-01	5.913D-06	1.122D-06	-2.335D-03	-9.126D-03
5.242D-01	5.899D-06	1.099D-06	-2.450D-03	-9.349D-03

Table A-2B BEAMVI Static Results.

LENGTH (in)	DEFLECTION (in)	SLOPE (radians)	MOMENT (in-lb)	SHEAR (lb)
5.366D-01	5.886D-06	1.074D-06	-2.568D-03	-9.572D-03
5.491D-01	5.873D-06	1.048D-06	-2.689D-03	-9.794D-03
5.616D-01	5.860D-06	1.021D-06	-2.813D-03	-1.002D-02
5.741D-01	5.847D-06	9.927D-07	-2.939D-03	-1.024D-02
5.866D-01	5.835D-06	9.631D-07	-3.068D-03	-1.046D-02
5.990D-01	5.823D-06	9.323D-07	-3.200D-03	-1.068D-02
6.115D-01	5.812D-06	9.001D-07	-3.335D-03	-1.091D-02
6.240D-01	5.801D-06	8.667D-07	-3.472D-03	-1.113D-02
6.284D-01	5.797D-06	8.546D-07	-3.521D-03	-1.093D-02
6.327D-01	5.793D-06	8.424D-07	-3.568D-03	-1.074D-02
6.371D-01	5.789D-06	8.300D-07	-3.614D-03	-1.054D-02
6.415D-01	5.786D-06	8.175D-07	-3.660D-03	-1.034D-02
6.459D-01	5.782D-06	8.048D-07	-3.705D-03	-1.015D-02
6.502D-01	5.779D-06	7.920D-07	-3.749D-03	-9.949D-03
6.546D-01	5.775D-06	7.790D-07	-3.792D-03	-9.753D-03
6.590D-01	5.772D-06	7.658D-07	-3.834D-03	-9.557D-03
6.633D-01	5.769D-06	7.526D-07	-3.875D-03	-9.361D-03
6.677D-01	5.765D-06	7.391D-07	-3.916D-03	-9.165D-03
6.721D-01	5.762D-06	7.256D-07	-3.955D-03	-8.969D-03
6.764D-01	5.759D-06	7.119D-07	-3.994D-03	-8.773D-03
6.808D-01	5.756D-06	6.981D-07	-4.032D-03	-8.578D-03
6.852D-01	5.753D-06	6.841D-07	-4.069D-03	-8.382D-03
6.896D-01	5.750D-06	6.700D-07	-4.105D-03	-8.187D-03
6.939D-01	5.747D-06	6.558D-07	-4.141D-03	-7.991D-03
6.983D-01	5.744D-06	6.415D-07	-4.175D-03	-7.796D-03
7.027D-01	5.742D-06	6.271D-07	-4.209D-03	-7.601D-03
7.070D-01	5.739D-06	6.125D-07	-4.242D-03	-7.406D-03
7.114D-01	5.736D-06	5.978D-07	-4.274D-03	-7.211D-03
7.158D-01	5.734D-06	5.831D-07	-4.305D-03	-7.016D-03
7.201D-01	5.731D-06	5.682D-07	-4.335D-03	-6.821D-03
7.245D-01	5.729D-06	5.532D-07	-4.364D-03	-6.626D-03
7.289D-01	5.726D-06	5.381D-07	-4.393D-03	-6.432D-03
7.332D-01	5.724D-06	5.229D-07	-4.421D-03	-6.237D-03
7.376D-01	5.722D-06	5.077D-07	-4.447D-03	-6.043D-03
7.420D-01	5.720D-06	4.923D-07	-4.473D-03	-5.848D-03
7.464D-01	5.717D-06	4.768D-07	-4.498D-03	-5.654D-03
7.507D-01	5.715D-06	4.613D-07	-4.523D-03	-5.460D-03
7.551D-01	5.713D-06	4.457D-07	-4.546D-03	-5.266D-03
7.595D-01	5.711D-06	4.300D-07	-4.569D-03	-5.072D-03
7.638D-01	5.710D-06	4.142D-07	-4.591D-03	-4.878D-03
7.682D-01	5.708D-06	3.983D-07	-4.611D-03	-4.684D-03
7.726D-01	5.706D-06	3.824D-07	-4.631D-03	-4.490D-03

Table A-2C BEAMVI Static Results.

LENGTH (in)	DEFLECTION (in)	SLOPE (radians)	MOMENT (in-lb)	SHEAR (lb)
7.769D-01	5.705D-06	3.664D-07	-4.651D-03	-4.296D-03
7.813D-01	5.703D-06	3.504D-07	-4.669D-03	-4.102D-03
7.857D-01	5.701D-06	3.343D-07	-4.687D-03	-3.908D-03
7.901D-01	5.700D-06	3.181D-07	-4.703D-03	-3.715D-03
7.944D-01	5.699D-06	3.019D-07	-4.719D-03	-3.521D-03
7.988D-01	5.697D-06	2.856D-07	-4.734D-03	-3.327D-03
8.032D-01	5.696D-06	2.692D-07	-4.748D-03	-3.134D-03
8.075D-01	5.695D-06	2.529D-07	-4.761D-03	-2.940D-03
8.119D-01	5.694D-06	2.364D-07	-4.774D-03	-2.747D-03
8.163D-01	5.693D-06	2.200D-07	-4.785D-03	-2.553D-03
8.206D-01	5.692D-06	2.035D-07	-4.796D-03	-2.360D-03
8.250D-01	5.691D-06	1.869D-07	-4.806D-03	-2.166D-03
8.294D-01	5.690D-06	1.704D-07	-4.815D-03	-1.973D-03
8.338D-01	5.690D-06	1.538D-07	-4.823D-03	-1.780D-03
8.381D-01	5.689D-06	1.371D-07	-4.831D-03	-1.586D-03
8.425D-01	5.688D-06	1.205D-07	-4.837D-03	-1.393D-03
8.438D-01	5.688D-06	1.157D-07	-4.839D-03	-1.337D-03
8.450D-01	5.688D-06	1.109D-07	-4.840D-03	-1.282D-03
8.463D-01	5.688D-06	1.061D-07	-4.842D-03	-1.226D-03
8.475D-01	5.688D-06	1.012D-07	-4.844D-03	-1.170D-03
8.488D-01	5.688D-06	9.643D-08	-4.845D-03	-1.114D-03
8.501D-01	5.688D-06	9.162D-08	-4.846D-03	-1.059D-03
8.513D-01	5.688D-06	8.681D-08	-4.848D-03	-1.003D-03
8.526D-01	5.687D-06	8.199D-08	-4.849D-03	-9.472D-04
8.538D-01	5.687D-06	7.717D-08	-4.850D-03	-8.915D-04
8.551D-01	5.687D-06	7.236D-08	-4.851D-03	-8.357D-04
8.564D-01	5.687D-06	6.754D-08	-4.852D-03	-7.800D-04
8.576D-01	5.687D-06	6.272D-08	-4.853D-03	-7.243D-04
8.589D-01	5.687D-06	5.790D-08	-4.854D-03	-6.686D-04
8.601D-01	5.687D-06	5.307D-08	-4.855D-03	-6.129D-04
8.614D-01	5.687D-06	4.825D-08	-4.855D-03	-5.571D-04
8.627D-01	5.687D-06	4.343D-08	-4.856D-03	-5.014D-04
8.639D-01	5.687D-06	3.861D-08	-4.857D-03	-4.457D-04
8.652D-01	5.687D-06	3.378D-08	-4.857D-03	-3.900D-04
8.664D-01	5.687D-06	2.896D-08	-4.858D-03	-3.343D-04
8.677D-01	5.687D-06	2.413D-08	-4.858D-03	-2.786D-04
8.690D-01	5.687D-06	1.930D-08	-4.858D-03	-2.229D-04
8.702D-01	5.687D-06	1.448D-08	-4.859D-03	-1.671D-04
8.715D-01	5.687D-06	9.653D-09	-4.859D-03	-1.114D-04
8.727D-01	5.687D-06	4.826D-09	-4.859D-03	-5.571D-05
8.740D-01	5.687D-06	1.219D-20	-4.859D-03	6.636D-18
8.753D-01	5.687D-06	-4.826D-09	-4.859D-03	5.571D-05

Table A-2D BEAMVI Static Results.

LENGTH (in)	DEFLECTION (in)	SLOPE (radians)	MOMENT (in-lb)	SHEAR (lb)
8.765D-01	5.687D-06	-9.653D-09	-4.859D-03	1.114D-04
8.778D-01	5.687D-06	-1.448D-08	-4.859D-03	1.671D-04
8.790D-01	5.687D-06	-1.930D-08	-4.858D-03	2.229D-04
8.803D-01	5.687D-06	-2.413D-08	-4.858D-03	2.786D-04
8.816D-01	5.687D-06	-2.896D-08	-4.858D-03	3.343D-04
8.828D-01	5.687D-06	-3.378D-08	-4.857D-03	3.900D-04
8.841D-01	5.687D-06	-3.861D-08	-4.857D-03	4.457D-04
8.853D-01	5.687D-06	-4.343D-08	-4.856D-03	5.014D-04
8.866D-01	5.687D-06	-4.825D-08	-4.855D-03	5.571D-04
8.879D-01	5.687D-06	-5.307D-08	-4.855D-03	6.129D-04
8.891D-01	5.687D-06	-5.790D-08	-4.854D-03	6.686D-04
8.904D-01	5.687D-06	-6.272D-08	-4.853D-03	7.243D-04
8.916D-01	5.687D-06	-6.754D-08	-4.852D-03	7.800D-04
8.929D-01	5.687D-06	-7.236D-08	-4.851D-03	8.357D-04
8.942D-01	5.687D-06	-7.717D-08	-4.850D-03	8.915D-04
8.954D-01	5.687D-06	-8.199D-08	-4.849D-03	9.472D-04
8.967D-01	5.688D-06	-8.681D-08	-4.848D-03	1.003D-03
8.979D-01	5.688D-06	-9.162D-08	-4.846D-03	1.059D-03
8.992D-01	5.688D-06	-9.643D-08	-4.845D-03	1.114D-03
9.005D-01	5.688D-06	-1.012D-07	-4.844D-03	1.170D-03
9.017D-01	5.688D-06	-1.061D-07	-4.842D-03	1.226D-03
9.030D-01	5.688D-06	-1.109D-07	-4.840D-03	1.282D-03
9.042D-01	5.688D-06	-1.157D-07	-4.839D-03	1.337D-03
9.055D-01	5.688D-06	-1.205D-07	-4.837D-03	1.393D-03
9.099D-01	5.689D-06	-1.371D-07	-4.831D-03	1.586D-03
9.142D-01	5.690D-06	-1.538D-07	-4.823D-03	1.780D-03
9.186D-01	5.690D-06	-1.704D-07	-4.815D-03	1.973D-03
9.230D-01	5.691D-06	-1.869D-07	-4.806D-03	2.166D-03
9.274D-01	5.692D-06	-2.035D-07	-4.796D-03	2.360D-03
9.317D-01	5.693D-06	-2.200D-07	-4.785D-03	2.553D-03
9.361D-01	5.694D-06	-2.364D-07	-4.774D-03	2.747D-03
9.405D-01	5.695D-06	-2.529D-07	-4.761D-03	2.940D-03
9.448D-01	5.696D-06	-2.692D-07	-4.748D-03	3.134D-03
9.492D-01	5.697D-06	-2.856D-07	-4.734D-03	3.327D-03
9.536D-01	5.699D-06	-3.019D-07	-4.719D-03	3.521D-03
9.579D-01	5.700D-06	-3.181D-07	-4.703D-03	3.715D-03
9.623D-01	5.701D-06	-3.343D-07	-4.687D-03	3.908D-03
9.667D-01	5.703D-06	-3.504D-07	-4.669D-03	4.102D-03
9.711D-01	5.705D-06	-3.664D-07	-4.651D-03	4.296D-03
9.754D-01	5.706D-06	-3.824D-07	-4.631D-03	4.490D-03
9.798D-01	5.708D-06	-3.983D-07	-4.611D-03	4.684D-03
9.842D-01	5.710D-06	-4.142D-07	-4.591D-03	4.878D-03

Table A-2E BEAMVI Static Results.

LENGTH (in)	DEFLECTION (in)	SLOPE (radians)	MOMENT (in-lb)	SHEAR (lb)
9.885D-01	5.711D-06	-4.300D-07	-4.569D-03	5.072D-03
9.929D-01	5.713D-06	-4.457D-07	-4.546D-03	5.266D-03
9.973D-01	5.715D-06	-4.613D-07	-4.523D-03	5.460D-03
1.002D+00	5.717D-06	-4.768D-07	-4.498D-03	5.654D-03
1.006D+00	5.720D-06	-4.923D-07	-4.473D-03	5.848D-03
1.010D+00	5.722D-06	-5.077D-07	-4.447D-03	6.043D-03
1.015D+00	5.724D-06	-5.229D-07	-4.421D-03	6.237D-03
1.019D+00	5.726D-06	-5.381D-07	-4.393D-03	6.432D-03
1.023D+00	5.729D-06	-5.532D-07	-4.364D-03	6.626D-03
1.028D+00	5.731D-06	-5.682D-07	-4.335D-03	6.821D-03
1.032D+00	5.734D-06	-5.831D-07	-4.305D-03	7.016D-03
1.037D+00	5.736D-06	-5.978D-07	-4.274D-03	7.211D-03
1.041D+00	5.739D-06	-6.125D-07	-4.242D-03	7.406D-03
1.045D+00	5.742D-06	-6.271D-07	-4.209D-03	7.601D-03
1.050D+00	5.744D-06	-6.415D-07	-4.175D-03	7.796D-03
1.054D+00	5.747D-06	-6.558D-07	-4.141D-03	7.991D-03
1.058D+00	5.750D-06	-6.700D-07	-4.105D-03	8.187D-03
1.063D+00	5.753D-06	-6.841D-07	-4.069D-03	8.382D-03
1.067D+00	5.756D-06	-6.981D-07	-4.032D-03	8.578D-03
1.072D+00	5.759D-06	-7.119D-07	-3.994D-03	8.773D-03
1.076D+00	5.762D-06	-7.256D-07	-3.955D-03	8.969D-03
1.080D+00	5.765D-06	-7.391D-07	-3.916D-03	9.165D-03
1.085D+00	5.769D-06	-7.526D-07	-3.875D-03	9.361D-03
1.089D+00	5.772D-06	-7.658D-07	-3.834D-03	9.557D-03
1.093D+00	5.775D-06	-7.790D-07	-3.792D-03	9.753D-03
1.098D+00	5.779D-06	-7.920D-07	-3.749D-03	9.949D-03
1.102D+00	5.782D-06	-8.048D-07	-3.705D-03	1.015D-02
1.107D+00	5.786D-06	-8.175D-07	-3.660D-03	1.034D-02
1.111D+00	5.789D-06	-8.300D-07	-3.614D-03	1.054D-02
1.115D+00	5.793D-06	-8.424D-07	-3.568D-03	1.074D-02
1.120D+00	5.797D-06	-8.546D-07	-3.521D-03	1.093D-02
1.124D+00	5.801D-06	-8.667D-07	-3.472D-03	1.113D-02
1.136D+00	5.812D-06	-9.001D-07	-3.335D-03	1.091D-02
1.149D+00	5.823D-06	-9.323D-07	-3.200D-03	1.068D-02
1.161D+00	5.835D-06	-9.631D-07	-3.068D-03	1.046D-02
1.174D+00	5.847D-06	-9.927D-07	-2.939D-03	1.024D-02
1.186D+00	5.860D-06	-1.021D-06	-2.813D-03	1.002D-02
1.199D+00	5.873D-06	-1.048D-06	-2.689D-03	9.794D-03
1.211D+00	5.886D-06	-1.074D-06	-2.568D-03	9.572D-03
1.224D+00	5.899D-06	-1.099D-06	-2.450D-03	9.349D-03
1.236D+00	5.913D-06	-1.122D-06	-2.335D-03	9.126D-03
1.249D+00	5.927D-06	-1.145D-06	-2.222D-03	8.904D-03

Table A-2F BEAMVI Static Results.

LENGTH (in)	DEFLECTION (in)	SLOPE (radians)	MOMENT (in-lb)	SHEAR (lb)
1.261D+00	5.942D-06	-1.166D-06	-2.113D-03	8.681D-03
1.274D+00	5.956D-06	-1.186D-06	-2.006D-03	8.459D-03
1.286D+00	5.971D-06	-1.205D-06	-1.902D-03	8.236D-03
1.299D+00	5.987D-06	-1.224D-06	-1.800D-03	8.013D-03
1.311D+00	6.002D-06	-1.241D-06	-1.702D-03	7.791D-03
1.324D+00	6.018D-06	-1.257D-06	-1.606D-03	7.568D-03
1.336D+00	6.033D-06	-1.272D-06	-1.513D-03	7.346D-03
1.349D+00	6.049D-06	-1.287D-06	-1.422D-03	7.123D-03
1.361D+00	6.065D-06	-1.300D-06	-1.335D-03	6.900D-03
1.374D+00	6.082D-06	-1.313D-06	-1.250D-03	6.678D-03
1.386D+00	6.098D-06	-1.325D-06	-1.168D-03	6.455D-03
1.399D+00	6.115D-06	-1.336D-06	-1.089D-03	6.233D-03
1.411D+00	6.132D-06	-1.346D-06	-1.013D-03	6.010D-03
1.424D+00	6.148D-06	-1.356D-06	-9.390D-04	5.787D-03
1.436D+00	6.165D-06	-1.365D-06	-8.681D-04	5.565D-03
1.448D+00	6.182D-06	-1.373D-06	-8.001D-04	5.342D-03
1.461D+00	6.200D-06	-1.381D-06	-7.348D-04	5.120D-03
1.473D+00	6.217D-06	-1.388D-06	-6.723D-04	4.897D-03
1.486D+00	6.234D-06	-1.394D-06	-6.125D-04	4.674D-03
1.498D+00	6.252D-06	-1.400D-06	-5.556D-04	4.452D-03
1.511D+00	6.269D-06	-1.405D-06	-5.014D-04	4.229D-03
1.523D+00	6.287D-06	-1.409D-06	-4.500D-04	4.007D-03
1.536D+00	6.304D-06	-1.414D-06	-4.014D-04	3.784D-03
1.548D+00	6.322D-06	-1.417D-06	-3.556D-04	3.561D-03
1.561D+00	6.340D-06	-1.421D-06	-3.125D-04	3.339D-03
1.573D+00	6.358D-06	-1.424D-06	-2.722D-04	3.116D-03
1.586D+00	6.375D-06	-1.426D-06	-2.347D-04	2.894D-03
1.598D+00	6.393D-06	-1.428D-06	-2.000D-04	2.671D-03
1.611D+00	6.411D-06	-1.430D-06	-1.681D-04	2.449D-03
1.623D+00	6.429D-06	-1.431D-06	-1.389D-04	2.226D-03
1.636D+00	6.447D-06	-1.433D-06	-1.125D-04	2.003D-03
1.648D+00	6.465D-06	-1.434D-06	-8.889D-05	1.781D-03
1.661D+00	6.482D-06	-1.434D-06	-6.806D-05	1.558D-03
1.673D+00	6.500D-06	-1.435D-06	-5.000D-05	1.336D-03
1.686D+00	6.518D-06	-1.435D-06	-3.472D-05	1.113D-03
1.698D+00	6.536D-06	-1.436D-06	-2.222D-05	8.904D-04
1.711D+00	6.554D-06	-1.436D-06	-1.250D-05	6.678D-04
1.723D+00	6.572D-06	-1.436D-06	-5.556D-06	4.452D-04
1.736D+00	6.590D-06	-1.436D-06	-1.389D-06	2.226D-04
1.748D+00	6.608D-06	-1.436D-06	5.204D-18	3.469D-18

38.1 mm Mark 25.4 mm Mark 12.7 mm Mark Center

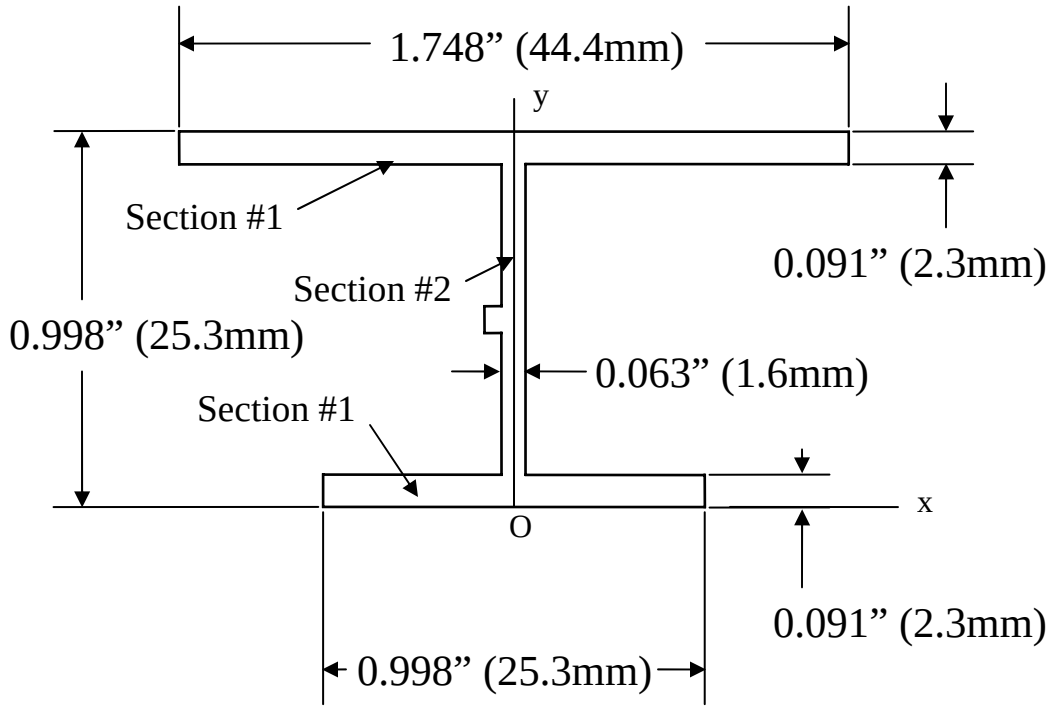

Figure A-3 I-Beam Cross-Section.

Step 1: Compute Centroid Location

Calculate the area of each section.

$A_1 = 44.4\text{mm}*2.3\text{mm}=102.6\text{mm}^2$

$A_2 = 20.7\text{mm}*1.6\text{mm}=33.1\text{mm}^2$

$A_3 = 25.3\text{mm}*2.3\text{mm}=58.2\text{mm}^2$

$\sum A_n = 193.9\text{mm}^2$

Calculate the distance from a reference (point O) to the centroid of each section.

$$\bar{y}_1 = 25.3\text{mm} - \frac{2.3\text{mm}}{2} = 24.2\text{mm}$$

$$\bar{y}_2 = \frac{20.7\text{mm}}{2} + 2.3\text{mm} = 12.7\text{mm}$$

$$\bar{y}_3 = \frac{2.3\text{mm}}{2} = 1.2\text{mm}$$

Calculate the centroid of the composite structure.

$$A_1\bar{y}_1 = 102.6\text{mm}^2 * 24.2\text{mm} = 2482.9\text{mm}^3$$
$$A_2\bar{y}_2 = 33.1\text{mm}^2 * 12.7\text{mm} = 420.4\text{mm}^3$$
$$A_3\bar{y}_3 = 58.2\text{mm}^2 * 1.2\text{mm} = 69.8\text{mm}^3$$
$$\sum A_n\bar{y}_n = 2973.1\text{mm}^3$$

$$\bar{Y} = \frac{\sum A_n\bar{y}_n}{\sum A_n} = \frac{2973.1\text{mm}^3}{193.9\text{mm}^2} = 15.3\text{mm}$$

The centroid of the I-beam is 15.3mm from the bottom (point O).

Step #2: Calculate the Moment of Inertia

Calculate the moment of inertia for each section with respect to its own centroid.

$$\bar{I}_{x'1} = \frac{bh^3}{12} = \frac{44.4\text{mm} * (2.3\text{mm})^3}{12} = 45.0\text{mm}^4$$
$$\bar{I}_{x'1} = \frac{1.6\text{mm} * (20.7\text{mm})^3}{12} = 1182.6\text{mm}^4$$
$$\bar{I}_{x'1} = \frac{25.3\text{mm} * (2.3\text{mm})^3}{12} = 25.7\text{mm}^4$$

Apply the parallel-axis theorem to determine the moment of inertia for each section with respect to the centroid or the I-beam.

$$I_{x1} = \bar{I}_{x'1} + A_1 * (\bar{y}_1 - \bar{Y})^2 = 45.0\text{mm}^4 + 102.6\text{mm}^2 (24.2\text{mm} - 15.3\text{mm})^2 = 8171.9\text{mm}^4$$
$$I_{x2} = 1182.6\text{mm}^4 + 33.1\text{mm}^2 (12.7\text{mm} - 15.3\text{mm})^2 = 1406.4\text{mm}^4$$
$$I_{x3} = 25.7\text{mm}^4 + 58.2\text{mm}^2 (1.2\text{mm} - 15.3\text{mm})^2 = 11596.4\text{mm}^4$$
$$\bar{I}_x = 8171.9\text{mm}^4 + 1406.4\text{mm}^4 + 11596.4\text{mm}^4 = 21174.7\text{mm}^4$$

This indicates that the moment of inertia about the x-axis for the I-beam is 21175mm^4.

Step #3: Calculate an equivalent specimen thickness for a base of 12.7mm.

$$\bar{I}_x = \frac{bh^3}{12}$$
$$h = \sqrt[3]{\frac{12\bar{I}_x}{b}} = \sqrt[3]{\frac{12 * 21174.7\text{mm}^4}{12.7\text{mm}}} = 27.1\text{mm}$$

Step #4: Determine ωl for the specimen.

$$\omega l = \sqrt{\frac{2G_a}{t_a E_s t_s}} * l = \sqrt{\frac{2 * 1.2\text{MPa}}{1.016\text{mm} * 70\text{GPa} * 27.1\text{mm}}} * 50.8\text{mm} = 0.057$$

This value is based on the highest value of G_a calculated during testing and therefore, represents the highest value of ωl for the specimen.

Appendix B

Fixture Drawings

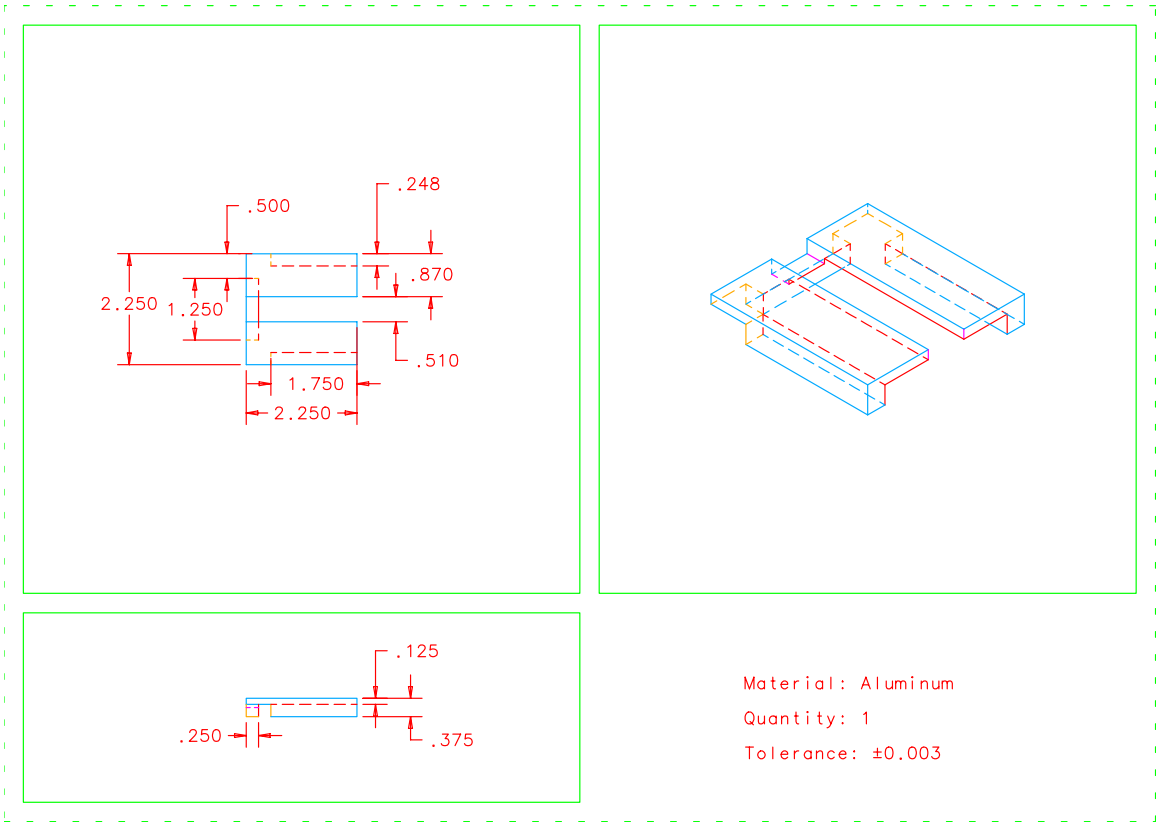

Figure B-1 Tape Alignment Fixture.

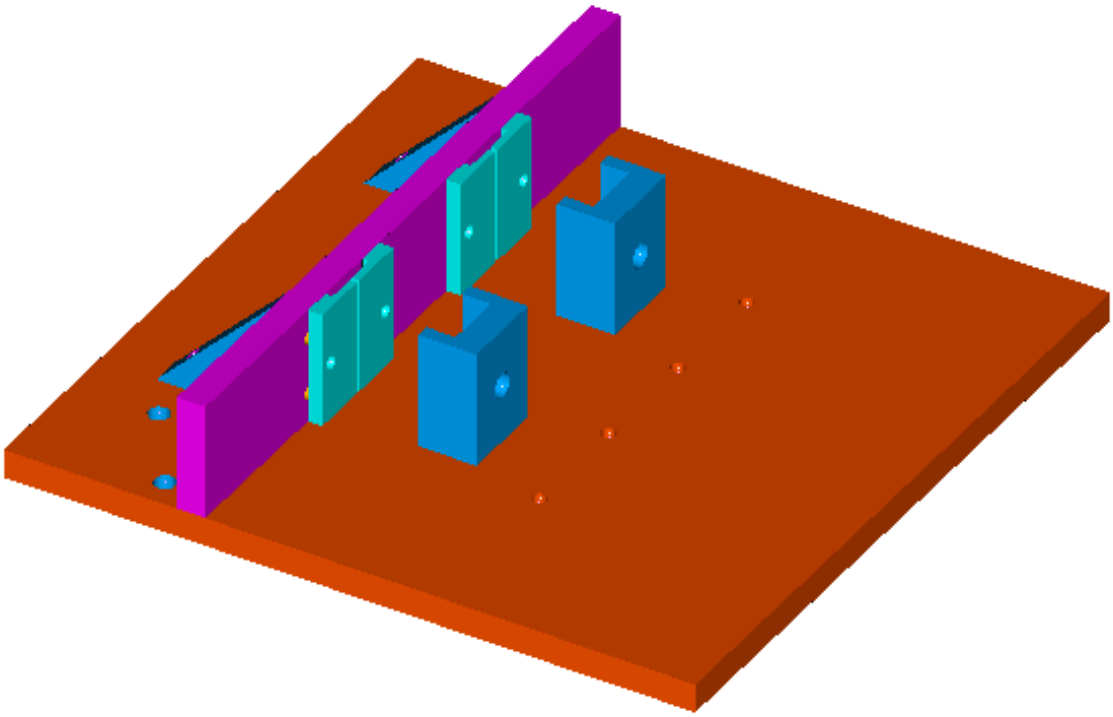

Figure B-2 Preload Fixture – Top Level.

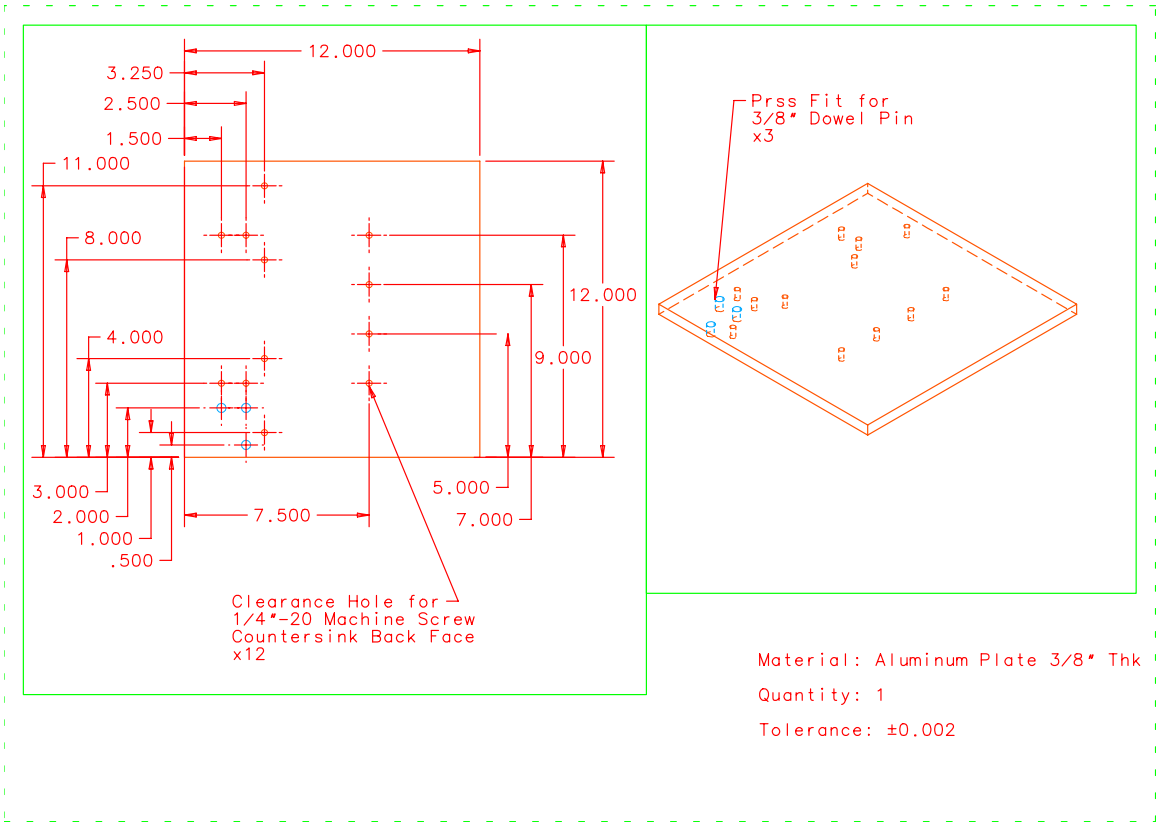

Figure B-3 Preload Fixture – Bottom Plate.

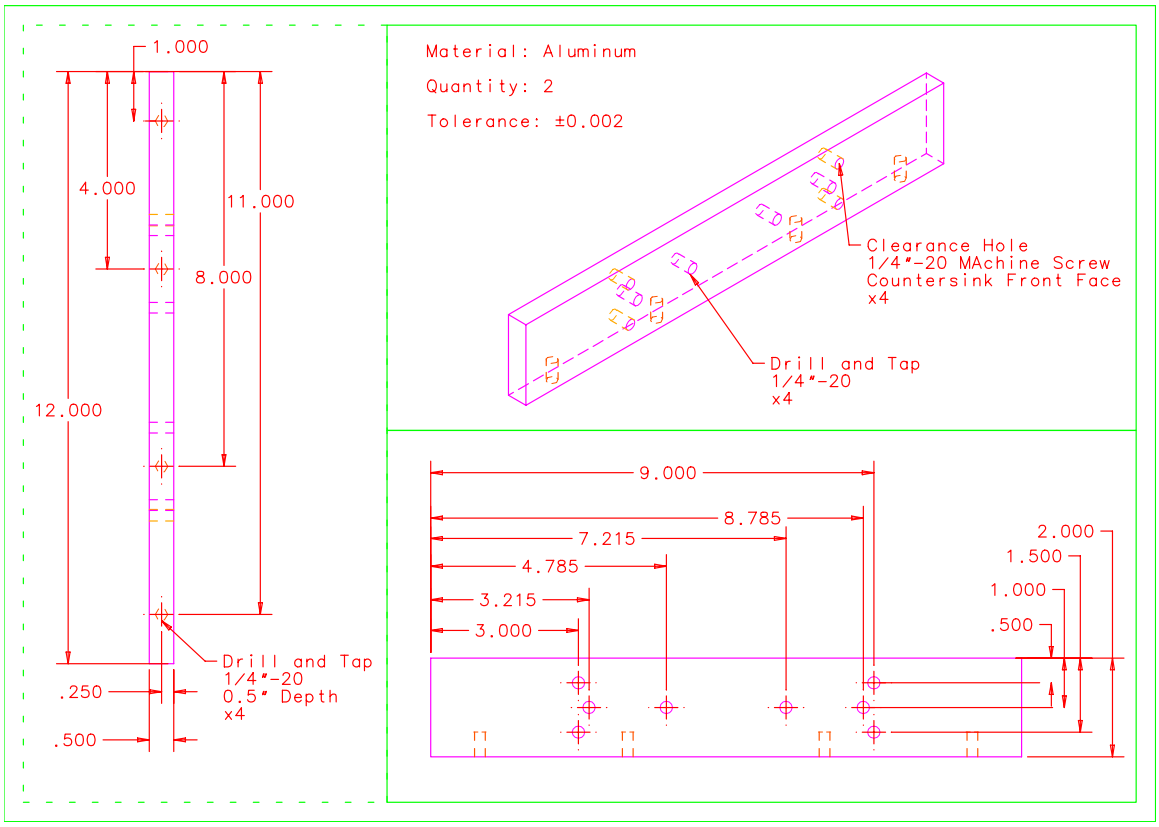

Figure B-4 Preload Fixture – Cross Member.

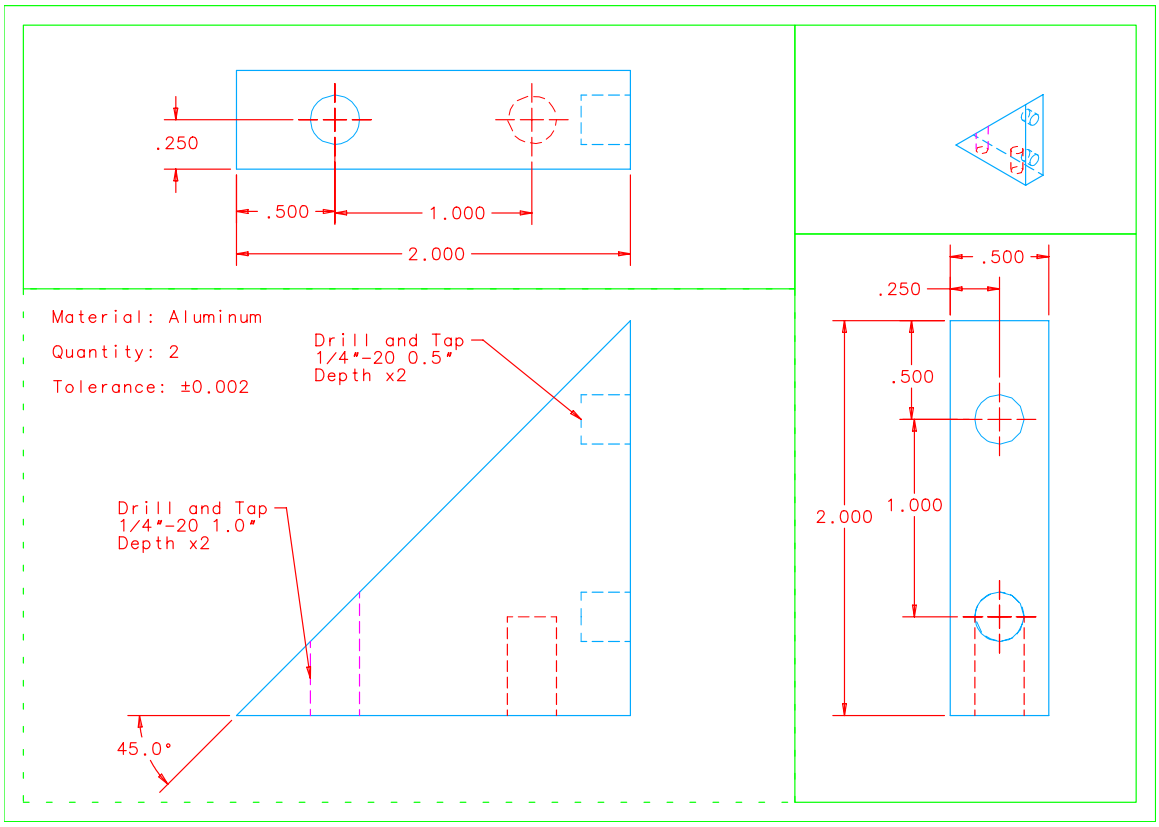

Figure B-5 Preload Fixture – Gusset.

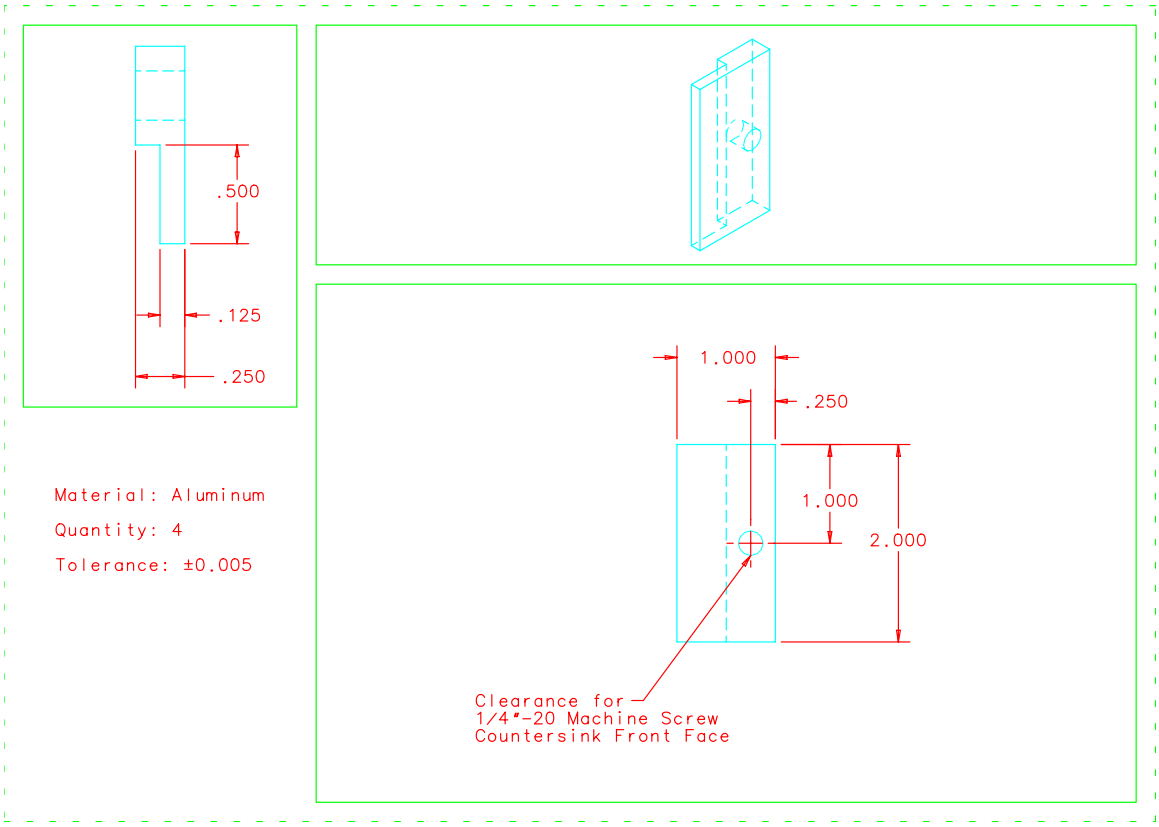

Figure B-6 Preload Fixture – Grip.

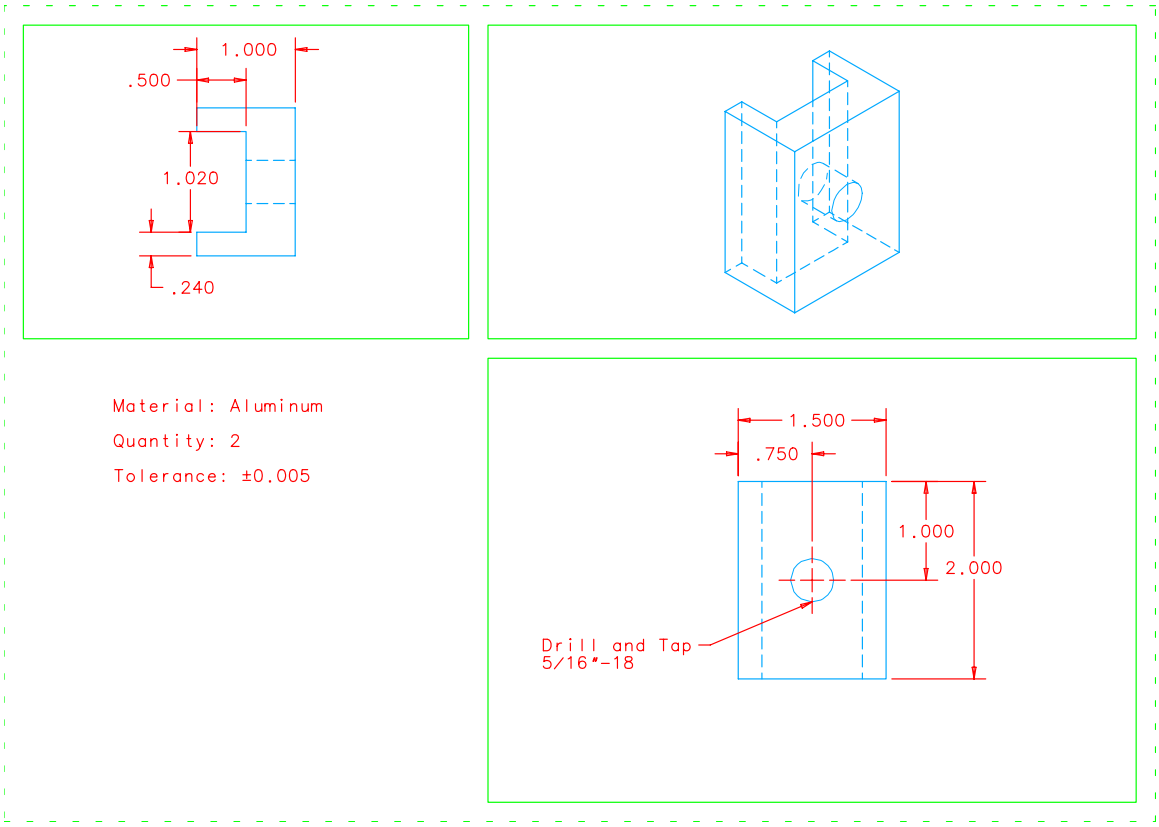

Figure B-7 Preload Fixture – Ram.

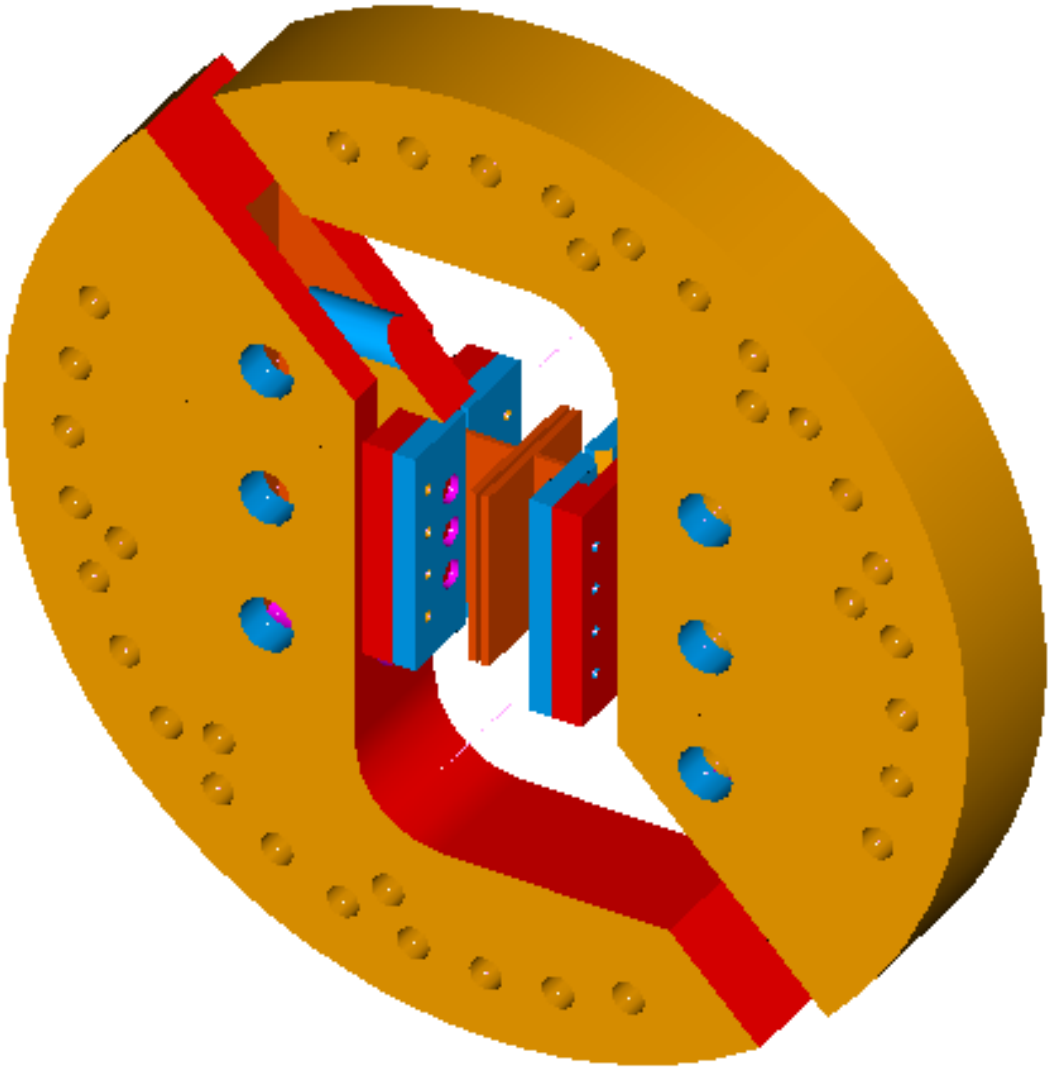

Figure B-8 Arcan$_m$ – Top Level.

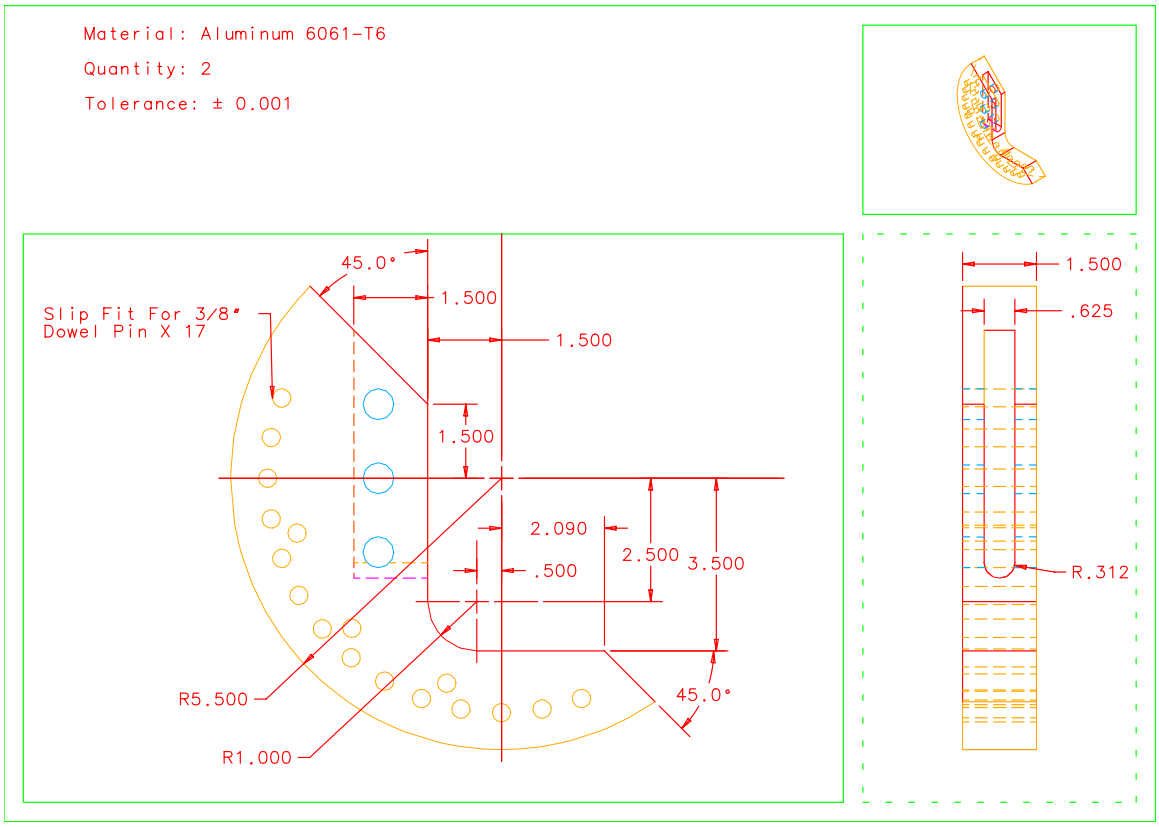

Figure B-9 Arcan$_m$ – Fixture A.

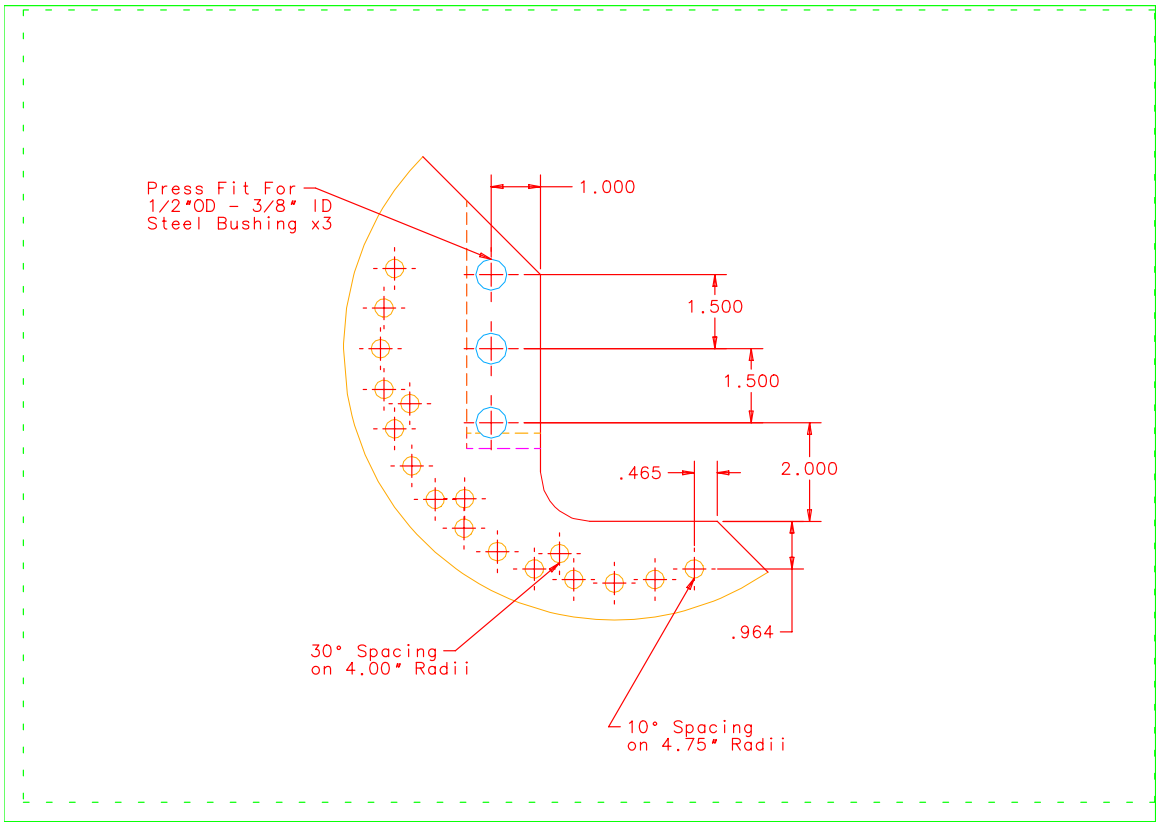

Figure B-10 Arcan$_m$ – Fixture B.

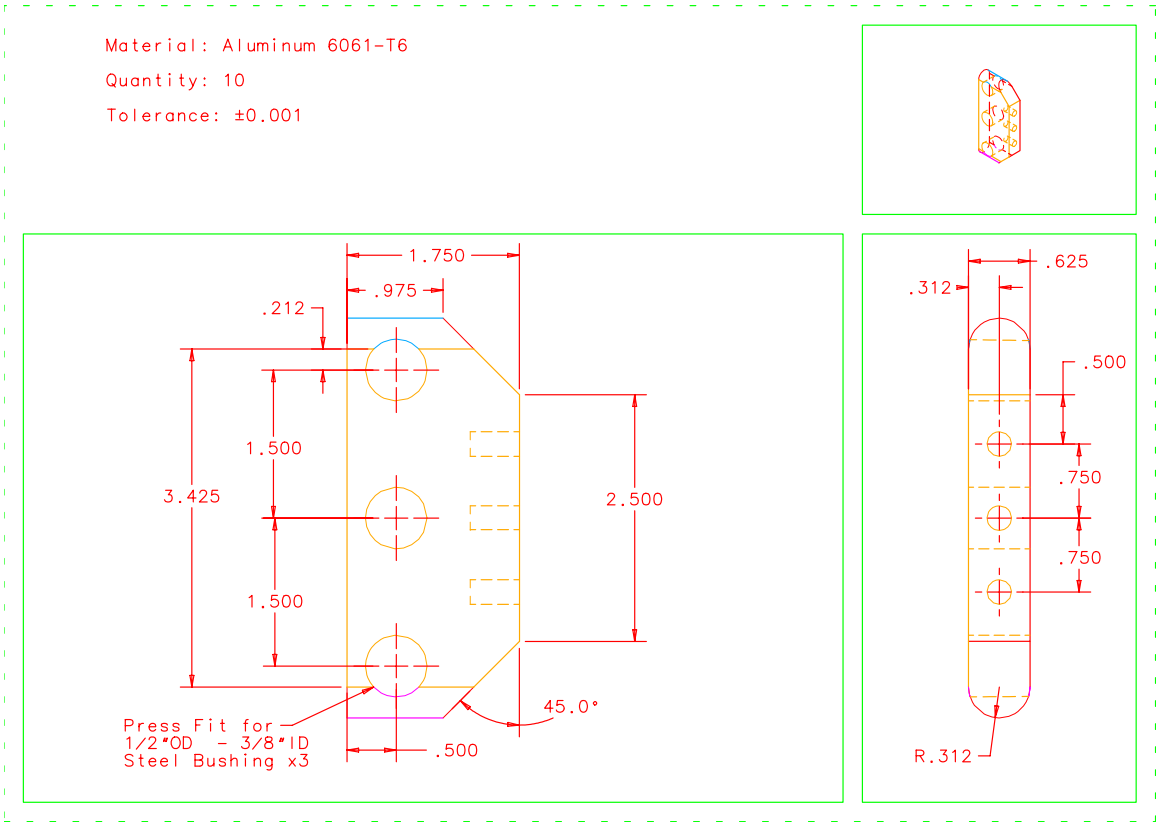

Figure B-11 Arcan$_m$ – Butterfly.

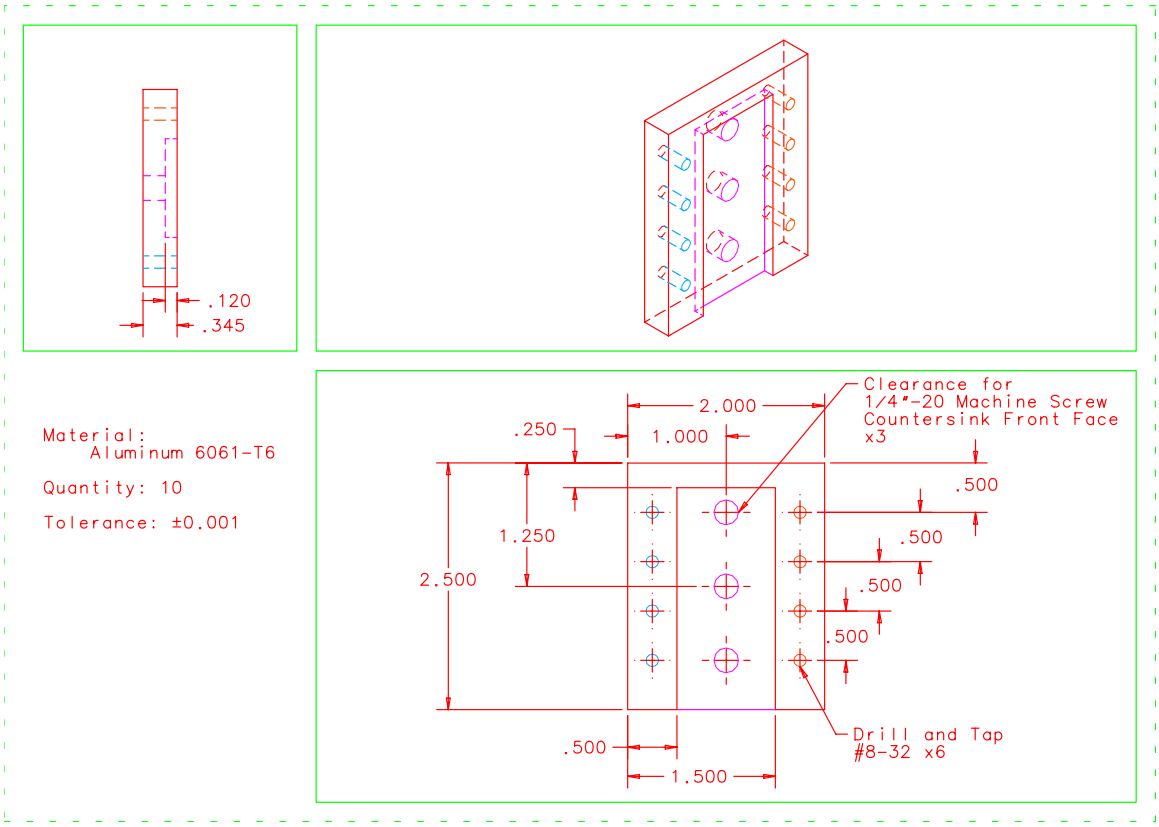

Figure B-12 Arcan$_m$ – Grip Base.

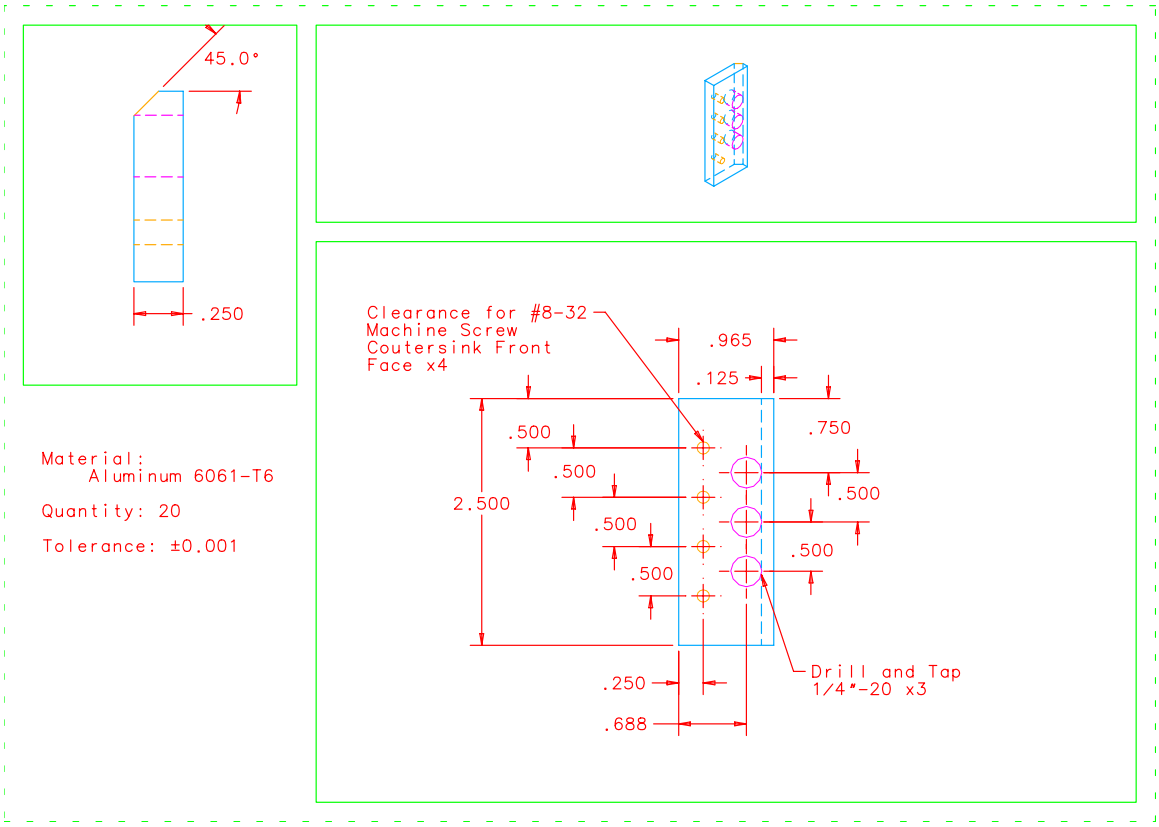

Figure B-13 $Arcan_m$ – Grip.

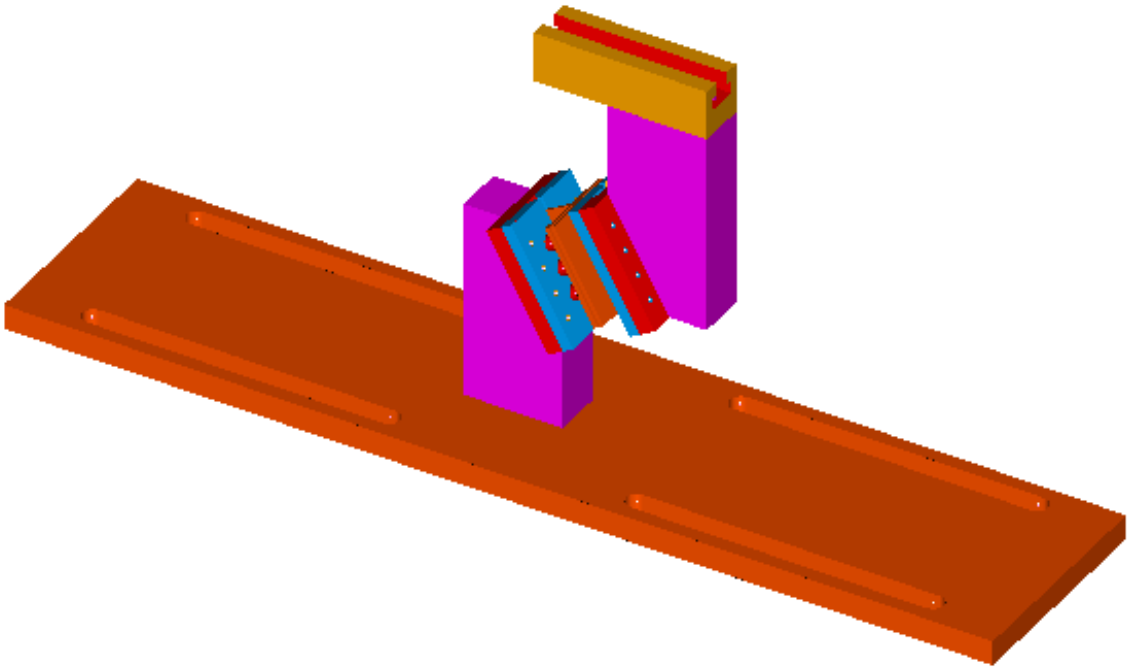

Figure B-14 Complex Loading Fixture – Top Level.

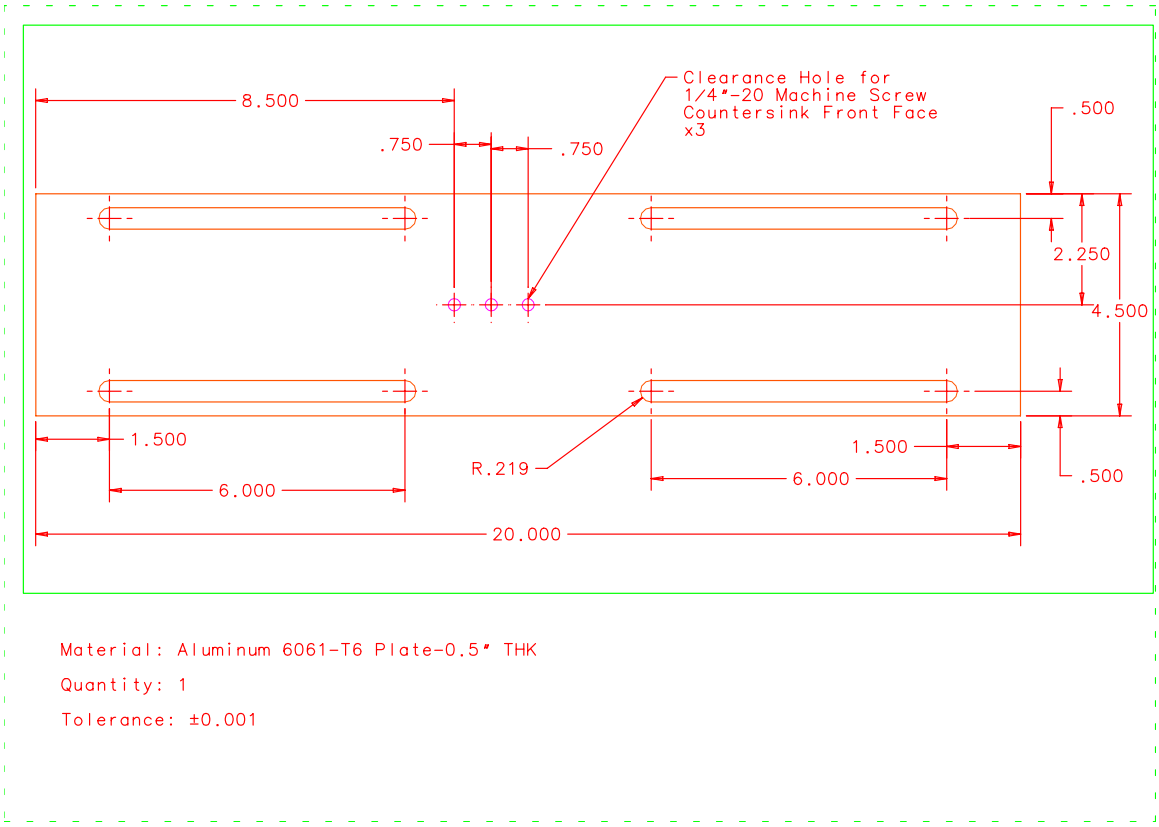

Figure B-15 Complex Loading Fixture – Bottom Plate.

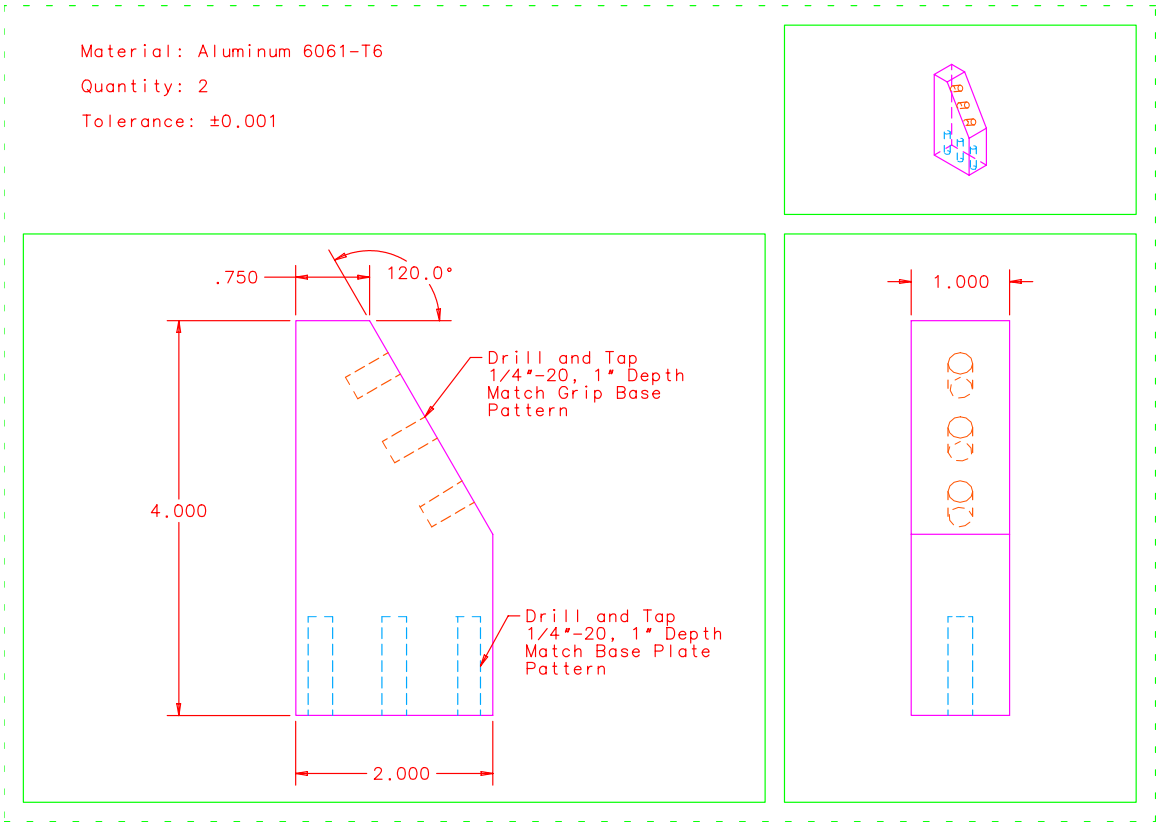

Figure B-16 Complex Loading Fixture – Grip Mount.

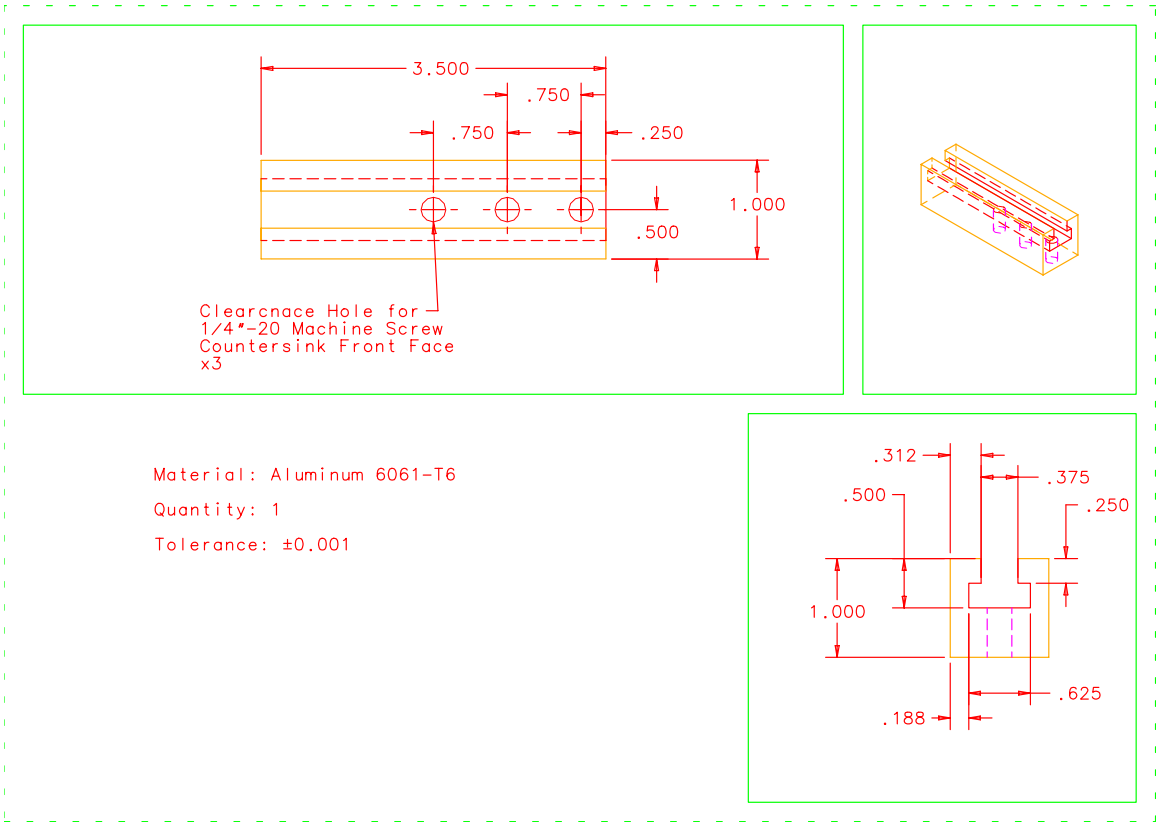

Figure B-17 Complex Loading Fixture – Moment Arm.

Appendix C

Experimental Data

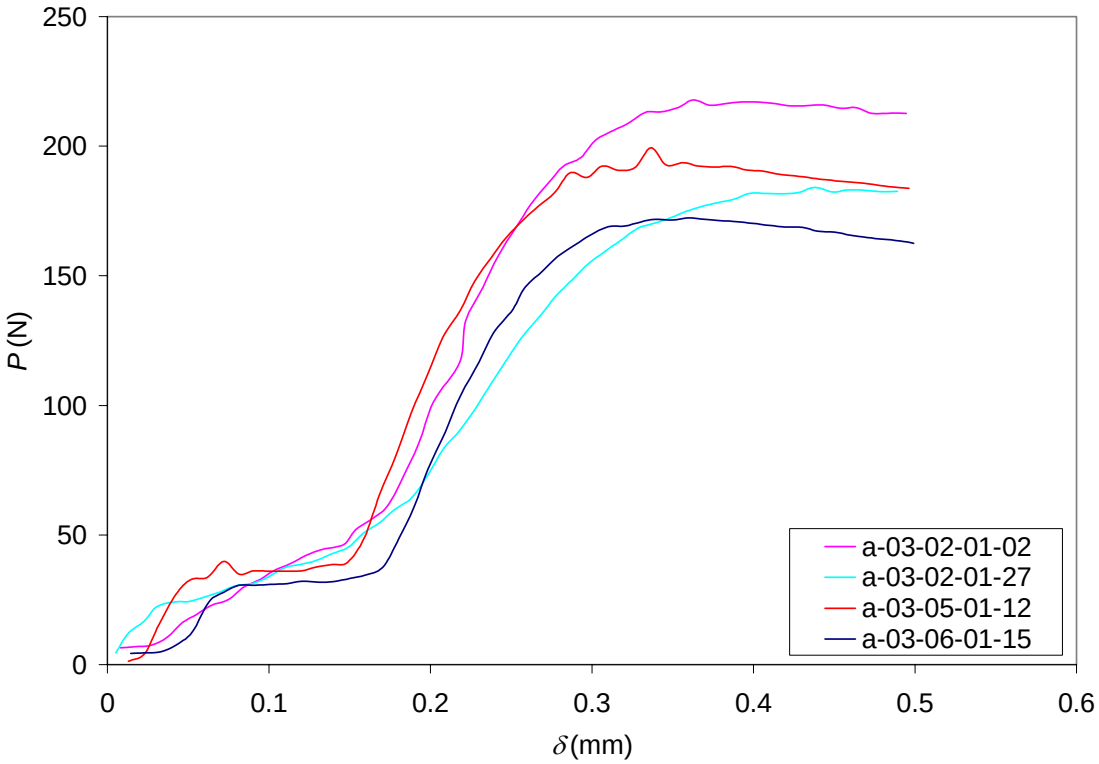

Figure C-1 Arcan Data (θ_{Arcan}=0°, R_d=0.05mm/min, *Temp*≈20°C, and *RH*≈25%).

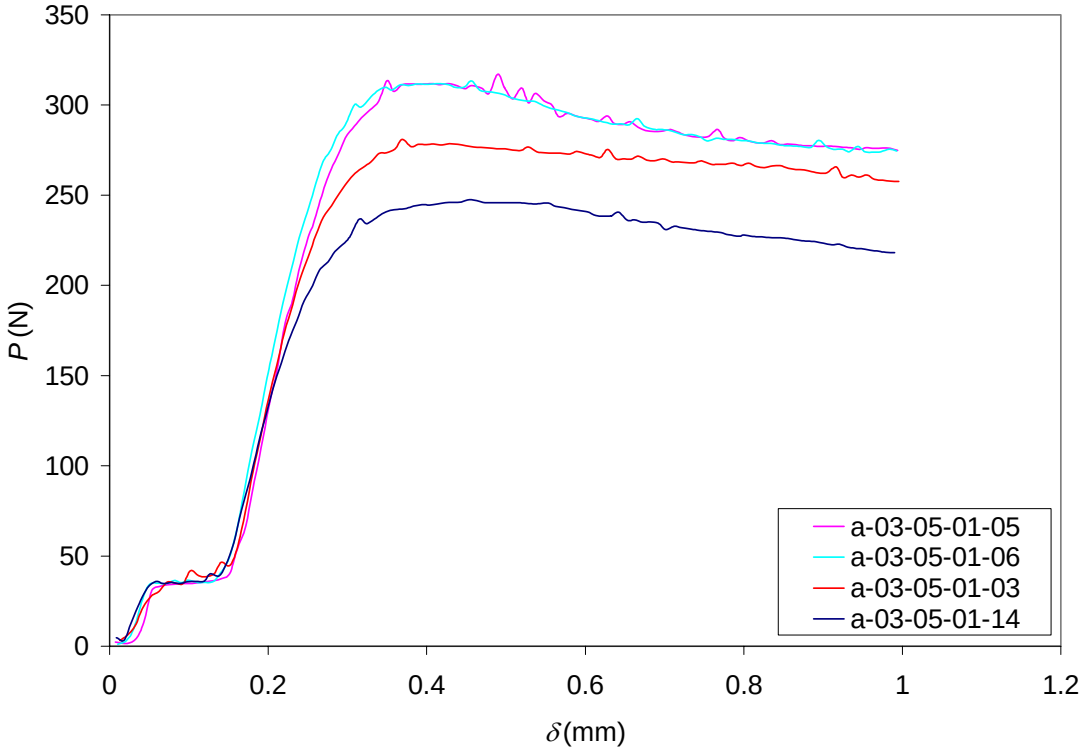

Figure C-2 Arcan Data (θ_{Arcan}=0°, R_d=0.5mm/min, *Temp*≈20°C, and *RH*≈25%).

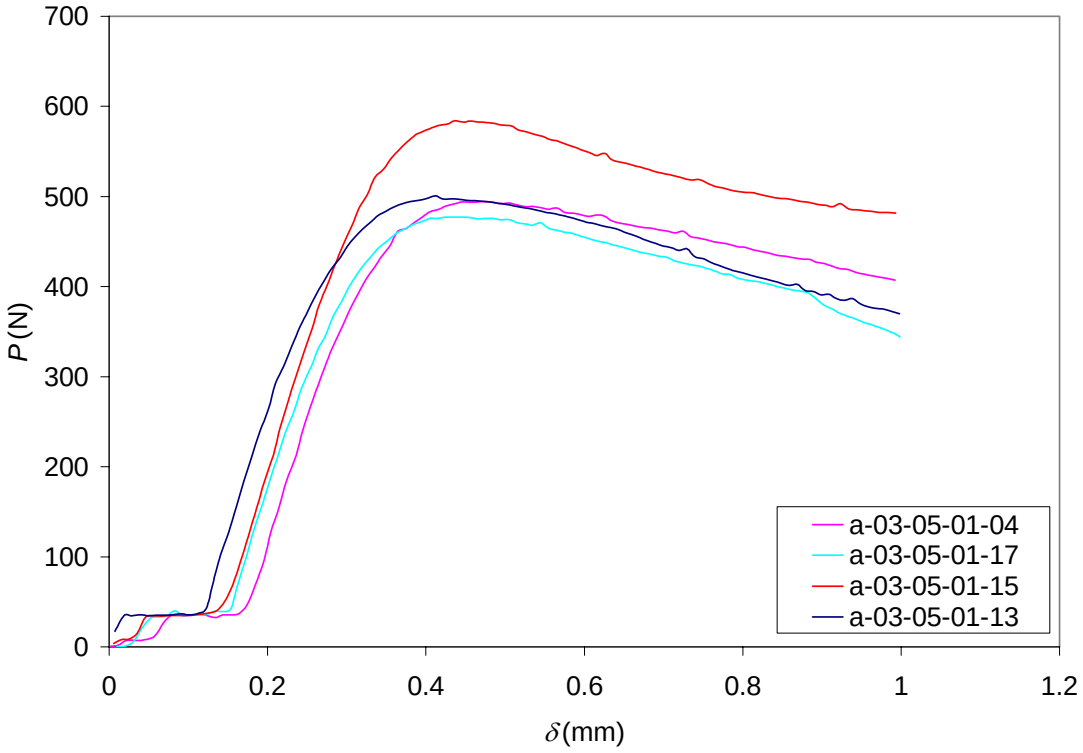

Figure C-3 Arcan Data (θ_{Arcan}=0°, R_d=5.0mm/min, *Temp*≈20°C, and *RH*≈25%).

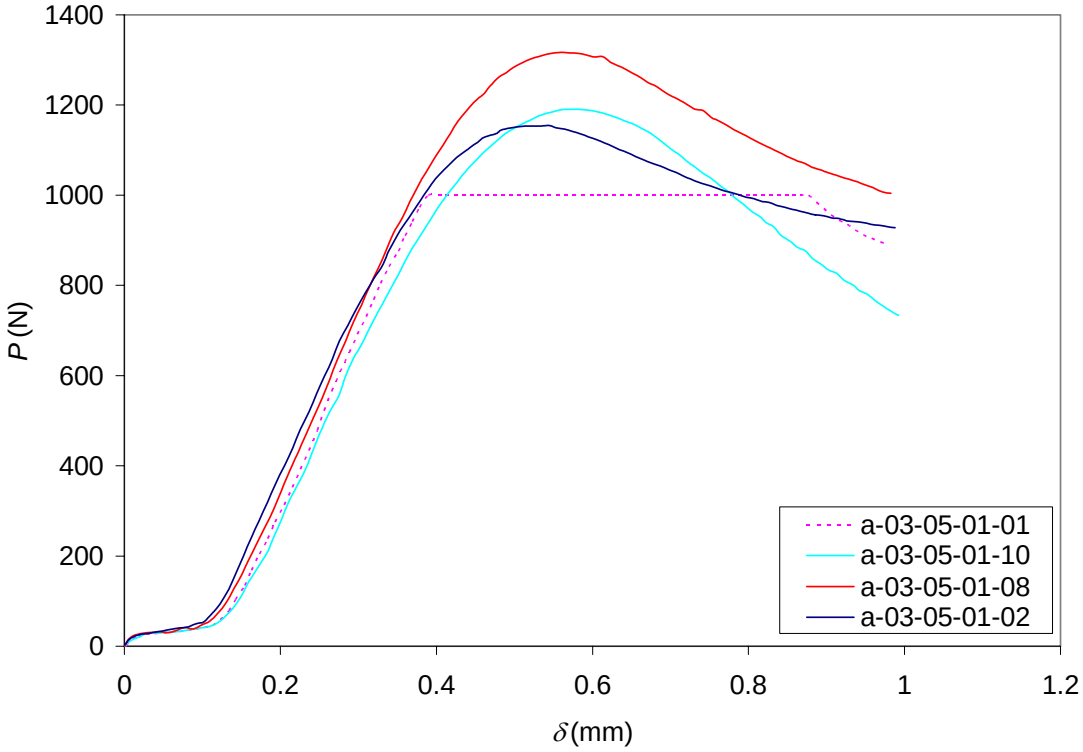

Figure C-4 Arcan Data (θ_{Arcan}=0°, R_d=50mm/min, *Temp*≈20°C, and *RH*≈25%).

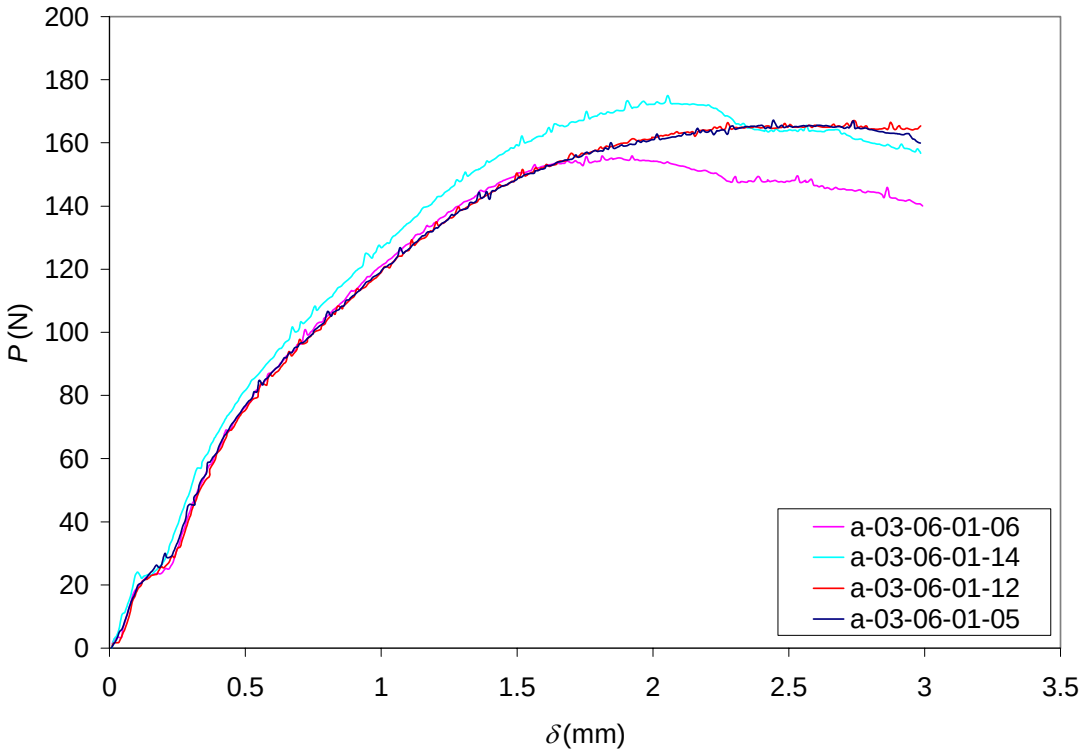

Figure C-5 Arcan Data (θ_{Arcan}=30°, R_d=0.05mm/min, *Temp*≈20°C, and *RH*≈25%).

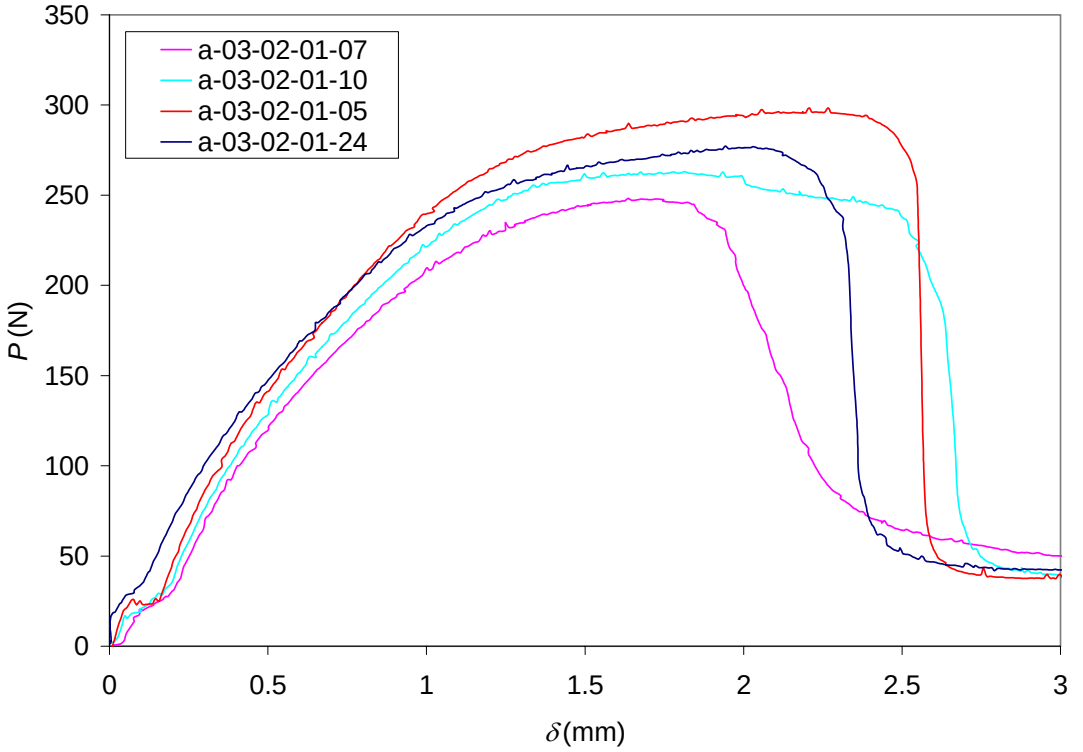

Figure C-6 Arcan Data (θ_{Arcan}=30°, R_d=0.5mm/min, *Temp*≈20°C, and *RH*≈25%).

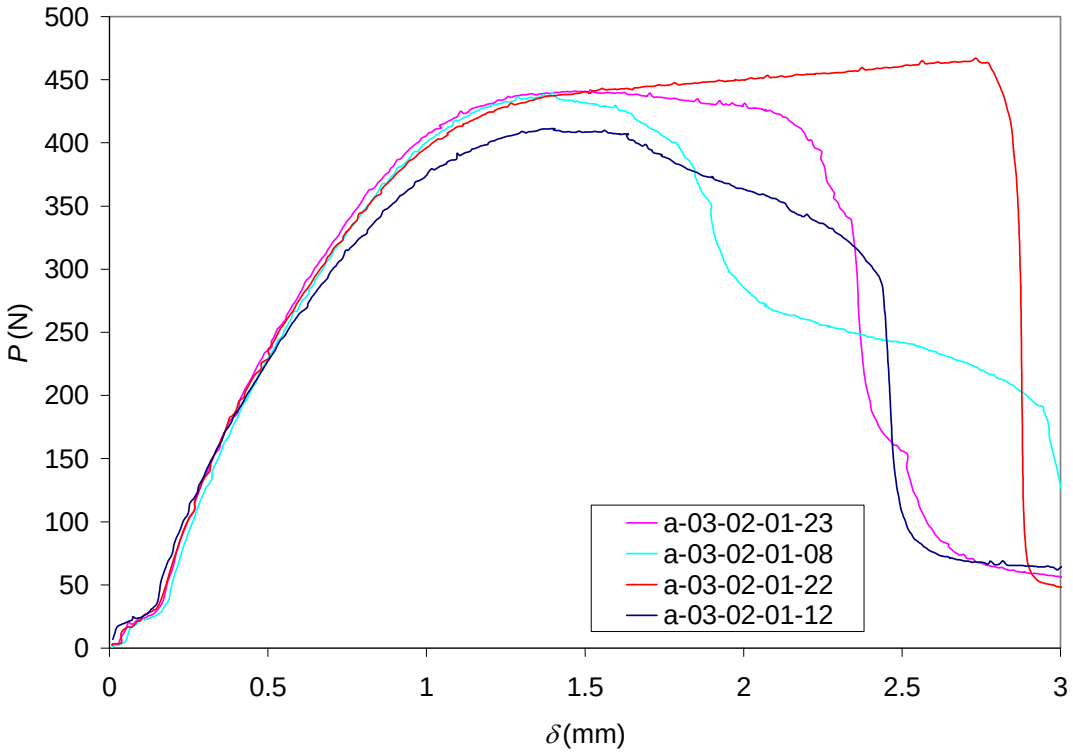

Figure C-7 Arcan Data (θ_{Arcan}=30°, R_d=5.0mm/min, *Temp*≈20°C, and *RH*≈25%).

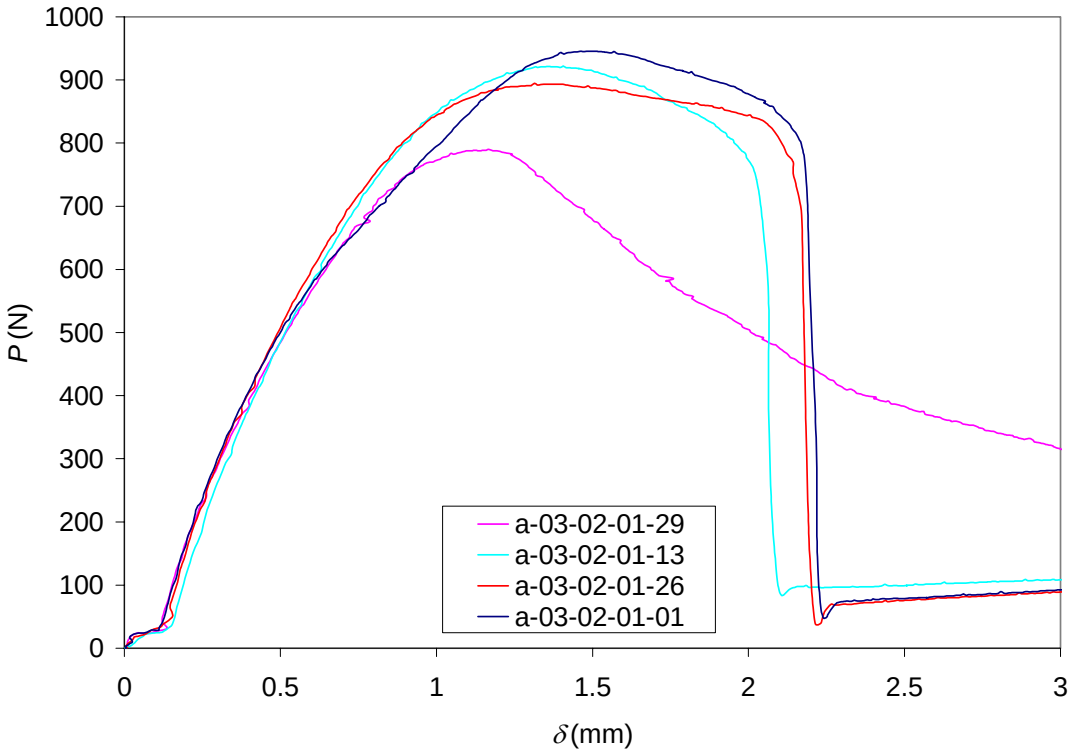

Figure C-8 Arcan Data (θ_{Arcan}=30°, R_d=50mm/min, *Temp*≈20°C, and *RH*≈25%).

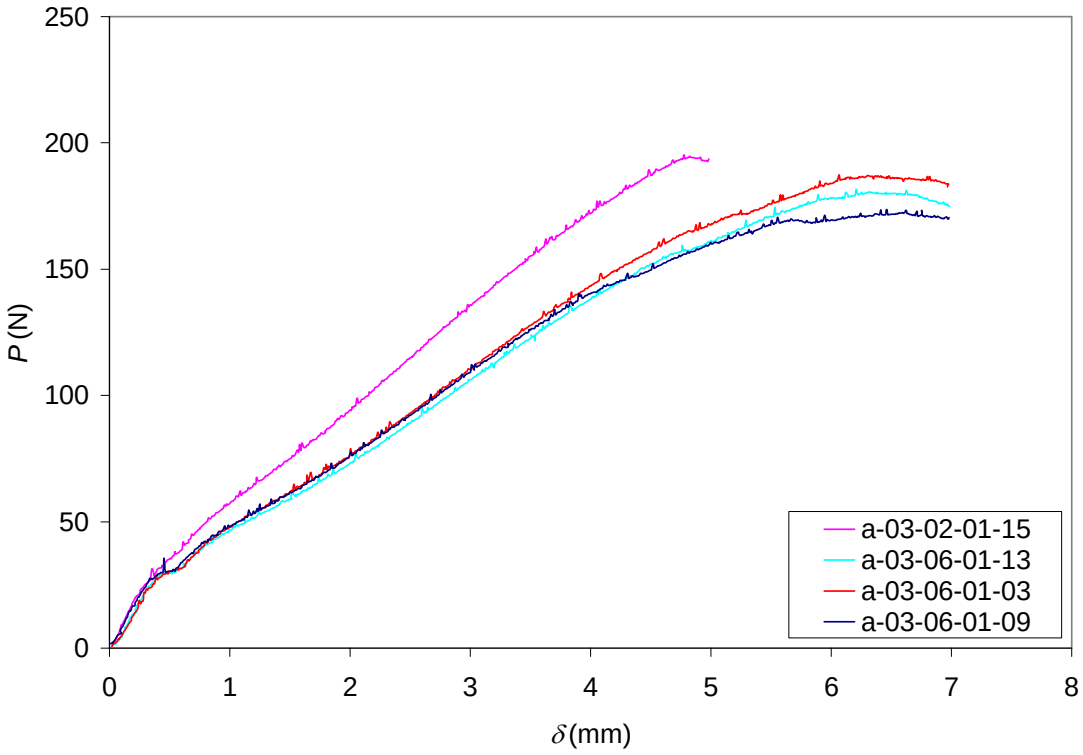

Figure C-9 Arcan Data (θ_{Arcan}=60°, R_d=0.05mm/min, *Temp*≈20°C, and *RH*≈25%).

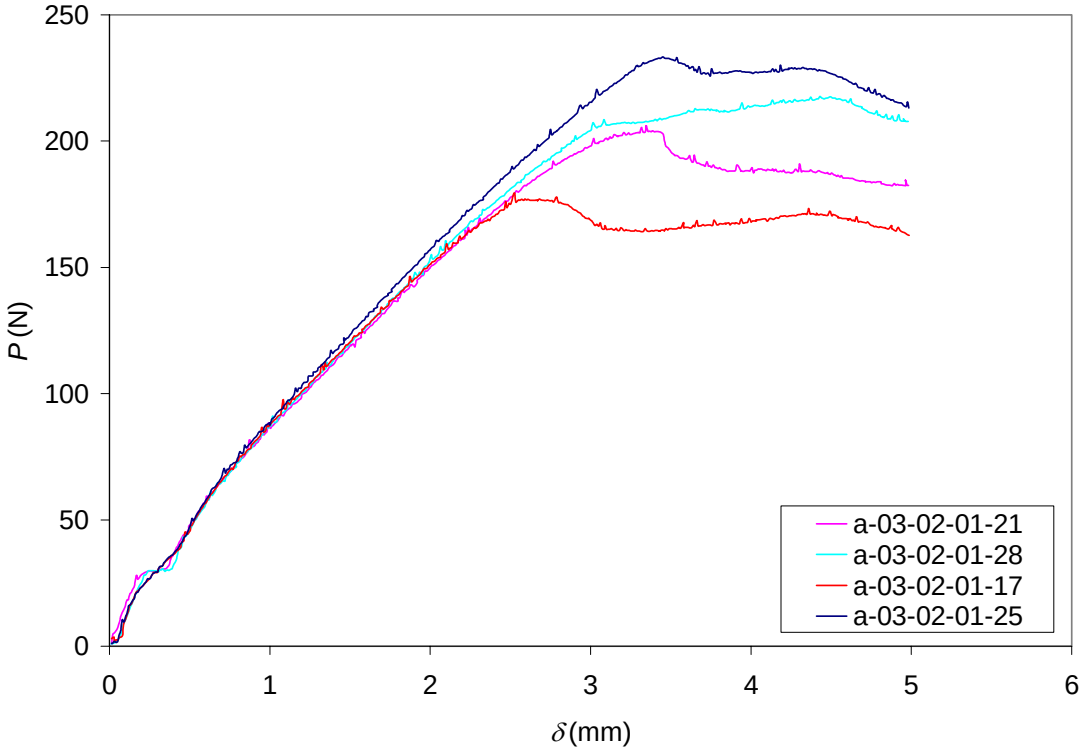

Figure C-10 Arcan Data (θ_{Arcan}=60°, R_d=0.5mm/min, *Temp*≈20°C, and *RH*≈25%).

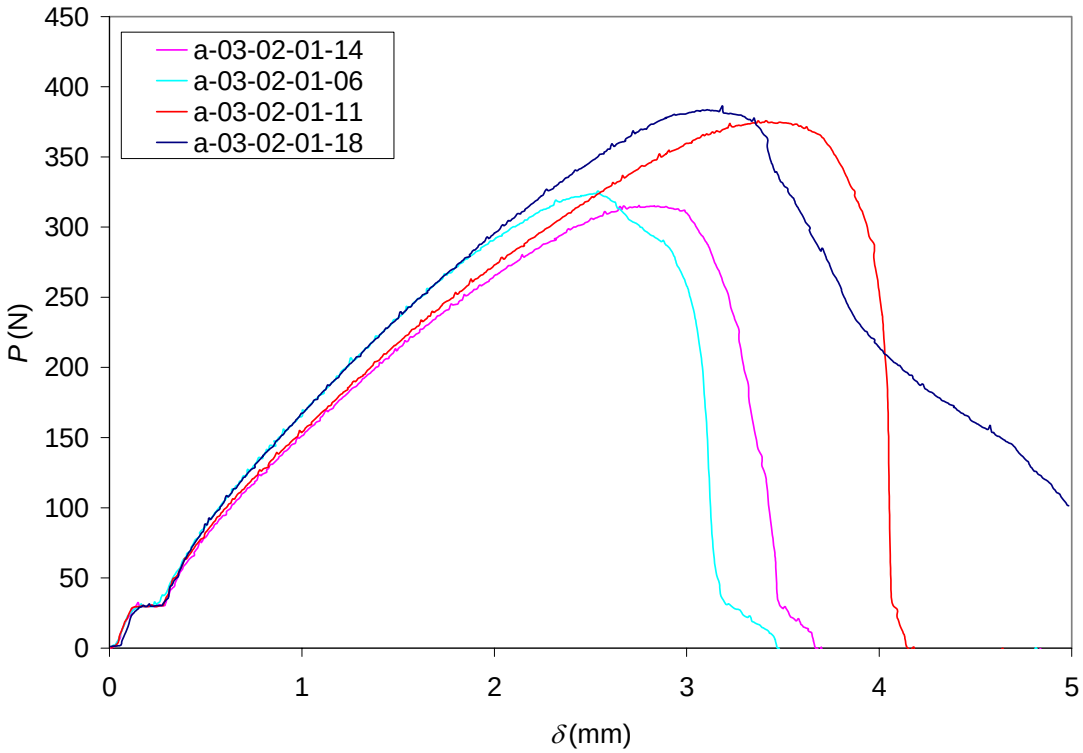

Figure C-11 Arcan Data (θ_{Arcan}=60°, R_d=5.0mm/min, *Temp*≈20°C, and *RH*≈25%).

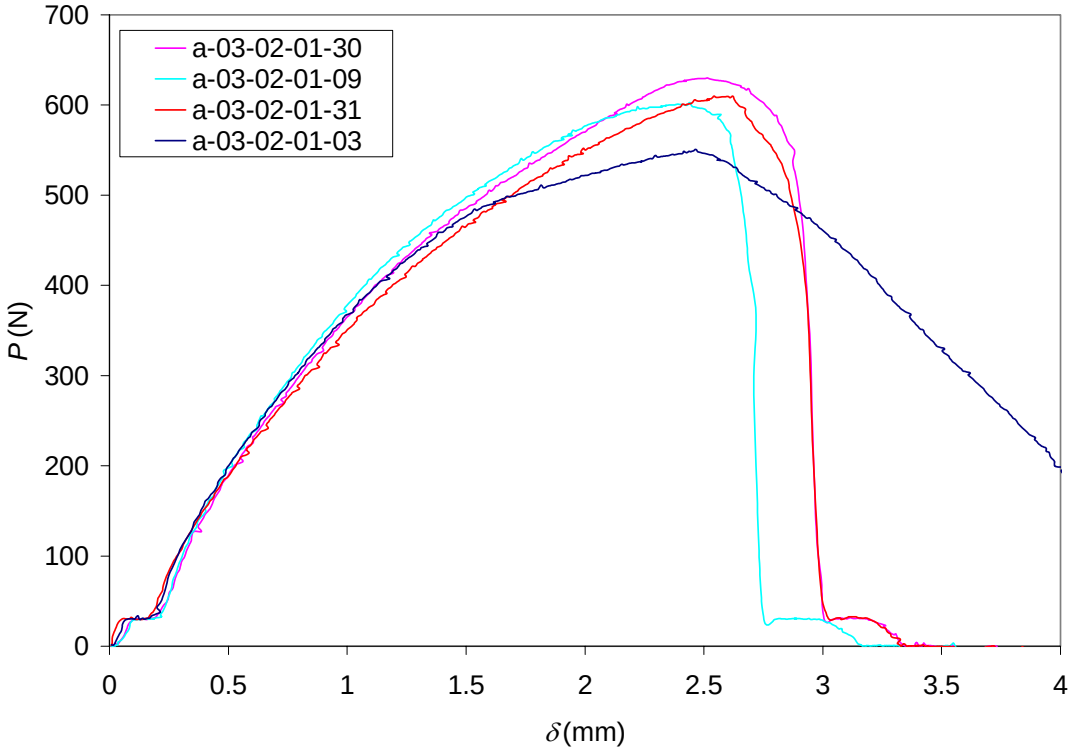

Figure C-12 Arcan Data (θ_{Arcan}=60°, R_d=50mm/min, *Temp*≈20°C, and *RH*≈25%).

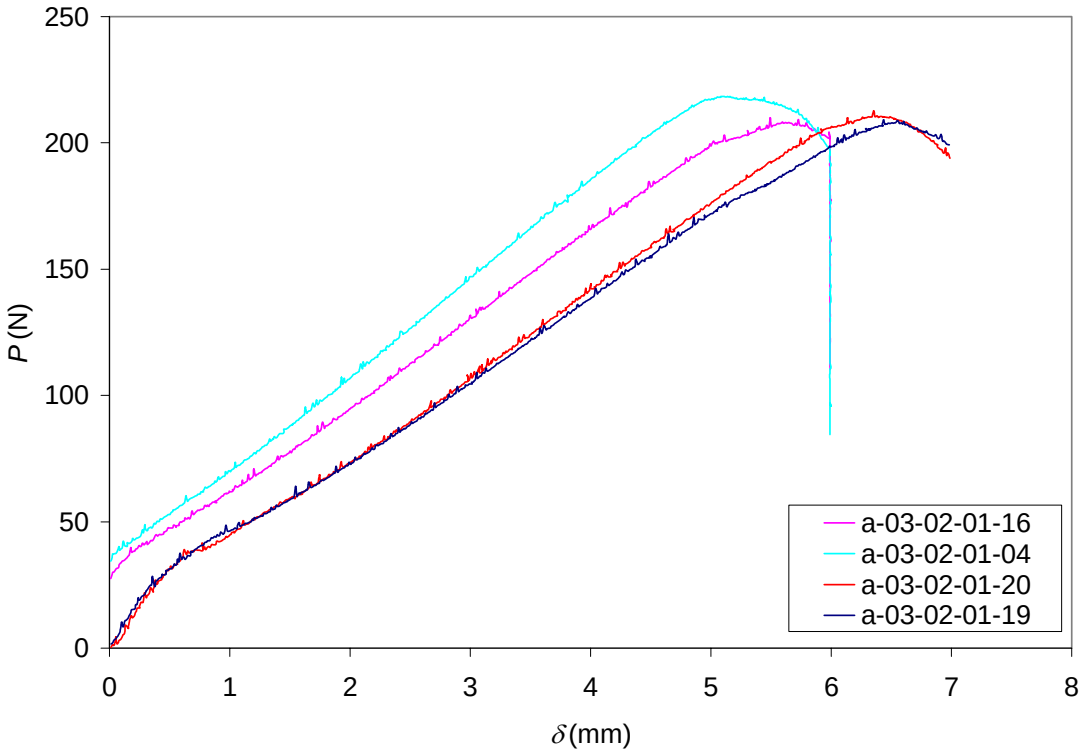

Figure C-13 Arcan Data (θ_{Arcan}=90°, R_d=0.05mm/min, *Temp*≈20°C, and *RH*≈25%). (Initial displacement was not zeroed on the first 2 specimens.)

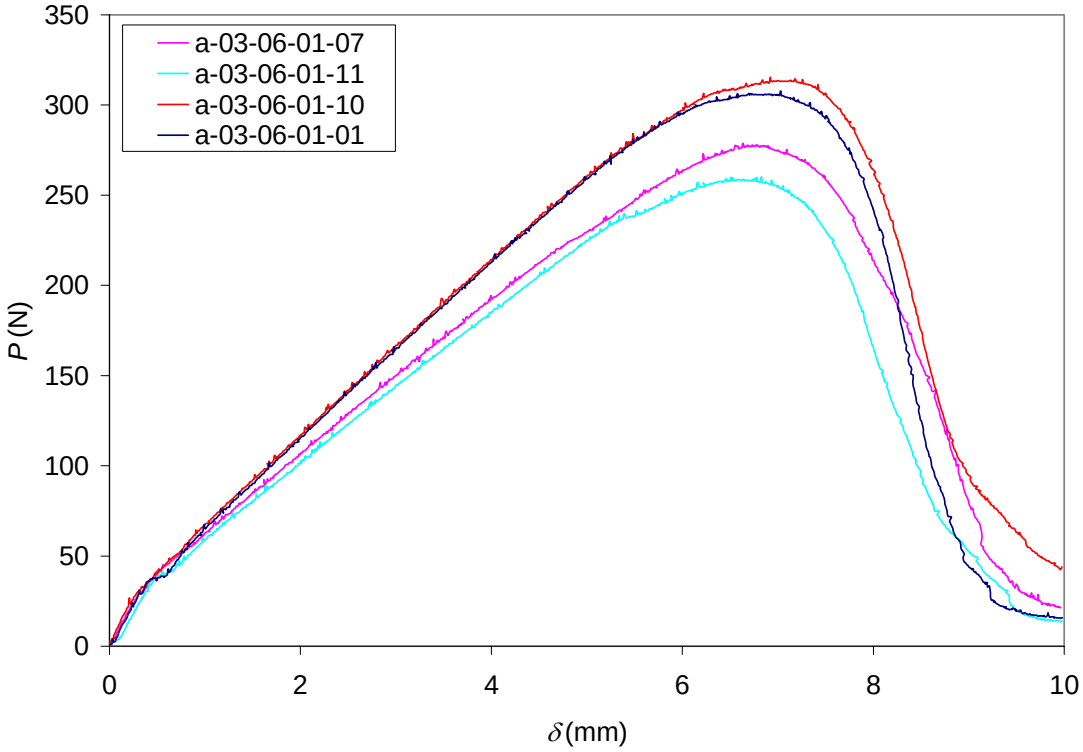

Figure C-14 Arcan Data (θ_{Arcan}=90°, R_d=0.5mm/min, *Temp*≈20°C, and *RH*≈25%).

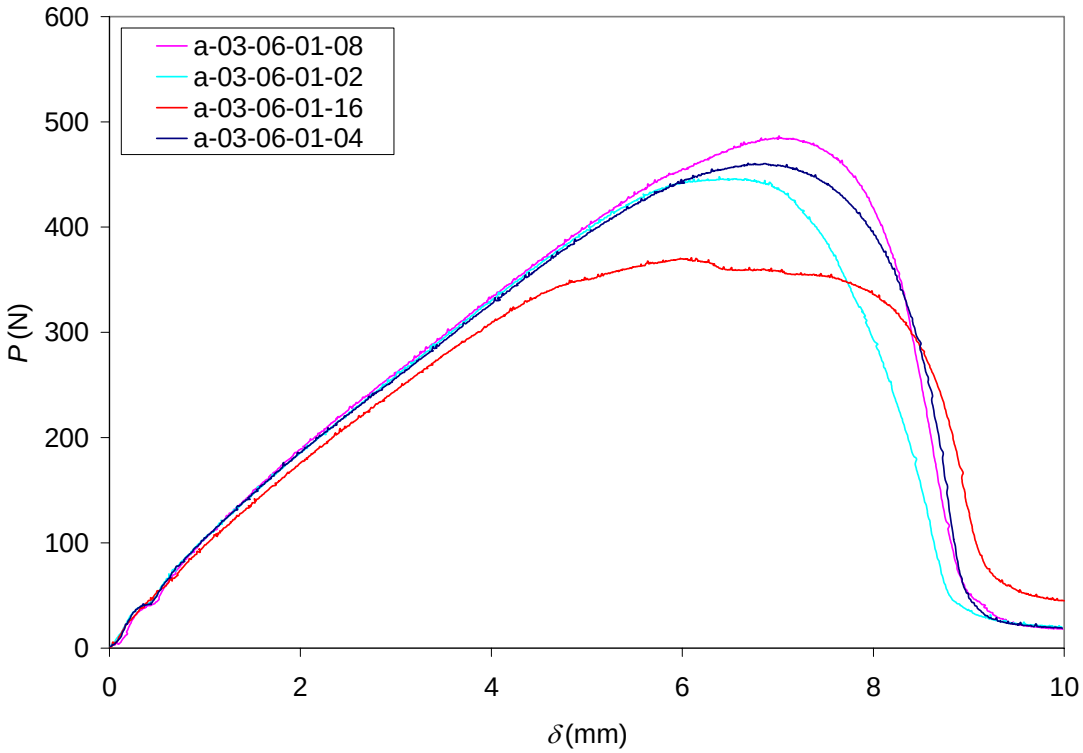

Figure C-15 Arcan Data (θ_{Arcan}=90°, R_d=5.0mm/min, *Temp*≈20°C, and *RH*≈25%).

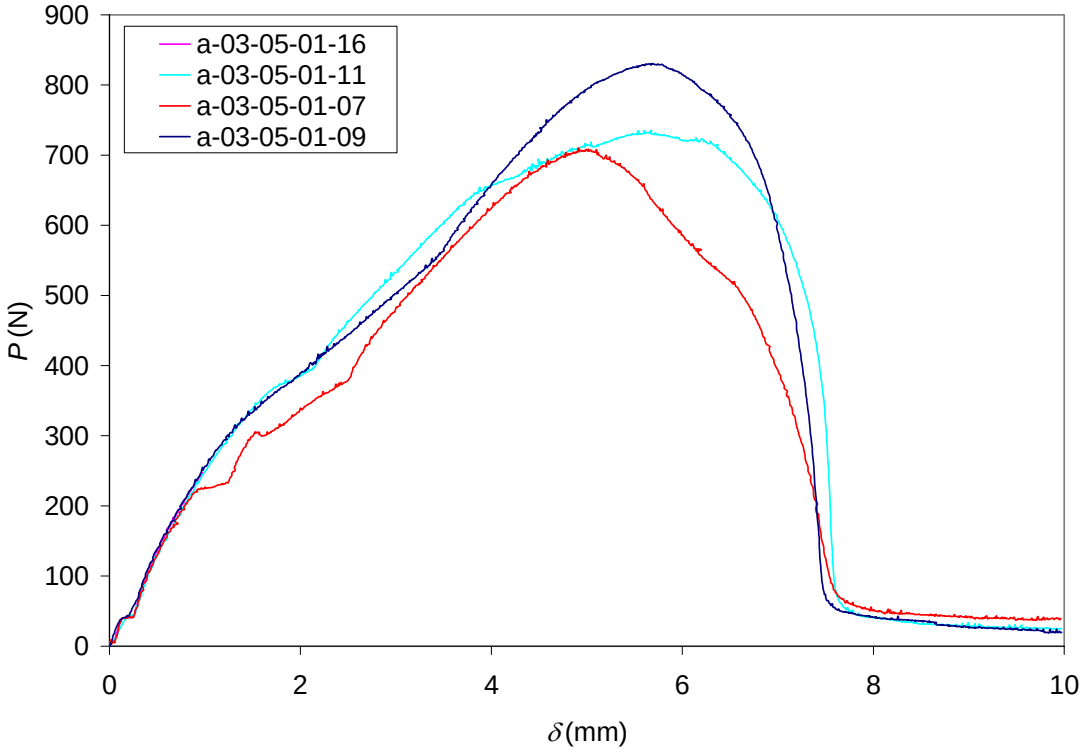

Figure C-16 Arcan Data (θ_{Arcan}=90°, R_d=50mm/min, *Temp*≈20°C, and *RH*≈25%).

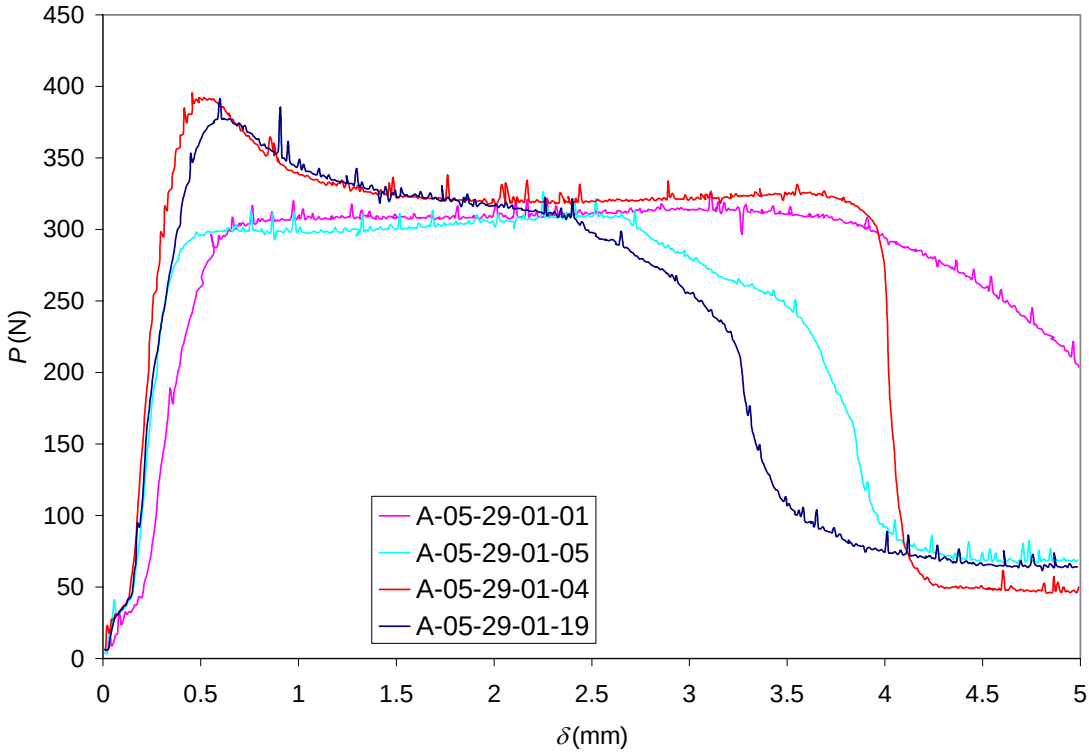

Figure C-17 Arcan Data (w_a=12.7mm, R_d=5.0mm/min, *Temp*≈20°C, and *RH*≈25%). (10kN load cell used by mistake resulting in higher load noise.)

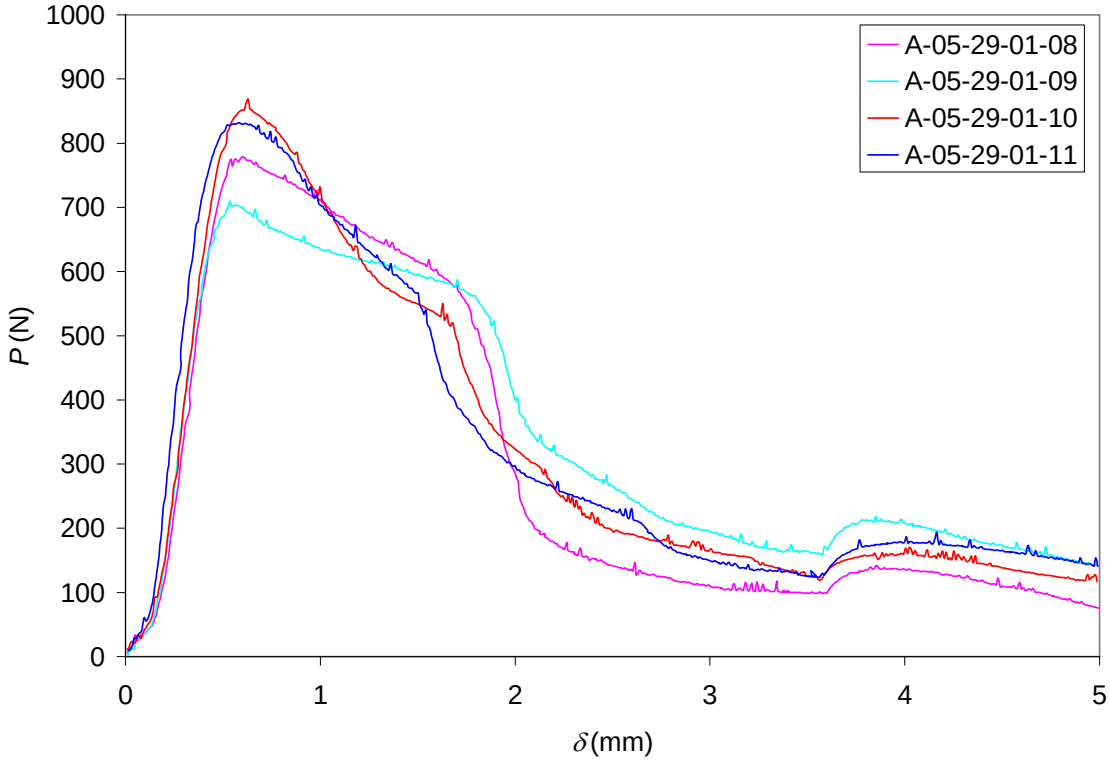

Figure C-18 Arcan Data (w_a=25.4mm, R_d=5.0mm/min, *Temp*≈20°C, and *RH*≈25%).

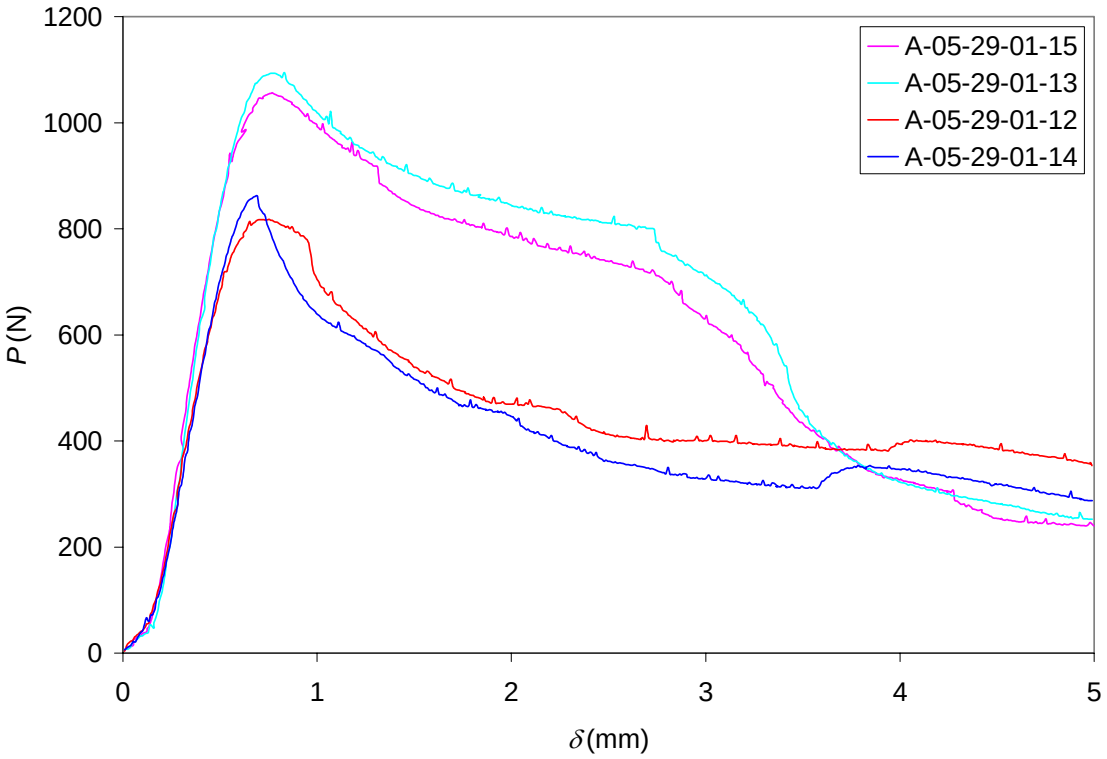

Figure C-19 Arcan Data (w_a=38.1mm, R_d=5.0mm/min, *Temp*≈20°C, and *RH*≈25%).

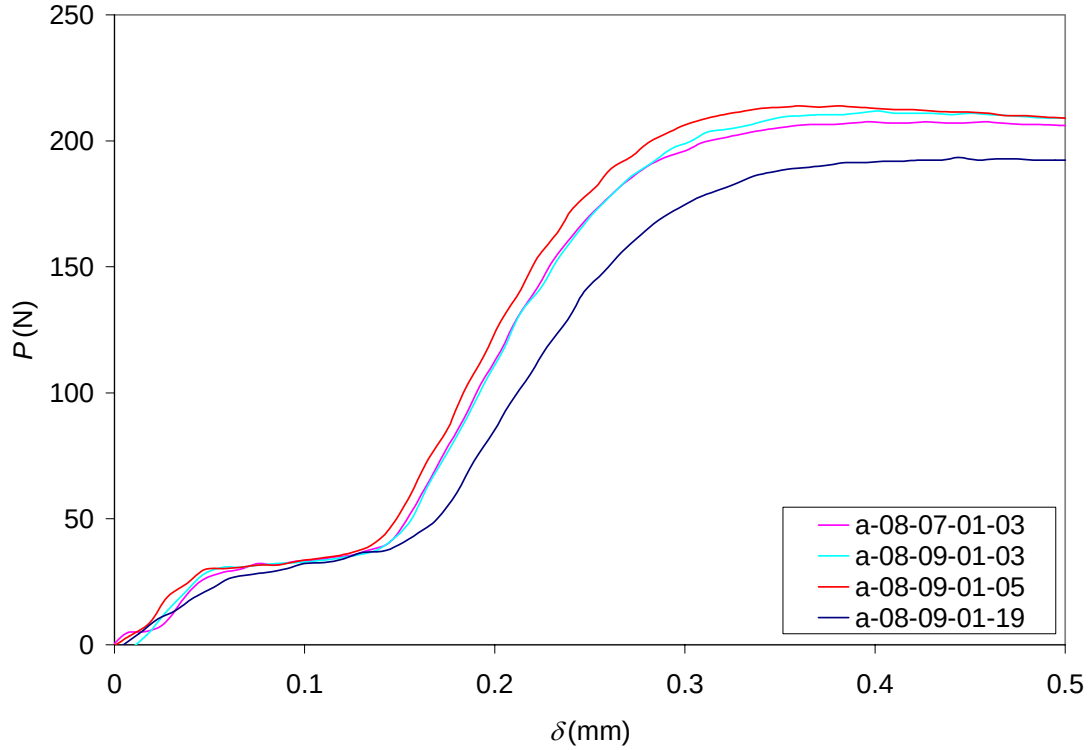

Figure C-20 Arcan Data (θ_{Arcan}=0°, R_d=0.5mm/min, *Temp*≈20°C, and *RH*≈25%).

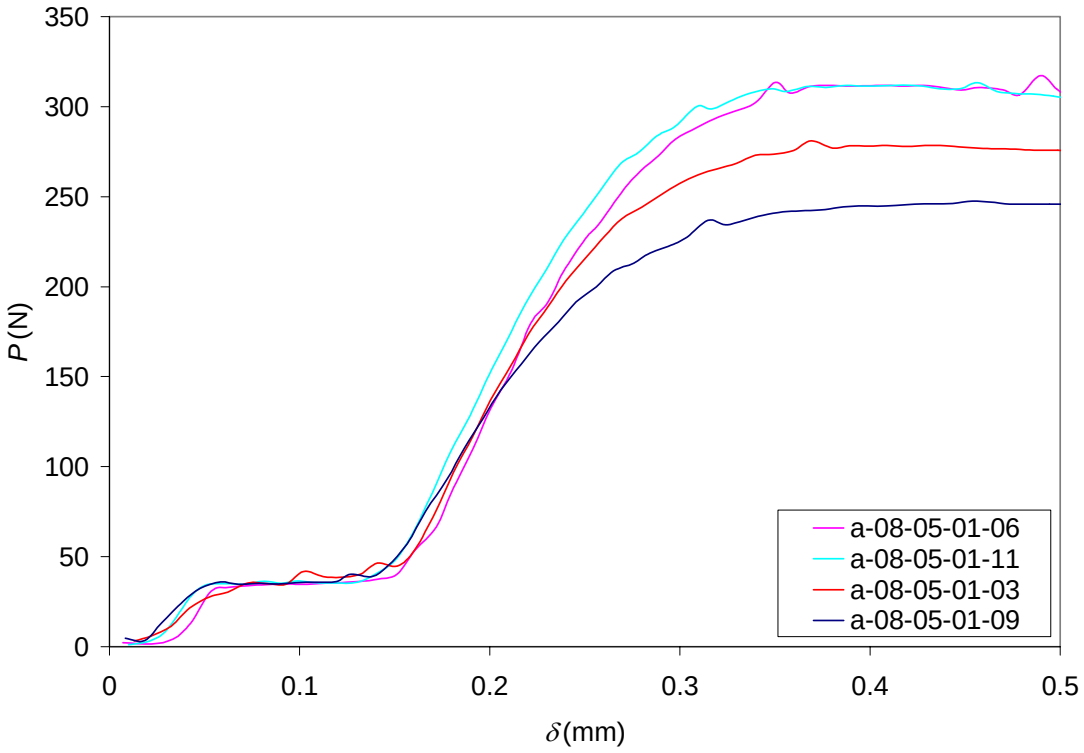

Figure C-21 Arcan Data (θ_{Arcan}=0°, R_d=5.0mm/min, *Temp*≈20°C, and *RH*≈25%).

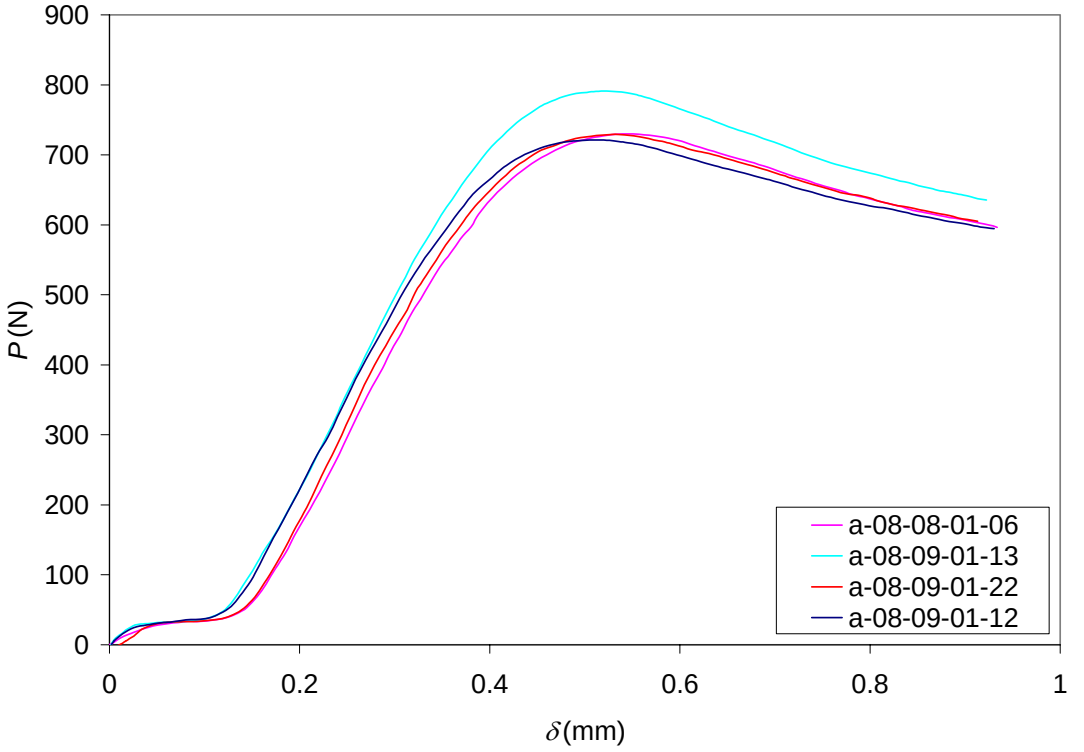

Figure C-22 Arcan Data (θ_{Arcan}=0°, R_d=50mm/min, *Temp*≈20°C, and *RH*≈25%).

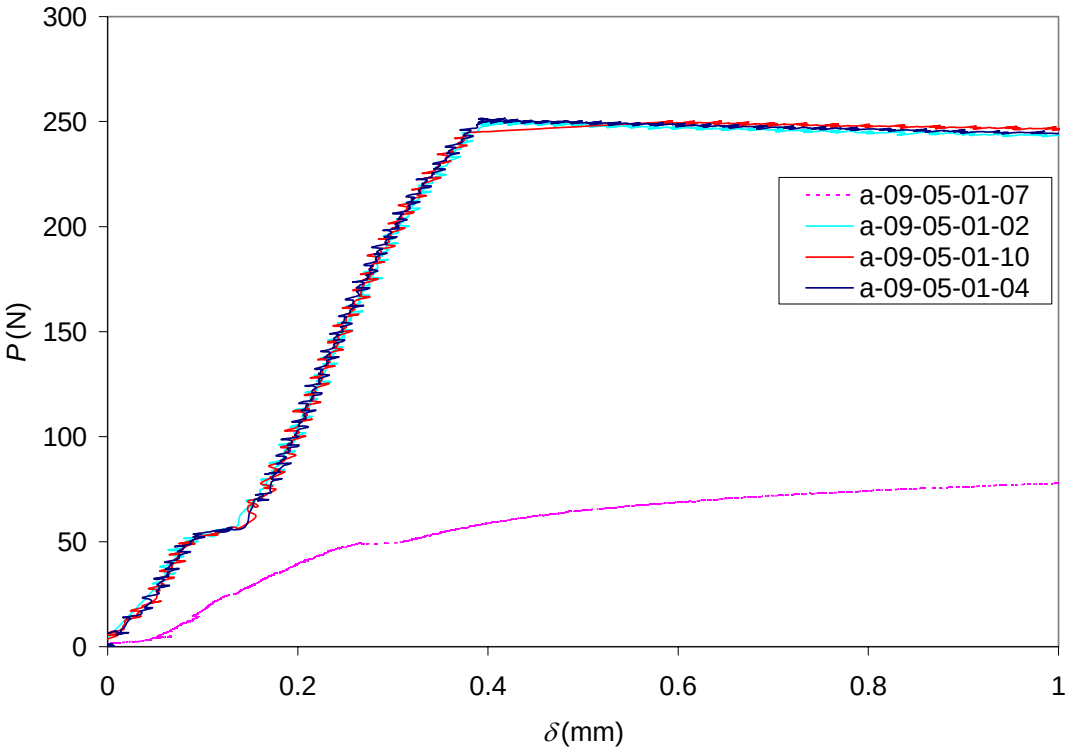

Figure C-23 Arcan Data (θ_{Arcan}=0°, R_l=10N/sec, *Temp*≈20°C, and *RH*≈25%). (Tests run at the end of the LVDT stroke resulting in displacement noise.)

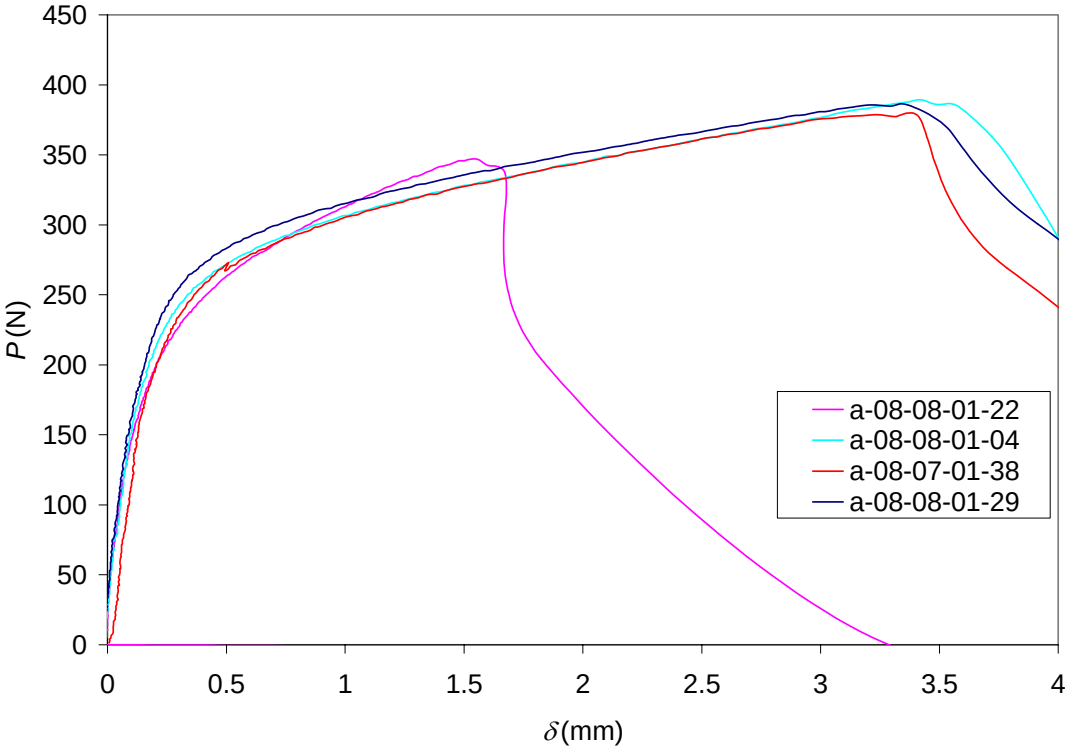

Figure C-24 Arcan Data (θ_{Arcan}=0°, R_l=15N/sec, *Temp*≈20°C, and *RH*≈25%).

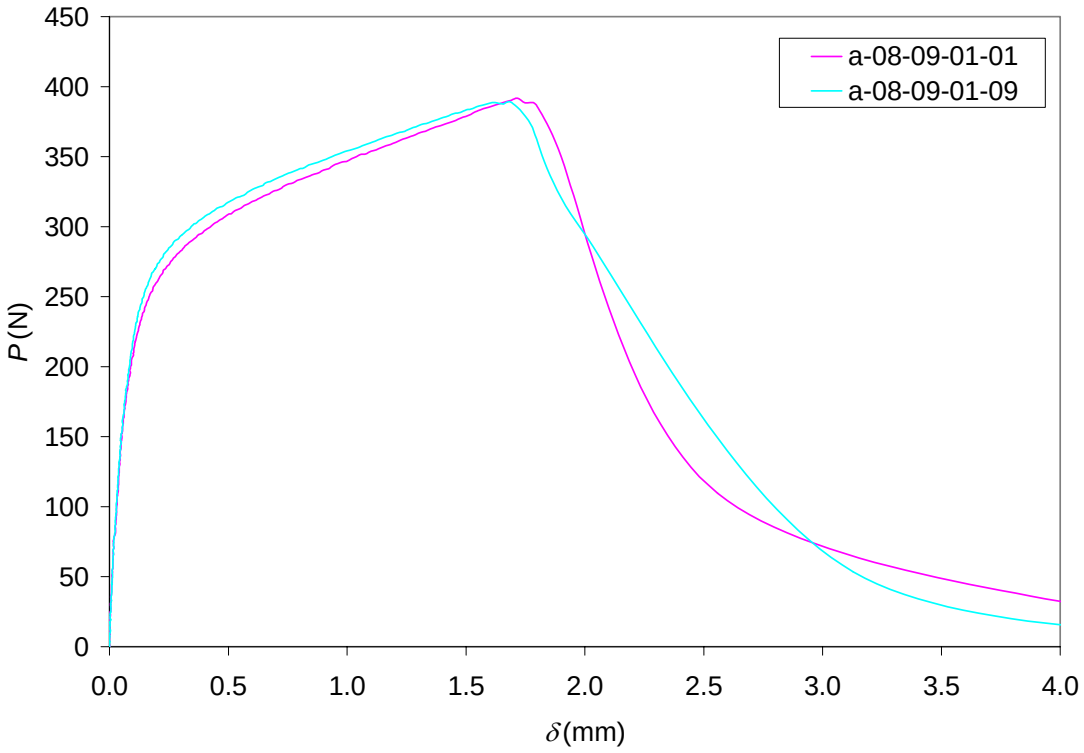

Figure C-25 Arcan Data (θ_{Arcan}=0°, R_l=200N/sec, *Temp*≈20°C, and *RH*≈25%).

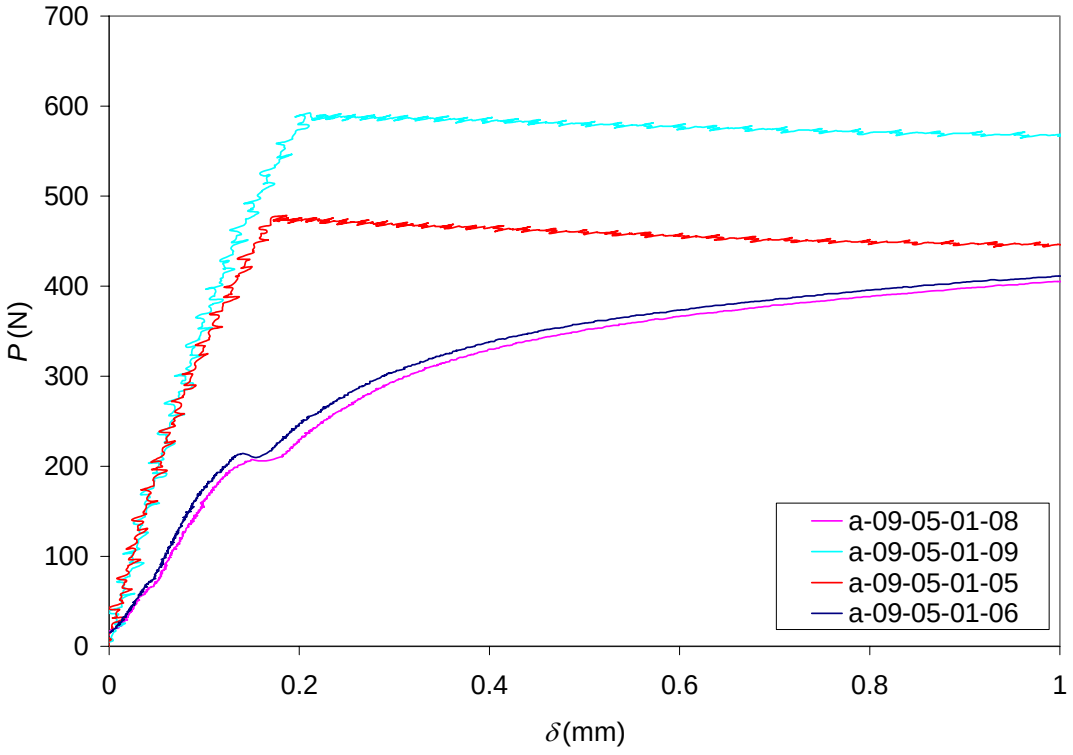

Figure C-26 Arcan Data (θ_{Arcan}=0°, R_l=2000N/sec, *Temp*≈20°C, and *RH*≈25%).

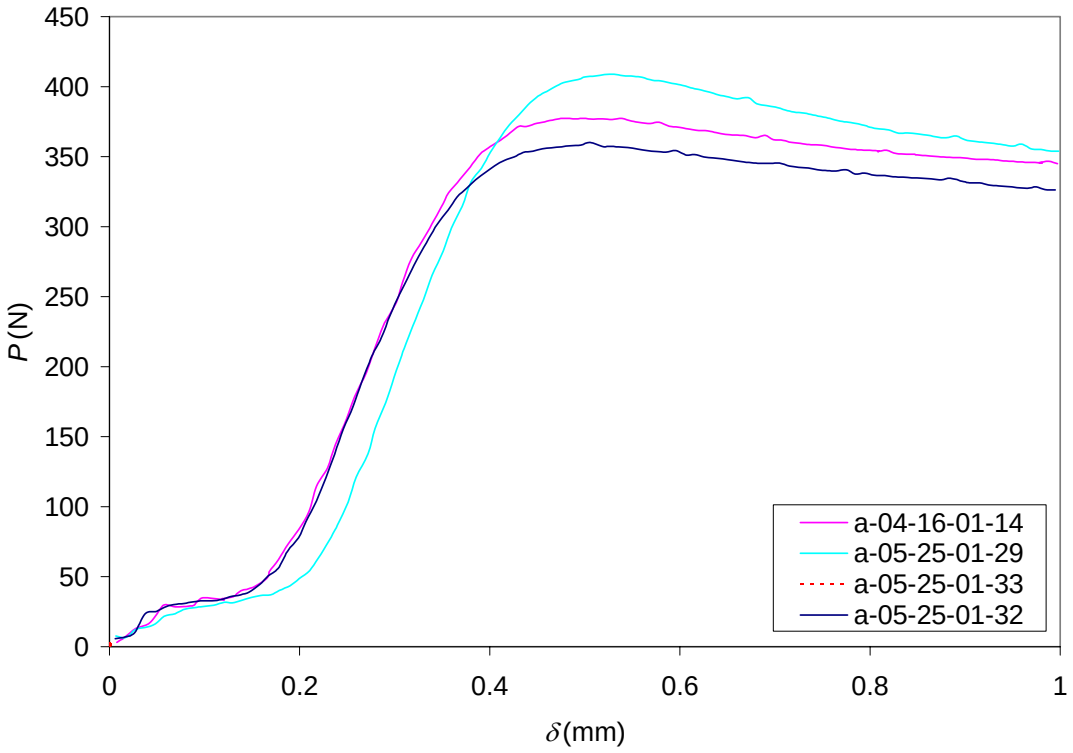

Figure C-27 Arcan Data (θ_{Arcan}=0°, R_d=5.0mm/min, *Temp*≈20°C, and *RH*≈25%).

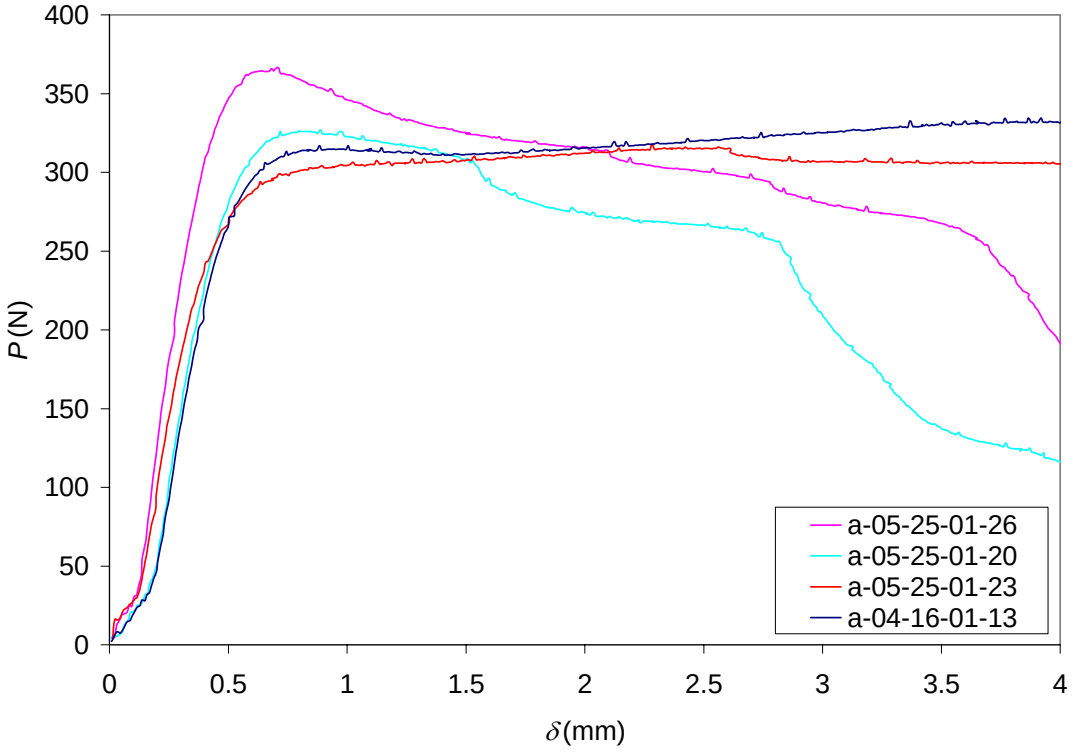

Figure C-28 Arcan Data (θ_{Arcan}=15°, R_d=5.0mm/min, *Temp*≈20°C, and *RH*≈25%).

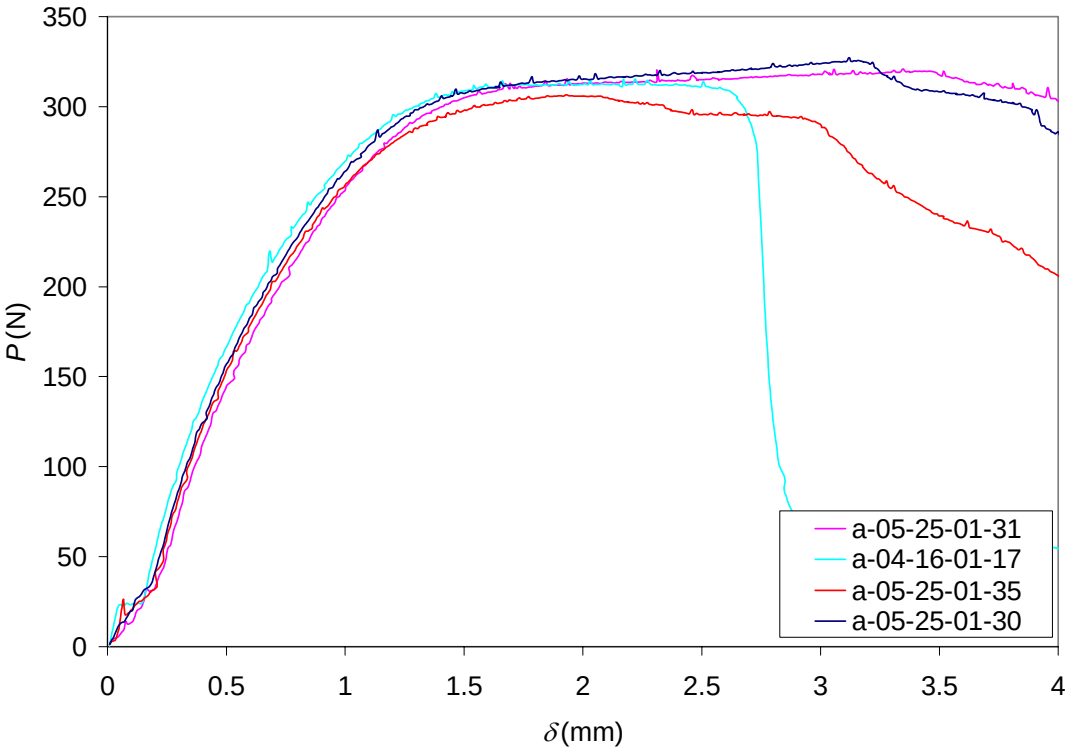

Figure C-29 Arcan Data (θ_{Arcan}=30°, R_d=5.0mm/min, *Temp*≈20°C, and *RH*≈25%).

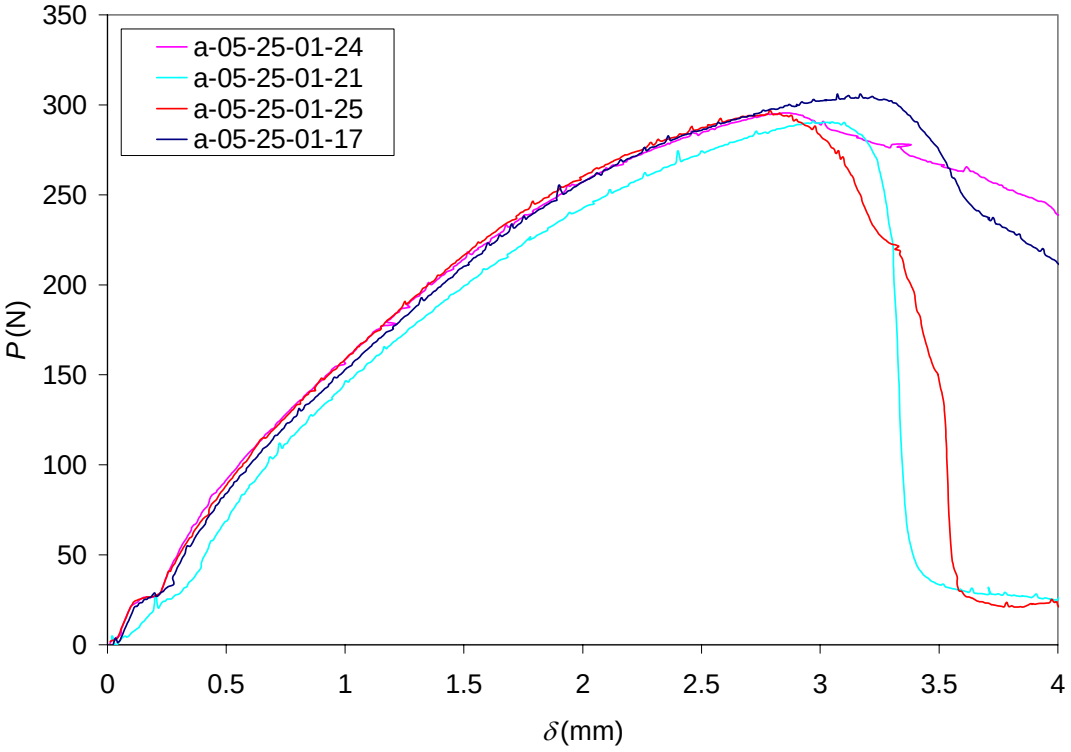

Figure C-30 Arcan Data (θ_{Arcan}=45°, R_d=5.0mm/min, *Temp*≈20°C, and *RH*≈25%).

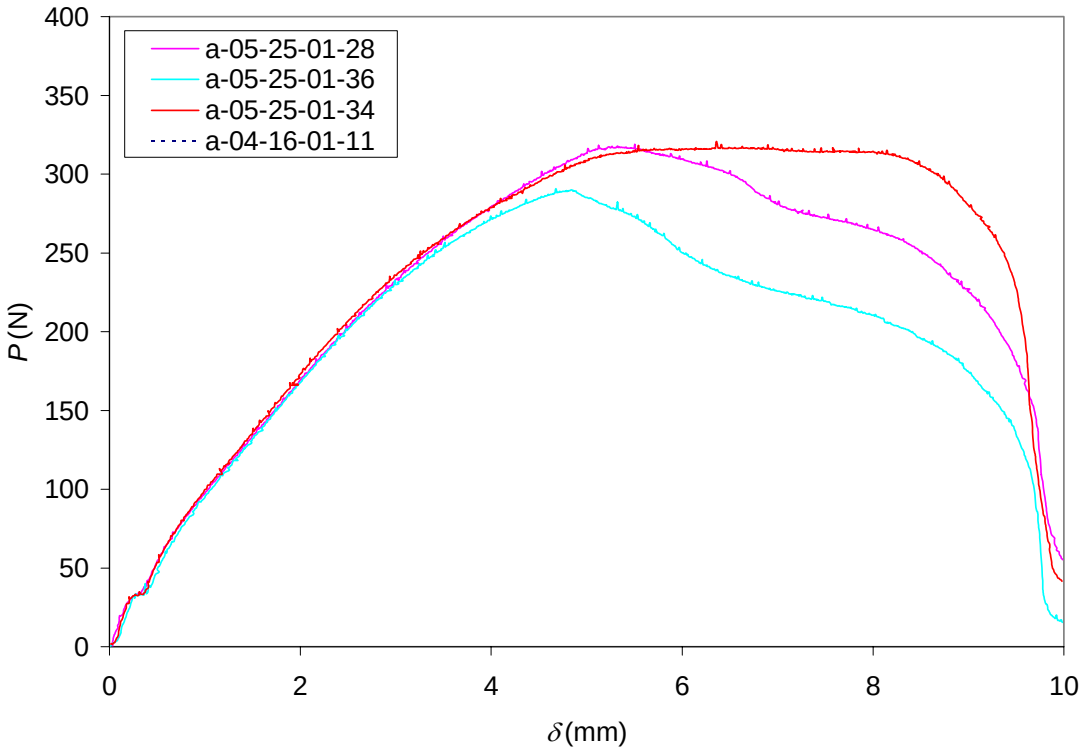

Figure C-31 Arcan Data (θ_{Arcan}=60°, R_d=5.0mm/min, *Temp*≈20°C, and *RH*≈25%).

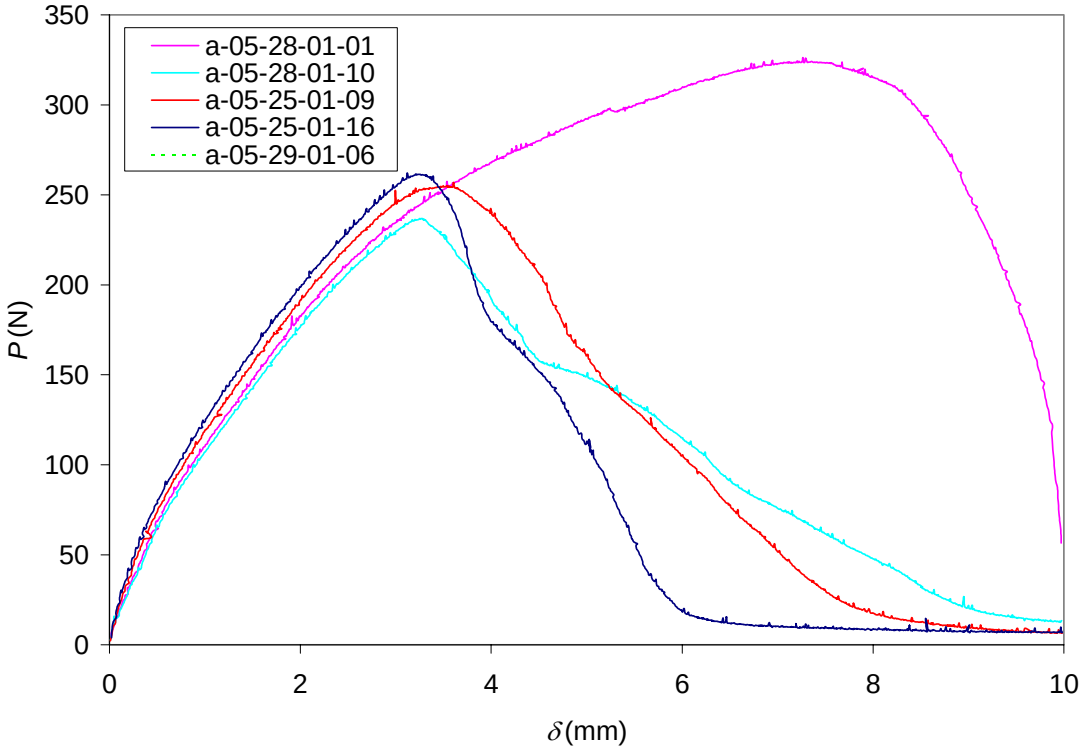

Figure C-32 Complex Data (L=0.0mm, R_d=5.0mm/min, *Temp*≈20°C, and *RH*≈25%).

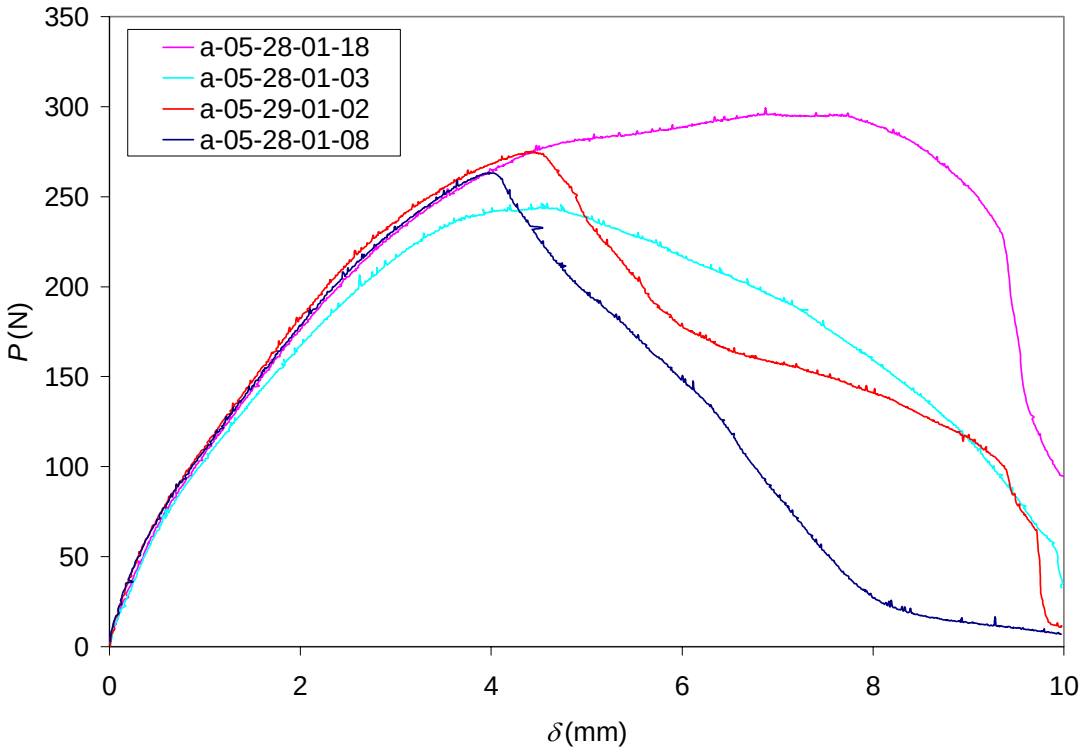

Figure C-33 Complex Data (L=6.0mm, R_d=5.0mm/min, *Temp*≈20°C, and *RH*≈25%).

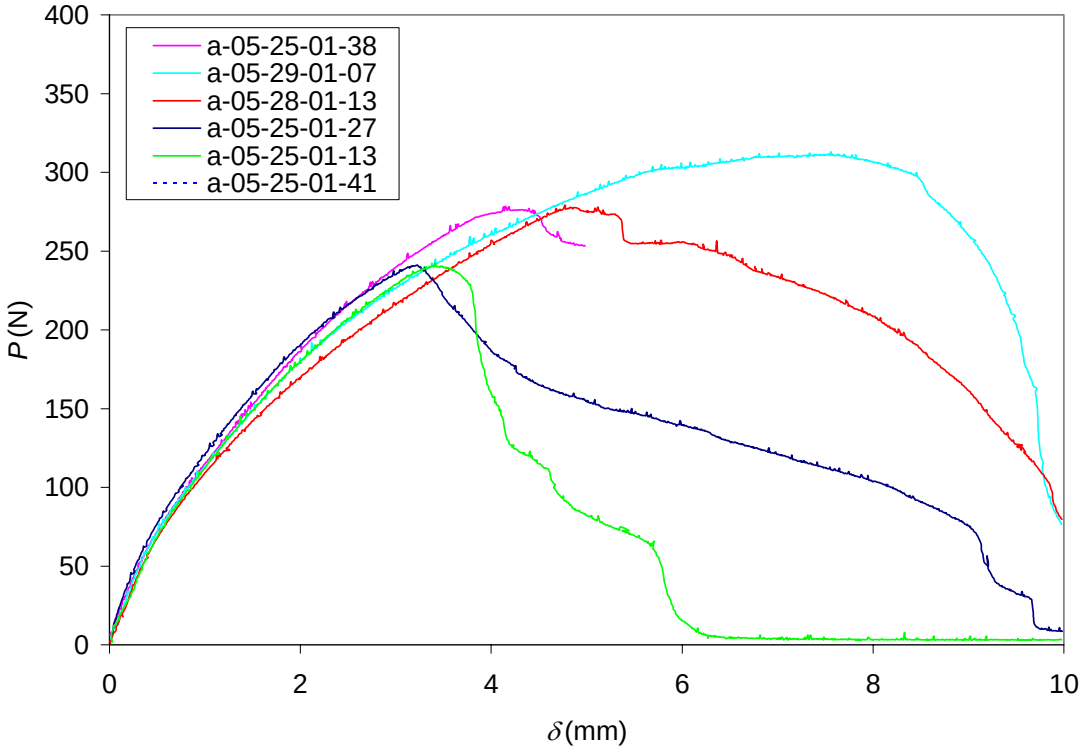

Figure C-34 Complex Data (L=12.0mm, R_d=5.0mm/min, *Temp*≈20°C, and *RH*≈25%).

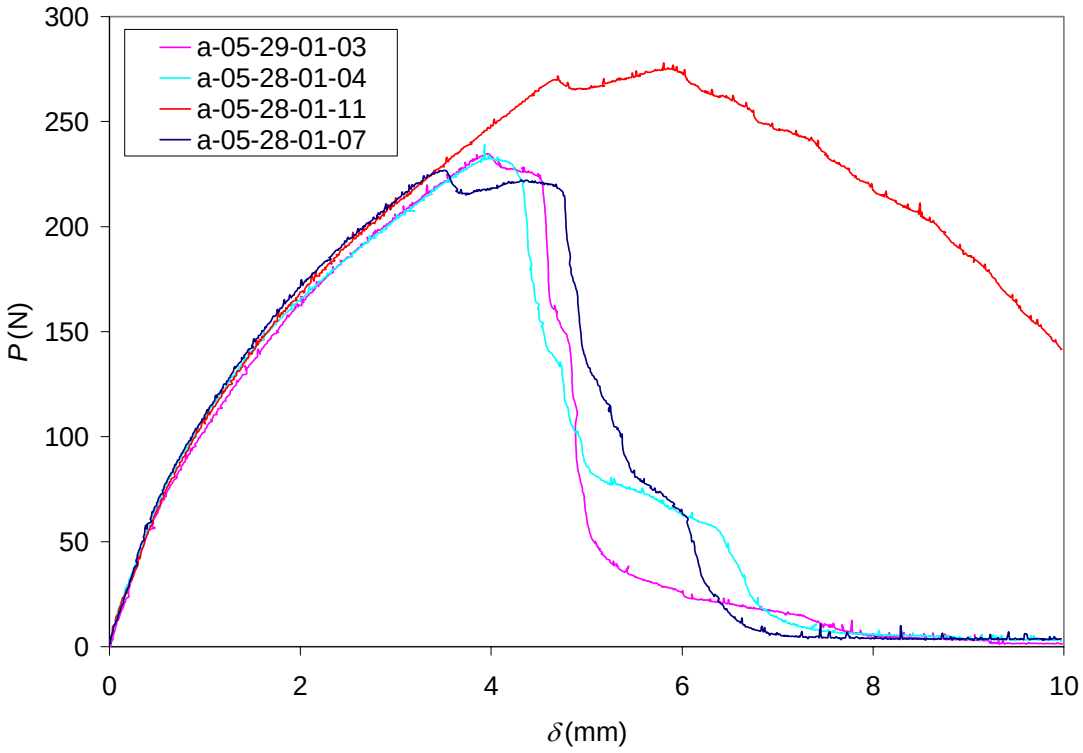

Figure C-35 Complex Data (L=16.0mm, R_d=5.0mm/min, *Temp*≈20°C, and *RH*≈25%).

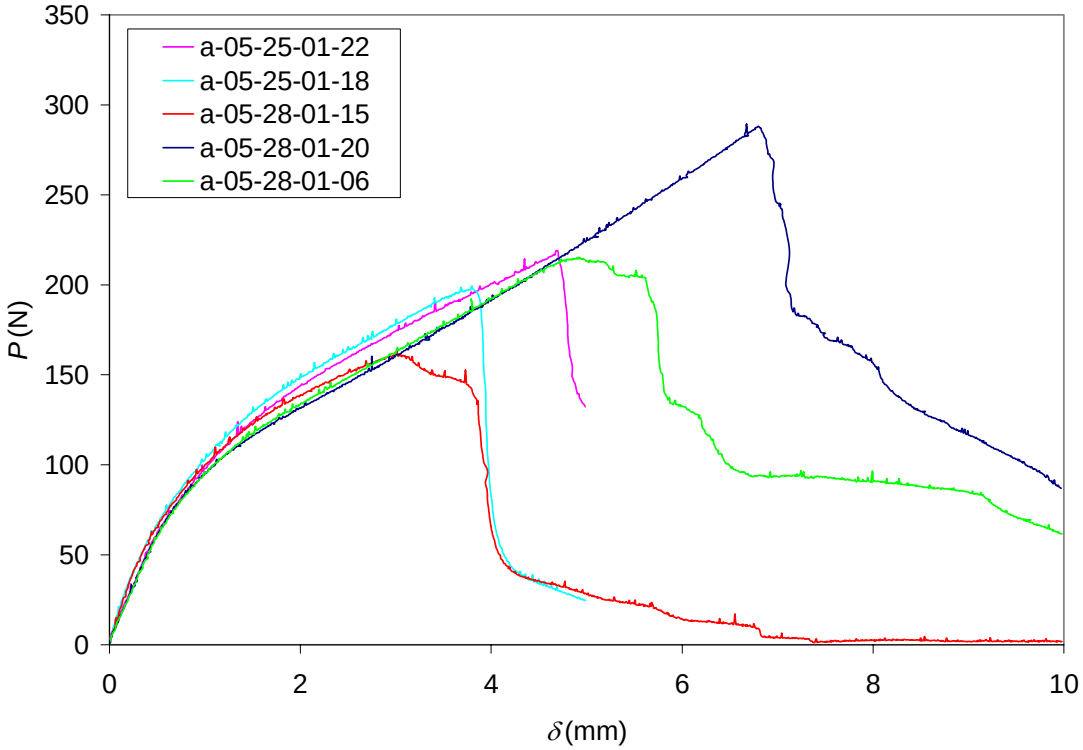

Figure C-36 Complex Data (L=20.0mm, R_d=5.0mm/min, *Temp*≈20°C, and *RH*≈25%).

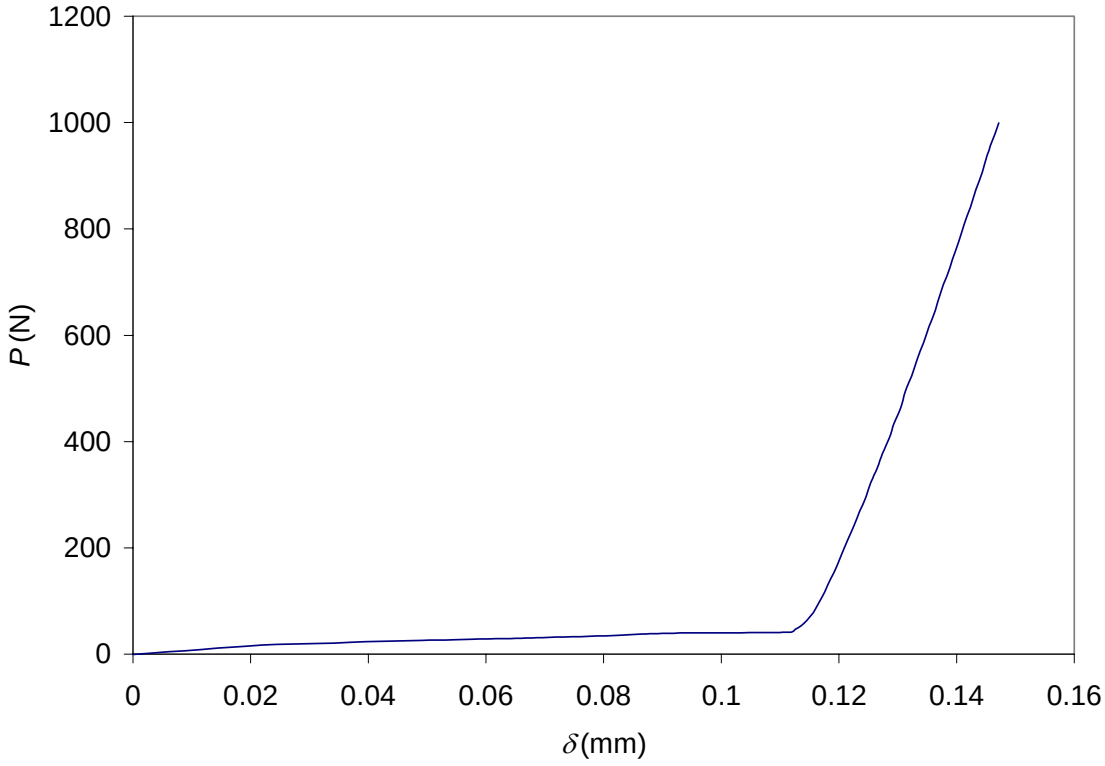

Figure C-37 Load-Train Data (θ_{Arcan}=0°, R_d=5.0mm/min, *Temp*≈20°C, and *RH*≈25%).

Appendix D

Failure Data

Table D-1A Arcan Strength Data.

Part #	θ_{Arcan} (°)	R_d (mm/min)	*Temp* (°C)	*RH* (%)	P_{max} (N)	δ_{max} (mm)	σ_a (MPa)	τ_a (MPa)	ε_a	γ_a
a-03-02-01-02	0	0.05	19	26	213.1	0.20	0.330	0.000	0.175	0.000
a-03-02-01-27	0	0.05	19	26	181.8	0.27	0.282	0.000	0.237	0.000
a-03-05-01-12	0	0.05	21	26	189.8	0.16	0.294	0.000	0.137	0.000
a-03-06-01-15	0	0.05	24	23	168.9	0.16	0.262	0.000	0.142	0.000
a-03-05-01-05	0	0.5	21	26	310.7	0.24	0.482	0.000	0.208	0.000
a-03-05-01-06	0	0.5	21	26	309.9	0.21	0.480	0.000	0.186	0.000
a-03-05-01-03	0	0.5	21	26	281	0.23	0.436	0.000	0.201	0.000
a-03-05-01-14	0	0.5	21	26	244	0.26	0.378	0.000	0.223	0.000
a-03-05-01-04	0	5	21	26	495.9	0.27	0.769	0.000	0.240	0.000
a-03-05-01-17	0	5	21	26	475.5	0.27	0.737	0.000	0.235	0.000
a-03-05-01-15	0	5	21	26	584.2	0.29	0.906	0.000	0.251	0.000
a-03-05-01-13	0	5	21	26	497.6	0.28	0.771	0.000	0.248	0.000
a-03-05-01-01	0	50	20	26	1283	0.46	1.989	0.000	0.403	0.000
a-03-05-01-10	0	50	20	26	1190	0.42	1.845	0.000	0.369	0.000
a-03-05-01-08	0	50	20	26	1315	0.41	2.038	0.000	0.358	0.000
a-03-05-01-02	0	50	20	26	1149	0.37	1.781	0.000	0.321	0.000
a-03-06-01-06	30	0.05	22	24	155.4	1.63	0.209	0.120	1.235	0.619
a-03-06-01-14	30	0.05	22	24	172.5	1.97	0.232	0.134	1.493	0.711
a-03-06-01-12	30	0.05	22	24	165.2	2.28	0.222	0.128	1.728	0.784
a-03-06-01-05	30	0.05	23	23	165.2	2.28	0.222	0.128	1.728	0.784
a-03-02-01-07	30	0.5	20	28	246.4	1.64	0.331	0.191	1.243	0.622
a-03-02-01-10	30	0.5	20	27	260.7	1.5	0.350	0.202	1.137	0.581
a-03-02-01-05	30	0.5	19	27	294.3	2.27	0.395	0.228	1.720	0.782
a-03-02-01-24	30	0.5	19	27	275.8	2.05	0.370	0.214	1.553	0.731
a-03-02-01-23	30	5	20	27	436.3	1.19	0.586	0.338	0.902	0.480
a-03-02-01-08	30	5	20	27	439.7	1.28	0.590	0.341	0.970	0.510
a-03-02-01-22	30	5	20	27	441.2	1.42	0.592	0.342	1.076	0.556
a-03-02-01-12	30	5	20	28	410.4	1.32	0.551	0.318	1.000	0.524
a-03-02-01-29	30	50	20	28	787.9	1.09	1.058	0.611	0.826	0.445
a-03-02-01-13	30	50	20	28	983.3	1.24	1.320	0.762	0.940	0.497
a-03-02-01-26	30	50	20	27	896.9	1.12	1.204	0.695	0.849	0.456
a-03-02-01-01	30	50	20	27	945.3	1.36	1.269	0.733	1.030	0.537

Table D-1B Arcan Strength Data.

Part #	θ_{Arcan} (°)	R_d (mm/min)	*Temp* (°)	*RH* (%)	P_{max} (N)	δ_{max} (mm)	σ_a (MPa)	τ_a (MPa)	ε_a	γa
a-03-02-01-15	60	0.05	19	25	194.0	4.87	0.150	0.260	2.130	1.306
a-03-06-01-13	60	0.05	24	23	180.5	6.26	0.140	0.242	2.738	1.363
a-03-06-01-03	60	0.05	24	23	186.8	6.14	0.145	0.251	2.686	1.359
a-03-06-01-09	60	0.05	24	24	169.1	5.54	0.131	0.227	2.423	1.337
a-03-02-01-21	60	0.5	19	28	206	3.25	0.160	0.277	1.422	1.185
a-03-02-01-28	60	0.5	19	28	206.8	3.05	0.160	0.278	1.334	1.162
a-03-02-01-17	60	0.5	19	28	176.7	2.56	0.137	0.237	1.120	1.095
a-03-02-01-25	60	0.5	19	28	233.3	3.35	0.181	0.313	1.465	1.195
a-03-02-01-14	60	5	19	29	314.2	2.66	0.244	0.422	1.164	1.110
a-03-02-01-06	60	5	19	29	323.5	2.44	0.251	0.434	1.067	1.075
a-03-02-01-11	60	5	19	28	374.5	3.39	0.290	0.503	1.483	1.200
a-03-02-01-18	60	5	19	28	383.1	3.03	0.297	0.514	1.325	1.160
a-03-02-01-30	60	50	19	29	630.1	2.36	0.488	0.846	1.032	1.061
a-03-02-01-09	60	50	19	29	597.5	2.13	0.463	0.802	0.932	1.016
a-03-02-01-31	60	50	19	29	610.2	2.52	0.473	0.819	1.102	1.088
a-03-02-01-03	60	50	19	29	547.4	2.39	0.424	0.735	1.045	1.066
a-03-02-01-16	90	0.05	18	24	207.9	6.24	0.000	0.322	0.000	1.390
a-03-02-01-04	90	0.05	17	25	210.5	6.41	0.000	0.326	0.000	1.394
a-03-02-01-20	90	0.05	18	25	218.3	5.92	0.000	0.338	0.000	1.380
a-03-02-01-19	90	0.05	19	25	207.7	6.67	0.000	0.322	0.000	1.401
a-03-06-01-07	90	0.5	24	25	277.4	6.64	0.000	0.430	0.000	1.400
a-03-06-01-11	90	0.5	24	25	259.9	6.63	0.000	0.403	0.000	1.400
a-03-06-01-10	90	0.5	22	24	312.4	7.07	0.000	0.484	0.000	1.411
a-03-06-01-01	90	0.5	22	24	306.6	6.66	0.000	0.475	0.000	1.401
a-03-06-01-08	90	5	24	25	483.9	6.92	0.000	0.750	0.000	1.407
a-03-06-01-02	90	5	24	25	445.3	6.22	0.000	0.690	0.000	1.389
a-03-06-01-16	90	5	24	25	367.1	6.05	0.000	0.569	0.000	1.384
a-03-06-01-04	90	5	24	25	458.6	6.82	0.000	0.711	0.000	1.405
a-03-05-01-16	90	50	21	26	863.2	6.09	0.000	1.338	0.000	1.385
a-03-05-01-11	90	50	21	26	731.6	5.49	0.000	1.134	0.000	1.366
a-03-05-01-07	90	50	21	26	708.1	4.87	0.000	1.098	0.000	1.340
a-03-05-01-09	90	50	21	26	829.1	5.63	0.000	1.285	0.000	1.370

Table D-2 Shape Factor Data.

Part #	w_a (mm)	R_d (mm/min)	*Temp* (°C)	*RH* (%)	P_{max} (N)	δ_{max} (mm)	σ_a (MPa)	ε_a
a-05-29-01-01	12.7	5	21	26	299.1	0.498	0.464	0.490
a-05-29-01-05	12.7	5	21	26	294.3	0.311	0.456	0.307
a-05-29-01-04	12.7	5	21	26	392.3	0.357	0.608	0.352
a-05-29-01-19	12.7	5	21	26	377.4	0.454	0.585	0.447
a-05-29-01-08	25.4	5	20	28	770.7	0.404	0.597	0.398
a-05-29-01-09	25.4	5	20	27	702.5	0.402	0.544	0.396
a-05-29-01-10	25.4	5	19	27	864.0	0.463	0.670	0.456
a-05-29-01-11	25.4	5	19	27	828.6	0.396	0.642	0.390
a-05-29-01-15	38.1	5	20	27	1052	0.576	0.544	0.567
a-05-29-01-13	38.1	5	20	27	1092	0.576	0.564	0.567
a-05-29-01-12	38.1	5	20	27	830.1	0.574	0.429	0.565
a-05-29-01-14	38.1	5	20	28	861.7	0.514	0.445	0.506

Table D-3A Load Control Data (Displacement Control Data).

Part #	θ_{Arcan} (°)	R_d (mm/min)	*Temp* (°C)	*RH* (%)	P_{max} (N)	δ_{max} (mm)	σ_a (MPa)	ε_a
a-08-07-01-03	0	0.5	23	35	196.3	0.181	0.304	0.178
a-08-09-01-03	0	0.5	23	35	204.6	0.212	0.317	0.209
a-08-09-01-05	0	0.5	23	35	210.4	0.211	0.326	0.208
a-08-09-01-19	0	0.5	23	35	182.6	0.186	0.283	0.183
a-08-05-01-06	0	5	23	35	293	0.188	0.454	0.185
a-08-05-01-11	0	5	23	35	289	0.177	0.448	0.174
a-08-05-01-03	0	5	23	35	257.3	0.17	0.399	0.167
a-08-05-01-09	0	5	23	35	223.6	0.18	0.347	0.177
a-08-08-01-06	0	50	23	35	717.3	0.344	1.112	0.339
a-08-09-01-13	0	50	23	35	772.5	0.348	1.197	0.343
a-08-09-01-22	0	50	23	35	719.3	0.355	1.115	0.349
a-08-09-01-12	0	50	23	35	709	0.342	1.099	0.337

Table D-3B Load Control Data (Load Control Data).

Part #	θ_{Arcan} (°)	R_l (N/sec)	*Temp* (°C)	*RH* (%)	P_{max} (N)	δ_{max} (mm)	σ_a (MPa)	ε_a
a-09-05-01-07	0	10	23	38	N/A	N/A		
a-09-05-01-02	0	10	23	38	250.1	0.33	0.388	0.325
a-09-05-01-10	0	10	23	38	244.8	0.288	0.379	0.283
a-09-05-01-04	0	10	23	38	251.4	0.303	0.390	0.298
a-08-08-01-22	0	15	23	34	242.6	0.342	0.376	0.337
a-08-08-01-04	0	15	23	34	248	0.337	0.384	0.332
a-08-07-01-38	0	15	23	34	248.2	0.349	0.385	0.344
a-08-08-01-29	0	15	23	34	259.6	0.333	0.402	0.328
a-08-09-01-01	0	200	24	35	272.2	0.245	0.422	0.241
a-08-98-01-09	0	200	24	35	286.2	0.259	0.444	0.255
a-09-05-01-08	0	2000	23	37	205.3	0.143	0.318	0.141
a-09-05-01-09	0	2000	23	37	587.1	0.213	0.910	0.210
a-09-05-01-05	0	2000	23	37	472.8	0.173	0.733	0.170
a-09-05-01-06	0	2000	23	37	213.3	0.138	0.331	0.136

Table D-4A Complex Load Data ($Arcan_m$ Testing).

Part #	θ_{Arcan} (°)	R_d (mm/min)	*Temp* (°C)	*RH* (%)	P_{max} (N)	δ_{max} (mm)	σ_a (MPa)	τ_a (MPa)
a-04-16-01-14	0	5	21	26	374.8	0.296	0.581	0.000
a-05-25-01-29	0	5	21	26	407	0.287	0.631	0.000
a-05-25-01-33	0	5	21	26	420.9	0.234	0.652	0.000
a-05-25-01-32	0	5	21	26	356.3	0.303	0.552	0.000
a-05-25-01-26	15	5	20	28	364	0.551	0.545	0.146
a-05-25-01-20	15	5	20	27	325.2	0.617	0.487	0.130
a-05-25-01-23	15	5	19	27	295.6	0.583	0.443	0.119
a-04-16-01-13	15	5	19	27	311.7	0.663	0.467	0.125
a-05-25-01-31	30	5	20	27	311.6	1.55	0.418	0.241
a-04-16-01-17	30	5	20	27	313.1	1.64	0.420	0.243
a-05-25-01-35	30	5	20	27	305.4	1.72	0.410	0.237
a-05-25-01-30	30	5	20	28	311.9	1.59	0.419	0.242
a-05-25-01-24	45	5	19	25	299.3	2.73	0.328	0.328
a-05-25-01-21	45	5	24	23	289	2.84	0.317	0.317
a-05-25-01-25	45	5	24	23	297.7	2.67	0.326	0.326
a-05-25-01-17	45	5	24	24	303.1	3.07	0.332	0.332
a-05-25-01-28	60	5	19	29	317.5	5.18	0.246	0.426
a-05-25-01-36	60	5	19	29	289.3	4.72	0.224	0.388
a-05-25-01-34	60	5	19	28	315.6	4.72	0.245	0.424
a-04-16-01-11	60	5	19	28	347.1	5.63	0.269	0.466

Table D-4B Complex Load Data (Complex Load Testing).

Part #	L (mm)	R_d (mm/min)	$Temp$ (°C)	RH (%)	P_{max} (N)	δ_{max} (mm)	σ_{a1} (Mpa)	σ_{a2} (Mpa)	$\sigma_{fixture}$ (MPa)	σ_{eng} (MPa)	τ_a (MPa)
a-05-28-01-01	0	5	21	26	264.5	3.86	0.205	0.000	0.026	0.231	0.355
a-05-28-01-10	0	5	21	26	236.8	3.27	0.184	0.000	0.026	0.210	0.318
a-05-25-01-09	0	5	21	26	252.4	3.48	0.196	0.000	0.026	0.222	0.339
a-05-25-01-16	0	5	21	26	261	3.29	0.202	0.000	0.026	0.229	0.350
a-05-28-01-18	6	5	20	27	283.1	5.23	0.219	0.311	0.026	0.504	0.380
a-05-28-01-03	6	5	19	27	239	4.33	0.185	0.263	0.026	0.421	0.321
a-05-29-01-02	6	5	19	27	273.5	4.52	0.212	0.300	0.026	0.486	0.367
a-05-29-01-08	6	5	20	27	262.4	4.05	0.203	0.288	0.026	0.465	0.352
a-05-25-01-38	12	5	20	27	276	4.34	0.214	0.606	0.026	0.794	0.370
a-05-29-01-07	12	5	20	27	302.4	5.85	0.234	0.664	0.026	0.872	0.406
a-05-28-01-13	12	5	20	28	277.1	4.91	0.215	0.609	0.026	0.797	0.372
a-05-25-01-27	12	5	19	25	237.3	3.24	0.184	0.521	0.026	0.679	0.319
a-05-25-01-13	12	5	24	23	240.1	3.46	0.186	0.527	0.026	0.687	0.322
a-05-29-01-03	16	5	24	24	232.2	3.95	0.180	0.680	0.026	0.834	0.312
a-05-28-01-04	16	5	19	29	232.1	4.01	0.180	0.680	0.026	0.833	0.312
a-05-28-01-11	16	5	19	29	269.3	4.7	0.209	0.789	0.026	0.971	0.361
a-05-28-01-07	16	5	19	28	226.8	3.51	0.176	0.664	0.026	0.814	0.304
a-05-25-01-22	20	5	19	28	218.8	4.7	0.170	0.801	0.026	0.944	0.294
a-05-28-01-18	20	5	19	28	196.3	3.84	0.152	0.719	0.026	0.845	0.264
a-05-28-01-15	20	5	19	28	162.8	3	0.126	0.596	0.026	0.696	0.219
a-05-28-01-20	20	5	19	28	287	6.83	0.222	1.051	0.026	1.247	0.385
a-05-28-01-06	20	5	19	28	214.1	4.8	0.166	0.784	0.026	0.924	0.287
a-04-16-01-09	20	5	19	28	254.9	5.14	0.198	0.933	0.026	1.105	0.342

Appendix E

Data Analysis

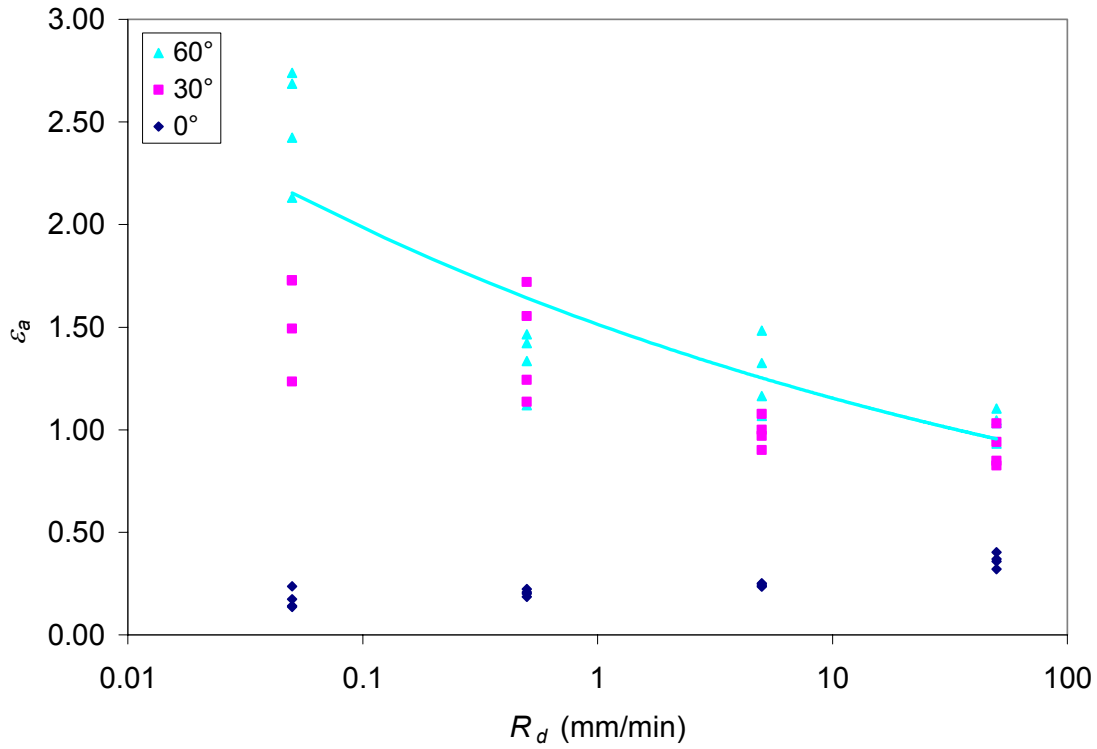

Figure E-1 ε_a vs. R_d – VHB 4950 at 20°C and 25%*RH*.

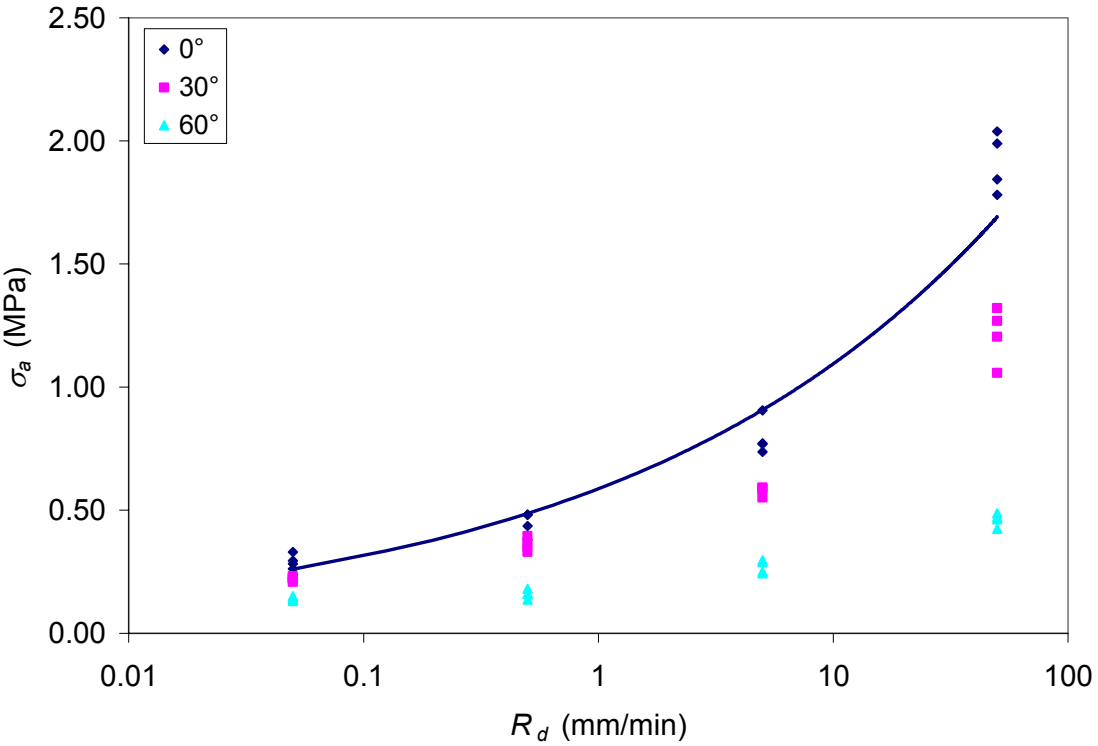

Figure E-2 σ_a vs. R_d – VHB 4950 at 20°C and 25%*RH*.

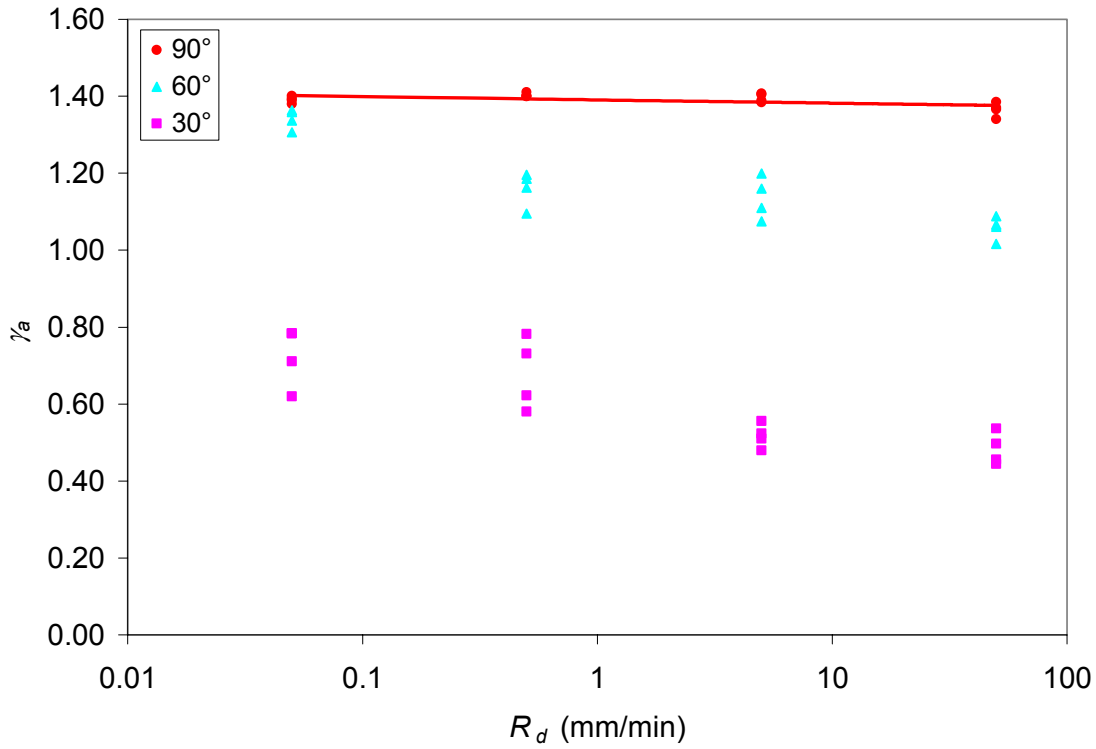

Figure E-3 γ_a vs. R_d – VHB 4950 at 20°C and 25%*RH*.

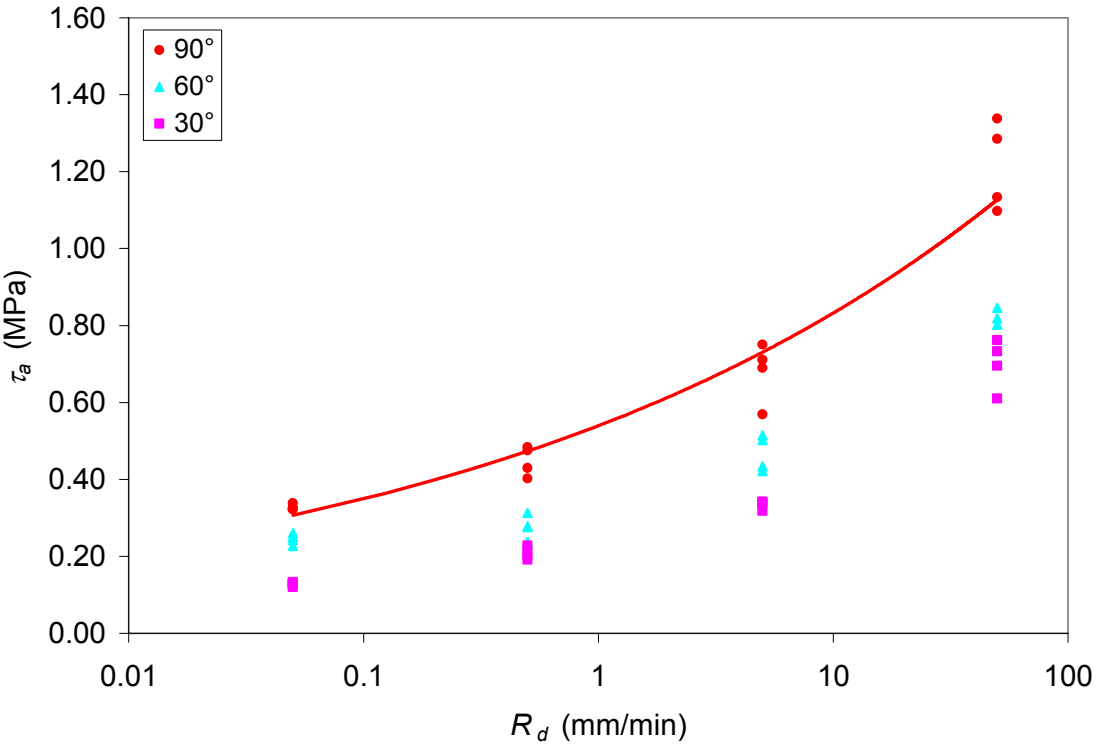

Figure E-4 τ_a vs. R_d – VHB 4950 at 20°C and 25%*RH*.

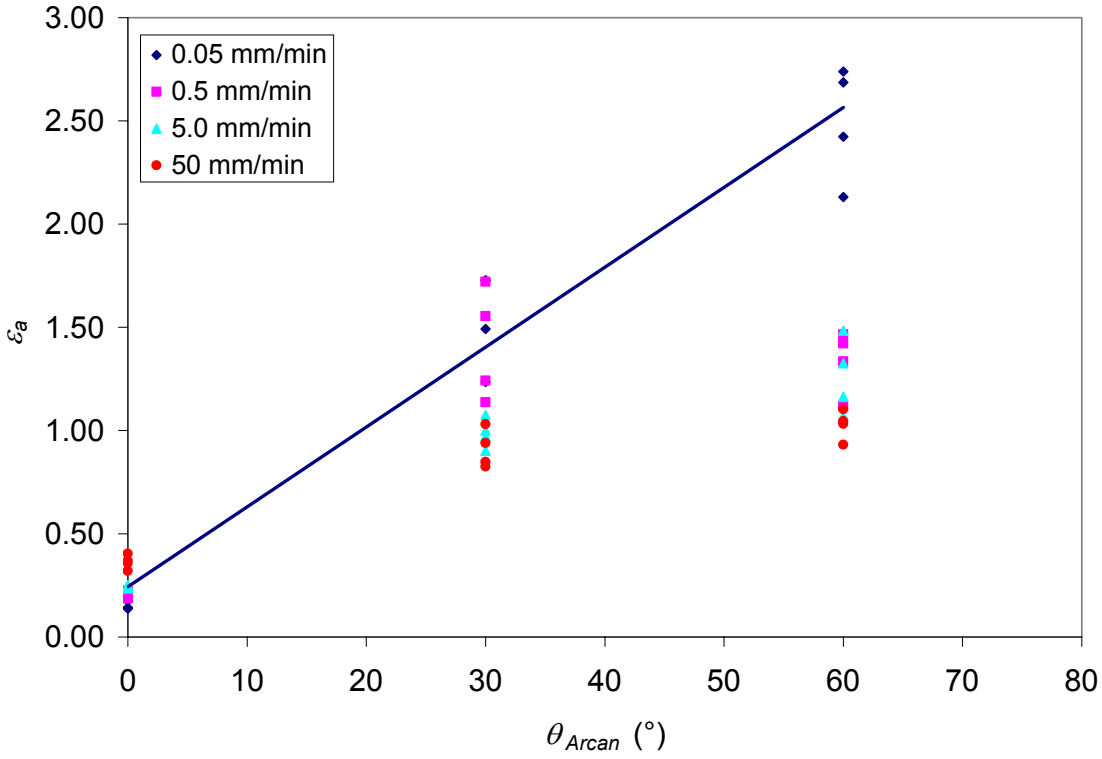

Figure E-5 ε_a vs. θ_{Arcan} – VHB 4950 at 20°C and 25%*RH*.

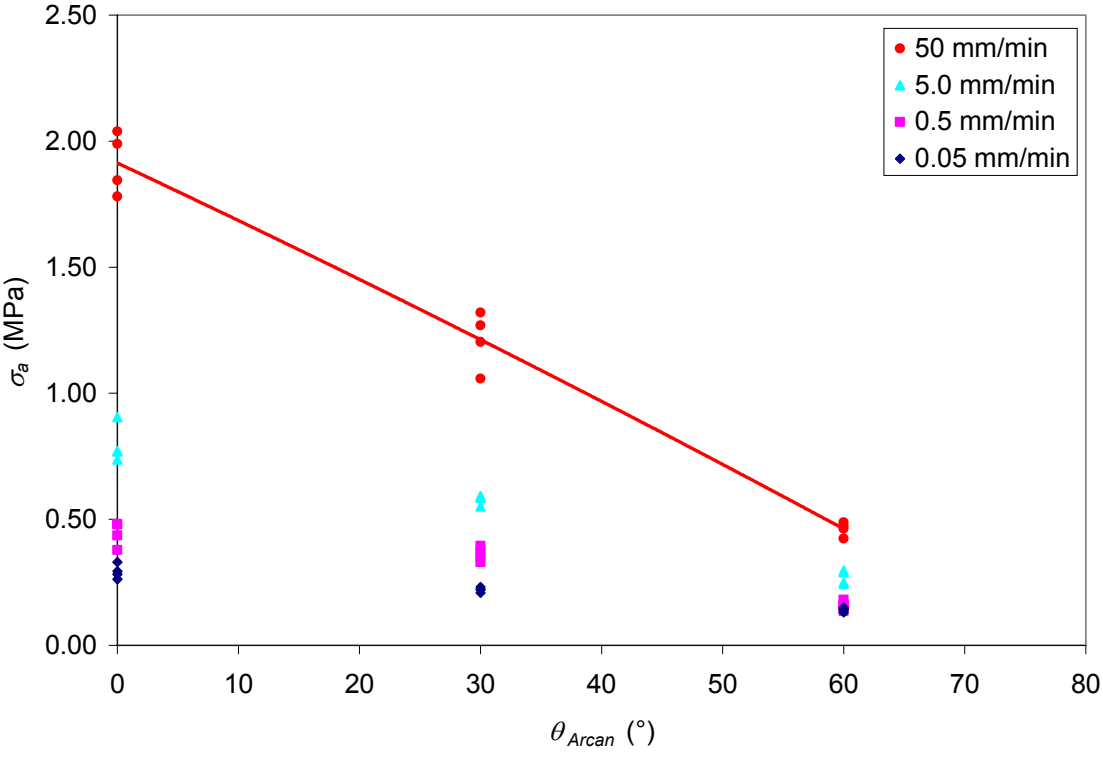

Figure E-6 σ_a vs. θ_{Arcan} – VHB 4950 at 20°C and 25%*RH*.

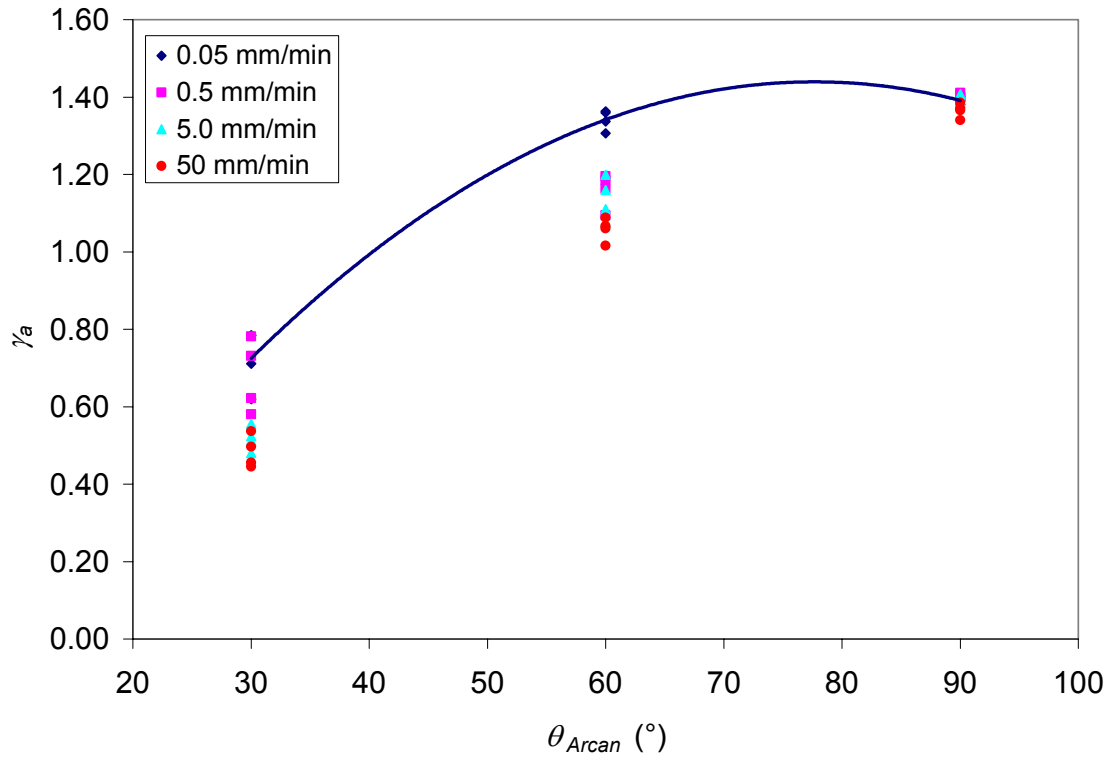

Figure E-7 γ_a vs. θ_{Arcan} – VHB 4950 at 20°C and 25%*RH*.

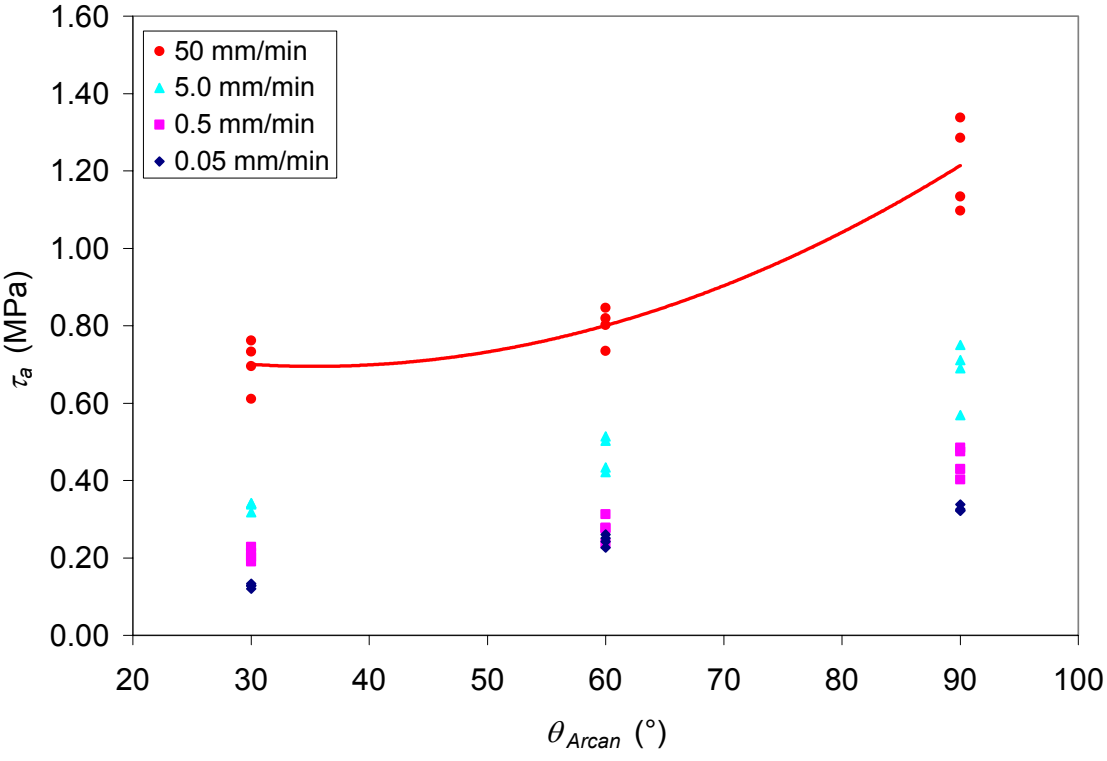

Figure E-8 τ_a vs. θ_{Arcan} – VHB 4950 at 20°C and 25%*RH*.

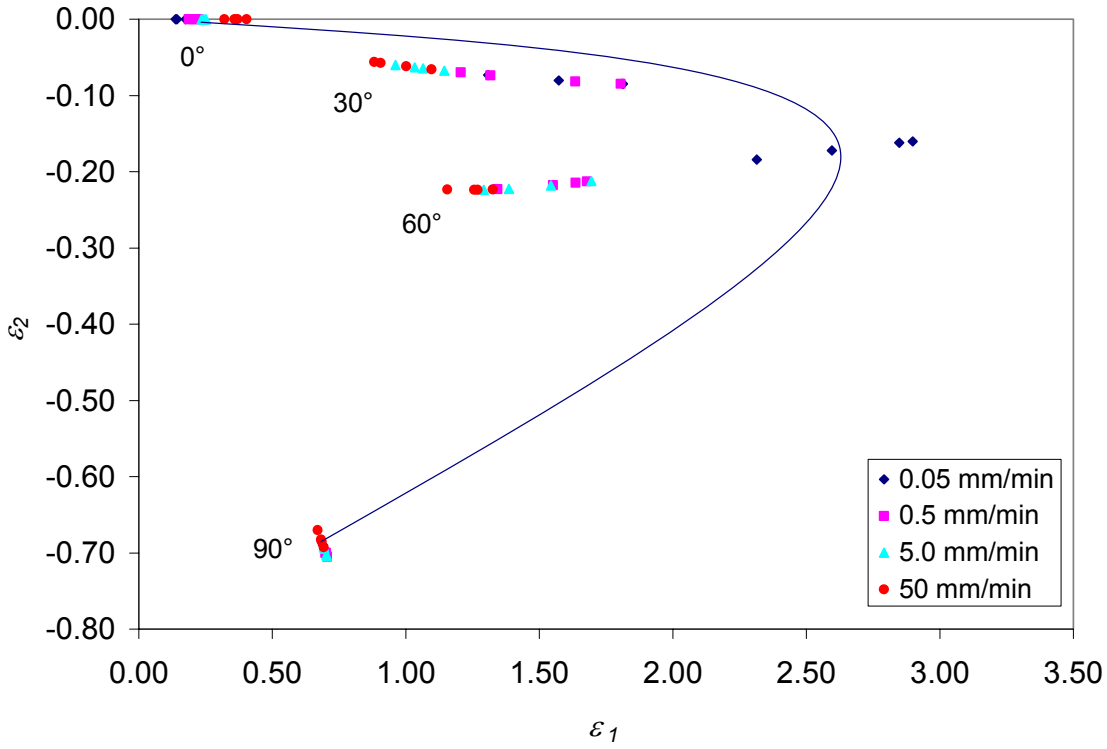

Figure E-9 Principal Strains – VHB 4950 at 20°C and 25%*RH*.

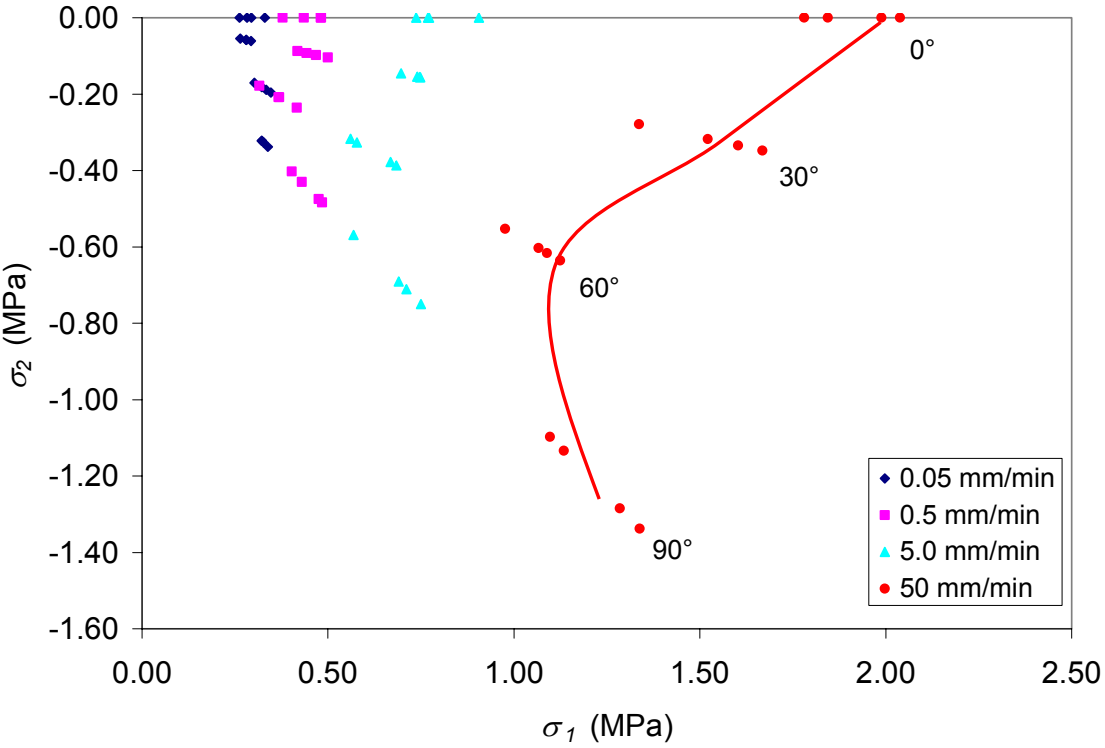

Figure E-10 Principal Stresses – VHB 4950 at 20°C and 25%*RH*.

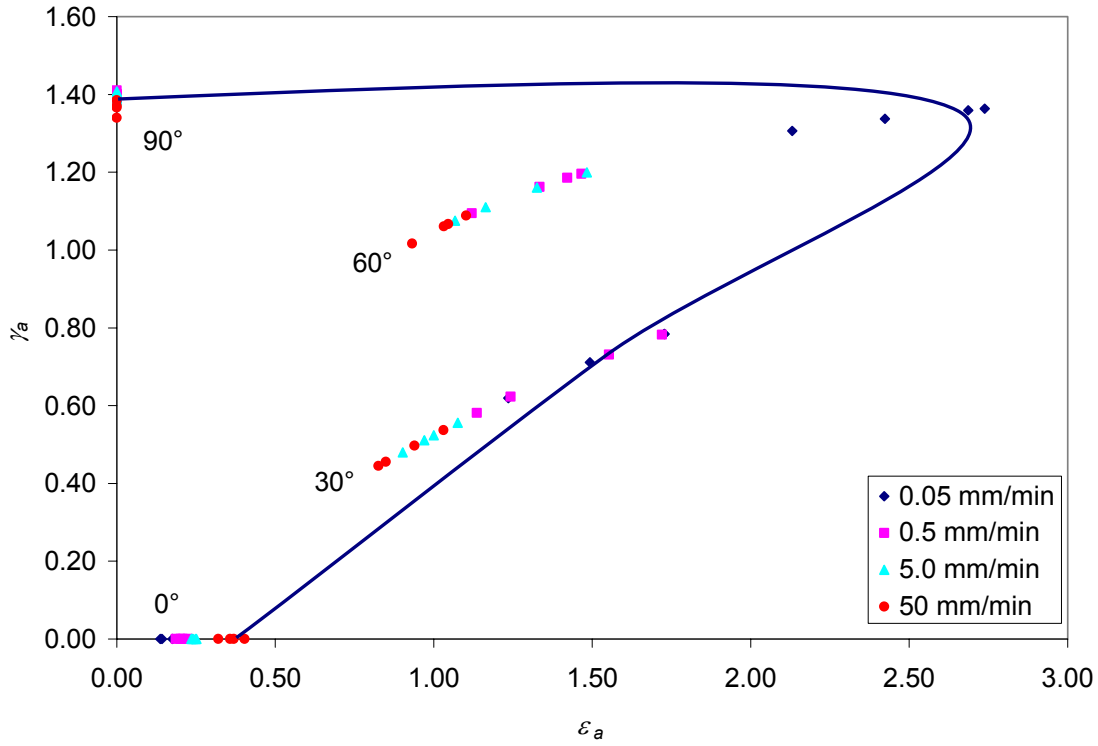

Figure E-11 Strain Based Design Envelope – VHB 4950 at 20°C and 25%*RH*.

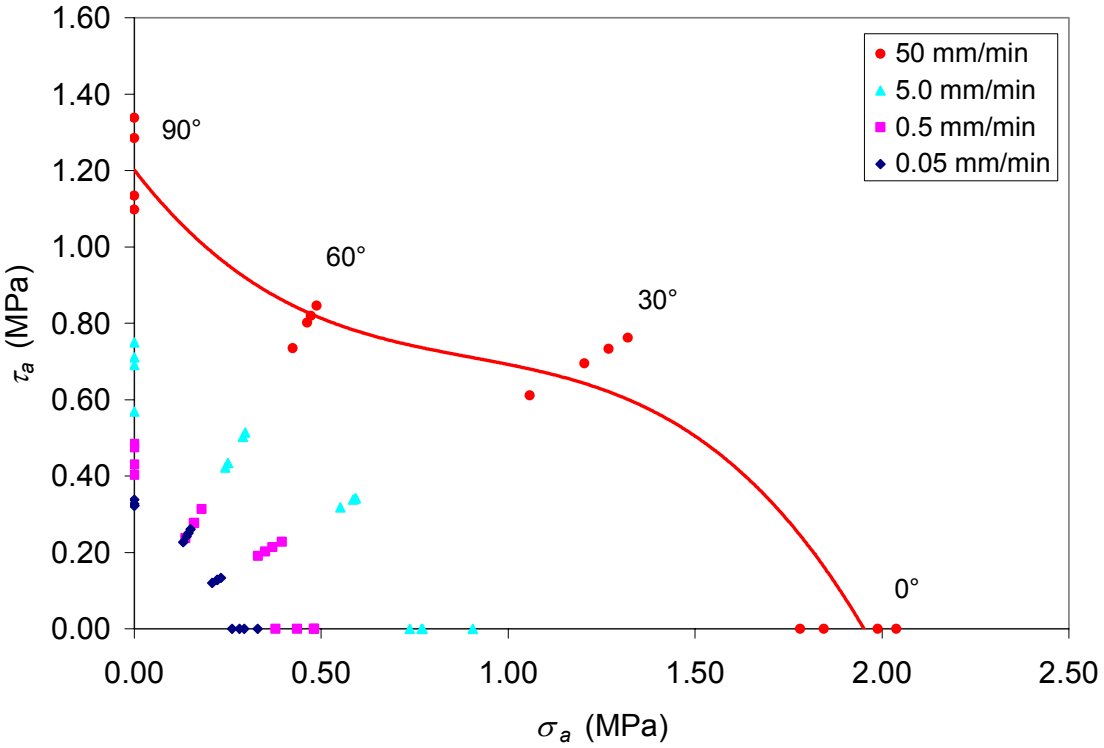

Figure E-12 Stress Based Design Envelope – VHB 4950 at 20°C and 25%*RH*.

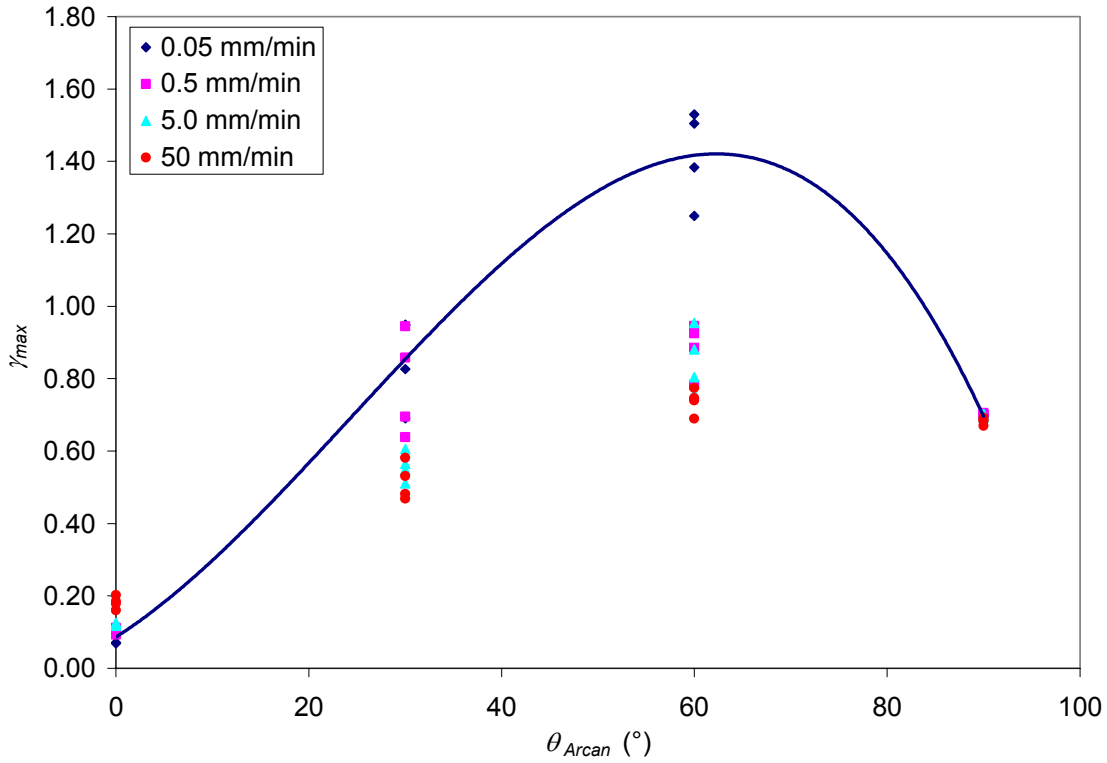

Figure E-13 Maximum Shear Strain vs. θ_{Arcan} – VHB 4950 at 20°C and 25%*RH*.

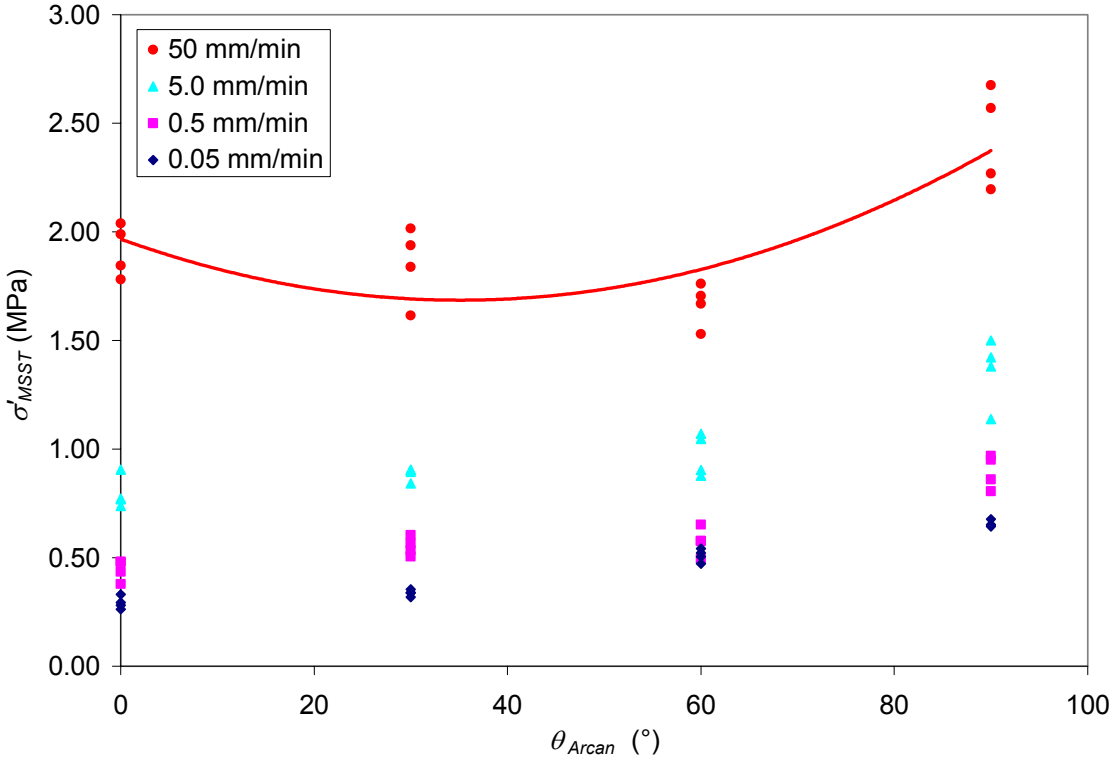

Figure E-14 MSST vs. θ_{Arcan} – VHB 4950 at 20°C and 25%*RH*.

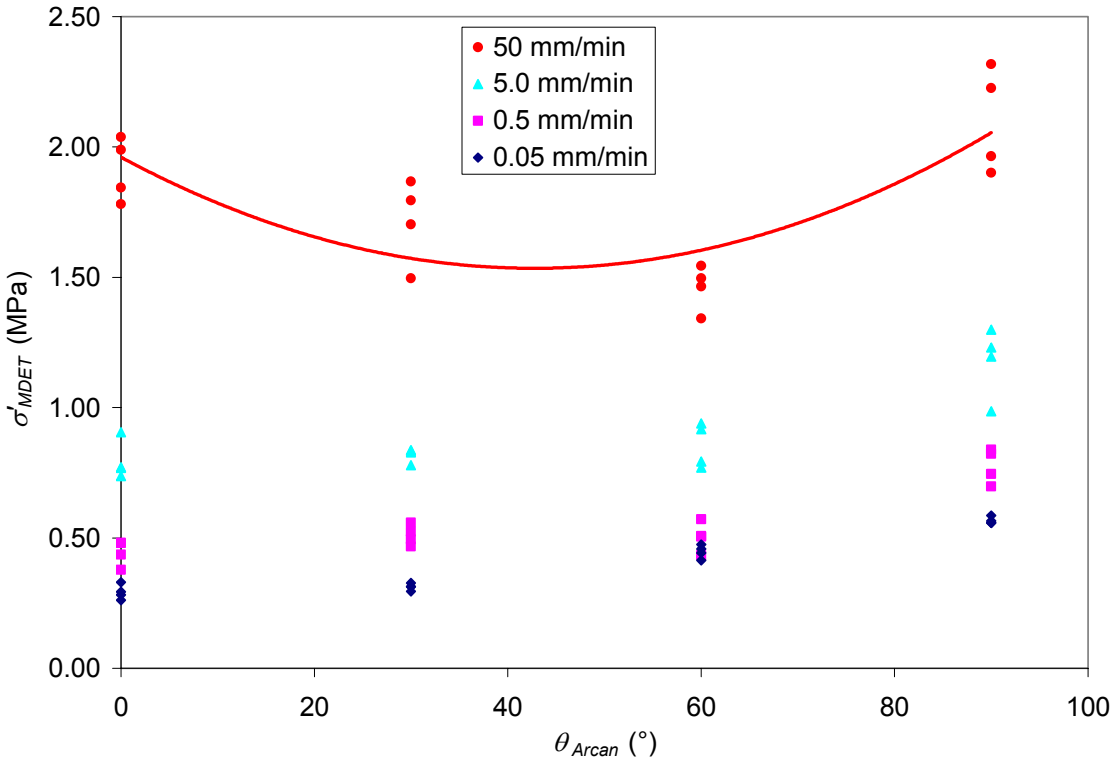

Figure E-15 MDET vs. θ_{Arcan} – VHB 4950 at 20°C and 25%*RH*.

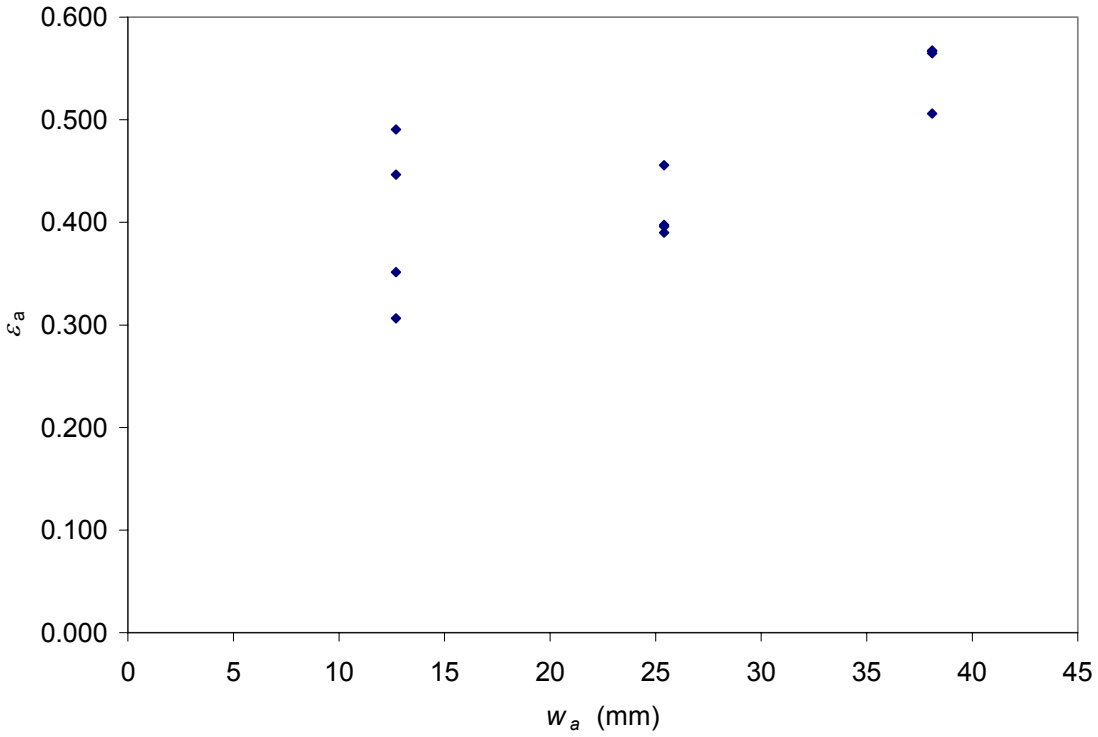

Figure E-16 ε_a vs. w_a – VHB 4950 at 20°C and 25%*RH*.

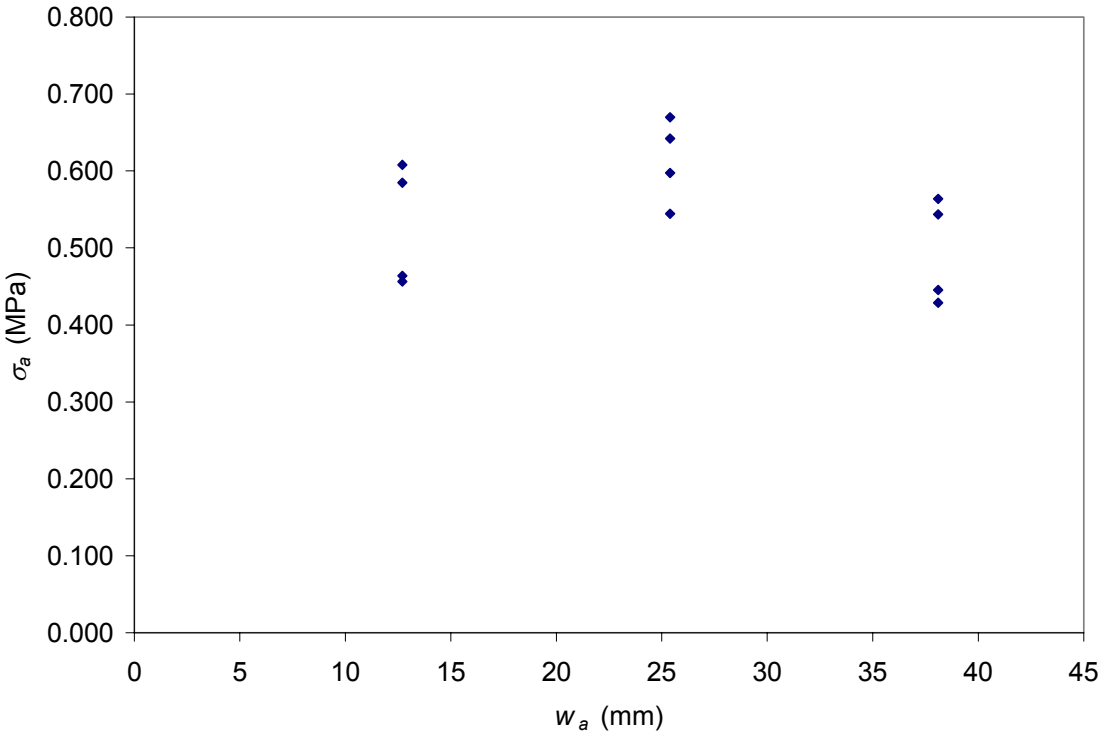

Figure E-17 σ_a vs. w_a – VHB 4950 at 20°C and 25%*RH*.

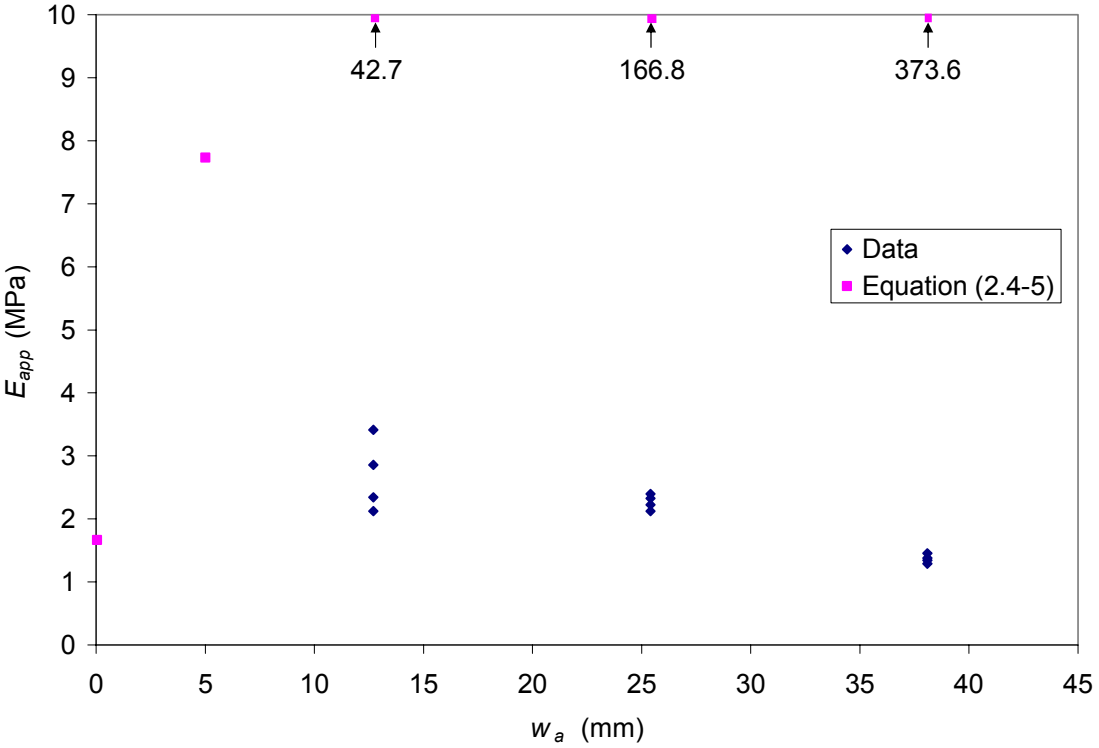

Figure E-18 E_{app} vs. w_a – VHB 4950 at 20°C and 25%*RH*.

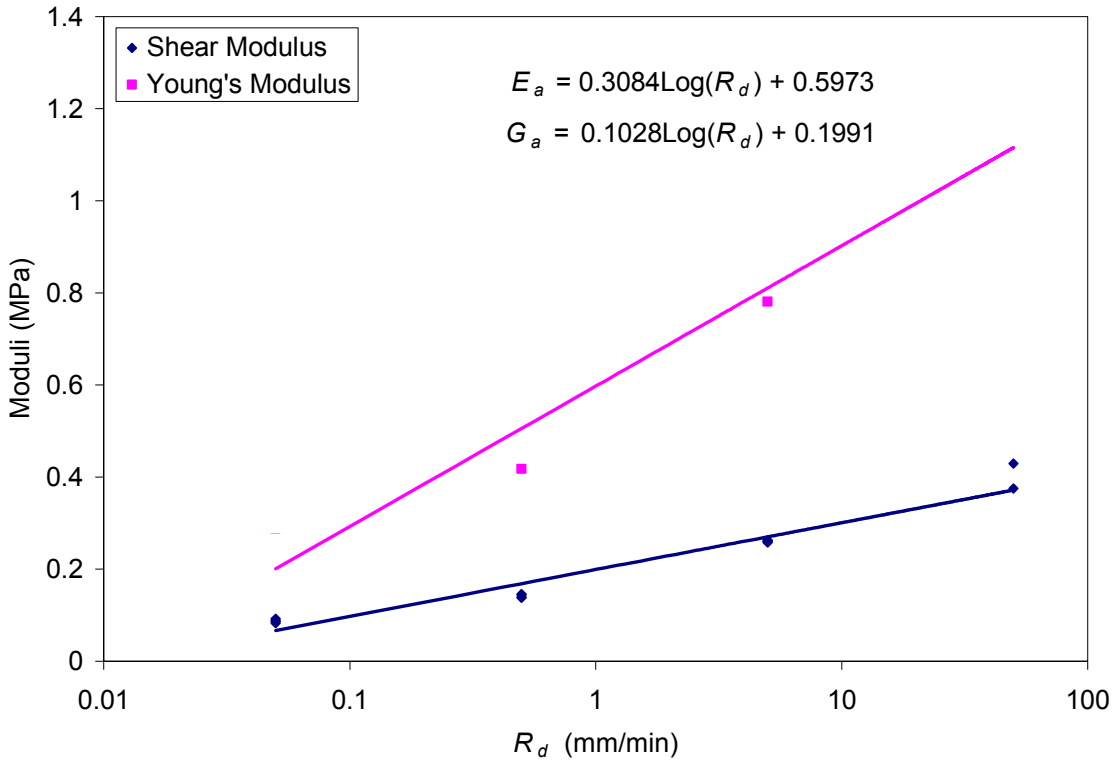

Figure E-19 Adhesive Moduli vs. R_d – VHB 4950 at 20°C and 25%*RH*.

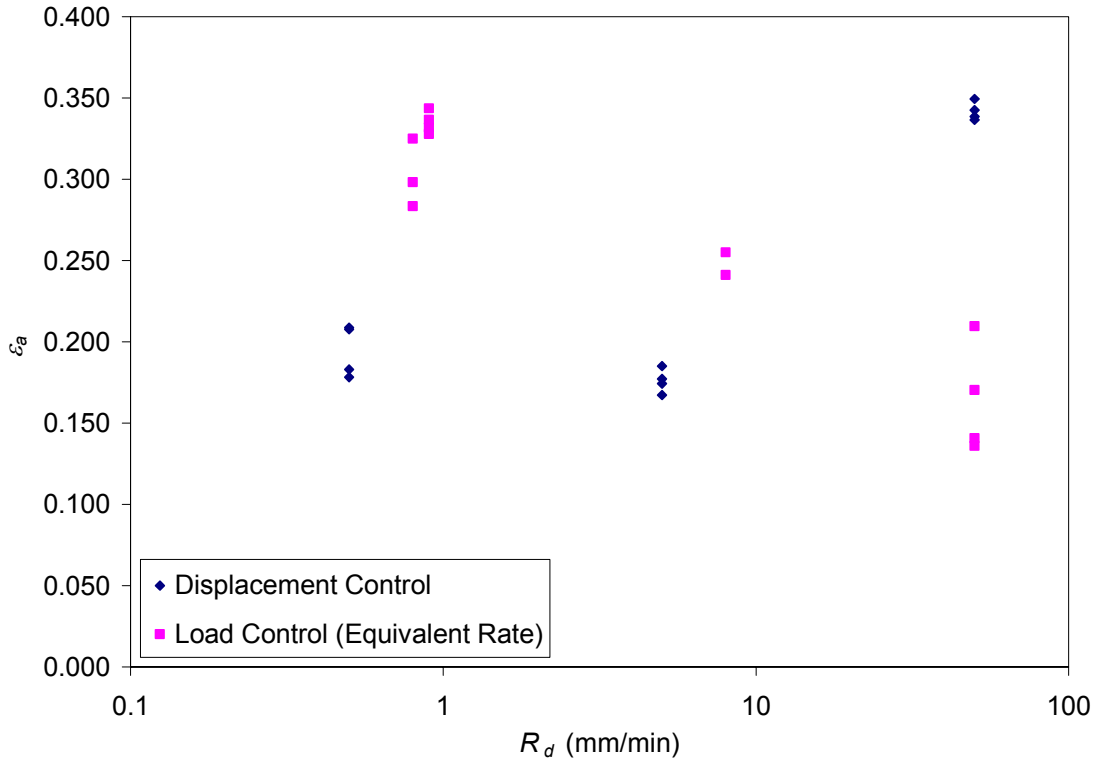

Figure E-20 ε_a vs. R_d – VHB 4950 at 25°C and 35%*RH*.

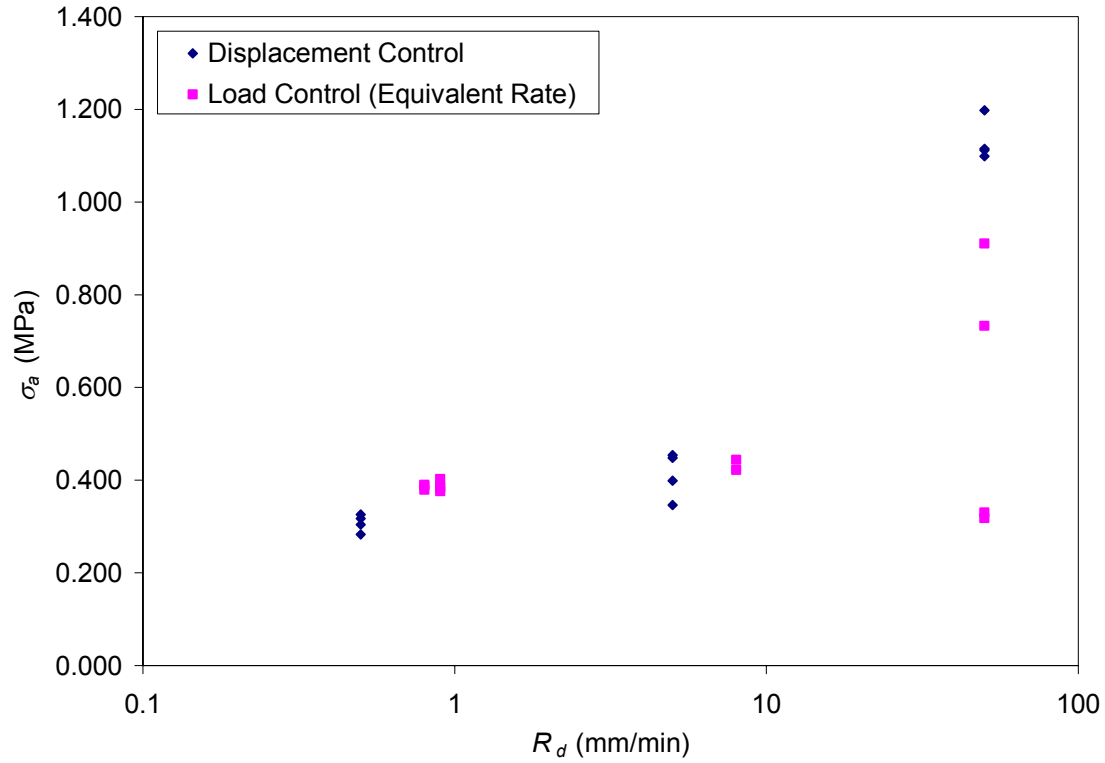

Figure E-21 σ_a vs. R_d – VHB 4950 at 20°C and 25%*RH*.

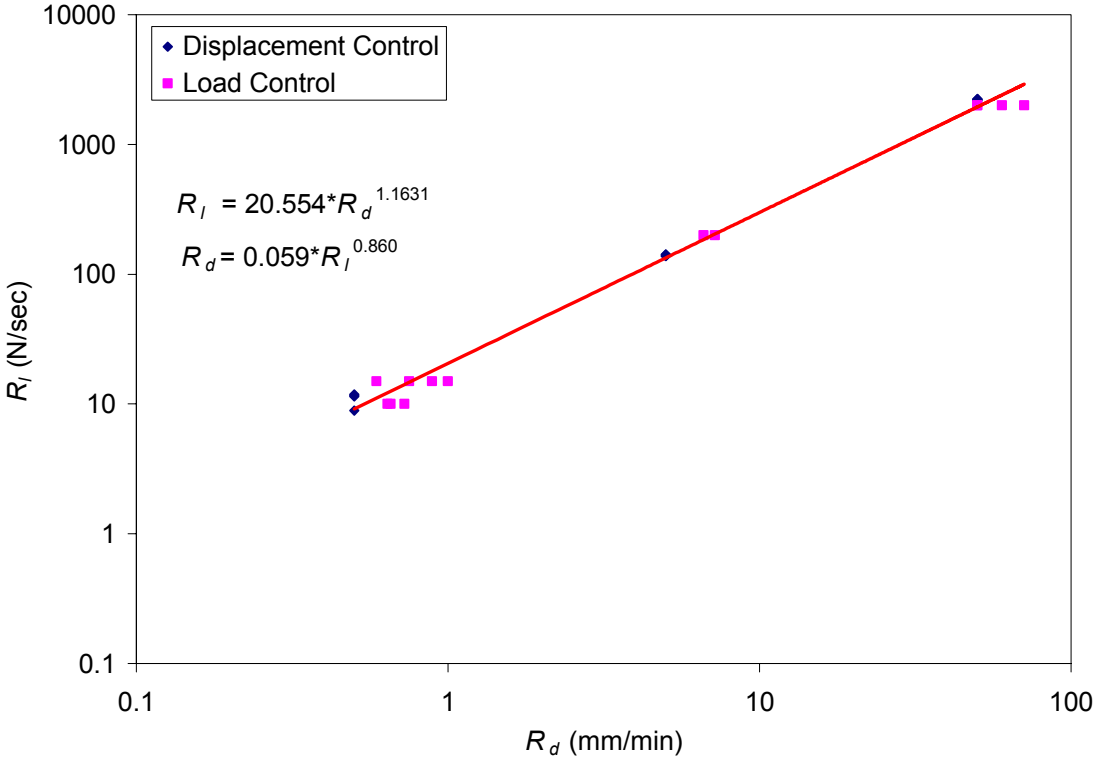

Figure E-22 Load/Displacement Rate Conversion– VHB 4950 at 25°C and 35%*RH*.

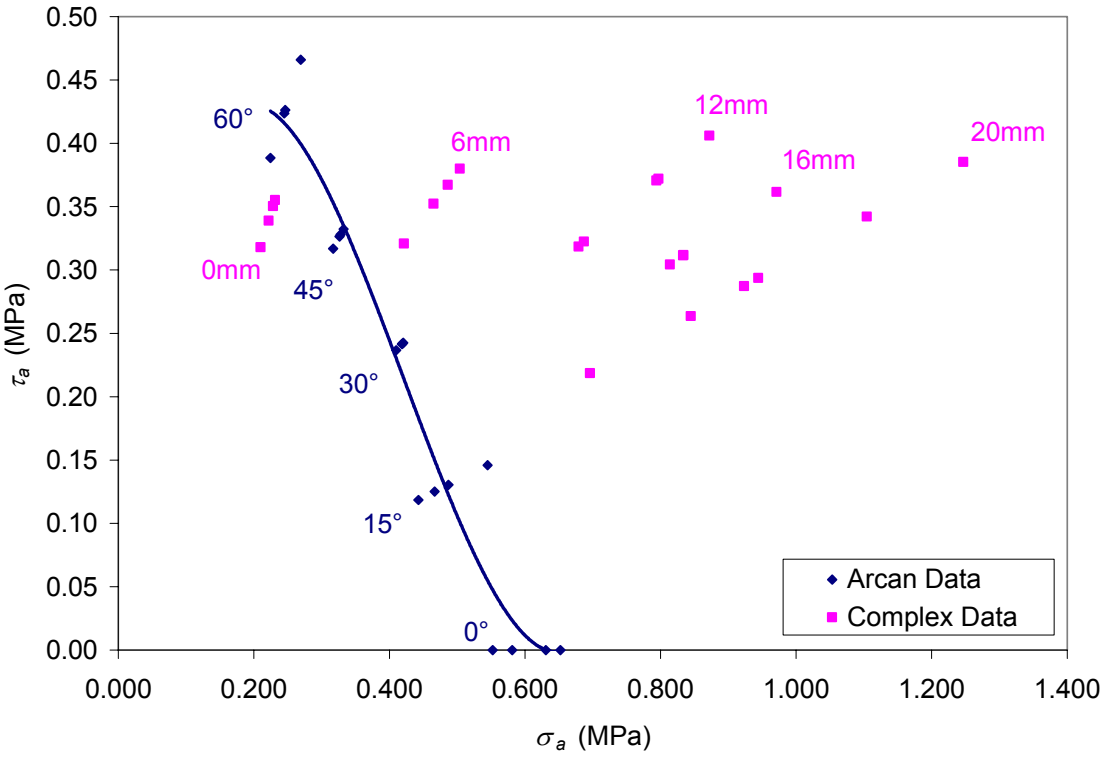

Figure E-23 Gradient Normal Stress Effect– VHB 4950 at 20°C and 25%*RH*.

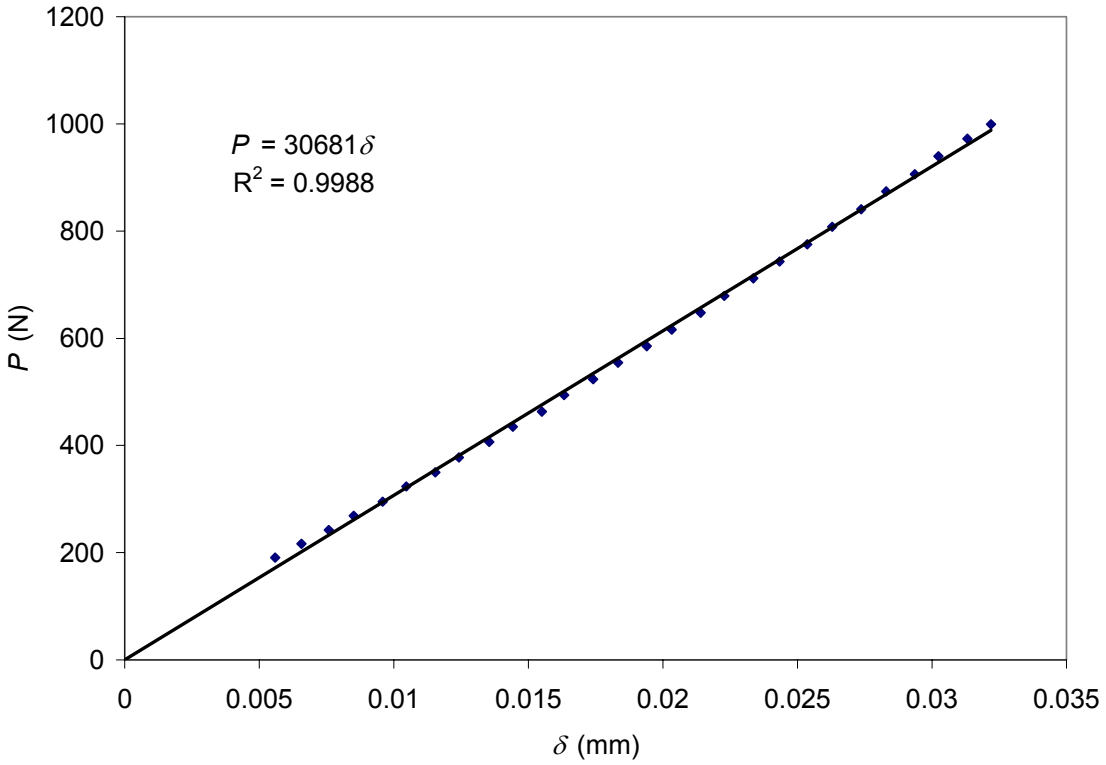

Figure E-24 Adjusted Load-Train Stiffness – VHB 4950 at 20°C and 25%*RH*.